A thesis submitted in partial fulfilment of the requirements for the degree of Doctor of Philosophy

Dynamics of Quantum Many-Body Systems with Long-Range Interactions

Anton S. Buyskikh

September 4, 2017

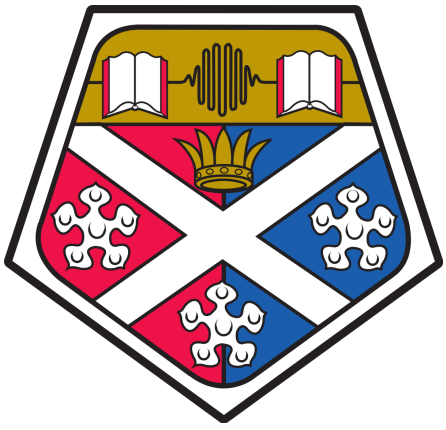

University of Strathclyde
Department of Physics

This thesis is the result of the author's original research. It has been composed by the author and has not been previously submitted for examination which has led to the award of a degree.

Signed:

Date:

Acknowledgments

At this point I would like to look back at the last five years and thank everyone who supported me during my PhD at both the University of Pittsburgh and the University of Strathclyde.

Firstly, I would like to express my gratitude to my advisor Andrew Daley for the continuous support of my PhD study and related research, for enthusiasm and immense knowledge. His guidance has helped me continuously during my research and the writing of this thesis.

Besides my advisor, I would like to thank my viva committee: Chris Hooley and Erling Riis for their insightful comments, but also for the hard questions which pushed me to widen my research from various perspectives.

My sincere thanks also goes to our collaborators on both continents: Ben Lanyon, David Pekker, Dirk Schuricht, Fabian Essler, Johannes Schachenmayer, Luca Tagliacozzo, and Maurizio Fagotti. It was my pleasure to work with you all.

I would like to thank all my close friends from Pittsburgh with whom I started this adventure together. In particular, I would like to mention Azarin, Ben, Binbin, Dritan, Kevin, Simone, Sumit, and Zhuoni. It was a great fun knowing you and I hope to see you again. And here comes the Strathclyde squad: Alex, Araceli, Enrico, Francois, Guanglei, Jacopo, Jennifer, Johan, Jorge, Liam, Matteo, Rosaria, Saubhik, and Suzanne. Thank you guys for all the fun we had and for the stimulating physics discussions. You guys made Glasgow.

Last but not the least, I would like to thank my girlfriend Rosy and my family for your exceptional patience due to the lack of communication with you over periods of intense work. Without any doubt your support was the one and major factor which helped me to overcome difficulties in my most difficult times.

Abstract

Constantly increasing experimental possibilities with strongly correlated systems of ultracold atoms in optical lattices and trapped ions make them one of the most promising candidates for quantum simulation and quantum computation in the near future, and open new opportunities for study many-body physics. Out-of-equilibrium properties of such complex systems present truly fascinating and rich physics, which is yet to be fully understood.

This thesis studies many-body dynamics of quantum systems with long-range interactions and addresses a few distinct issues. The first one is related to a growing interest in the use of ultracold atoms in optical lattices to simulate condensed matter systems, in particular to understand their magnetic properties. In our project on tilted optical lattices we map the dynamics of bosonic particles with resonantly enhanced long-range tunnelings onto a spin chain with peculiar interaction terms. We study the novel properties of this system in and out of equilibrium. The second main topic is the dynamical growth of entanglement and spread of correlations between system partitions in quench experiments. Our investigation is based on current experiments with trapped ions, where the range of interactions can be tuned dynamically from almost neighboring to all-to-all. We analyze the role of this interaction range in non-equilibrium dynamics. The third topic we address is a new method of quantum state estimation, certified Matrix Product State (MPS) tomography, which has potential applications in regimes unreachable by full quantum state tomography.

The investigation of quantum many-body systems often goes beyond analytically solvable models; that is where numerical simulations become vital. The majority of results in this thesis were obtained via the Density Matrix Renormalization Group (DMRG) methods in the context of the MPS and Matrix Product Operator (MPO) formalism. Further developing and optimizing these methods made it possible to obtain eigenstates and thermal states as well as to calculate the time-dependent dynamics in quenches for experimentally relevant regimes.

Contents

1. Introduction **1**

I. Background 11

2. Atomic Physics **13**
2.1. Alkali Atom Physics . . . 13
2.1.1. An Atom in the Electromagnetic Field . . . 15
2.2. A Dilute, Ultracold Gas of Atoms . . . 18
2.2.1. The Gross-Pitaevskii Equation . . . 20
2.2.2. Feshbach Resonances . . . 22
2.3. Optical Lattice Models . . . 23
2.3.1. Band Structure . . . 23
2.3.2. Bose-Hubbard Model . . . 27
2.4. Trapped Ions . . . 31
2.4.1. Linear Paul Trap . . . 32
2.4.2. Penning Trap . . . 34
2.5. Conclusions . . . 35

II. Numerical Methods 37

3. Full Hilbert Space Methods **39**
3.1. Closed Quantum Systems . . . 39
3.1.1. Krylov Subspace Algorithms . . . 42
3.1.2. Suzuki-Trotter Decomposition . . . 43
3.1.3. Symmetries . . . 46
3.1.4. Imaginary Time Evolution . . . 47
3.2. Open Quantum Systems . . . 48
3.2.1. Quantum Trajectories . . . 50
3.3. Conclusions . . . 53

4. Reduced Hilbert Space Methods **55**
4.1. Matrix Product States (MPS) . . . 56
4.1.1. Orthonormal Forms of MPS . . . 59
4.1.2. Entanglement . . . 61
4.1.3. Area Law . . . 65

4.2. Matrix Product Operators (MPO) . . . 65
4.2.1. Examples of Hamiltonians . . . 68
4.2.2. Examples of Projectors . . . 70
4.3. Methods . . . 71
4.3.1. Time Evolving Block Decimation (TEBD) . . . 71
4.3.2. Variational State Search . . . 73
4.3.3. Time Dependent Variational Principle (TDVP) . . . 74
4.4. Conclusions . . . 76

III. Resonance Tunneling in Tilted Optical Lattices 77

5. Effective Spin Models for Resonant Tunneling Dynamics of Bosons in a Tilted Optical Superlattice 79
5.1. Introduction . . . 79
5.2. The Models . . . 81
5.2.1. $E = U$ Regime . . . 82
5.2.2. $E = U/2$ Regime . . . 84
5.2.3. Benchmarking of the Effective Models . . . 89
5.3. Effective Models in Limiting Cases . . . 90
5.3.1. $E = U$ Regime . . . 90
5.3.2. $E = U/2$ Regime . . . 94
5.4. Phase Transition Analysis . . . 97
5.4.1. $E = U$ Regime . . . 98
5.4.2. $E = U/2$ Regime . . . 102
5.5. Finite Temperature Calculations . . . 108
5.6. Quench Dynamics . . . 110
5.7. Comments on Numerical Techniques . . . 112
5.7.1. Realization of Constraints via Projectors . . . 112
5.7.2. T-MPS Calculations . . . 113
5.8. Conclusions . . . 114

IV. Trapped Ions With Long-Range Interactions 117

6. Global Quench Dynamics with Long-Range Interactions 119
6.1. Introduction and Overview . . . 120
6.2. Models with Long-Range Interactions . . . 121
6.2.1. Long-Range Transverse Field Ising (LRTI) Model . . . 121
6.2.2. Long-Range Fermionic Hopping (LRFH) Model . . . 123
6.3. Spreading of Correlations in Time . . . 125
6.3.1. Comparison of the LRTI and LRFH Models . . . 126
6.3.2. Dynamics with Short-Range Interactions $\alpha > 2$ . . . 128

6.3.3. Dynamics with Intermediate and Long-Range Interactions ($\alpha < 2$) in the LRFH Model . . . 132
6.3.4. Holstein-Primakoff Approximation for the LRTI Model . . 133
6.4. Entanglement Growth . . . 136
6.4.1. Entanglement Growth in the LRTI Model . . . 137
6.4.2. Entanglement Growth in the LRFH Model . . . 140
6.5. Summary and Outlook . . . 144

7. Certified MPS Tomography of Quantum States 147
7.1. Introduction . . . 147
7.2. Notation . . . 148
7.3. Methods . . . 149
7.3.1. Full Quantum State Tomography (QST) . . . 151
7.3.2. Certified MPS Tomography . . . 152
7.4. Experimental Results . . . 154
7.4.1. Logarithmic Negativity . . . 154
7.4.2. Results of MPS Tomography . . . 155
7.5. Resource Cost . . . 160
7.6. Conclusions . . . 162

8. Conclusions and Outlook 163

Bibliography 165

1. Introduction

During the last few decades a great interest has developed towards strongly correlated quantum many-body systems in the context of atomic, molecular, and optical (AMO) physics. The main reason for the success of these platforms for quantum simulations arises from substantial experimental advances allowing us to control almost every parameter of the system and practically isolate it from the environment, particularly in systems of ultracold neutral and ionized atoms [1,2]. Consequently it provides an opportunity to dig down to the physics of the underlying system dynamics with a minimal number of theoretical assumptions. The applied interest that we have in investigating these systems is to achieve in experiments regimes where a certified quantum simulation or quantum computation answers a practical question inaccessible by other means, for instance finding a new configuration of atoms leading to high-T_c superconductivity [3] or the prime factorization problem for large numbers via Shor's algorithm [4].

Cold Atoms

The background of this field is based on the experimental realization of the Bose-Einstein Condensate (BEC) [5–8], which was first discovered for liquefied ^{4}He, with dilute cold gases of ^{87}Rb [9], ^{7}Li [10], and ^{23}Na [11]. Shortly after that, a whole list of successful experiments was performed with other atomic species [8].

In contrast to liquefied helium (with the typical density $\sim 10^{22}$ cm^{-3} and condensation temperature of $\sim$ 2.17 K), dilute gases reach densities of only $\sim 10^{13} - 10^{15}$ cm^{-3} with around 10^5 atoms in the cloud. As a result they form the BEC state at much lower temperatures, $< 10^{-5}$ K. The systematic improvement of experimental techniques such as laser cooling [12] and evaporative cooling [13] has allowed us to obtain BEC clouds of dilute gas with significantly lower temperatures, below one nanokelvin [14].

The diluteness of gases ensures that the interatomic interactions have a weak effect on the condensation mechanism. As a result, a much larger fraction of the matter can be in the BEC state, comparing to strongly interacting liquefied helium. Another feature of the systems worth noting is that experiments with cold atomic gases have a large degree of controllability by means of external fields and electromagnetic radiation. For instance, in the limit of low temperatures the interatomic interactions in dilute gases can be well explained by low-energy scattering theory with an effective interaction potential depending on a single

parameter — the scattering length. By means of magnetic and optical Feshbach resonances [15–18] it is possible to continuously tune the scattering length in a wide range with high precision. It is possible within the same experimental setup, with the same atomic species, to investigate the dynamics of repulsive and attractive interaction potentials between atoms by simply adjusting their Feshbach resonances [17, 19, 20]. It is also possible to couple atoms in molecules and study the BEC of molecular gases [21, 22].

Furthermore, a lot of progress has been made with dilute gases of fermionic atomic species, which at low temperatures form a Degenerate Fermi Gas (DFG). In the pioneering experiments with fermionic isotopes ^{40}K [23, 24] and ^{6}Li [25, 26], atomic gases were cooled below the Fermi temperature. Elastic scattering of fermionic atoms behaves differently from bosonic species, due to the antisymmetry of the wave function the scattering cross section vanishes for a single species fermions. The evaporative cooling relies on elastic scattering being more efficient than inelastic, as a result cooling of fermions requires a new approach. As a solution evaporative cooling was performed with either two species of fermions or via addition of bosonic species; the latter method is referred as sympathetic cooling. The efficiency of cooling is also statistic dependent and decreases as fermions become degenerate [8]. It was shown experimentally [23, 27–30] that a two-component Fermi gas can be converted to a molecular Bose gas by adiabatic passage through a Feshbach resonance with typical densities reaching $\sim 10^{13} - 10^{14}$ cm^{-3}. Due to the use of multiple atomic species and the Fermi pressure of the gas, typical densities reached with fermions are lower than only with bosons. Then these bosonic molecules can be condensed in the BEC state as well [21, 22, 29].

To summarize, the experimental progress in laser and evaporative cooling techniques lets us obtain systems of extremely sensitive but yet highly controlled weakly interacting BECs of atomic and molecular gases, as well as degenerate Fermi gases, which have been realized with a large variety of bosonic and fermionic species. In what follows we will see how on the basis of the BEC with dilute gases one can engineer highly correlated quantum systems, which have promising applications for quantum simulations and quantum computations.

Atoms in Optical Lattices

Following the realization of a stable BEC of dilute gases, the idea of its manipulation via electromagnetic radiation was further developed over the next years, with a practical goal being the use of cold atom systems as a toolbox for reaching strongly correlated regimes [31]. A major experimental development happened in 2002 when it was demonstrated [32, 33] that a BEC of dilute gases of bosonic species could realize a Bose-Hubbard model when confined in periodic 3D optical potentials. In this case the system can undergo the quantum phase transition from a superfluid to a Mott insulator state when the ratio of interaction and

kinetic energies in the system is varied by adjusting the optical potential depth. Later, more experiments with not only bosonic species, but also with fermions [34] or mixture of both [35], were realized. Analogous to experiments with the BEC of free dilute gases the interatomic interactions can be tuned via magnetic and optical Feshbach resonances [15–18] giving not only one more degree of freedom in the experiment, but also allowing binding atoms in molecules inside the lattice: Cs_2 [36] and KRb [37].

The geometry of the lattice is defined by the intensity of laser beams generating the optical potential. Other geometries, besides simple orthogonal ones, can be achieved by making lasers not collinear (triangular [38], Kagome [39], honeycomb [40], or quasi-periodic lattices [41]). The addition of extra laser frequencies can also be used for making a superlattice geometry [42], or quasi-disordered lattices in the case of an irrational ratio between the lasers wavelengths. A disorder in the lattice can also be achieved by exposing the periodic laser potential with a speckle pattern, which provides an experimental sandbox for the study of many-body localization. The interplay between laser polarizations can provide a species-dependent lattice [43], where depending on the internal state of the atom it complies with a different potential.

In addition to having so much flexibility and so many degrees of freedom for systems of ultracold atoms loaded in optical lattices there is also a wide range of possible measurements that can be made. For example, there are measurements of the interference pattern of atoms suddenly released from the optical potential [32, 33], or measurements of noise correlations [44]. As a result the momentum distribution of particles can be obtained. Due to the closeness of the lattice sites (~ 500 nm) it was a significant challenge for a long time to obtain any information about single sites. Only recently with the development of quantum gas microscope techniques [45, 46] did it become possible to directly detect strongly correlated states of matter via single-atom and single-site-resolved fluorescence imaging. This was a truly important achievement as it allows us to directly trace the dynamics of individual atoms on the lattice in the same way that we would like to detect spatial correlation functions in solid state devices. Atoms in the optical lattice, which can be cooled to record temperatures of the order of 1 nK, have characteristic interaction frequencies $10 - 10^4$ Hz and can be traced precisely. Besides bosonic species the single-atom-resolved imaging experiments were recently successfully realized with fermionic species [47–49].

Summarizing everything mentioned above, ultracold atoms in optical lattices provide an excellent platform for quantum simulations. The level of control and measurement precision in the experiment allows us to study ground state properties [50, 51] or out-of-equilibrium dynamics following a parameter quench [32, 52] in these quantum many-body systems that would be impossible to control in traditional condensed matter systems. The high fidelity of the state initialization, combined with manipulation of single atoms [53] allows us to define the initial point of the quantum simulation with high fidelity. The high level of isolation

from the environment allows us to keep atoms for times of the order of seconds, which in comparison to interaction and tunneling times (of the order of a millisecond) provides enough possibilities for quantum simulation.

A particular interest in recent years has been the use of optical lattices to perform quantum simulation of condensed matter physics. For instance simulations of the exotic forms of magnetism is one of the central goals towards complete understanding of high-temperature superconductors, this is a problem of extreme complexity for modern classical computers. Recent experimental work with Mott insulator states showed very promising results with simulations of densely loaded optical lattices in the presence of a tilted potential allowing long-range resonant tunneling [54–56]. It was found that when the tilt per site is tuned to integer fractions of the Mott gap, high order tunneling processes over up to five lattice sites can be observed. The tilt results in coherent oscillations of local occupation numbers in time detected experimentally via oscillations in the number of doubly occupied lattice sites. Truly many-body dynamics can be observed, which is far away from the regime of a simple quantum walk of a single particle [57, 58]. Followed by preliminary theoretical work [59,60] we can map the dynamics of atoms with dynamics of spins in a chain. We investigate this issue and discuss our new understanding in Chap. 5.

Trapped Ions

Manipulation of a BEC of dilute gases or, indeed, a DFG exposed to a periodic optical potential is not the only possible way to realize strongly correlated quantum systems of many components with cold atoms. A quite different path can be taken if one uses ionized atoms that, in the presence of the confining external fields, self-organize in a quasi-periodic structure due to repulsive Coulomb interactions. Following previous experimental developments with trapped ions for atomic clock experiments [61], quantum state tomography [62], and quantum computation [2, 63–65], these systems have become one of the most suitable candidates for quantum simulation as well. A number of experimental groups have reported successful work with ions of $^{171}Yb^{+}$ [66] and $^{40}Ca^{+}$ [67] confined in linear Paul traps, or $^{9}Be^{+}$ [68] confined in a Penning trap, in the two dimensional configuration. The internal hyperfine levels of each ion can be interpreted as spin states [69] and via external fields coupled with transverse phonon modes of the ion crystal, such that coherent interactions between distant ions can be established [70–73]. The peculiar property of these ion-ion interactions is that their range can be continuously varied from almost next-neighbor to the all-to-all regime. This makes it truly a unique platform for quantum simulations allowing us to study the effects of long-range interactions on many-body systems. The long lived hyperfine states ($\gtrsim 1$ s) allow us to perform coherent simulations with short typical interaction times ($\lesssim 0.1$ ms).

From this, completely new kinds of question can be asked: What sort of non-equilibrium dynamics should we expect from such systems with explicit long-range interactions? How does it affect the locality and the information propagation [74]? And how does the entanglement spread in the system? We address these questions in Chap. 6.

The full quantum state of even a simple qubit has, in principle, an infinite amount of information, which in principle would require an infinite measurement time to extract. It is a notoriously difficult task to obtain this information which is normally achieved by means of full quantum state tomography (QST) [75]. The problem becomes intractably complicated when the number of system constituents grows, then QST just becomes practically inapplicable. In Chap. 7 we present a conceptually new method of quantum state estimation, Matrix Product State tomography [76], applied to systems of trapped ions.

Numerical Methods

The investigation of quantum many-body systems is often related to studying Hamiltonians that do not have known analytical solutions. Whereas the use of approximate analytical methods allows us to investigate special cases, it is quite often not enough for gaining a full understanding. That is why an integral part of most investigations is in numerical simulation for either checking the validity of approximate solutions or obtaining results in regimes inaccessible by other methods.

A numerical simulation of a problem is not a trivial task. In the case of a quantum many-body system just storing the system state in the memory quickly becomes impossible due to the exponential growth of the Hilbert space with the number of system constituents. For instance, a simple qubit requires storage of a complex number on a classical computer, for each one of two possible states. Then two qubits requires a number for each one of four combinations of states, which leads to the general case of M qubits with 2^M combinations. This simple mathematical fact means that the total number of combinations of 300 qubits is comparable to the number of atoms in the observable part of the universe and so becomes physically impossible to store. In the case of N bosonic atoms confined on M discrete sites of an optical lattice, the total number of combinations, $(N+M-1)!/N!(M-1)!$, also grows exponentially and all these states have to be taken into account in order to capture quantum effects due to the superposition principle.

Faced with this problem one can split it into subproblems according to the conservation of a certain variable, which implies that the system has a corresponding symmetry, for instance translational symmetry leads to the conservation of the momentum. One can also parallelize the calculation, such that the entire state is stored in separate machines and processed simultaneously. This all forms the basis of so-called exact diagonalization methods [77], which enables one to calculate

all desired properties of the quantum system.

However, in the majority of cases we do not need to know *all* the properties of the system, but instead just a few. One can use methods that rely on properties of the system Hamiltonian, for instance its sparseness can be used to obtain certain system properties iteratively without calculation of all eigenstates [78, 79]. These kinds of approximate method still rely on the full Hilbert space, though, and inevitably stop being feasible due to exponential growth of the computational cost. Another approach is to consider only a subspace of the most relevant states, instead of the entire Hilbert space — the basic idea behind the Density Matrix Renormalization Group (DMRG) methods [80, 81]. These methods combined together with distributed storage of data in tensor networks become a truly breakthrough approach for dealing with strongly correlated quantum many-body systems.

The DMRG started with publications of S. R. White [82, 83] on the time independent algorithm, which allowed the ground state calculations of 1D models. It was later shown [84, 85] that the ground state obtained via DMRG algorithms can always be written in the Matrix Product State (MPS) form. In [86] it was quantified how well MPS can approximate exact ground states of one-dimensional quantum systems, which gave a theoretical justification for the high accuracy of DMRG algorithms even in the case of critical systems.

In [87–89] it was shown independently that DMRG methods can be used effectively for time evolution calculations. Those methods were referred to by different names, such as the Time Evolving Block Decimation (TEBD) algorithm or just t-DMRG to emphasize the time dependence, but they exploited the same idea of the adaptive change of the Hilbert space basis, DMRG optimizations, and truncation of the expanding Hilbert space.

A logical extension of MPS followed when the Matrix Product Operators (MPO) formalism [90, 91] was incorporated in new methods, which vastly extended possibilities. It allowed us to use a wide range of Hamiltonians, for instance with long-range interactions [90–92] or use MPO for realization of symmetries (see Sec. 3.1.3). Also, the same MPO description can be used for representation of density matrices of mixed states, which made it possible to perform calculations with finite temperatures [93].

Currently DMRG methods in combination with MPS and MPO representations of states and operators provide one of the most powerful tools for treating quantum many-body systems in one dimension. The systems can be treated not only in complete isolation from the environment, but also coupled to it, for instance, quantum trajectories methods [94, 95].

Overview

This thesis is arranged in four parts. The last two parts present our original research results, which are obtained using the theoretical knowledge and methods presented in the first two parts.

We start in Part I from the fundamental principles of light-matter interactions, and show how experimental advances with ultracold atomic gases allow us to construct strongly correlated many-body systems. Two types of system are considered: neutral atoms confined in periodic optical potentials and ionized atoms trapped by time-dependent electric fields.

In Part II we cover the numerical techniques that are used for the simulation of quantum many-body problems, especially out-of-equilibrium dynamics studied in this thesis. In Chap. 3 we first present exact diagonalization methods that take into account the entire Hilbert space and hence become exponentially costly as the number of system constituents grows. We then reveal how using only the relevant part of the Hilbert space with low entangled states one can obtain the essential physics (Chap. 4) of any size systems at short times. These DMRG methods with MPS and MPO are used extensively in our theoretical investigation of quantum systems in the following chapters.

In Part III we consider the dynamics of bosons confined in a deep 1D optical lattice. The dynamics can be enhanced via introduction of a tilted potential that allows atoms to resonantly tunnel over several sites. We present the investigation of the two particular tilt values facilitating nearest-neighbor and next-nearest-neighbor tunnelings. In the case of an extra superlattice geometry we map the dynamics of atoms onto constrained spin chains. This greatly reduces the complexity of the model and allows us to study the nature of the systems. In addition it demonstrates the possibility of using cold atoms in tilted optical lattices for studying new types of exotic magnetism.

In Part IV we investigate a system of ions trapped in a linear chain with tunable long-range interactions between internal electronic states of each ion. In Chap. 6 we first investigate global quench dynamics and how they depend on the effective interaction range between spins. In particular, the questions of entanglement growth and correlation spread are investigated in comparison with an exactly solvable long-range Kitaev chain of fermions. In Chap. 7 we proceed with presenting a new method for quantum state estimation — the certified Matrix Product State (MPS) tomography, which is realized in a system of trapped ions.

In the final Chap. 8 we summarize the main results of this thesis and provide an overview of the future directions that each of the projects can take.

Contributions During PhD

Publications

- A. S. Buyskikh, L. Tagliacozzo, D. Pekker, C. A. Hooley, D. Schuricht, and A. J. Daley, "Spin models for resonant tunneling dynamics of bosons in tilted optical lattices," *In preparation, to be submitted to Phys. Rev. A*, 2017

  The author of this thesis performed all of the analytical and numerical calculations, wrote most of the article, and produced all of the plots.

- A. S. Buyskikh, L. Tagliacozzo, D. Pekker, C. A. Hooley, D. Schuricht, and A. J. Daley, "Spin model for 2-site resonant tunneling dynamics of bosons in a tilted optical superlattice," *In preparation, to be submitted to Phys. Rev. Lett.*, 2017

  The author of this thesis performed all of the analytical and numerical calculations, wrote most of the article, and produced all of the plots.

- B. P. Lanyon, C. Maier, M. Holzäpfel, T. Baumgratz, C. Hempel, P. Jurcevic, I. Dhand, A. S. Buyskikh, A. J. Daley, M. Cramer, M. B. Plenio, R. Blatt, and C. F. Roos, "Efficient tomography of a quantum many-body system," *arXiv:1612.08000 (accepted for publication in Nature Physics)*

  The author of this thesis performed calculations to compare with experimental time evolution and to analyze the scaling of the measurement scheme, and wrote the code used for calculation of reduced density matrices.

- A. S. Buyskikh, M. Fagotti, J. Schachenmayer, F. Essler, and A. J. Daley, "Entanglement growth and correlation spreading with variable-range interactions in spin and fermionic tunneling models," *Phys. Rev. A*, vol. 93, p. 053620, 2016

  The author of this thesis performed all of the analytical and numerical calculations for the spin model, analytical derivations for the fermionic model, wrote most of the article, and produced all of the plots.

Conference Presentations

- A. Buyskikh, L. Tagliacozzo, D. Pekker, C. Hooley, D. Schuricht, and A. J. Daley, "Spin models, probes, and atoms in tilted optical lattices," in *QuProCS II*, (Palma, Spain), 2017
- A. Buyskikh, L. Tagliacozzo, D. Pekker, C. Hooley, D. Schuricht, and A. J. Daley, "Quench dynamics in quantum many-body systems with long-range interactions," in *Long-Range Interactions in the Ultracold*, (Ercolano, Naples, Italy), 2016

- A. Buyskikh, "Spin models for 2-site resonant tunnelling dynamics of bosons in a tilted optical lattice," in *Strathclyde Symposium on Quantum Information, Simulation and Metrology*, (Glasgow, UK), 2016
- A. Buyskikh, D. Pekker, and A. J. Daley, "Spin models for 2-site resonant tunnelling dynamics of bosons in a tilted optical lattice," in *APS DAMOP Meeting*, (Providence, RI, USA), 2016
- A. Buyskikh, "Quench dynamics in quantum many-body systems with long-range interactions," in *School in Computational Condensed Matter Physics: From Atomistic Simulations to Universal Model Hamiltonians*, (Trieste, Italy), 2015
- A. Buyskikh, J. Schachenmayer, F. Essler, M. Fagotti, B. Lanyon, C. Roos, and A. J. Daley, "Quench dynamics in quantum many-body systems with long-range interactions," in *Windsor 2015 CCPQ Workshop*, (Windsor, UK), 2015
- A. Buyskikh, J. Schachenmayer, F. Essler, M. Fagotti, and A. Daley, "Quench dynamics in quantum many-body systems with long-range interactions," in *SUSSP71*, (Glasgow, UK), 2015
- A. Buyskikh, J. Schachenmayer, B. Lanyon, C. Roos, and A. J. Daley, "Non-equilibrium dynamics and spread of correlations in systems with variable-range interactions," in *Pittsburgh Quantum Institute Conference: Quantum Coherence*, (Pittsburgh, PA, USA), 2015
- A. Buyskikh, S. Langer, J. Schachenmayer, B. Lanyon, C. Roos, and A. J. Daley, "Non-equilibrium dynamics in ion chains with variable-range interactions," in *Workshop on Many-body Dynamics and Open Quantum Systems*, (Glasgow, UK), 2014
- A. Buyskikh, S. Langer, J. Schachenmayer, B. Lanyon, C. Roos, and A. J. Daley, "Quench dynamics in ion chains with variable-range interactions," in *The 24th International Conference on Atomic Physics*, (Washington, D.C., USA), 2014
- A. Buyskikh, "Non-equilibrium dynamics and magnetic correlations with atomic chains," in *APS DAMOP Meeting*, (Madison, WI, USA), 2014

Part I.

Background

2. Atomic Physics

In this Chapter we present the background of physical systems that we will study in this thesis, consisting of two basic components: cold atoms and electromagnetic waves. Recent experimental developments have given us an opportunity to manipulate such systems in a way that quantum effects play the leading role in the nature of the systems. The understanding of the fundamental principles of atom-atom and atom-light interaction further allows us to use these building blocks for construction of quantum many-body systems and investigation of their nature.

We first start with some basic principles of atomic physics, mainly focusing on alkali atoms. Then we consider the interaction of a single atom with electromagnetic radiation as well as key elements of the theory of BEC in atomic gases. Afterwards we combine these components in Sec. 2.3 to discuss interacting atoms trapped in optical lattices and related theoretical models. In the end we conclude by providing another example of quantum many-body systems, based on trapped ions instead of neutral atoms.

2.1. Alkali Atom Physics

Atoms consist of massive nuclei and light electrons orbiting around them. As the matter of this work we are interested in the electronic states of the atom, which are described by laws of quantum physics. It means that electrons can occupy only a discrete set of levels, which can be described by a set of quantum numbers.

We will discuss only the case of alkali atoms, i.e. atoms with only one electron in the external shell. Alkali atoms are hydrogen-like atoms for which the electronic state is determined under typical conditions by the state of the outermost shell electron. All other electrons form closed lower shells and screen out the charge of the nucleus. Each outer electron has spin $\vec{S}$, which has a single quantum number $S = 1/2$. The state of the electron in the atom is defined by a set of quantum numbers. The principal quantum number $n = 1, 2, 3, ...$ defines the main energy level of the electron. The orbital motion of the electron around the nucleus is described by the angular momentum $\vec{L}$, which can take one of the quantum numbers $L = 0, 1, 2, 3, ...$ and are often referred to in spectroscopic notation by letters, as follows: $S, P, D, F, ...$. The interaction between both forms the spin-orbital coupling with the total electronic angular momentum $\vec{J} = \vec{S} + \vec{L}$, which can take one of the quantum numbers $|L - S| \leq J < L + S$. The hyperfine interaction

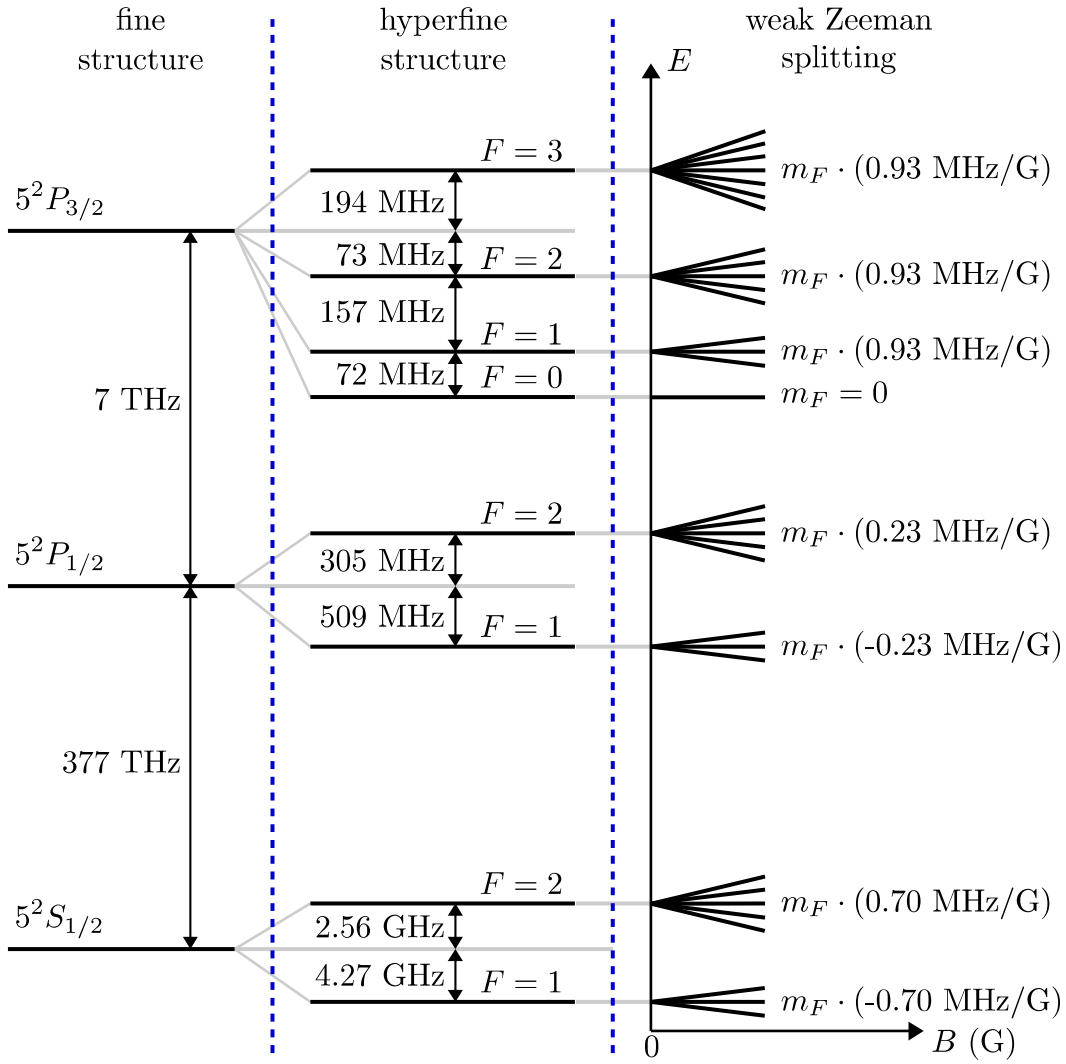

Figure 2.1.: Rubidium 87 energy structure reproduced from [96]. The energies of the outermost electron on the fifth shell split via spin-orbit interactions into $5^2S_{1/2}$, $5^2P_{1/2}$, and $5^2P_{3/2}$ (levels with larger angular momenta are not shown). The spin-orbit structure is often referred to as the fine structure, the interaction with the nucleus spin $I = 3/2$ adds a comparatively weaker hyperfine interaction. It leads to splitting of the fine structure levels to hyperfine structure levels with the same total electronic angular momentum F. The degeneracy of those levels can be lifted by applying, for instance, the magnetic field B due to the Zeeman effect. For small magnetic fields, the projection of the total electronic angular momentum $-F \leq m_F \leq F$ is a good quantum number with the shift prefactor proportional to the Landé g_F-factor.

originates from the coupling of the nuclear spin $\vec{I}$ with the total electronic angular momentum $\vec{F} = \vec{J}+\vec{I}$, which can take one of the quantum numbers $|J-I| \leq F < J + I$. A typical spectroscopic notation that describes the state of the electron

has the following form $n^{2S+1}L_J$, on the top of that one would define values of the hyperfine splitting. In Fig. 2.1, we show an example of the energy diagram for ^{87}Rb, one of the most commonly used atomic species in the field of cold atoms. Besides the spin-orbit and hyperfine structures energy levels can be shifted by external magnetic fields, which is known as the Zeeman effect, or by application of an electric field, which is referred to as the Stark effect.

Transitions between different atomic levels can be induced by the electromagnetic field, the amplitude, polarization, and frequency of which define the effectiveness of the process. Together with the manipulation of atomic levels by external fields, mentioned above, we can control motional and internal degrees of freedom of individual atoms. For instance, in the following sections we will discuss how by means of a far detuned AC Stark shift one can trap atoms in the periodic potential created by a pair of counter-propagating laser beams. Then a cloud of weakly interacting atomic gas can be cooled down and trapped in the optical potential. By means of a Feshbach resonance the scattering properties of atoms can be changed allowing us to attain regimes with strong interactions and observe many-body quantum effects.

2.1.1. An Atom in the Electromagnetic Field

In this section we overview some ideas of confining neutral atoms in the potential generated by laser fields. A detailed review can be found in [8, 97, 98]. Let us consider an electron in an atom in the presence of an external electric field $\vec{E}(\vec{r},t)$ in the semi-classical approach. At the moment we are only interested in the spectral components of the field, not its spatial distribution, so in the most general way the electric field can be presented as

$$\vec{E}(\vec{r},t) = \left[E_0(\vec{r})\hat{\vec{\epsilon}}\exp(-i\omega_{\mathrm{L}}t) + E_0^*(\vec{r})\hat{\vec{\epsilon}}^*\exp(i\omega_{\mathrm{L}}t)\right], \tag{2.1}$$

where $E_0(\vec{r})$ is the spatial dependence of the plane wave amplitude, $\hat{\vec{\epsilon}}$ is the unit vector of polarization, and ω_{L} is the angular frequency of the laser light. The energy structure of a typical alkali atom is presented in Fig. 2.1, where we denote each energy level as E_n and a corresponding state-vector as $|n\rangle$. For simplicity we assume that all levels are non-degenerate. Exposed to a weak laser field the atom attains a time-dependent dipole moment

$$\vec{d}(\vec{r},t) = \left[\vec{d}_0(\vec{r})\exp(-i\omega_{\mathrm{L}}t - i\phi) + \vec{d}_0^*(\vec{r})\exp(i\omega_{\mathrm{L}}t + i\phi)\right],$$

which in the case of weak driving acquires the same frequency as the driving field and some phase ϕ. The interaction with the field can be given as the interaction Hamiltonian

$$H_{\mathrm{int}}(\vec{r},t) = -\vec{d}(\vec{r},t)\cdot\vec{E}(\vec{r},t). \tag{2.2}$$

We would like to consider here the effects of this interaction term on the atom in the non-degenerate ground state $|0\rangle$ with energy E_0. In the absence of the field the dipole moment of the atom also vanishes and the atomic state stays unperturbed. For a weak field we can use the perturbative approach in the interaction picture. We first note that the first order correction

$$\Delta E^{(1)}(\vec{r}) = -\langle 0|\vec{d_0}(\vec{r}) \cdot E_0(\vec{r})\hat{\vec{\epsilon}}|0\rangle = 0, \tag{2.3}$$

vanishes due to parity of the atom eigenstates. Hence the first non-vanishing correction to the energy is at second order, where the ground state interacts with excited states. The corresponding correction to the energy then takes the following form

$$\begin{aligned}\Delta E^{(2)}(\vec{r}) = &\sum_{n\neq 0} \langle 0|\vec{d_0}(\vec{r}) \cdot E_0(\vec{r})\hat{\vec{\epsilon}}|n\rangle \frac{1}{E_0 - E_n + \hbar\omega_{\mathrm{L}}} \langle n|\vec{d_0}(\vec{r}) \cdot E_0^*(\vec{r})\hat{\vec{\epsilon}}|0\rangle \\ &+ \sum_{n\neq 0} \langle 0|\vec{d_0}(\vec{r}) \cdot E_0^*(\vec{r})\hat{\vec{\epsilon}}|n\rangle \frac{1}{E_0 - E_n - \hbar\omega_{\mathrm{L}}} \langle n|\vec{d_0}(\vec{r}) \cdot E_0(\vec{r})\hat{\vec{\epsilon}}|0\rangle, \end{aligned} \tag{2.4}$$

where the first sum corresponds to the interaction with excited states accompanied by the absorption of a single photon with energy $\hbar\omega_{\mathrm{L}}$ and the second sum — emission of a photon. After simplification we obtain

$$\Delta E^{(2)}(\vec{r}) = \underbrace{\sum_{n\neq 0} |\langle 0|\vec{d_0}(\vec{r}) \cdot \hat{\vec{\epsilon}}|n\rangle|^2 \left(\frac{1}{E_0 - E_n + \hbar\omega_{\mathrm{L}}} + \frac{1}{E_0 - E_n - \hbar\omega_{\mathrm{L}}} \right)}_{\equiv \alpha(\omega_{\mathrm{L}})} |E_0(\vec{r})|^2, \tag{2.5}$$

where $\alpha(\omega_{\mathrm{L}})$ is the dynamic polarizability. Note that for alkali atoms, the ground states of which are spherically symmetric S states, the polarizability is a scalar and does not depend on the direction of the field. In the experiments on BEC, electric fields are weak enough to consider only the given perturbation corrections. Eq. (2.5) describes the AC Stark shift — in analogy with the constant field Stark shift it modifies the energy proportional to the intensity of the field.

In many cases of interest the frequency of the laser field is close to one of the atomic transitions; then a good approximation is to neglect all other transitions. Let us denote the ground state of the atom with $|0\rangle = |g\rangle$ with energy $E_0 = E_{\mathrm{g}}$ and the excited state close to resonance as $|n'\rangle = |e\rangle$ with energy $E_{n'} = E_{\mathrm{e}}$. The angular frequency corresponding to the transition between those two levels is equal to

$$\omega_{\mathrm{eg}} = \frac{E_{\mathrm{e}} - E_{\mathrm{g}}}{\hbar}, \tag{2.6}$$

where $\hbar$ is the Planck constant. Only the term with the smallest denominator is

kept in the polarizability then

$$\alpha(\omega_{\mathrm{L}}) = \frac{1}{\hbar}\frac{|\langle 0|\vec{d}_0(\vec{r})\cdot\hat{\vec{\epsilon}}|n\rangle|^2}{\Delta}, \tag{2.7}$$

where

$$\Delta = \omega_{\mathrm{L}} - \omega_{\mathrm{eg}}, \tag{2.8}$$

is the laser detuning, which shows the deviation from the resonance. Here we should give an important definition for the matrix element of the transition

$$\Omega_{\mathrm{R}}(\vec{r}) = \frac{\langle 0|\vec{d}_0(\vec{r})\cdot\hat{\vec{\epsilon}}E_0(\vec{r})|n\rangle}{\hbar}, \tag{2.9}$$

known as the Rabi frequency. Note that the contributions of the oscillations with optical frequencies are ignored in this treatment as they will be averaged out at experimental timescales. The only relevant time dependence can be due to time dependence of $\vec{E}_0(\vec{r})$ in (2.1), which is due to slow variations of the intensity of the laser. Then the perturbation expansion condition can be rewritten as $\Omega_{\mathrm{R}} \ll \Delta \ll \omega_{\mathrm{L}}$.

Then the energy shift takes the following form

$$\Delta E^{(2)}(\vec{r}) = \frac{\hbar|\Omega_{\mathrm{R}}(\vec{r})|^2}{\Delta} \propto \frac{I(\vec{r})}{\Delta}, \tag{2.10}$$

where $I(\vec{r})$ is the intensity of the laser field.

This equation is very simple, but yet has a significant meaning: a neutral atom prepared in the ground state $|g\rangle$ effectively stays unexcited by the off resonant laser light and instead feels an optical potential, which is proportional to the intensity of the laser light. The contributions of the fast optical oscillations of the intensity are averaged out in this treatment, so the only relevant time dependence present in (2.10) can be due to time dependence of $\vec{E}_0(\vec{r})$ in (2.1), which is due to slow variations of the intensity of the laser. Hence the potential to which the atom is exposed is just

$$V_{\mathrm{opt}}(\vec{r}) \propto \frac{I(\vec{r})}{\Delta}. \tag{2.11}$$

This equation forms the basis for the manipulation of atoms by an optical potential. Note that if the laser field is red-detuned ($\Delta < 0$), the potential has a minimum in the regions of high intensity and atoms are attracted there. In the opposite case of the blue-detuned ($\Delta > 0$), atoms are pushed away from the regions of the higher light intensity.

By adding a counter-propagating laser beam with the same frequency and polarization, an interference pattern is created in space — the formation of a standing

wave. Thus atoms will feel this spatially periodic potential as

$$V_{\text{opt}}(x) = V_0 \sin^2(k_{\text{L}} x), \tag{2.12}$$

where $k_{\text{L}} = 2\pi/\lambda$, λ is the wavelength of the laser beams propagating along the x axis, and V_0 is the depth of the optical potential proportional to the intensity. If three pairs of counter propagating beams are chosen in orthogonal directions then a 3D optical lattice will be formed. By tuning relative polarizations, wavelengths (hence resonances), and orientations of the laser beams, one can obtain different geometries as well as optical lattices that depend on the state of the atom (known as spin-dependent lattices).

2.2. A Dilute, Ultracold Gas of Atoms

In this section we present the theoretical description of the non-uniform dilute Bose gas at low temperatures. The purpose is to highlight the most important part of the formalism, and much more detailed reviews can be found in [7, 8].

Here we will discuss the phenomenon of Bose-Einstein condensation, which occurs when a dilute gas of bosons is cooled to temperatures near absolute zero. Under such conditionsa significant portion of bosons occupy the lowest eigenstate, which leads to the formation of a giant matter wave, the Bose-Einstein condensate (BEC), and macroscopic effects can be observed.

In the limit of a non-interacting (ideal) gas trapped in a 3D box the critical temperature for BEC can be obtained as

$$T_{\text{c}} \approx \frac{2\pi\hbar^2}{k_{\text{B}} m} \left(\frac{n}{2.612} \right)^{2/3}, \tag{2.13}$$

where k_{B} is the Boltzmann constant, and n is the density of bosons of mass m. This expression depends on the form of the trapping potential as well as on dimensionality. Then the number of particles in the condensate will read

$$N_0(T) = N \left[1 - \left(\frac{T}{T_{\text{c}}} \right)^{3/2} \right], \tag{2.14}$$

where N is the total number of particles. As one can see at temperatures close to zero a large fraction of atoms are in the condensate state. In order to start the mathematical description, we need to introduce the field operator describing the state of the gas

$$\hat{\Psi}(\vec{r}) = \sum_i \phi_i(\vec{r}) \hat{a}_i, \tag{2.15}$$

where $\hat{a}_i$ is the annihilation operator of a single boson in the state $\phi_i(\vec{r})$. As BEC

is associated with the condition when

$$N_0 \approx N, \tag{2.16}$$

a large number of particles occupy the ground state, i.e.

$$N_0 \equiv \langle \hat{a}_0^\dagger \hat{a}_0 \rangle \gg 1, \tag{2.17}$$

and creation or annihilation of some extra particles in that state gives a negligible effect. Then one can perform a transition to the classical field by replacing $\hat{a}_0$ with $\sqrt{N_0}$, then

$$\hat{\Psi}(\vec{r}) = \underbrace{\sqrt{N_0}\phi_0(\vec{r})}_{\equiv\Psi_0(\vec{r})} + \underbrace{\sum_{i\neq 0} \phi_i(\vec{r})\hat{a}_i}_{\equiv\delta\hat{\Psi}(\vec{r})}, \tag{2.18}$$

where $\Psi_0(\vec{r})$ is the classical field, meaning that the system behaves as a classical object with small quantum fluctuations $\delta\hat{\Psi}(\vec{r})$ in addition. The field $\Psi_0(\vec{r})$ also plays a role of the order parameter as the correctness of the following description relies on the fact that a significant portion of bosons occupy the ground state.

While the ideal BEC is a very peculiar system by itself we shall proceed to make things more realistic, i.e. look at the effect of interatomic interactions in BEC. We focus of the case of a dilute gas, i.e. the density of atoms is low. But how low? To answer this question we need to clarify what interaction processes we look at.

We want to have a weakly interacting Bose gas, which has only two-body interactions at most. This requires

$$r_{\mathrm{aa}} \ll n^{-1/3}, \tag{2.19}$$

where r_{aa} is the range of the atom-atom interactions and $n = N/V$ is the average density of N particles trapped in a large volume V. At such conditions atom-atom collisions are so unlikely that simultaneous collision of three and more particles can be neglected. As a consequence of such low density the separation between particles is always larger than their physical size and scattering theory can be used to describe collisions.

Having atoms in the BEC state means that their temperature is below T_{c}, which means that the wave functions of individual atoms start overlapping. This leads to the condition

$$n^{-1/3} \lesssim \lambda_{\mathrm{dB}} = \frac{2\pi\hbar}{p}, \tag{2.20}$$

where λ_{dB} is the de Broglie wavelength, and

$$p \propto \sqrt{m k_{\mathrm{B}} T}, \tag{2.21}$$

is the momentum of particles, where the prefactor depends on the dimensionality of the gas. This automatically implies that the momenta of particles p is so low that the size of atoms is negligible comparing with their thermal wavelengths

$$r_{\mathrm{aa}} \ll \lambda_{\mathrm{dB}}, \tag{2.22}$$

additionally it implies that the physical size of the BEC should be much larger than the atom-atom interaction range.

Together Eqs. (2.19) and (2.20) are the main conditions for density and temperature, respectively, to have weakly interacting BEC.

In addition, Eq. (2.22) implies that the atom-atom interaction can be described by $s-$wave scattering theory, i.e. the scattering amplitude and angle do not depend on the energy of colliding particles. According to scattering theory this process is determined only by the scattering length a. Then the diluteness condition (2.19) can be replaced by

$$n a^3 \ll 1. \tag{2.23}$$

Note that near Feshbach resonances (see Sec. 2.2.2) the last condition can be broken, whereas (2.19) is still valid.

Now we will describe the theory that in the limit $a \ll \lambda_{\mathrm{dB}}$ uses the Born approximation to described the interatomic collisions and obtain the Gross-Pitaevskii Equation.

2.2.1. The Gross-Pitaevskii Equation

The Hamiltonian of the system of interacting bosons reads

$$\begin{aligned} \hat{H} = &\frac{\hbar^2}{2m} \int \nabla \hat{\Psi}^\dagger(\vec{r}) \nabla \hat{\Psi}(\vec{r}) \mathrm{d}^3 r + \int \hat{\Psi}^\dagger(\vec{r}) V_{\mathrm{ext}}(\vec{r}, t) \hat{\Psi}(\vec{r}) \mathrm{d}^3 r \\ &+ \frac{1}{2} \int \hat{\Psi}^\dagger(\vec{r}) \hat{\Psi}^\dagger(\vec{r}') V(\vec{r}' - \vec{r}) \hat{\Psi}(\vec{r}) \hat{\Psi}(\vec{r}') \, \mathrm{d}^3 r \, \mathrm{d}^3 r', \end{aligned} \tag{2.24}$$

where $\hat{\Psi}(\vec{r})$ is the bosonic annihilation operator. The first term describes the kinetic energy of bosons with mass m, the second term is the interaction of particles with the external potential, and the last term describes two-body interaction processes between bosons. The external potential can be an optical potential as described in Sec. 2.1.1 or a potential created by external magnetic or electric fields due to the Zeeman or Stark effects respectively.

In order to obtain the dependence of the field operators on time, i.e. in the Heisenberg picture one can write down the following equation by simply commuting the field operator $\hat{\Psi}(\vec{r},t)$ and the Hamiltonian (2.24) with the potential term

$$\begin{aligned} i\hbar\frac{\partial}{\partial t}\hat{\Psi}(\vec{r},t) &= [\hat{\Psi}(\vec{r},t),\hat{H}] \\ &= \left[-\frac{\hbar^2\nabla^2}{2m} + V_{\text{ext}}(\vec{r},t) + \int \hat{\Psi}^\dagger(\vec{r}',t)V(\vec{r}'-\vec{r})\hat{\Psi}(\vec{r}',t)\mathrm{d}^3r'\right]\hat{\Psi}(\vec{r},t), \end{aligned} \tag{2.25}$$

where we have used the commutation relations for bosonic field operators,

$$[\hat{\Psi}(\vec{r}),\hat{\Psi}^\dagger(\vec{r}')] = \delta^{(3)}(\vec{r}'-\vec{r}). \tag{2.26}$$

The main difficulty with this equation is in the interaction term. Here we describe the list of assumptions and requirements leading to the analytical resolution of this term. Typical BEC experiments fulfill these conditions.

The interaction term can be treated using low energy scattering theory, which in general considers the behavior of the scattering objects, two particles in our case, at large distances from the scattering center, i.e. $|\vec{r}'-\vec{r}| \gg r_{\text{aa}}$. As the scattering process depends only on the relative motion of the particles it is common to consider the center of mass reference frame, where the particles approach each other with the relative wave vector k. The temperature condition (2.22) implies $kr_{\text{aa}} \ll 1$ so the scattering amplitude becomes independent of the scattering direction, so-called $s-$wave regime. One can use the effective pseudo potential $V_{\text{eff}}(|\vec{r}'-\vec{r}|)$ with contact interaction and obtain the same scattering properties as the original potential $V(\vec{r}'-\vec{r})$. In the case of weak interaction potentials, i.e. $ka \ll 1$, the Born approximation also becomes valid. In the case of the pseudo potential it becomes possible to replace the field operator $\hat{\Psi}(\vec{r},t)$ by the classical state function $\Psi_0(\vec{r},t)$, which varies slowly on the range of interaction. This last substitution is valid for temperatures below T_{c}, which is a prerequisite for BEC in the first place.

Under these conditions the interaction integral can be simplified in Eq. (2.24) and one obtains the time-dependent Gross-Pitaevskii Equation (GPE),

$$i\hbar\frac{\partial}{\partial t}\Psi_0(\vec{r},t) = \left[-\frac{\hbar^2\nabla^2}{2m} + V_{\text{ext}}(\vec{r},t) + g\,|\Psi_0(\vec{r},t)|^2\right]\Psi_0(\vec{r},t), \tag{2.27}$$

for the order parameter $\Psi_0(\vec{r},t)$, where

$$g = \frac{4\pi\hbar^2 a}{m}, \tag{2.28}$$

is the interaction constant. This is an important theoretical tool for understanding the dynamics of a non-uniform dilute Bose gas at low temperatures. As a

result of the scattering-like interaction between pairs of particles the GPE also conserves the total number of particles,

$$N = \int |\Psi_0(\vec{r}, t)|^2 \, \mathrm{d}^3 r. \tag{2.29}$$

Also, in the case of the time independent external potential $V_{\mathrm{ext}}(\vec{r})$ the energy of the system is conserved. Then one can obtain a time-independent version of Eq. (2.27) as

$$E = \int \left[\frac{\hbar^2}{2m} |\nabla \Psi_0(\vec{r})|^2 + V_{\mathrm{ext}}(\vec{r}) \, |\Psi_0(\vec{r})|^2 + \frac{g}{2} |\Psi_0(\vec{r})|^4 \right] \mathrm{d}^3 r. \tag{2.30}$$

While Eqs. (2.27) and (2.30) contain rich physics because of their non-linear nature and have generated a whole field of study by themselves, we continue to specialize our considerations and now are going to look at the case of a periodic potential and effective discrete models for strongly interacting systems (see Sec. 2.3). But before this let us quickly review how one can control the scattering length via Feshbach resonances.

2.2.2. Feshbach Resonances

Feshbach resonances are essential for the study of ultracold gases as they let us modify the interaction between particles via tuning of the scattering length a. A Feshbach resonance occurs due to a resonant coupling of a scattering pair of atoms with an energetically closed molecular state. This can be controlled for instance by external magnetic field B [19, 20]. As was mentioned above, the atom-atom interaction in dilute gases is well understood in terms of low energy scattering theory with an effective contact pseudo-potential. This effective potential depends on a single parameter, the scattering length a. When the molecular state become resonantly coupled with the state of the free moving scattering particles, they can transfer to this bound state and effectively stick together and greatly alter the scattering length a. The effectiveness of this process depends on the relative energies of the states, which can be altered externally. The s-wave scattering length a in the vicinity of a Feshbach resonance is parameterized by

$$a(B) = a_0 \left(1 - \frac{\Delta B}{B - B_0} \right), \tag{2.31}$$

where a_0 is the background scattering length in absence of coupling to the molecular state, B_0 is the resonance position and ΔB is the magnetic field width of the resonance.

2.3. Optical Lattice Models

At this point we have all the necessary components in order to present theoretical models describing the behavior of cold atoms trapped in an optical lattice. In the previous sections one can find how cold atoms interact with light and with each other; in this section we will combine both descriptions in one unified model describing interacting particles trapped in a periodic optical potential.

2.3.1. Band Structure

As the first step let us consider the coherent dynamics of a single atom in a one dimensional potential formed by a standing wave. The laser frequency is far detuned so that, as discussed in Sec. 2.1.1, the Hamiltonian reads

$$\hat{H}_0(x) = -\frac{\hbar^2\nabla^2}{2m} + V_0 \sin^2(k_{\mathrm{L}}x), \tag{2.32}$$

where $k_{\mathrm{L}} = \pi/a_{\mathrm{L}}$ is the wave vector of the laser light and a_{L} is the period of the optical lattice, $a_{\mathrm{L}} = \lambda_{\mathrm{L}}/2$, with λ_{L} the laser wavelength, $\lambda_{\mathrm{L}} \sim 1\ \mu$m. The potential depth V_0 is determined by the atom-light interaction, proportional to the intensity of the light and the polarizability $\alpha(\omega_{\mathrm{L}})$. The eigenstates of this Hamiltonian can be found via application of Bloch's theorem to be given by

$$\phi_q^{(n)}(x) = u_q^{(n)}(x)\mathrm{e}^{iqx}, \tag{2.33}$$

where q is the quasimomentum q from the interval $(-\pi/a_{\mathrm{L}}, \pi/a_{\mathrm{L}}]$, which is called the first Brillouin zone. The functions $u_q^{(n)}(x)$ are called Bloch functions, and are eigenstates of the Hamiltonian

$$H_q(x) = \frac{(p+q)^2}{2m} + V_0 \sin^2(k_{\mathrm{L}}x), \tag{2.34}$$

with the same periodicity as the potential, i.e. $u_q^{(n)}(x + a_{\mathrm{L}}) = u_q^{(n)}(x)$. Here we used $\hat{p} = -i\hbar\nabla$. The energy eigenvalues $E_q^{(n)}$ of the Hamiltonian (2.32) are defined as

$$\hat{H}_0\,(x)\,\phi_q^{(n)}(x) = E_q^{(n)}\phi_q^{(n)}(x), \tag{2.35}$$

along with one more quantum number of the system, the quasimomentum

$$\hat{Q}\phi_q^{(n)}(x) = q\phi_q^{(n)}(x). \tag{2.36}$$

Together they provide the following equation for orthonormality

$$\frac{2\pi}{a_{\mathrm{L}}}\int_0^{a_{\mathrm{L}}} \phi_q^{(n)*}(x)\phi_{q'}^{(m)}(x)\,\mathrm{d}x = \delta_{nm}\delta_{qq'}, \tag{2.37}$$

where wave functions are orthogonal not only for different energy eigenstates, but also for the quasimomenta.

One can numerically obtain the band structure of eigenenergies of (2.34) by substituting the Fourier expansion of the Bloch functions as

$$u_q^{(n)}(x) = \frac{1}{\sqrt{2\pi}} \sum_k \tilde{u}_q^{(n)}(k) \exp(-i2k_{\mathrm{L}}a_{\mathrm{L}}x), \tag{2.38}$$

and solving the resulting system of linear equations for $\tilde{u}_q^{(n)}(k)$. The most natural energy scale in the lattice is given by the recoil energy

$$E_{\mathrm{R}} = \frac{\hbar^2 k_{\mathrm{L}}^2}{2m}, \tag{2.39}$$

which has the meaning of the kinetic energy that one particle in rest obtains by emitting or absorbing a photon of momentum $\hbar k_{\mathrm{L}}$. In Fig. 2.2 we show the result of band structure calculations for different depths of the potential V_0 compared to the recoil energy. One can immediately see that in the absence of the potential, the band structure is identical to a quadratic dispersion relation folded within the first Brillouin zone. In that case, the Bloch ansatz is not particularly useful. However, once the potential rises the low-energy part of the spectrum starts forming bands, whereas high energy particles move almost freely, i.e. their energies are just slightly perturbed by a low potential. The higher is the potential, the more energy bands $E_q^{(n)}$ appear and they become more and more isolated from each other, i.e. the energy gap between them increases. In the case of deep potentials the dispersion relation of the lowest energy band approaches that of the standard tight binding model, $E_q^{(0)} \propto -\cos(qa_{\mathrm{L}})$.

The formalism of Bloch functions is not the only useful basis for solving single particle problems in the presence of a periodic potential. Quite often, and in our case also, it is more convenient to consider another set of basis functions — Wannier functions. These functions in the case of one dimensional lattice are defined via Bloch functions as

$$w_n(x - x_j) \equiv \sqrt{\frac{a}{2\pi}} \int_{-\pi/a_{\mathrm{L}}}^{\pi/a_{\mathrm{L}}} u_q^{(n)}(x) \mathrm{e}^{-iqx_j} \,\mathrm{d}q, \tag{2.40}$$

where $x_j = a_{\mathrm{L}} j$ corresponds to the positions of minima of the periodic potential. The Bloch function can be analogously defined via the set of Wannier functions. The Wannier functions are orthonormal

$$\int_{-\infty}^{+\infty} w_n^*(x - x_i) w_m(x - x_j) \,\mathrm{d}x = \delta_{nm}\delta_{ij}, \tag{2.41}$$

i.e. they form a basis. Note that the wave function $\phi_q^{(n)}(x)$ as well as the Bloch function $u_q^{(n)}(x)$ are defined only up to their global phase, so the definition of Wannier function (2.40) is not unique. However, it was shown [99] that there ex-

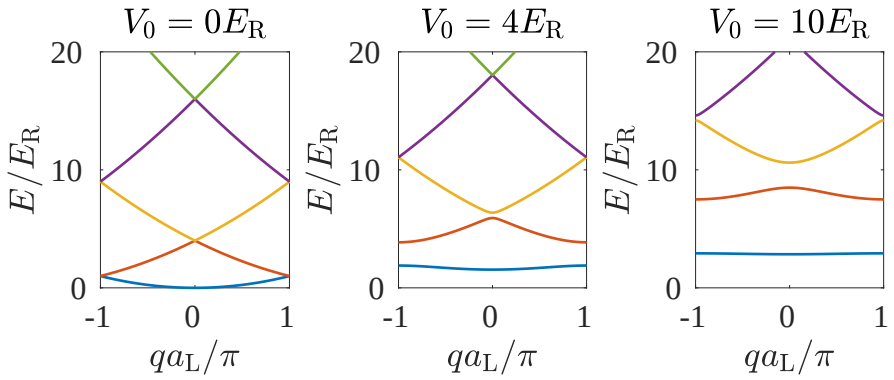

Figure 2.2.: Band structure of a particle in the laser optical lattice. Energies of the Bloch states versus quasimomentum q in the first Brillouin zone plotted for different lattice depths V_0 expressed in units of recoil energy E_R. The higher the potential the more energy bands $E_q^{(n)}$ appear from the spectrum of the free particle and the separation between them increases as well. In the case of the deep potential the dispersion relation of the lowest energy band approaches one of the standard tight binding model results $E_q^{(0)} \propto -\cos(qa_\mathrm{L})$. Further increase of the potential flattens out the bands leaving them equally spaced, this corresponds to the fact that the deep optical potential resembles a simple harmonic trap.

ists only one completely real Wannier function for each band that is exponentially localized. These functions are either symmetric or antisymmetric with respect to a reflection around either the local maxima or minima of the potential, and decay exponentially from the center of the site where they are localized. Hence this form of Wannier function is called maximally localized, and it is the one we are the most interested in as we are going to build a discrete model for excitations localized on the lattice sites. In Fig. 2.3 one can find a couple of examples of Wannier functions for the lowest two bands of the optical lattice potentials of different depths. As the form is chosen to be maximally localized, the imaginary part of the functions is automatically zero.

An interesting regime can be approached in the limit of the deep lattice, i.e. $V_0 \gg E_\mathrm{R}$, where the potential is so deep that the band structure that can be seen in Fig. 2.2 flattens out at equaldistantly spaced. In this regime, the Wannier functions of confined bands can be well approximated by harmonic oscillator functions. In other words, the lattice potential near local minimum at each site can be well approximated by the quadratic potential

$$V_\mathrm{ext}(x) = V_0 \sin^2(k_\mathrm{L}x) \approx V_0 k_\mathrm{L}^2 x^2 = \frac{m\omega_\mathrm{trap}^2 x^2}{2}, \tag{2.42}$$

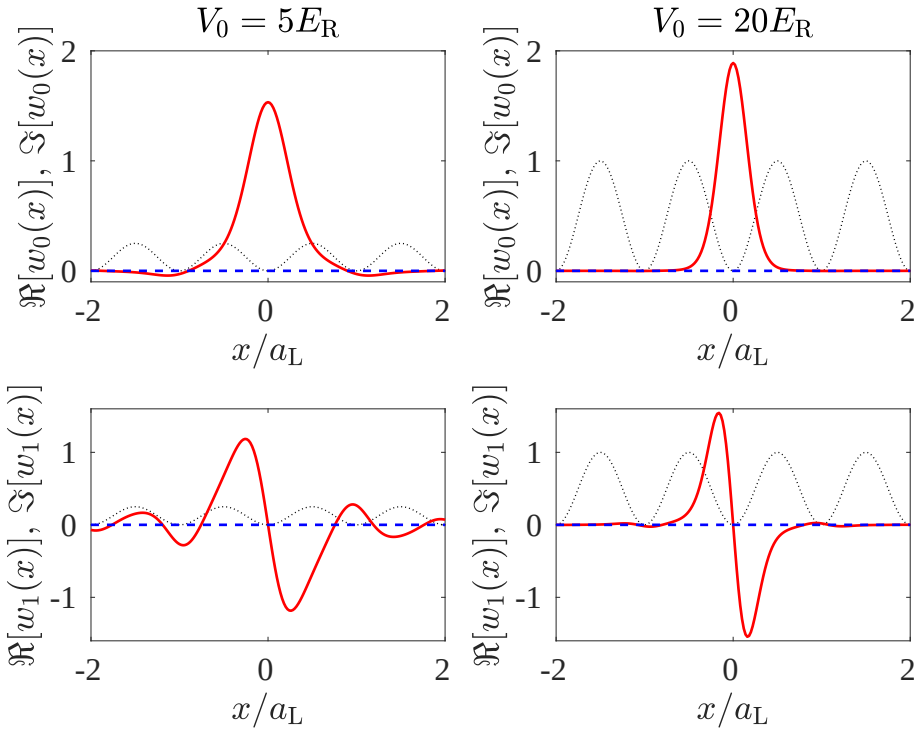

Figure 2.3.: Examples of maximally localized Wannier functions, $w_0(x)$ and $w_1(x)$, for the lowest two bands for optical lattices with potential heights in units of recoil energy $V_0/E_R = 5$ and 20. In each plot one can see a sketch of the potential in arbitrary units to give an intuition of the lattice sites (black dotted line). The real part of Wannier functions is represented by red solid lines, and dashed blue line shows the imaginary part always staying at zero. One can note that in order to minimize the overlap between functions localized on neighboring site one needs to have relatively deep lattices.

where the trapping frequency is defined as

$$\omega_{\text{trap}} \equiv \sqrt{\frac{2V_0 k_L^2}{m}} = \frac{2\sqrt{V_0 E_R}}{\hbar}. \tag{2.43}$$

Then the eigenstates will be expressed through Hermite polynomials and the ground state will read

$$\phi_{\text{ho}}(x) = \frac{1}{\pi^{1/4}\sqrt{a_{\text{ho}}}} \exp\left(-\frac{x^2}{2a_{\text{ho}}^2}\right), \tag{2.44}$$

where

$$a_{\text{ho}} = \sqrt{\frac{\hbar}{m\omega_{\text{trap}}}}, \tag{2.45}$$

is the oscillator characteristic length, i.e. it reflects the typical size of the wave function. The limit of the deep lattice, when the simple harmonic oscillator approximation is good, can be rewritten in another form that also finds a wide application when considering effects related to shallow lattices. The relation

$$\eta \equiv k_{\mathrm{L}} a_{\mathrm{ho}} = \pi \frac{a_{\mathrm{ho}}}{a} \ll 1, \tag{2.46}$$

should be satisfied in order to justify this tight binding approximation. The parameter η is called Lamb-Dicke parameter showing how much smaller is the oscillator characteristic length comparing to the lattice spacing. Its squared value is equivalent to the ratio between the recoil energy E_{R} and the energy of the harmonic oscillator $\hbar\omega_{\mathrm{trap}}$, which is equivalent to the spacing between energy bands as well.

2.3.2. Bose-Hubbard Model

Using the basis of single particle wave functions one can now derive the many-body lattice model for bosons — the Bose-Hubbard model, which will be outlined in this section. The Hamiltonian can be derived directly from the microscopic second-quantized Hamiltonian for the cold atomic gas (see Sec. 2.2.1)

$$\hat{H} = \int_{-\infty}^{+\infty} \hat{\Psi}^{\dagger}(\vec{r}) \left[-\frac{\hbar^2 \nabla^2}{2m} + V_{\mathrm{ext}}(\vec{r}) \right] \hat{\Psi}(\vec{r})\, \mathrm{d}^3 r + \frac{g}{2} \int_{-\infty}^{+\infty} \hat{\Psi}^{\dagger}(\vec{r}) \hat{\Psi}^{\dagger}(\vec{r}) \hat{\Psi}(\vec{r}) \hat{\Psi}(\vec{r})\, \mathrm{d}^3 r, \tag{2.47}$$

where the first term describes the kinetic energy of single particles and their interactions with the external potential

$$V_{\mathrm{ext}}(\vec{r}) = V_0^x \sin^2(k_{\mathrm{L}}^x x) + V_0^y \sin^2(k_{\mathrm{L}}^y y) + V_0^z \sin^2(k_{\mathrm{L}}^z z) + V_1(\vec{r}), \tag{2.48}$$

which has the periodic potential of the laser fields along x, y, and z directions and, some extra non-uniform potential $V_1(\vec{r})$ associated with additional external fields. The second term of (2.47) takes into account interatomic interactions.

Assuming that the non-uniform potential $V_1(\vec{r})$ can be factorized as well, we will factorize the state function as $\hat{\Psi}(\vec{r})$, consider from now on only the x component $\hat{\Psi}(x)$. The following treatment is also valid for y and z components. We first expand the field operators in terms of Wannier functions:

$$\hat{\Psi}(x) = \sum_{i=-\infty}^{+\infty} \sum_{n=0}^{\infty} w_n(x - x_i) \hat{b}_{n,i}, \tag{2.49}$$

where $\hat{b}_{n,i}$ is the annihilation operator of a boson in the n^{th} band on the site i. Note that the Wannier functions we use here now are all real. As one can see, the

consideration of all possible terms at the same time can be quite messy; that is why we will consider terms with the most significant contribution first and then describe why other terms can be neglected under well-controlled approximations.

In what follows we will discuss the single band model, where one has only the Wannier function of the first band. Hence

$$\hat{\Psi}(x) = \sum_{i=-\infty}^{+\infty} w_0(x - x_i)\hat{b}_i, \tag{2.50}$$

where the band index is omitted. The first integral of the Hamiltonian splits up in three kinds of terms. The first one is

$$J_0 = -\int_{-\infty}^{+\infty} w_0(x)\left[-\frac{\hbar^2\nabla^2}{2m} + V_0\sin^2(k_{\mathrm{L}}x)\right] w_0(x)\,\mathrm{d}x, \tag{2.51}$$

which is just a site-independent constant contribution which has the same origin as the vacuum energy and hence can be omitted. The second one is

$$\epsilon_r = \int_{-\infty}^{+\infty} |w_0(x - x_r)|^2 V_1(x)\,\mathrm{d}x, \tag{2.52}$$

which gives a non-uniform contribution to energies and has the physical meaning of the chemical potential. The third kind of terms in the absence of the non-uniform contribution to the potential $V_1(x)$ reads

$$J_k = -\int_{-\infty}^{+\infty} w_0(x - ka)\left[-\frac{\hbar^2\nabla^2}{2m} + V_0\sin^2(k_{\mathrm{L}}x)\right] w_0(x)\,\mathrm{d}x, \tag{2.53}$$

and has a meaning of the transition amplitude between any two sites separated by $(k-1)$ sites. In the presence of the non-uniform contribution to the potential those transition amplitudes can be site-dependent.

The largest contribution from the second integral of (2.47) is in the case when all four wave functions are located on the same site, i.e.

$$U = g\int_{-\infty}^{+\infty} |w_0(x)|^4\,\mathrm{d}x, \tag{2.54}$$

which has the physical meaning of the interaction energy between two and more particles occupying the same site.

The resulting Hamiltonian then is the single-band Bose-Hubbard Hamiltonian with long range tunnelings

$$\hat{H}_{BH}^{\mathrm{lr}} = -\sum_{r,k} J_k(\hat{b}_r^\dagger\hat{b}_{r+k} + \hat{b}_r^\dagger\hat{b}_{r-k}) + \frac{U}{2}\sum_r \hat{n}_r\left(\hat{n}_r - 1\right) + \sum_r \epsilon_r\hat{n}_r, \tag{2.55}$$

where $\hat{n}_r = \hat{b}_r^\dagger\hat{b}_r$ is the occupation number operator. The first sum describes

tunneling over several sites, the second sum counts the number of interatomic interactions on each site, and the last term can be treated as non-uniform chemical potential created by non-uniform external fields. The main reason why inter-site terms were omitted is because of the exponential localization of Wannier functions. Even the tunneling terms J_k are exponentially suppressed with distance. In Fig. 2.4 one can see how by varying just the depth of the optical potential V_0 one can control the tunneling between neighboring sites J_k, on-site interaction U, and neighboring site interactions

$$\begin{cases} U_{\mathrm{n1}} = g \int_{-\infty}^{+\infty} w_0^2(x) \cdot w_0^2(x - a_{\mathrm{L}})\, \mathrm{d}x \\ U_{\mathrm{n2}} = g \int_{-\infty}^{+\infty} w_0^3(x) \cdot w_0(x - a_{\mathrm{L}})\, \mathrm{d}x \end{cases} . \tag{2.56}$$

There are two important messages one can conclude from these dependences. The first one is that indeed all the terms that have integrals between Wannier functions localized on different sites quickly become insignificant with the increase of the potential height V_0. Even for the small potential depths V_0/E_{R} the difference can be of a few orders of magnitude. Besides that by changing the depth of the potential one can change the ratio J_k/U which plays a significant role in the behavior of the system.

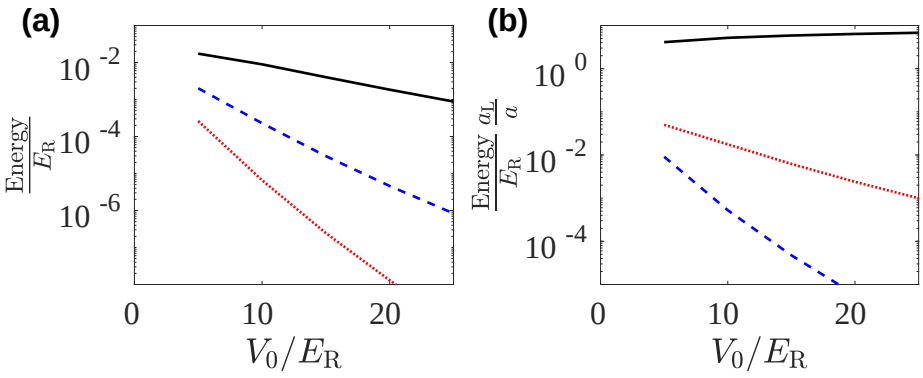

Figure 2.4.: (a) Dependence of the tunneling amplitudes J_1 (solid black line), J_2 (dashed blue line), and J_3 (dotted red line) on the depth of the periodic potential V_0. (b) Dependence of the on-site interaction U (solid black line), neighboring site interactions U_{n1} (dashed blue line) and U_{n2} (dotted red line) on the depth of the periodic potential V_0. By varying V_0 one can change the ratio between tunneling and interaction terms.

In the simplest form the Bose-Hubbard Hamiltonian has only the neighboring tunneling terms

$$\hat{H}_{BH} = -J_1 \sum_{\langle r,k \rangle} \hat{b}_r^\dagger \hat{b}_k + \frac{U}{2} \sum_r \hat{n}_r \left(\hat{n}_r - 1\right) + \sum_r \epsilon_r \hat{n}_r, \tag{2.57}$$

where $\langle r, k \rangle$ means summation only over neighboring sites. Let us call the number

of sites M and the number of particles N, which is conserved by the Hamiltonian. One can confirm it by computing the commutator

$$[\hat{H}_{BH}, \sum_r \hat{n}_r] = 0. \tag{2.58}$$

The ground state of the system can exist in two different phases, depending on the ratio U/J. For large U/J bosons are exponentially localized on the particular sites, this state is called Mott insulator (MI), given in the extreme limit $U/J \to \infty$ by

$$|\psi_{\mathrm{MI}}\rangle = \prod_r |\bar{n}\rangle_r, \tag{2.59}$$

where $\bar{n} = N/M$ is the average filling number. On the other hand for small ratios of U/J bosons are delocalized over the entire lattice, this is the superfluid (SF) state, given for $U/J \to 0$ by

$$|\psi_{\mathrm{SF}}\rangle = \left(\frac{1}{\sqrt{M}} \sum_r \hat{b}_r^\dagger\right)^N |0\rangle, \tag{2.60}$$

which in the bulk limit ($N/M = \mathrm{const}$, $N, M \to \infty$) becomes

$$|\psi_{\mathrm{SF}}\rangle = \prod_r \exp\left(\sqrt{\frac{N}{M}} \hat{b}_r^\dagger\right) |0\rangle, \tag{2.61}$$

with Poisson number statistics on each site. One can think about this state as localization of bosons, but in momentum space. An analytical solution for the ground state in 1D case was obtained using the Luttinger liquid field theory [100] and the phase transition is found to be at $(U/J)_{\mathrm{crit}} \approx 3.30$ in the case of the unit filling, i.e. $N = M$. The same result was also confirmed by DMRG calculations [101,102]. In should be noted the transition point, a quantum critical point, depends on the shape of the trapping potential, whether it is just a box or parabolic potential, as well as the dimensionality of the problem. In the last case the number of neighboring sites moves the position of the transition.

The single band Hamiltonian presented here can be extended to the case of multiple dimensions in a similar fashion. One first obtains the solution of the single particle problem in terms of the Bloch functions. Then configurations of exponentially localized Wannier functions along each directions can be defined. These multidimensional Wannier functions play a role of the basis states for the many-body problem. The leading terms of the multidimensional Bose-Hubbard model will have similar scales between terms. In general one should expect that terms with integral of Wannier functions localized on different sites will decay exponentially with distance between them, hence the most significant contributions will be from the on-site interaction U and neighboring tunneling J.

In a similar fashion, multiple bands can be considered in the model. In that case one should consider all possible cross-band terms in both integrals of (2.47). One can think of the resulting Hamiltonian as a combination of terms from the single band model (2.55), but for each considered band, plus interacting terms that couple bands.

In certain cases the use of the multi-band model is indeed required, especially if inter-band interactions are enhanced via Feshbach resonances, and higher bands can be explicitly populated. However, quite often the single-band model (2.55) is enough. Let us summarize the main conditions that should be met.

- The diluteness of the gas should be sufficiently low to have only two body interactions (see Eq. (2.19)).
- The temperature and hence momenta of particles should be sufficiently low so the collision of particles can be described by the $s-$wave scattering theory with a well behaved effective interaction potential that can be treated in the Born approximation (see Eq. (2.23)).
- The periodic potential applied by the optical lattice should be deep enough that long range tunneling and inter-site interactions are negligible (see Fig. 2.4).
- The temperature should be much lower than the inter-band separation in the lattice, which for deep lattices approaches $\hbar\omega_{\text{trap}}$ (see Fig. 2.2).

Last but not least, the above described procedure can be applied to the cold gas of fermionic species. In the case of only neighboring tunneling the corresponding single band model (Fermi-Hubbard model) will read

$$\hat{H}_{FH} = -J \sum_{\langle r,k\rangle,\sigma} \hat{c}^{\dagger}_{r,\sigma}\hat{c}_{k,\sigma} + U\sum_{r} \hat{n}_{r,\uparrow}\hat{n}_{r,\downarrow} + \sum_{r,\sigma} \epsilon_{r,\sigma}\hat{n}_{r,\sigma}, \tag{2.62}$$

where one can note the appearance of the spin component $\sigma = \{\uparrow,\downarrow\}$, which has to be taken into account due to the Pauli exclusion principle. Here we have $\hat{c}_{r,\sigma}$ and $\hat{n}_{r,\sigma} = \hat{c}^{\dagger}_{r,\sigma}\hat{c}_{r,\sigma}$ corresponding to annihilation and number occupation operators of the corresponding fermions. Also note that in principle it is possible to create spin-dependent interactions with the external field $\epsilon_{r,\sigma}$.

In this section we highlighted the main ideas and requirements behind derivations of simple lattice models for cold atoms. The validity of many other configurations has been derived and even tested experimentally, opening a lot of possibilities for testing our fundamental understanding of light-matter interaction and many-body physics in highly controlled systems.

2.4. Trapped Ions

Trapped ions have been under a lot of investigation for a number of decades independently of the experiments with BEC of dilute gases presented in the previous

sections. The development of experimental techniques for preparation, control, and measurement of a single or several trapped ions made it possible to realize the full state tomography [62] of the quantum system. The high control of laser driving made it possible to use trapped ions for atomic clock experiments [61] and quantum computation [2, 63–65]. In the context of this thesis, recent works have brought a lot of attention to trapped ions as potential candidates for the quantum simulation and study of many-body physics.

A cold gas of ions confined by external fields can self arrange in a stable crystal-like configuration, where internal and motional degrees of freedom can be coupled. A number of experimental groups relatively recently reported successful works with ions of $^{171}Yb^{+}$ [66] and $^{40}Ca^{+}$ [67] confined in one dimensional Paul traps, or $^{9}Be^{+}$ [68] confined in the Penning trap in two dimensional configuration. Via driving lasers a collection of hyperfine levels were singled out, such that the dynamics among atomic states is confined only within these states. Depending on the geometry of the experiment those atomic states of different ions were coupled in a coherent way such that ion-ion coupling was created.

In the rest of the section we will take a look at a couple of examples of such couplings and obtain theoretical models guiding the dynamics of the systems.

2.4.1. Linear Paul Trap

In recent papers [103, 104] it was argued that a one-dimensional system of atomic ions can be accurately described by a lattice model of interacting spins. The peculiar thing about such systems is that it was possible to tune the ion–ion interaction range from almost nearest-neighbour to infinite range, i.e. when all ions interact with each other in a coherent way. Even though those experiments were performed with different atomic species and slightly different geometries, the resulting microscopic models were quite similar, which is why below we will discuss only one of them.

In [104] a collection of $^{40}Ca^{+}$ was trapped in a one-dimensional configuration at a separation distance of approximately 5 microns. Two Zeeman states were identified in the experiment: $|S_{1/2}, m = +1/2\rangle$, which was associated with a spin-down $|\downarrow\rangle$ and $|D_{5/2}, m' = +5/2\rangle$ — a spin-up $|\uparrow\rangle$. The metastable state $D_{5/2}$ has a lifetime of the order of a second — sufficiently long for performing state manipulation and observing coherent dynamics in the experiment. Then preparation of ions in the state corresponding to $|\downarrow\rangle$ can be efficiently done via optical pumping techniques.

Let us now see how a 1D array of M trapped ions was experimentally manipulated in such a way that its dynamics can be described by an effective model for spin states

$$H = \sum_{r<l}^{M} J_{rl}\sigma_r^x\sigma_l^x + B\sum_{r}^{M}\sigma_r^z, \tag{2.63}$$

($\hbar = 1$) where the spin-spin coupling matrix approximately reads

$$J_{rl} = \frac{J}{|r-l|^{\alpha}}, \tag{2.64}$$

where α is the exponent of the algebraic decay, which can be tuned between 0 and 3, and J is the interaction matrix element for neighboring spins. Note that the Hamiltonian (2.63) is just an extended model of the Ising chain in the transverse field B in the case of spin-spin interactions decaying algebraically with distance. Let us overview the way this model can be realized.

One can find the original proposal on creation of variable-range interactions between spin states of trapped ions in [105]. First ions are trapped in a linear Paul trap. Then they are globally addressed with a laser beam in the orthogonal direction to the ion string axis. The proposed idea makes it possible to couple the spin states with the phonon modes of the string (collective modes of motion) in the transverse direction to the axis of the chain. In particular, this was realized via a Mølmer-Sørensen type interaction [106], where the laser carries two frequencies $\omega_{\pm} = \omega_0 \pm \Delta$. Here Δ denotes the deviation from ω_0, which is the energy difference between $|\downarrow\rangle$ and $|\uparrow\rangle$ states. It is done by coupling spin states to all first-order sidebands of the transverse collective modes of motion. In the limit of weak coupling, the induced effective interaction between the spins is given by

$$J_{rl} = \Omega_r \Omega_l \frac{\hbar^2 k^2}{2m} \sum_{n=1}^{2M} \frac{b_{r,n} b_{l,n}}{\Delta^2 - \nu_n^2}, \tag{2.65}$$

where Ω_r denotes the Rabi frequency of each component of the bichromatic ($\omega_{\pm} = \omega_0 \pm \Delta$) beam on the r^{th} ion, k is the wave vector of the laser, m is the ion mass, ν_n are the transverse mode frequencies, and $b_{r,n}$ are proportional to the displacement of the r^{th} ion in the n^{th} collective mode. The summation goes over all $2M$ transverse phonon modes. When the laser detuning Δ is set to a value higher than the frequency of the highest transverse mode $\nu_n^{\max}$, the coupling becomes antiferromagnetic with a range that is described approximately by a power-law dependence (2.64). By increasing the laser detuning or by bunching up the transverse modes in frequency space by trapping the ions in a strongly anisotropic potential, it is possible to make the denominators of different modes ν_n more alike. By doing so one can shorten the range of the interaction, i.e. raise α in Eq. (2.64) to approximately 3. In the opposite limit of small detuning one can obtain the regime where interactions only slowly decay with distance, i.e. lower α to approximately 0.

The implementation of the local term in (2.63) can be obtained by shifting both frequency components of the bichromatic beam by an additional amount $\delta = 2B$, so $\omega_{\pm} = \omega_0 \pm \Delta + 2B$. By doing this one tunes the transition between $|\downarrow\rangle_r|\downarrow\rangle_l$ and $|\uparrow\rangle_r|\uparrow\rangle_l$ out of resonance whereas the transition between $|\downarrow\rangle_r|\uparrow\rangle_l$ and $|\uparrow\rangle_r|\downarrow\rangle_l$ is not affected. In the limit of the large field, i.e. $B \gg J$, joint spin flips coupling $|\downarrow\rangle_r|\downarrow\rangle_l$

to $|\uparrow\rangle_r|\uparrow\rangle_l$ are suppressed. In this regime the number of excited spin-ups and spin-downs is conserved, as only the spin-exchange transitions between $|\downarrow\rangle_r|\uparrow\rangle_l$ and $|\uparrow\rangle_r|\downarrow\rangle_l$ are present. Experimentally, this spin–spin dynamics was followed over timescales of tens of milliseconds, which is significantly shorter than the lifetime of the excited state $|D_{5/2}, m' = +5/2\rangle$. This makes it possible to study the coherent dynamics in the absence of dephasing processes.

2.4.2. Penning Trap

In [68, 107] it was demonstrated that Ising-type spin-spin interactions can also be achieved in 2D triangular crystal lattice of hundreds of $^9Be^+$ ions stored in a Penning trap. Similarly to the 1D case, spin states can be encoded in the hyperfine states of ions, and the range of the interactions can be tuned such that the spin-spin matrix element follows the power law (2.64) with the exponent $0 < \alpha < 3$.

Analogously to the 1D setup, spin states are encoded on a couple of fine electronic levels of the atom ($2^2S_{1/2}$,$m_J = \pm 1/2$), and coupling between spins of different atoms is realized via their coupling with collective motional degrees of freedom — phonon modes. In the experiment ions are confined in a pancake geometry by a homogeneous magnetic field. The Penning trap holds ions in a static quadrupole electric potential and the rotation of the plane of ions with the frequency ω_r produces a radial restoring potential due to the Lorentz force.

By a couple of laser beams with frequency difference Δ descending on the plane of ions one generates the spin-dependent optical force, which couples each ion's spin to collective motional modes in the normal direction to the plane of confinement. In the regimes of small displacement the interaction Hamiltonian

$$\hat{H}_I = \frac{1}{M} \sum_{r<l}^{M} J_{rl} \hat{\sigma}_r^z \hat{\sigma}_l^z, \tag{2.66}$$

can be realized. Similarly to the 1D case the interactions can be tuned closely to the power-law (2.64) with the exponent $0 < \alpha < 3$, which is controlled by detuning of Δ from the axial trapping frequency. Besides that an effective magnetic field can be realized by microwave coupling of the spin states, i.e. the Hamiltonian

$$\hat{H}_B = \sum_{\beta=x,y,z} \sum_{r}^{M} B^\beta \hat{\sigma}_r^\beta, \tag{2.67}$$

can be realized, and the global rotation of all spins is implemented. Here we should emphasize that simulations of both non-commuting Hamiltonians (for spin-spin interactions $\hat{H}_I$ and the field $\hat{H}_B$) will open possibilities for studying quantum phase transition effects in 2D. However even without this one can ob-

serve quite interesting effects with just the interaction part, such as spin squeezing.

2.5. Conclusions

In this Chapter we presented the background theory for cold atoms and considered two methods of atom manipulation via electromagnetic waves and external electric and magnetic fields. Both of the following methods have been successfully realized in a number of laboratories.

The first method involves confinement of ultracold gases of atoms in a periodic optical potential. In the dilute gas regime and low enough temperatures we showed how one can engineer the discrete model of bosons tunneling between sites of the lattice — Bose-Hubbard model (2.57). In the regime of deep lattice potentials the model ground state is in the Mott Insulator (MI) state where atoms are exponentially localized on the lattice sites. In Chap. 5 we investigate the dynamics of atoms in the MI state in the presence of a linear external potential allowing resonant transitions between neighboring sites.

The second method is confining ionized atoms in linear or planar traps via external fields. In this case, the repulsive Coulomb force keeps the atoms from colliding so they form a quasi-periodic ion crystal. Internal electronic states of different atoms are coupled via collective phonon modes of the crystal, which allows one to tailor variable-range interactions and study the coherent dynamics of the system governed by (2.63). In Chap. 6 we investigate the spread of correlations and growth of entanglement after a global parameter quench in a 1D ion crystal. In Chap. 7 we present a new method of a quantum state measurement — matrix product state tomography, which in comparison to a conventional quantum state tomography requires only polynomial growth of the number of measurements. The method was successfully tested on a 1D ion crystal.

The quantum many-body models derived here (see Eqs. (2.57) and (2.63)) do not have known analytical solutions and we investigate them via numerical methods. In Chap. 3 we present general purpose methods, which have found use on relatively small systems. In Chap. 4 we discuss DMRG methods, which have found a wide application in the investigation of quantum many-body systems.

Part II.

Numerical Methods

3. Full Hilbert Space Methods

In this section we will discuss general numerical methods to solve quantum spin and lattice models for strongly interacting particles applied to state representations involving Hilbert space. As the numerical cost of calculations is proportional to the Hilbert space, the exact methods have a great limitation — the Hilbert space scales exponentially as the system size grows linearly. Nonetheless, these relatively simple methods will form a basis for more advanced methods described in Chap. 4. Good reviews on general numerical methods can be found in [78, 79] and specifically on quantum systems in [77].

In Sec. 3.1 we will talk about about closed quantum systems, i.e. those for which the dynamics is described by the Schrödinger equation. In Sec. 3.2 we will talk about open quantum systems coupled to an environment, i.e. described by the master equation with dissipative terms.

3.1. Closed Quantum Systems

The central role in the formulation of problems in non-relativistic quantum mechanics is taken by the time-dependent Schrödinger equation

$$i\hbar\frac{\mathrm{d}|\psi(t)\rangle}{\mathrm{d}t} = \hat{H}(t)|\psi(t)\rangle, \tag{3.1}$$

and the time-independent version

$$E|\psi\rangle = \hat{H}|\psi\rangle, \tag{3.2}$$

where the Planck constant $\hbar \equiv 1$ is set to the identity for the convenience of numerical calculations, $\hat{H}(t)$ is the Hamiltonian of the system (in general it is time-dependent), $|\psi(t)\rangle$ is the time-dependent state-vector in the Schrödinger picture, and E is the energy of the system.

There is a large number of methods for solving the eigenvalue problem (3.2). Exact methods rely on the full diagonalization of the Hamiltonian $\hat{H}$ in a matrix representation with a fixed set of basis states $\{|\phi_n\rangle\}$. This method will produce the complete set of eigenvalues $\{E_n\}$, which form the spectrum of the system. The important point is that all possible states of the system can be expanded as

a sum over basis states

$$|\psi\rangle = \sum_n |\phi_n\rangle\langle\phi_n|\psi\rangle = \sum_n c_n|\phi_n\rangle, \tag{3.3}$$

where c_n is the contribution of each basis state.

However, quite often the calculation of the whole spectrum is costly or not necessary, i.e. when we are interested only in the states with the lowest or highest eigenvalues. In this case, there are approximate methods based on the power expansion (e.g. expansion in Lanczos basis via Arnoldi iteration [77, 79]). This becomes especially efficient in the case of sparse Hamiltonians, which have only a small fraction of non-zero elements. In that case, the speed of the algorithm will be proportional to the number of these non-zero elements, and not the size of the matrix.

Regarding the calculations of the time-dependent Schrödinger equation (3.1), one has to propagate the initial state $|\psi_0\rangle$ at time $t = 0$. In the case of the time-independent Hamiltonian $\hat{H}(t) = \hat{H}$, the time-evolution operator has the following form

$$\hat{U}(t) = e^{-i\hat{H}t} = \sum_n e^{-iE_n t}|\phi_n\rangle\langle\phi_n|, \tag{3.4}$$

and the state-vector of the system takes the form

$$|\psi(t)\rangle = \hat{U}(t)|\psi_0\rangle = \sum_n e^{-iE_n t}|\phi_n\rangle\langle\phi_n|\psi_0\rangle = \sum_n c_{0,n}e^{-iE_n t}|\phi_n\rangle, \tag{3.5}$$

where $c_{0,i}$ is the contribution of each basis state in the initial state. It is an expensive calculation, as it requires the entire spectrum first and then one needs to propagate each basis state. Moreover, this expression is not valid for the case of a time-dependent Hamiltonian, where the eigenbasis changes.

More efficient numerical techniques are based on the discretization of time and propagation of the state vector between times t_i and $t_{i+1} = t_i + \Delta t$ using one of many available algorithms. A great example of such algorithms is the Runge-Kutta method [108] which is a combination of implicit and explicit iterative methods, which includes the well-known routine called the Euler Method [108], used in temporal discretization for the approximate solutions of ordinary differential equations. A popular example of the method requires the 4th order expansion of the time-evolution operator and produces the resulting state-vector with error after each time step of the order $\mathcal{O}(\Delta t^5)$.

It also should be noted that the prefactor in front of the error term can vary quite dramatically depending on the method. All methods of time propagation can be split in two main groups — explicit and implicit [108]. Explicit methods calculate the state of a system at a later time $|\psi_{i+1}\rangle = |\psi(t_{i+1})\rangle$ from the state of the system at the current time $|\psi_i\rangle$, while implicit methods find a solution by solving an equation involving both the current state $|\psi_i\rangle$ of the system and the

later one $|\psi_{i+1}\rangle$. The main difference between the methods can be seen from the following example.

The explicit method for the time evolution of a state gives

$$|\psi_{i+1}\rangle = e^{-i\hat{H}\Delta t}|\psi_i\rangle = \underbrace{(\mathcal{I} - i\hat{H}\Delta t)}_{\hat{U}_{\mathrm{e}}(\Delta t)}|\psi_i\rangle + \mathcal{O}(\Delta t^2), \tag{3.6}$$

where besides a large numerical error the time explicit evolution operator $\hat{U}_{\mathrm{e}}(\Delta t)$ is not unitary. Hence the state has to be renormalized after each time step.

The starting point for the implicit method can be obtained as

$$|\psi_i\rangle = e^{i\hat{H}\Delta t}|\psi_{i+1}\rangle = (\mathcal{I} + i\hat{H}\Delta t)|\psi_{i+1}\rangle + \mathcal{O}(\Delta t^2), \tag{3.7}$$

which one would have to solve for $|\psi_{i+1}\rangle$, i.e. the method does not give the explicit expression for the state-vector at the next time step.

It is clear that implicit methods require some extra work to resolve the system of equations, rather than the explicit methods that give the result explicitly. Implicit methods are used because many problems arising in practice are stiff. A stiff differential equation is numerically unstable, unless the step size Δt is taken to be extremely small. The main idea is that the equation includes some terms that can lead to rapid variation in the solution. For such problems, to achieve a given accuracy, it takes much less computational time to use an implicit method with larger time steps, even taking into account that one needs to solve an equation of the form (3.7) at each time step. That said, whether one should use an explicit or implicit method depends upon the problem to be solved.

It is also common to combine explicit and implicit methods and obtain a semi-implicit version (Crank-Nicholson method [108]), which is basically the case of half-evolution of the state forward and backward.

$$\begin{cases} |\psi_{i+1/2}\rangle = e^{-i\hat{H}\Delta t/2}|\psi_i\rangle = (\mathcal{I} - i\hat{H}\Delta t/2)|\psi_i\rangle + \mathcal{O}(\Delta t^2), \\ |\psi_{i+1/2}\rangle = e^{+i\hat{H}\Delta t/2}|\psi_{i+1}\rangle = (\mathcal{I} + i\hat{H}\Delta t/2)|\psi_{i+1}\rangle + \mathcal{O}(\Delta t^2), \end{cases} \tag{3.8}$$

Here we see the appearance of the intermediate state $|\psi_{i+1/2}\rangle$ which plays the role of the connection for both solutions and hence the state at the time t_{i+1} can be obtained as

$$|\psi_{i+1}\rangle = \underbrace{\frac{\mathcal{I} - i\hat{H}\Delta t/2}{\mathcal{I} + i\hat{H}\Delta t/2}}_{\hat{U}_{\mathrm{si}}(\Delta t)}|\psi_i\rangle + \mathcal{O}(\Delta t^2), \tag{3.9}$$

where $\hat{U}_{\mathrm{si}}(\Delta t)$ is a semi-implicit unitary operator and hence preserves the norm of the state, but it still requires inversion of the Hamiltonian (for instance via the Gaussian elimination method [109]). It might be profitable to avoid doing it

in the case of sparse Hamiltonians, as the application of the Hamiltonian on the state scales as the number of non-zero elements only. A further trick relies on the fact the intermediate state can be obtained iteratively by iterating the following expression a few times

$$|\psi_{i+1/2}\rangle = |\psi_i\rangle - i\hat{H}\frac{\Delta t}{2}|\psi_{i+1/2}\rangle + \mathcal{O}(\Delta t^2). \tag{3.10}$$

Then the required state-vector at the time t_{i+1} would read

$$|\psi_{i+1}\rangle = 2|\psi_{i+1/2}\rangle - |\psi_i\rangle + \mathcal{O}(\Delta t^2). \tag{3.11}$$

Depending on the problem stiffness, reasonable time steps of the time evolution, and difficulty of the equations in the explicit method one needs to choose the appropriate method.

Below we would like to mention two completely different approaches to time evolution that can produce results where all said above fails.

3.1.1. Krylov Subspace Algorithms

As we could see above, explicit methods of time evolution relies on the Taylor expansion of the time evolution operator

$$\hat{U}(t) = e^{-i\hat{H}t} = \mathcal{I} + \frac{-i\hat{H}t}{1!} + \frac{(-i\hat{H}t)^2}{2!} + \frac{(-i\hat{H}t)^3}{3!} + ..., \tag{3.12}$$

thus the evolution of the initial vector becomes

$$|\psi(t)\rangle = \hat{U}(t)|\psi_0\rangle = |\psi_0\rangle + \frac{-i\hat{H}t}{1!}|\psi_0\rangle + \frac{(-i\hat{H}t)^2}{2!}|\psi_0\rangle + \frac{(-i\hat{H}t)^3}{3!}|\psi_0\rangle + ...; \tag{3.13}$$

it can be truncated after the first m terms, leading to an approximation

$$|\psi(t)\rangle = |\psi_0\rangle + c_1\hat{H}t|\psi_0\rangle + c_2(\hat{H}t)^2|\psi_0\rangle + ... + c_{m-1}(\hat{H}t)^{m-1}|\psi_0\rangle + \mathcal{O}(t^m), \tag{3.14}$$

with coefficients $c_k = (-i)^k/k!$. This truncated subspace

$$K_m(\hat{H}t, |\psi_0\rangle) = \mathrm{Span}\{|\psi_0\rangle, \hat{H}t|\psi_0\rangle, (\hat{H}t)^2|\psi_0\rangle, ..., (\hat{H}t)^{m-1}|\psi_0\rangle\}, \tag{3.15}$$

is called the Krylov subspace of dimension m, and is spanned by non-orthogonal vectors, in general. For this reason the coefficients c_k of the Taylor expansion are not necessarily the best coefficients and one can search for a better linear combination of vectors.

Elements of the Krylov subspace are better manipulated via their representation onto an orthonormal basis. For instance, the Arnoldi procedure [79] constructs

such a basis. This procedure is mathematically equivalent, but numerically superior to the Modified Gram-Schmidt procedure [79]. A detailed review and more efficient implementations of the above algorithm can be found in [110].

The superiority of this method becomes substantially noticeable for sparse matrices and it relies only on the construction of the Krylov subspace. For instance, the critical transverse Ising chain of 20 spins-1/2 can be time-evolved via the above method within a several minutes on a modern laptop, with a relative numerical error $\sim 10^{-15}$. This speed becomes more striking when one estimates the size of the time evolution operator $\hat{U}(t)$ as 16TB if stored in double precision. One needs to understand that even in the case of a sparse Hamiltonian the time-evolution operator $\hat{U}(t)$ will most likely not be sparse.

3.1.2. Suzuki-Trotter Decomposition

As we can see in the previous sections the computational cost comes from several sources: the efficiency of the algorithm, the number of the computational operations, and the size of the system. The method described in this section allows us to push the system sizes to higher values. The idea here is to avoid storing a large Hamiltonian in memory, which can be large even in the sparse case, but rather store it by parts. Then a single step of the time evolution will consist of consequent updates with the Hamiltonian components. The idea of this method will be further developed in Sec. 4.3.1, where the state vector will be stored in a new form.

First, we need to introduce some graphical notation, which will be useful in Chap. 4 as well. Let us consider a one dimensional system constructed of local constituents with the local Hilbert space dimension d. This could be a spin-1/2 chain with $d = 2$, for spin up and down. Then the dimension of the Hilbert space will be equal to the multiplication of local dimensions $\dim(\mathcal{H}) = d^M$, where M is the number of local constituents. The state-vector will take the following form

$$|\psi(t)\rangle = \sum_{\{r_\alpha\}=1}^{d} c_{r_1,r_2,...,r_M}(t)|r_1, r_2, ..., r_M\rangle, \tag{3.16}$$

where $\{r_\alpha\}$ are counters of local dimensions and $|r_\alpha\rangle$ are state-vectors of the local constituents. In the case of spin-1/2: $|r_1\rangle = |\downarrow\rangle$ and $|r_2\rangle = |\uparrow\rangle$.

A Hamiltonian in general takes an analogous form

$$\hat{H} = \sum_{\{r_\alpha\}=1}^{d} \sum_{\{r'_\alpha\}=1}^{d} d^{r'_1,r'_2,...,r'_M}_{r_1,r_2,...,r_M}|r_1, r_2, ..., r_M\rangle\langle r'_1, r'_2, ..., r'_M|. \tag{3.17}$$

One can see in Fig. 3.1 both tensors of the state and Hamiltonian represented as diagrams. For operators, in general, it is more convenient to separate input and

output index groups, which is why we choose to draw input $\{r'_\alpha\}$ at the top and output $\{r_\alpha\}$ at the bottom.

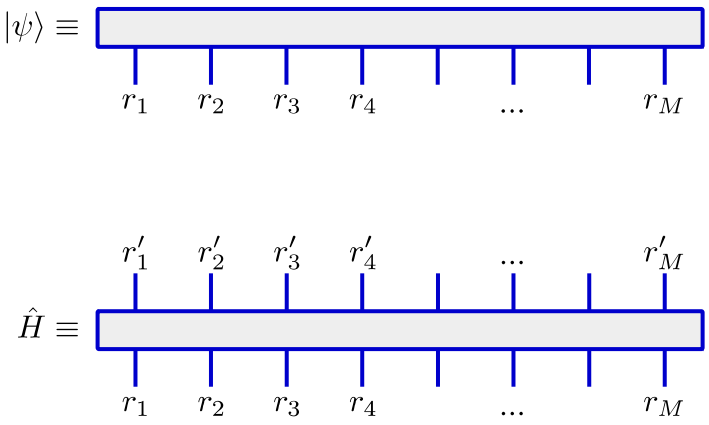

Figure 3.1.: Diagrammatic representation of the state $|\psi\rangle$ and Hamiltonian $\hat{H}$ tensors. Note that the number of legs on the diagram is equal to the number of indices on the tensors.

Let us also consider a Hamiltonian that can be expanded as a sum of local Hamiltonians. For the sake of an instructive example we can consider local Hamiltonians acting on at most 2 neighboring constituents:

$$\hat{H} = \sum_k \hat{h}_{k,k+1}, \tag{3.18}$$

which means that $\hat{h}_{r,r+1}$ only acts on constituents r and $r+1$ (neighboring interactions),

$$\hat{h}_{k,k+1} = \sum_{r_k,r_{k+1}=1}^{d} \sum_{r'_k,r'_{k+1}=1}^{d} f^{r'_k,r'_{k+1}}_{r_k,r_{k+1}} |r_k, r_{k+1}\rangle\langle r'_k, r'_{k+1}|, \tag{3.19}$$

and the time evolution operator reads

$$\hat{U}(\Delta t) = e^{-i\hat{H}\Delta t} \approx \prod_r \underbrace{e^{-i\hat{h}_{r,r+1}\Delta t}}_{U_{r,r+1}(\Delta t)} + \mathcal{O}(\Delta t^2), \tag{3.20}$$

where the error is due to the fact that in general local Hamiltonians do not commute between each other:

$$[\hat{h}_{r,r+1}, \hat{h}_{r+1,r+2}] \neq 0. \tag{3.21}$$

This expansion is just the lowest order expansion of the Baker–Campbell–Hausdorff formula [111]. The single time-evolution step consists of a consecutive evolution of all partitions of the state vector $|\psi(t)\rangle$, as it is shown in Fig. 3.2.

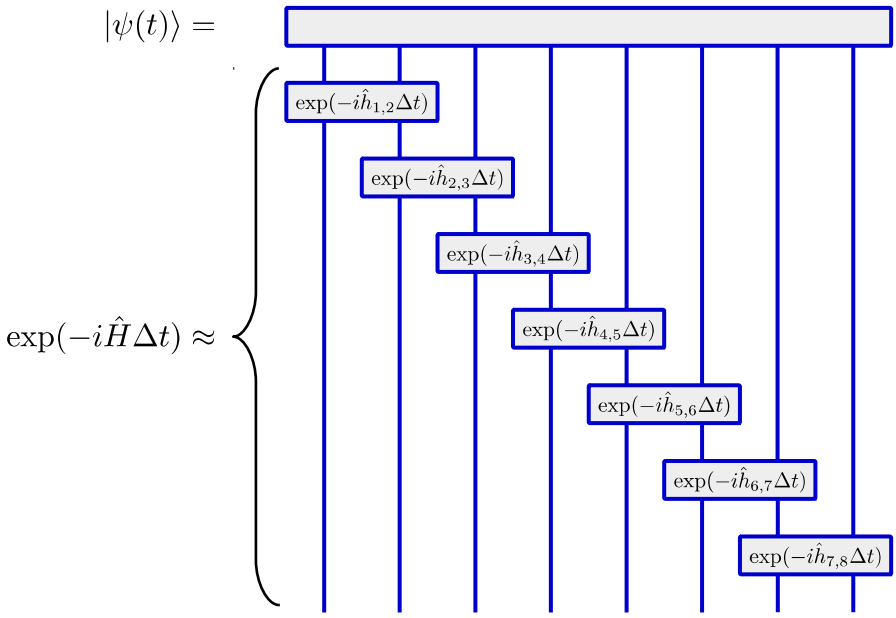

Figure 3.2.: Diagrammatic representation of a single time-evolution step of the tensor $c_{r_1,r_2,\ldots,r_M}(t)$. After the contraction of all internal legs this scheme produces $c_{r_1,r_2,\ldots,r_M}(t+\Delta t)$.

At this point one can see that there is no need to store the entire Hamiltonian in memory. By using this technique one can perform time-evolution of system sizes unreachable via by methods operating with the whole Hamiltonian. Note that now it is only the state $|\psi(t)\rangle$ which scales exponentially with the system size and hence will take most of the memory. For instance, a state vector for 28 spins-1/2 will require 4GB of memory in double precision, which makes it tractable for modern personal computers.

In general, even time-evolution of the Hamiltonian with long-range interactions can be simulated using Suzuki-Trotter decomposition, via application of swap gates

$$\hat{S}_{i,i+1}|i,i+1\rangle = |i+1,i\rangle, \tag{3.22}$$

but it leads to the increase of the decomposition error and hence makes the simulation more costly.

Besides that, the method described above is not limited to Hamiltonians with two-body interactions. For instance in the case of three body interactions one

will use gates $\hat{h}$ spanning over three sites. This will of course require the expansion of the Hamiltonian of each particular problem individually.

3.1.3. Symmetries

Lastly, we will consider examples of the methods when the Hamiltonian has a particular symmetry which leads to the reduction of the computational cost. Ultimately every symmetry of the Hamiltonian is related to a conservation law, for instance magnetization, momentum, parity, spin inversion, and/or number of particles in the system.

Using conservation laws (symmetries) of the Hamiltonian $\hat{H}$ we can choose the basis in such a way that the matrix representation of $\hat{H}$ becomes block-diagonal (Fig. 3.3). Then each block can be diagonalized independently.

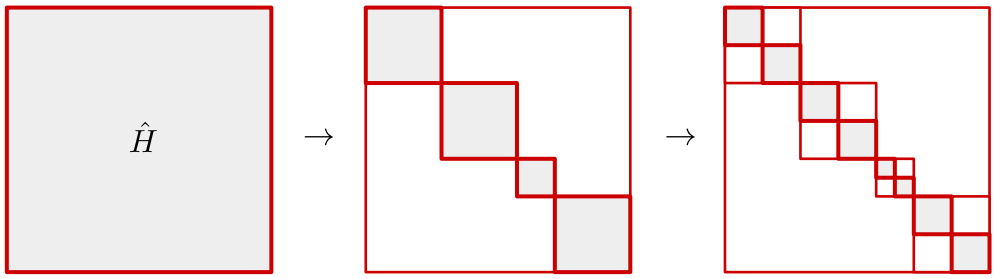

Figure 3.3.: Block diagonalization of the Hamiltonian allows us to solve each of the blocks independently and hence reduce the computational cost.

The conservation of the particle number in the Bose-Hubbard model (2.57) means that from the Hilbert space with an infinite number of possibilities we need to consider only $(N+M-1)!/[N!(M-1)!]$ states, where N is the number of particles and M is the number of sites.

For homogeneous systems with periodic boundary conditions we have translational symmetry associated with the translation operator

$$\hat{T}|a,b,c\rangle = |b,c,a\rangle, \tag{3.23}$$

where a, b, c are local states of the 3 equal constituents of the whole system. Also homogeneous systems have a reflection symmetry associated with the parity operator

$$\hat{P}|a,b,c\rangle = |c,b,a\rangle. \tag{3.24}$$

It means that the system Hamiltonian $\hat{H}$ commutes with both of these operators

$$\begin{cases} [\hat{H}, \hat{T}] = 0, \\ [\hat{H}, \hat{P}] = 0, \end{cases} \tag{3.25}$$

hence the solutions of the eigenproblem (3.2) for each of the symmetry sectors can be found independently. The implementation of symmetries requires writing a completely new set of codes for each particular symmetry and Hamiltonian.

3.1.4. Imaginary Time Evolution

Time evolution algorithms with a minor modification can also be used to obtain the ground state of the system. In order to do so one evolves an initial state with imaginary time. As one can see below all components of the state different from the ground state will have an exponentially small suppression prefactor.

The algorithm starts as one chooses the evolution time $t = -i\tau$, where $\tau \to +\infty$. Then

$$|\psi(\tau)\rangle = \lim_{\tau \to +\infty} \frac{e^{-\hat{H}\tau}|\psi(0)\rangle}{\|e^{-\hat{H}\tau}|\psi(0)\rangle\|} \to |\phi_0\rangle, \tag{3.26}$$

where $|\psi(0)\rangle$ is the initial state. One needs to renormalizes the state because of the non-unitary evolution operator. It is easy to see why this indeed gives the ground state by looking at the expanded expression in the denominator

$$\begin{aligned} e^{-\hat{H}\tau}|\psi(0)\rangle &= \sum_n e^{-E_n\tau}|\phi_n\rangle\langle\phi_n|\psi(0)\rangle \\ &= e^{-E_0\tau}\left(|\phi_0\rangle\langle\phi_0|\psi(0)\rangle + e^{-(E_1-E_0)\tau}|\phi_1\rangle\langle\phi_1|\psi(0)\rangle + ...\right) \\ &= e^{-E_0\tau}\left(|\phi_0\rangle\langle\phi_0|\psi(0)\rangle + \mathcal{O}(e^{-(E_1-E_0)\tau})\right), \end{aligned} \tag{3.27}$$

where we see that the contribution of all excited state are exponentially suppressed by at least a factor $e^{-\tau\Delta E}$ defined via the energy gap $\Delta E = E_1 - E_0$.

In principle one can start with any initial state $|\psi(0)\rangle$, even with a state completely orthogonal to the target ground state. The reason for this is in numerical errors that eventually add up to a small component of the ground state. Having a finite gap between the ground state and the rest of the spectrum will lead to the exponential increase of the ground state component and suppression of all other eigenstates. For exactly this reason it might be practically difficult to use imaginary time evolution when one wants to preserve a certain symmetry in the system. For instance, if one desires to obtain the ground state $|\phi_0^{[N]}\rangle$ of the Bose-Hubbard model (2.57) with a fixed number of bosons N, then a small numerical error introduces a component of the state $|\phi_0^{[N']}\rangle$ that is a ground state of the

system with N' bosons. If the corresponding ground state energy $E^{[N']} < E^{[N]}$, then the algorithm will converge to $|\phi_0^{[N']}\rangle$ instead of $|\phi_0^{[N]}\rangle$.

One can also obtain the lowest excited states by subtracting the components of lower eigenstates (found beforehand) after each time step. By choosing $t = +i\tau$, where $\tau \to +\infty$ we can also obtain the highest eigenstates.

3.2. Open Quantum Systems

In the previous section we discussed some numerical techniques that can be implemented for so-called closed systems, i.e. systems for which the whole Hamiltonian is known. However, in reality quantum many-body systems cannot be truly isolated from the environment. Furthermore, the environment can be quite large and too complex to be included into the model [112]. That is why approaches have been developed to treat such systems.

The entire composite system is governed by the Hamiltonian

$$\hat{H} = \hat{H}_{\text{sys}} + \hat{H}_{\text{env}} + \hat{H}_{\text{int}}, \tag{3.28}$$

where $\hat{H}_{\text{sys}}$ describes the system of interest, $\hat{H}_{\text{env}}$ describes the environment, and $\hat{H}_{\text{int}}$ is for their interaction. Then the pure unentangled state of the composite system takes form

$$|\psi\rangle = |\psi\rangle_{\text{sys}} \otimes |\psi\rangle_{\text{env}}, \tag{3.29}$$

where $|\psi\rangle_{\text{sys}}$ is the partition of the system of interest and $|\psi\rangle_{\text{env}}$ describes the state of the environment. Here we are genuinely interested in the dynamics of the system only that is why the environment part of the system is traced out as

$$\hat{\rho} \equiv \hat{\rho}_{\text{sys}} = \text{tr}_{\text{env}} \left(|\psi\rangle\langle\psi| \right), \tag{3.30}$$

i.e. the components of the state-vector representing the environment part are averaged. Initially $\hat{\rho}$ is a pure matrix that corresponds to the fact that the environment has not interacted with the system yet.

After some time evolution the system interacts with the environment and the total state of the system can not be written as a simple product of the system and environment part any more. The state of the system becomes mixed, in general, so is the density matrix of the system. From now on we will omit the subscripts related to the system of interest, the environment parts leave the consideration of the problem explicitly and stay in the following equations in the integrated form of jump operators.

In the case of Markovian dynamics the master equation has the Lindblad form

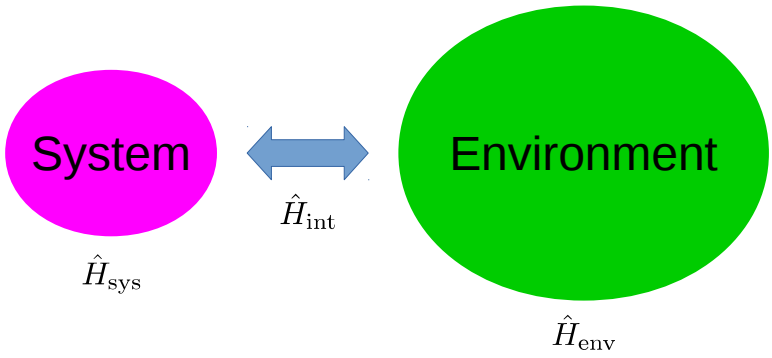

Figure 3.4.: Diagram of the global system decomposed into the system of interest $\hat{H}_{\text{sys}}$, environment $\hat{H}_{\text{env}}$, and their interaction $\hat{H}_{\text{int}}$. The system of interest is made of the degrees of freedom of the atoms of interest and described by the state $\hat{\rho}$. The environment can include other atoms' and electromagnetic field's degrees of freedom, which interact with the atoms of the system.

[112]

$$\frac{\mathrm{d}\hat{\rho}(t)}{\mathrm{d}t} = -i[\hat{H}, \hat{\rho}(t)] + \mathcal{L}[\hat{\rho}(t)], \tag{3.31}$$

where $\hbar \equiv 1$, and

$$\mathcal{L}[\hat{\rho}(t)] = \frac{1}{2}\sum_{\alpha}\left[2\hat{L}_{\alpha}\hat{\rho}(t)\hat{L}_{\alpha}^{\dagger} - \hat{L}_{\alpha}^{\dagger}\hat{L}_{\alpha}\hat{\rho}(t) - \hat{\rho}(t)\hat{L}_{\alpha}^{\dagger}\hat{L}_{\alpha}\right], \tag{3.32}$$

is the Lindblad term with a set of so-called jump operators $\{\hat{L}_{\alpha}\}$ that act on the system coupling it with the environment. Those jump operators can be local or global, depending on the nature of the interaction between the system and the bath. A great example of the jump operators is the decay operator that transfers the population down to lower levels and causes the system to emit a packet of energy to the environment — photons, in the case of coupling to the radiation field.

One can note that in the absence of the Lindblad term $\mathcal{L}[\hat{\rho}(t)]$ the master equation (3.31) becomes identical to (3.1) for the density matrix $\hat{\rho}(t) = |\psi(t)\rangle\langle\psi(t)|$.

An obvious way of numerical implementation of the time evolution is to vectorize (3.31). For this, one reshapes the density matrix to a vector form

$$\hat{\rho}(t) \to |\rho(t)\rangle \tag{3.33}$$

by reordering indices. Then the master equation will take the form

$$\frac{\mathrm{d}|\rho(t)\rangle}{\mathrm{d}t} = -i\left[(\mathcal{I}\otimes\hat{H}^{T}) - (\hat{H}\otimes\mathcal{I})\right]|\rho(t)\rangle + \tilde{\mathcal{L}}[|\rho(t)\rangle], \tag{3.34}$$

where

$$\tilde{\mathcal{L}}[|\rho(t)\rangle] = \frac{1}{2}\sum_{\alpha}\left[2\hat{L}_{\alpha}^{\dagger}\otimes\hat{L}_{\alpha}^{T} - \mathcal{I}\otimes(\hat{L}_{\alpha}^{\dagger}\hat{L}_{\alpha})^{T} - \hat{L}_{\alpha}^{\dagger}\hat{L}_{\alpha}\otimes\mathcal{I}\right]|\rho(t)\rangle. \tag{3.35}$$

One can implement any of the techniques described in Sec. 3.1. This algorithm is very expensive computationally because of the enormous size of the super operators contracted here for the time evolution of the vectorized density matrix.

That is why the method of quantum trajectories becomes a favorable choice when one wants to obtain the time-evolution of an open quantum system. The method is very flexible in its implementation and can be used for a large variety of systems in combination with other methods, such as DMRG (see Chap. 4). Below we introduce the quantum trajectory method, but a more detailed review can be found in [95].

3.2.1. Quantum Trajectories

The general idea of the quantum trajectory method [94] is that instead of evolving the density matrix of the system using the master equation (3.31), one writes down an equivalent set of equations that describe a stochastic process in the open quantum system, namely all interactions with the environment become probabilistic events.

Then in order to calculate the time-evolution of a certain observable, one considers the initial states of the system as a pure state $|\psi(0)\rangle$. If the initial state $\hat{\rho}(0)$ is not pure, then the initial state vectors $|\psi(0)\rangle$ should be sampled and evolved with the set of the stochastic equations performing probabilistic events (i.e. interaction with the environment) according to the predefined rules. For each quantum trajectory one calculates the required variables as done for standard unitary time evolution (properly normalizing the state if needed). Then this process is repeated for a whole set of quantum trajectories and the value of the expectation variable is averaged over all these trajectories in the end.

Now let us consider a concrete example that will show how the method of quantum trajectories can be implemented, and that it is indeed equivalent to the evolution via the master equation.

First, we rewrite (3.31) in the following form

$$\frac{\mathrm{d}\hat{\rho}(t)}{\mathrm{d}t} = -i[\hat{H}_{\mathrm{eff}}\hat{\rho}(t) - \hat{\rho}(t)\hat{H}_{\mathrm{eff}}^{\dagger}] + \sum_{\alpha}\hat{L}_{\alpha}\hat{\rho}(t)\hat{L}_{\alpha}^{\dagger}, \tag{3.36}$$

where we refer to

$$\hat{H}_{\mathrm{eff}} = \hat{H} - \frac{i}{2}\sum_{\alpha}\hat{L}_{\alpha}^{\dagger}\hat{L}_{\alpha} \tag{3.37}$$

as the effective Hamiltonian for the system coupled with environment (note that it is not Hermitian any more, so the system experiences losses due to coupling to the environment). The last term of (3.36) is then called the recycling term as it restores the norm of the state vector due to losses caused by the non-Hermiticity of the effective Hamiltonian.

The whole evolution of the single trajectory will consist of the following steps. First, we perform the evolution of the state vector $|\psi(t)\rangle$ by time δt, so

$$|\psi(t+\delta t)\rangle = (1 - i\hat{H}_{\text{eff}}\delta t)|\psi(t)\rangle, \tag{3.38}$$

and we calculate the norm of the resulting state vector, which will be less than one because $\hat{H}_{\text{eff}}$ is not Hermitian:

$$\langle\psi(t+\delta t)|\psi(t+\delta t)\rangle = 1 - \delta p + \mathcal{O}(\delta t^2). \tag{3.39}$$

The value δp arises from the non-Hermitian part of the effective Hamiltonian and can be split in the sum over all possible channels of losses

$$\begin{aligned}\delta p &= \delta t\langle\psi(t)|i(\hat{H}_{\text{eff}} - \hat{H}_{\text{eff}}^{\dagger})|\psi(t)\rangle \\ &= \delta t\sum_{\alpha}\langle\psi(t)|\hat{L}_{\alpha}^{\dagger}\hat{L}_{\alpha}|\psi(t)\rangle \equiv \sum_{\alpha}\delta p_{\alpha}.\end{aligned} \tag{3.40}$$

By doing this we can interpret a single δp_{α} as the relative probability of the action described by the jump operator $\hat{L}_{\alpha}$ that acts on the state vector $|\psi(t)\rangle$.

Secondly, we take into account the recycling term in a probabilistic manner. From the perspective of numerical calculations we choose a random number r_1 from the interval $[0, 1]$, and comparing it with the norm of the state vector $1 - \delta p$.

- With probability $1 - \delta p$ the state vector gets renormalized, i.e.

$$|\psi(t+\delta t)\rangle = \frac{|\psi(t+\delta t)\rangle}{\sqrt{1-\delta p}} \tag{3.41}$$

- With probability δp the quantum jump happens, i.e.

$$|\psi(t+\delta t)\rangle = \frac{\hat{L}_{\alpha}|\psi(t)\rangle}{\sqrt{\delta p_{\alpha}/\delta t}}, \tag{3.42}$$

  where only one particular jump α occurs. In order to identify which particular jump happens, one needs to draw another random number r_2 from the interval $[0, 1]$, and compare it with the cumulative distribution function of all jumps

$$\Pi_{\alpha} = \sum_{\beta=1}^{\alpha}\frac{\delta p_{\alpha}}{\delta p}. \tag{3.43}$$

The location of r_2 will then determine which particular quantum jump happens.

By following the described procedure, one will obtain the evolution of a single quantum trajectory. In order to convince ourselves that this stochastic method is indeed equivalent to the master equation (3.31), we can construct the density operator and show that after averaging, it produces the exact result up to second order corrections in the time step.

Without loss of generality, let us consider the case with the initial pure state $|\psi(t)\rangle$, then its density matrix reads

$$\hat{\rho}_{\mathrm{qt}}(t) = |\psi(t)\rangle\langle\psi(t)|. \tag{3.44}$$

Following the above described procedure we obtain that the averaged value of the density operator after one time-step reads

$$\begin{aligned}\langle\hat{\rho}_{\mathrm{qt}}(t+\delta t)\rangle_{\mathrm{avr}} =&(1-\delta p)\frac{|\psi(t+\delta t)\rangle}{\sqrt{1-\delta p}}\frac{\langle\psi(t+\delta t)|}{\sqrt{1-\delta p}}\\ &+\delta p\sum_\alpha \frac{\delta p_\alpha}{\delta p}\frac{\hat{L}_\alpha|\psi(t)\rangle}{\sqrt{\delta p_\alpha/\delta t}}\frac{\langle\psi(t)|\hat{L}_\alpha^\dagger}{\sqrt{\delta p_\alpha/\delta t}}+\mathcal{O}(\delta t^2).\end{aligned} \tag{3.45}$$

After simplification one can rewrite it as

$$\frac{\langle\hat{\rho}_{\mathrm{qt}}(t+\delta t)\rangle_{\mathrm{avr}}-\hat{\rho}_{\mathrm{qt}}(t)}{\delta t} = -i(\hat{H}_{\mathrm{eff}}\hat{\rho}_{\mathrm{qt}}(t)-\hat{\rho}_{\mathrm{qt}}(t)\hat{H}_{\mathrm{eff}}^\dagger)+\sum_\alpha \hat{L}_\alpha\hat{\rho}_{\mathrm{qt}}(t)\hat{L}_\alpha^\dagger+\mathcal{O}(\delta t). \tag{3.46}$$

This result is also valid for a mixed state $\hat{\rho}_{\mathrm{qt}}(t)$, where one samples among the initial state vectors as well. Now we can see that the quantum trajectories method is equivalent to the first order approximation of the master equation.

Note that in order to calculate the expectation values of an operator $\hat{O}$ one needs to take the ensemble average over the trajectories

$$\langle\hat{O}\rangle = \mathrm{tr}(\hat{O}\hat{\rho}_{\mathrm{qt}}(t)) = \frac{1}{N_{\mathrm{qt}}}\sum_n^{N_{\mathrm{qt}}}\langle\psi^{[n]}(t)|\hat{O}|\psi^{[n]}(t)\rangle, \tag{3.47}$$

where $|\psi^{[n]}(t)\rangle$ is a single realization of N_{qt} quantum trajectories. The error of the expectation value is calculated as the standard deviation of the mean, equivalent to the standard deviation multiplied by $1/\sqrt{N_{\mathrm{qt}}}$. Thus, by performing the procedure described above we have shown that in the case of a large number of quantum trajectories $N_{\mathrm{qt}} \to \infty$ and small time steps $\delta t \to 0$, one can numerically simulate the evolution under the Lindblad master equation (3.31).

Using this first order method relies on small time steps because of two independent factors. First, the time step should be small as the time evolution is realized via

the first order expansion in δt. Secondly, this method of quantum trajectories relies on the fact that within one step at most one quantum jump can happen, i.e. δp is kept small. There are several techniques [95] that one can implement to improve the order of the method. For instance one notices that the quantum jump always occurs at the end of the time step, whereas in reality it happens within the step. This leads to an underestimation of the emission rate. Another issue is related to the use of only the first order time evolution in (3.38); an appropriate evolution using higher order methods can increase the accuracy of the method.

3.3. Conclusions

In this chapter we considered general numerical methods taking in consideration the entire Hilbert space of the system. In the case of the closed quantum system the solution of the problem always comes to solving the time-dependent (3.1) or time-independent (3.2) Schrödinger equations with a known Hamiltonian. If one is interested in only a small subsystem it is possible to use the open system approach and trace out the part of system which forms the environment. Then the dynamics of the system obeys the master equation (3.31). Among the methods we mentioned here are various approximate methods of time evolution, the decomposition of the Hamiltonian, use of symmetries, and the stochastic approach of quantum trajectories.

In Chap. 4 we will consider advanced methods of dealing with exponential growth of the Hilbert space via the use of the subspace of only relevant states. On the top of those methods one can always use methods presented in this chapter.

4. Reduced Hilbert Space Methods

In this chapter we will focus our attention on one of the most powerful numerical methods in the area of correlated quantum many-body systems — Density Matrix Renormalization Group (DMRG) combined with Matrix Product representation of States and Operators (MPS and MPO). These methods have found a lot of implementations outside of this area of physics, but we will focus our attention only on quantum many-body systems. A much more detailed and broad overview of the methods can be found in the following reviews [80, 81]. The main idea of those methods is the reformulation of problems of many-body quantum mechanics in the language of tensor networks (see Fig. 4.1) and the use of ideas based on the concept of entanglement to extract accurately certified approximate solutions.

The starting point of the method coincides with the development of the time-independent DMRG algorithm by S. R. White [82, 83], which allowed ground state calculations of 1D models. In subsequent works [84, 85] it was shown that the ground state obtained via the DMRG algorithm can be always written as an MPS. In [86] it was quantified how well MPS approximate exact ground states of one-dimensional quantum systems, which gave a theoretical justification for the high accuracy of DMRG algorithms even in the case of critical systems, making use of entanglement.

The next important development in the field was when time evolution codes using DMRG methods were developed [87–89]. Those methods were independently developed by different groups at the same time and were referred to by different names, such as TEBD and t-DMRG, but exploited the same idea of the adaptive change of the Hilbert space basis, DMRG optimizations, and truncation of the expanding Hilbert space.

Later development of the methods made it possible to include matrix product representation of operators (MPO) and develop algorithms that were more efficient for long-range Hamiltonians [90–92]. Also, the same MPO description was successfully used for representation of density matrices of thermal states and their evolution [93].

In addition to these developments for 1D systems, there were also quite successful attempts to numerically treat 2D and 3D systems with other tensor networks such as PEPS [80] and MERA [113], but these works are only indirectly related to the work in this thesis.

In Sec. 4.1 we will discuss the general structure of MPS, the role of entanglement and area laws in quantum many-body systems. We will then proceed (Sec. 4.2)

to MPOs and give some examples of construction of useful operators, such as Hamiltonians or projectors. In Sec. 4.3 we conclude by giving an overview of some methods for solving quantum mechanical problems in 1D that are most relevant for us, such as calculation of eigenstates and thermal states, and time evolution simulations.

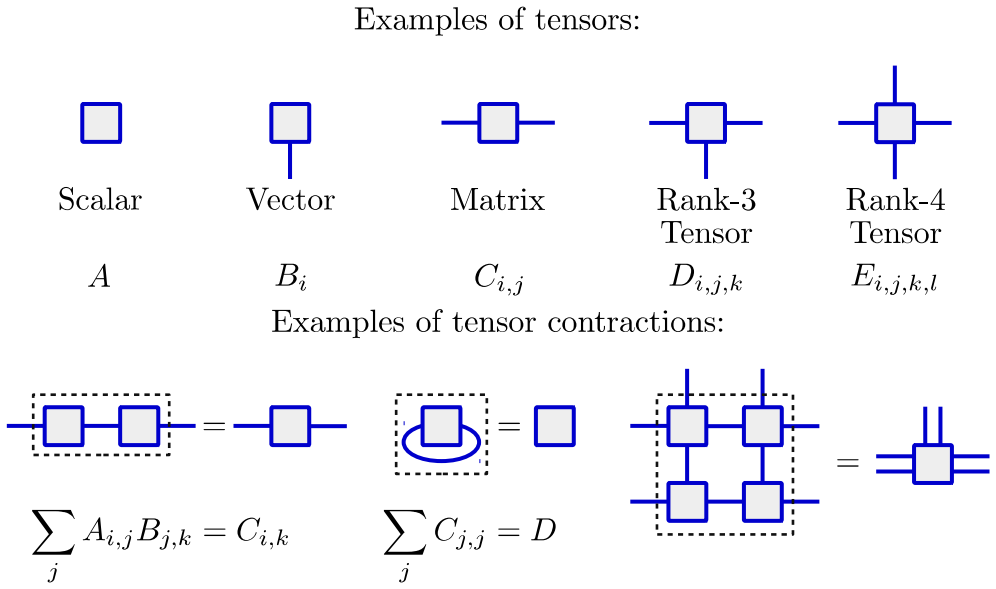

Figure 4.1.: Graphical notation we use to represent tensor networks. Each tensor (shown as a box) has a number of indices, which are represented as legs coming out of the box. The tensor with zero legs is just a scalar, with one leg a vector, two legs a matrix, and with three and more a higher-rank tensor. When two or more tensors are connected, it means that they are to be contracted (dash boxes show it) with the corresponding indices. A contraction can be done between indices of the same tensor as well. Then contraction of multiple tensors can produce tensors of higher rank.

4.1. Matrix Product States (MPS)

The Hilbert space of a quantum mechanical many-body system is exponentially large in the number of constituents of the system. For example the Hilbert space of one qubit is two-dimensional, two qubits have 4-dimensional space, and 2^M-dimensional for M qubits. In order to store the information of an arbitrary state vector

$$|\psi\rangle = \sum_{\{r_\alpha\}=1}^{d_\alpha} c_{r_1,r_2,...,r_M}|r_1, r_2, ..., r_M\rangle, \tag{4.1}$$

one needs to store the tensor $c_{r_1,r_2,...,r_M}$, which is the expansion of the state in local bases $\{|r_\alpha\rangle\}$ with dimensions d_α (Fig. 4.2). For instance, a system of M identical qubits will have a Hilbert space of 2^M elements, which is the number of elements in the tensor $c_{r_1,r_2,...,r_M}$.

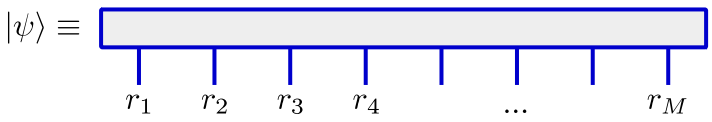

Figure 4.2.: Graphical representation of the tensor associated with the state vector $|\psi\rangle$ (4.1).

Let us consider an example one dimensional system that consist of M subsystems with identical local d-dimensional Hilbert spaces spanned by the set of state vectors $\{|r_\alpha\rangle\}$ where $\alpha = 1, 2, ..., M$ is the counter of the subsystems. Then, instead of storing the state vector in the standard form (4.1) one can use the following form

$$|\psi_{\text{MPS}}\rangle = \sum_{\{r_\alpha\}=1}^{d_\alpha} A^{[1]r_1} A^{[2]r_2} ... A^{[M]r_M} |r_1, r_2, ..., r_M\rangle, \tag{4.2}$$

where each object $A^{[\alpha]r_\alpha}$ is a $D_L^{[\alpha]} \times D_R^{[\alpha]}$ matrix, and $[\alpha]$ denotes the index of the subsystem. The state can also be graphically illustrated as in Fig. 4.3 where each element $A^{[\alpha]}$ has three indices, i.e. it is a rank-3 tensor (see Fig. 4.1). One immediately sees that in order for this expression to be correct for an arbitrary state vector the dimensions of these matrices should match, i.e. $D_R^{[\alpha]} = D_L^{[\alpha+1]}$. Also, as the result of the contraction of all matrices $A^{[\alpha]}$ for a fixed set of $\{r_\alpha\}$ should produce a scalar equal to $c_{\{r_\alpha\}}$ the following must be true: $D_L^{[1]} = 1$ and $D_R^{[M]} = 1$. From now on we will be calling $A^{[\alpha]}$ local tensors, $D_{L/R}^{[\alpha]}$ the bond dimensions, and d the local dimension. This representation of the state vector is a Matrix Product State (MPS).

Note that the tensor diagrams, the MPS $|\psi_{\text{MPS}}\rangle$ and the definition (4.2) that we have just considered correspond to the case of open boundary conditions. In the case of periodic boundary conditions, the first and the last tensor will be also connected. The best graphical representation of such a tensor network is where local tensors $A^{[\alpha]}$ are placed on a ring, not on a line. Then

$$|\psi_{\text{MPS}}^{\text{PBC}}\rangle = \sum_{\{r_\alpha\}=1}^{d_\alpha} \text{tr}\left[A^{[1]r_1} A^{[2]r_2} ... A^{[M]r_M}\right] |r_1, r_2, ..., r_M\rangle, \tag{4.3}$$

where the requirement that $D_L^{[1]} = 1$ and $D_R^{[M]} = 1$ is lifted. However both,

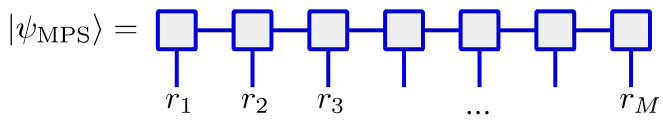

Figure 4.3.: Graphical representation of the tensor network associated with the state vector $|\psi_{\mathrm{MPS}}\rangle$ (4.2). Each subsystem has a corresponding rank-3 tensor $A^{[\alpha]}$. In the case of the first and the last tensor one of their bond dimensions is equal to one. Each connected link between tensors indicates summation, and each open link means an open index r_α. The representation like this, where tensors are ordered in a chain is called Matrix Product State (MPS) with Open Boundary Conditions (OBC).

representations are equivalent with the difference only in algorithms that can be implemented on them. The form for PBC (4.3) has the advantage in the case when the Hamiltonian has PBC as well, as $|\psi^{\mathrm{PBC}}_{\mathrm{MPS}}\rangle$ will have smaller bond dimensions for the same amount of entanglement in the state.

In order to be concrete with definitions let us consider a couple of examples of such matrix product states:

- The bosonic Gutzwiller state is a very simple state where all bond dimensions $D = 1$, i.e. all matrices $A^{[\alpha]r_\alpha}$ become just scalars. These states are also called product states as the global state is the direct product of local states. For instance, a state of 2 spins

$$|\psi_{\mathrm{prod}}\rangle = \frac{|0\rangle + |1\rangle}{\sqrt{2}} \otimes \frac{|0\rangle - |1\rangle}{\sqrt{2}} \tag{4.4}$$

  is a product state with $c_{0,0} = -c_{0,1} = c_{1,0} = -c_{1,1} = 1/2$. In an MPS form for $d = 2$ this state will be stored as

$$\begin{cases} A^{[1]0} = \frac{1}{\sqrt{2}}, & A^{[2]0} = \frac{1}{\sqrt{2}} \\ A^{[1]1} = \frac{1}{\sqrt{2}}, & A^{[2]1} = -\frac{1}{\sqrt{2}} \end{cases}. \tag{4.5}$$

- Now let us look at a different example, a Bell state

$$|\psi_{\mathrm{Bell}}\rangle = \frac{|0\rangle \otimes |0\rangle - |1\rangle \otimes |1\rangle}{\sqrt{2}}, \tag{4.6}$$

  which has only two non-zero elements $c_{0,0} = -c_{1,1} = 1/\sqrt{2}$. In this case the minimal bond dimension between the spins will be $D = 2$, and the

corresponding MPS matrices can take the following form

$$\begin{cases} A^{[1]0} = \begin{pmatrix} 1 & 0 \end{pmatrix}, & A^{[2]0} = \begin{pmatrix} 0 \\ -1/\sqrt{2} \end{pmatrix} \\ A^{[1]1} = \begin{pmatrix} 0 & 1 \end{pmatrix}, & A^{[2]1} = \begin{pmatrix} 1/\sqrt{2} \\ 0 \end{pmatrix} \end{cases}. \tag{4.7}$$

Note that this state cannot be represented by an MPS with bond dimensions $D = 1$. In Sec. 4.1.2 we will connect it with the important concept of spatial entanglement.

4.1.1. Orthonormal Forms of MPS

As one can see from the definition (4.2) and especially from the two examples above the definition of MPS does not uniquely specify the local tensors $A^{[\alpha]}$. For instance, one can insert $\mathcal{I} = X^{-1}X$ on a bond between two local tensors $A^{[\beta]}$ and $A^{[\beta+1]}$. Then by redefining these tensors as

$$\tilde{A}^{[\beta]r_\beta} = A^{[\beta]r_\beta}X^{-1}, \quad \tilde{A}^{[\beta+1]r_{\beta+1}} = XA^{[\beta+1]r_{\beta+1}}, \tag{4.8}$$

one can define a new MPS

$$|\tilde{\psi}_{\mathrm{MPS}}\rangle = \sum_{\{r_\alpha\}=1}^{d_\alpha} A^{[1]r_1}...\tilde{A}^{[\beta]r_\beta}\tilde{A}^{[\beta+1]r_{\beta+1}}...A^{[M]r_M}|r_1, r_2, ..., r_M\rangle, \tag{4.9}$$

which is identical to the original $|\psi_{\mathrm{MPS}}\rangle$. This means that each MPS has gauge freedom.

However, there is a set of convenient forms of MPS that can greatly reduce the amount of numerical calculations. Those forms are called, left-, right-, or mixed-orthonormal. In literature the term "orthonormal" is often substituted by normalized or canonical.

If all local tensors $A^{[\alpha]}$ satisfy the left gauge condition

$$\sum_{r_\alpha=1}^{d_\alpha} \left(A^{[\alpha]r_\alpha}\right)^\dagger A^{[\alpha]r_\alpha} = \mathcal{I}, \tag{4.10}$$

where $\mathcal{I}$ is a $D_R^{[\alpha]} \times D_R^{[\alpha]}$ identity matrix, then the state $|\psi_{\mathrm{MPS}}\rangle$ is left-orthonormal. If all local tensor $A^{[\alpha]}$ satisfy the right gauge condition

$$\sum_{r_\alpha=1}^{d_\alpha} A^{[\alpha]r_\alpha} \left(A^{[\alpha]r_\alpha}\right)^\dagger = \mathcal{I}, \tag{4.11}$$

where $\mathcal{I}$ is a $D_L^{[\alpha]} \times D_L^{[\alpha]}$ identity matrix, then the state $|\psi_{\mathrm{MPS}}\rangle$ is right-orthonormal.

If for a certain site β all local tensors to the left are left-orthonormal and all local tensors to the right are right-orthonormal, then the MPS is called mixed orthonormal. We can refer to the site β as the orthonormal center. Then one can immediately see that left and right orthonormal form are just special cases of the mixed orthonormal form.

The great advantage of the mixed orthonormal form is that it reduces the computational effort when one wants to calculate an expectation value of a local operator $\hat{O}^{[\beta]}$ acting only on the site β. Then all local tensors to the left and to the right from the orthonormal center will produce identities once they are contracted in the order starting from the edges of MPS and the calculation will read

$$\langle\psi_{\mathrm{MPS}}|\hat{O}^{[\beta]}|\psi_{\mathrm{MPS}}\rangle = \sum_{r_\beta, r'_\beta=1}^{d_\beta} \left(A^{[\beta]r'_\beta}\right)^\dagger O_{r'_\beta, r_\beta} A^{[\beta]r_\beta}, \tag{4.12}$$

where O is the matrix representation of $\hat{O}^{[\beta]}$ in the basis $|r_\beta\rangle$. For this particular reason we will refer to all other form as mixed forms, i.e. not orthonormal.

In order to perform left orthogonalization of a given mixed orthonormal state, one should perform consecutive transformation of the local tensors, starting from the left edge. First one needs to reshape a local tensor $A^{[\beta]r_\beta}_{n,m}$ into a matrix $\bar{A}_{(r_\beta n),m}$ where the local and left bond indices are combined in one index. The next step is to perform the singular value decomposition of this matrix

$$\bar{A}_{(r_\beta n),m} = \sum_q U_{(r_\beta n),q} S_{q,q} \left(V^\dagger\right)_{q,m}, \tag{4.13}$$

where U and $V^\dagger$ are unitary matrices, and $S_{q,q}$ is a diagonal matrix of the singular values λ_q. Then we redefine the local tensor by reshaping the left unitary matrix

$$A^{[\beta]r_\beta}_{n,q} = U_{(r_\beta n),q}, \tag{4.14}$$

so the condition (4.10) is satisfied automatically, and then we absorb the rest in the local tensor of the next site to the right

$$\tilde{A}^{[\beta+1]r_{\beta+1}}_{q,p} = \sum_m \lambda_q \left(V^\dagger\right)_{q,m} A^{[\beta+1]r_{\beta+1}}_{m,p}. \tag{4.15}$$

After that, one needs to move to the next site to the right and repeat the process. For this reason this procedure should be performed starting from the left edge of the MPS.

In order to perform right orthogonalization one needs to perform a mirror imaged procedure to the one described above, i.e. starting from the right edge. First one needs to reshape a local tensor $A^{[\beta]r_\beta}_{n,m}$ into a matrix $\bar{A}_{n,(r_\beta m)}$ where the local and right bond indices were combined in one index. Then the next step is to perform

the singular value decomposition of this matrix

$$\bar{A}_{n,(r_\beta m)} = \sum_q U_{n,q} \lambda_q \left(V^\dagger\right)_{q,(r_\beta m)}. \tag{4.16}$$

Then we redefine the local tensor by reshaping the right unitary matrix

$$A^{[\beta] r_\beta}_{q,m} = \left(V^\dagger\right)_{q,(r_\beta m)}, \tag{4.17}$$

so that the condition (4.11) is satisfied automatically, and the rest can be absorbed in the local tensor of the next site to the left

$$\tilde{A}^{[\beta-1] r_{\beta-1}}_{p,q} = \sum_n A^{[\beta-1] r_{\beta-1}}_{p,n} U_{n,q} \lambda_q. \tag{4.18}$$

If one starts converting the state to an orthonormal form starting from both edges, then they will inevitably meet at the orthonormal center and the resulting state will be mixed-orthonormal.

4.1.2. Entanglement

Now we are at the position to introduce one of the most important concepts in this method, spatial entanglement and its measures. Let us consider a normalized state in the MPS form, where we split the system in two parts (Fig. 4.4)

$$|\psi\rangle = \sum_q \lambda^{[\beta]}_q |\psi^{[1,2,\ldots,\beta]}_q\rangle |\psi^{[\beta+1,\ldots,M]}_q\rangle, \tag{4.19}$$

where $\lambda^{[\beta]}_q$ are called Schmidt values. They are all real positive and map each state from the left-hand side of the system with a corresponding state from the right-hand side of the system. One can note that if all states $|\psi^{[1,2,\ldots,\beta]}_q\rangle$ and $|\psi^{[\beta+1,\ldots,M]}_q\rangle$ are orthonormal then from the normalization of $|\psi\rangle$ we get

$$\sum_q |\lambda^{[\beta]}_q|^2 = 1. \tag{4.20}$$

We say that left-hand side of the system is not entangled with the right-hand side if and only if there is only one non-zero Schmidt value, which is equal to 1. If there is more than one such value the two parts of the system are entangled. There are different measures of entanglement available [114].

4.1.2.1. Von Neumann Entanglement Entropy

If the entire system is split in two parts A and B (not necessary left and right hand sides), the bipartite von Neumann entanglement entropy of the pure state

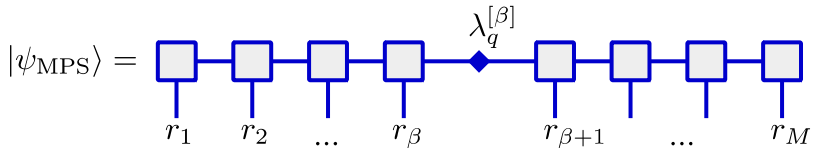

Figure 4.4.: Graphical representation of the tensor network associated with the state vector $|\psi\rangle$ (4.19). Schmidt values $\lambda_q^{[\beta]}$ map each state from the left-hand side of the system with a corresponding state from the right-hand side.

$\hat{\rho}$ is defined as

$$S_{\mathrm{vN}}(\hat{\rho}_A) = -\mathrm{tr}\left[\hat{\rho}_A \log_2 \hat{\rho}_A\right] = -\mathrm{tr}\left[\hat{\rho}_B \log_2 \hat{\rho}_B\right] = S_{\mathrm{vN}}(\hat{\rho}_B), \tag{4.21}$$

where

$$\hat{\rho}_A = \mathrm{tr}_B \hat{\rho}, \quad \hat{\rho}_B = \mathrm{tr}_A \hat{\rho}, \tag{4.22}$$

and $\mathrm{tr}_{A,B}$ are partial traces over A or B subsystems. Note that the result is equal for A and B.

Coming back to the above example we have the density matrix in the form

$$\hat{\rho} = |\psi\rangle\langle\psi| = \sum_{q,q'} \lambda_q^{[\beta]} \lambda_{q'}^{[\beta]} |\psi_q^{[1,2,\ldots,\beta]}\rangle |\psi_q^{[\beta+1,\ldots,M]}\rangle \langle\psi_{q'}^{[1,2,\ldots,\beta]}| \langle\psi_{q'}^{[\beta+1,\ldots,M]}|, \tag{4.23}$$

so that after tracing out either left or right hand sides we obtain the same value of the von Neumann entanglement entropy

$$S_{\mathrm{vN}} = -\sum_{q=1}^{D^{[\beta]}} \left(\lambda_q^{[\beta]}\right)^2 \log_2 \left[\left(\lambda_q^{[\beta]}\right)^2\right], \tag{4.24}$$

where summation goes over all Schmidt values $D^{[\beta]}$. One can see that the maximum entanglement entropy is achieved in the case of all $\lambda_q^{[\beta]} = 1/\sqrt{D^{[\beta]}}$, which is $S_{\mathrm{vN}}^{\max} = \log_2 D^{[\beta]}$.

For instance, the product state (mean field Gutzwiller ansatz) (4.4) has only one Schmidt value $\lambda = 1$ and $S_{\mathrm{vN}} = 0$, hence its spins are not entangled. On the other hand the fully entangled Bell state has the maximum number of Schmidt values and they are equal, $\lambda_1 = \lambda_2 = 1/\sqrt{2}$, so $S_{\mathrm{vN}} = 1$, which is maximum in this case.

4.1.2.2. Renyi Entanglement Entropies

Another common measure of bipartite entanglement is Renyi entanglement entropies

$$S_n(\hat{\rho}_A) = \frac{1}{1-n}\log_2\left[\mathrm{tr}\hat{\rho}_A^n\right] = \frac{1}{1-n}\log_2\left[\mathrm{tr}\hat{\rho}_B^n\right] = S_n(\hat{\rho}_B), \tag{4.25}$$

where $n > 0$ and $n \neq 1$. It also relies on splitting of the system into two parts and it also produces the same result independently of the chosen partition for pure total states.

Note that in the limit $n \to 1$ the Renyi entanglement entropy approaches the von Neumann entropy.

4.1.2.3. Truncation Error

In order to store the entire MPS exactly, one needs to store all Schmidt coefficients $\lambda_q^{[\beta]}$ at each inter-site bond. However, the larger is the Schmidt coefficient, the larger is its contribution to the total state (4.19).

This is when another important concept needs to be introduced — truncation of the MPS. We are going to store only the first few largest Schmidt coefficients of the state (4.19), let us call this number $D_{\mathrm{trunc}}^{[\beta]}$. Then the missing part of the norm is

$$1 - \langle\psi|\psi\rangle = \sum_{q=D_{\mathrm{trunc}}^{[\beta]}+1}^{D^{[\beta]}} \left(\lambda_q^{[\beta]}\right)^2 \equiv \varepsilon_{\mathrm{trunc}}^{[\beta]}, \tag{4.26}$$

which can be interpreted as the missing information about the state.

The fundamental difference between states possessing some amount of entanglement and not (independently of the chosen measure as they all are equal to 0 for non-entangled states) is that the parts of the quantum states with spatial entanglement cannot be described exactly as independent systems. So if some of the Schmidt coefficients are truncated, then the state loses some information as well.

Whereas it is difficult to visualize this lost information in the quantum system, we can take a look at a simple analog from linear algebra. Instead of the quantum density matrix $\hat{\rho}$ we want to see how a matrix M loses information if some of its Schmidt coefficients are truncated. We first perform the singular value decomposition of the matrix

$$M_{ik} = \sum_j U_{ij} \cdot S_{jj} \cdot (V^\dagger)_{jk}, \tag{4.27}$$

in analogy to Sec. 4.1.1. Now we reconstruct M, but only with D_{trunc} largest singular values

$$\tilde{M}_{ik} = \sum_{j=1}^{D_{\text{trunc}}} U_{ij} \cdot S_{jj} \cdot (V^{\dagger})_{jk}, \tag{4.28}$$

and ask how close $\tilde{M}$ is to the original M.

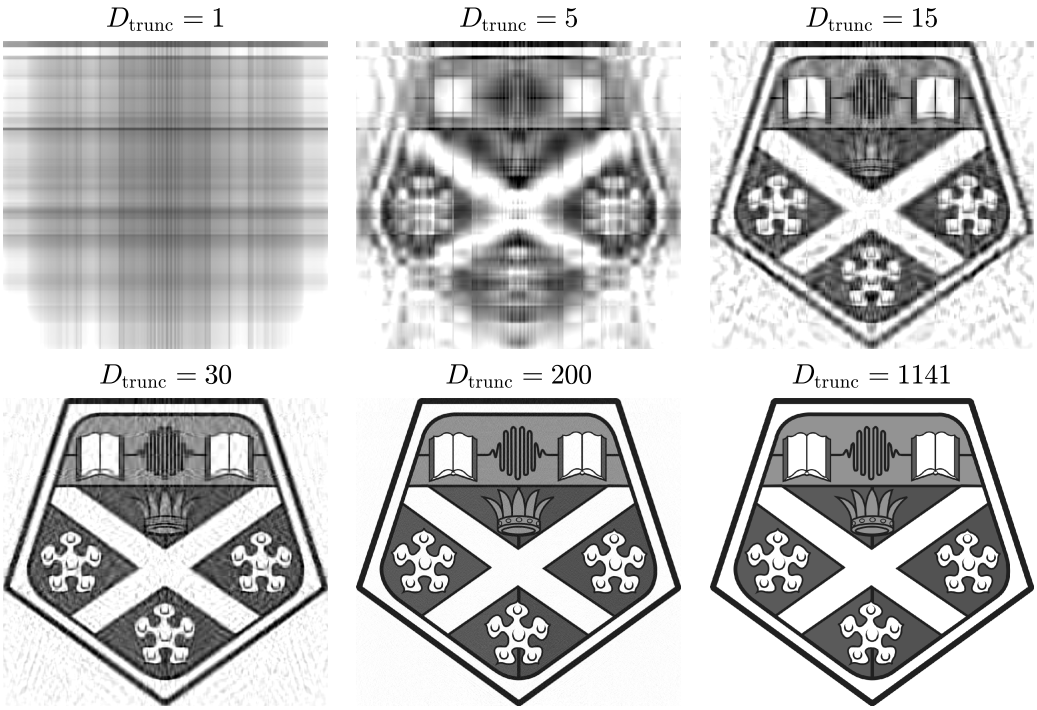

Figure 4.5.: Example of the truncation of Schmidt coefficients of the Strathclyde logo represented as a 1200×1141 matrix where each element stores the gray-scale intensity. It was singular value decomposed and then composed 6 times with a different number of the first D_{trunc} largest Schmidt coefficients. The example shows that a "decent" result can be achieved even with a small fraction of Schmidt coefficients.

In Fig. 4.5 one can see a graphical representation of a 1200×1141 matrix M, where each element is a number between 0 and 1, indicating the intensity on the gray scale. If one keeps all 1141 Schmidt coefficients, the matrix M is reconstructed completely. However, if one truncates the reconstruction worsens, until the image becomes unrecognizable with just one largest coefficient. The important thing is that the original image can be reconstructed quite well with only 200 largest coefficients. This basic principle of keeping only the largest contributions to the state underlies the idea of truncation of quantum states with low entanglement.

4.1.3. Area Law

Now we have approached an important point where we can explain why MPS is such a success for treating quantum many-body systems. It has been shown that the bipartite entanglement of the ground state of a gapped 1D system does not depend on its size [115]. And such a state can be represented in MPS form with a fixed bond dimension D [86]. This concept is called the area law, which means that the bipartite entanglement of a system only depends of the size of the boundary between its partitions and not their volumes. A good review with many examples can be found in Ref. [116].

Quantitatively it has been shown [117,118] that for gapped 1D quantum systems at the critical point the von Neumann entanglement entropy of the ground state scales as

$$S_{\mathrm{vN}} \sim \mathcal{N}\frac{c}{6}\log L + c_1, \tag{4.29}$$

where c is the central charge of the corresponding Conformal Field Theory (CFT), $\mathcal{N}$ is the number of boundaries between subsystems, L is the system size, and c_1 is a non-universal constant. For the same system but away from the critical point

$$S_{\mathrm{vN}} \sim \mathcal{N}\frac{c}{6}\log \xi + c_1, \tag{4.30}$$

where ξ is the correlation length, which can be large but is always finite. This means that the fastest growth of the entanglement entropy with the system size occurs at the critical point. In this case, the MPS bond dimension required to faithfully store the state will grow only polynomially.

4.2. Matrix Product Operators (MPO)

The next vital step in reformulation of quantum mechanical problems in the language of tensor networks is finding an appropriate notation for operators. A natural generalization of MPS described in Sec. 4.1 is given by Matrix Product Operators (MPO).

A generic operator that one would use for a quantum many-body system will have the following form

$$\hat{O} = \sum_{\{r_\alpha, r'_\alpha\}=1}^{d_\alpha} c^{r'_1,r'_2,\ldots,r'_M}_{r_1,r_2,\ldots,r_M} |r_1, r_2, ..., r_M\rangle\langle r'_1, r'_2, ..., r'_M|, \tag{4.31}$$

where analogously to the MPS one needs to store a multidimensional tensor $c^{r'_1,r'_2,\ldots,r'_M}_{r_1,r_2,\ldots,r_M}$ in the fixed basis $\{|r_\alpha\rangle\}$, where each element $|r_\alpha\rangle$ corresponds to the

local d_α-dimensional Hilbert space for a part of the system, e.g. a spin, a site of the optical lattice, or a superconducting qubit (Fig. 4.6). For instance, a system of M identical spins-1/2 will require storage of 2^{2M} elements.

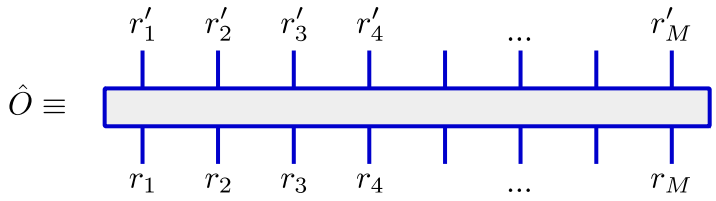

Figure 4.6.: Graphical representation of the tensor associated with the generic operator $\hat{O}$ (4.31).

The possibility of using MPO representations is useful because most of the operators encountered are extremely sparse, hence can be effectively represented as a product of local tensors, analogous to MPS. Then a generic form of an operator in MPO representation will read

$$\hat{O}_{\mathrm{MPO}} = \sum_{\{r_\alpha, r'_\alpha\}=1}^{d_\alpha} B^{[1]}_{r_1,r'_1} B^{[2]}_{r_2,r'_2} ... B^{[M]}_{r_M,r'_M} |r_1, r_2, ..., r_M\rangle\langle r'_1, r'_2, ..., r'_M|, \tag{4.32}$$

where each object $B^{[\alpha]}_{r_\alpha,r'_\alpha}$ is a $D^{[\alpha]}_L \times D^{[\alpha]}_R$ matrix, and $[\alpha]$ is the counter of the system parts (Fig. 4.7). Analogously to the case of MPS, the dimension of the first and last tensor are chosen such that multiplication of the matrices with the fixed set $\{r_\alpha, r'_\alpha\}$ will produce a scalar, i.e. $D^{[1]}_L = 1$ and $D^{[M]}_R = 1$. Analogously to MPS $B^{[\alpha]}$ are called local tensors, $D^{[\alpha]}_{L/R}$ bond dimensions, and $d_\alpha = d$ (for simplicity) is the local dimension.

The notation (4.32) can be used for storing the density matrix $\hat{\rho}$ of the system, instead of the state vector. This allows us to work with mixed states, for instance for an open quantum system obeying the master equation (3.31). One can also implement all the ideas of orthogonalization that were described in Sec. 4.1.1. For this one needs to implement the mapping

$$|r_\alpha\rangle\langle r'_\alpha| \leftrightarrow |(r_\alpha, r'_\alpha)\rangle\rangle, \tag{4.33}$$

which pairs up local input and output indices. In other words the local dimensionality now becomes equal to d^2 instead of d and $\hat{\rho}$ can be written down in a vectorized form $|\rho\rangle\rangle$ with the standard MPS form (4.2). The important thing is that since the state is mixed the meaning of entanglement described in Sec. 4.1.2 is lost. One needs instead to look at another measure suitable for a mixed state, e.g. the negativity [114].

However, we will take one more step and introduce another form of MPO, which will be especially useful for construction of operators manually, i.e. Hamiltonian

and projectors. One can note that the state vector

$$|r_1, r_2, ..., r_M\rangle = \prod_{\alpha=1}^{M} |r_\alpha\rangle, \tag{4.34}$$

is a product state, hence its parts can be absorbed by local tensors $B^{[\alpha]}$, such as

$$\hat{\mathcal{B}}^{[\alpha]}_{r_\alpha, r'_\alpha} \equiv \sum_{r_\alpha, r'_\alpha=1}^{d} B^{[\alpha]}_{r_\alpha, r'_\alpha} |r_\alpha\rangle\langle r'_\alpha|. \tag{4.35}$$

Then (4.32) can be rewritten as

$$\hat{O}_{\mathrm{MPO}} = \hat{\mathcal{B}}^{[1]}_{r_1, r'_1} \hat{\mathcal{B}}^{[2]}_{r_2, r'_2} ... \hat{\mathcal{B}}^{[M]}_{r_M, r'_M}, \tag{4.36}$$

where each $\hat{\mathcal{B}}^{[\alpha]}$ is a matrix with the same bond dimensions as $B^{[\alpha]}_{r_\alpha, r'_\alpha}$, but with operators instead of each element.

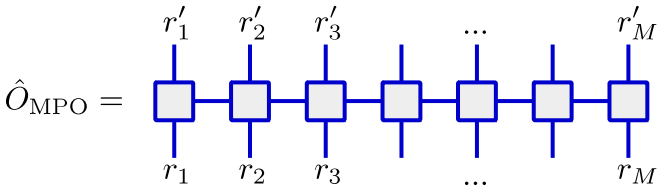

Figure 4.7.: Graphical representation of the tensor network associated with the operator $\hat{O}_{\mathrm{MPO}}$ (4.32). Each part of the systems has a corresponding rank-4 tensor $B^{[\alpha]}$. In the case of the first and the last tensor, one of their bond dimensions is equal 1. Each connected link between tensors means the summation over corresponding indices, and each open link mean an open index r_α. The representation in this form, where tensors are ordered in a chain, is called a Matrix Product Operator (MPO) with Open Boundary Conditions (OBC).

Note that there is also an alternative way of writing an operator in MPO form

$$\hat{O}^{\mathrm{PBC}}_{\mathrm{MPO}} = \sum_{\{r_\alpha, r'_\alpha\}=1}^{d_\alpha} \mathrm{tr}\left[B^{[1]}_{r_1, r'_1} B^{[2]}_{r_2, r'_2} ... B^{[M]}_{r_M, r'_M}\right] |r_1, r_2, ..., r_M\rangle\langle r'_1, r'_2, ..., r'_M|, \tag{4.37}$$

where the requirements for the first and last bond dimensions to be equal unity are lifted. Such a representation is especially useful for implementation of periodic boundary conditions, however it will not be used here as PBC can be implemented in a different way (see examples below).

Let us now consider a number of concrete examples of how one can rewrite an operator in MPO form. The following examples are also going to be used in subsequent chapters, so it make sense to introduce them here in a more pedagogical way.

4.2.1. Examples of Hamiltonians

We start with the transverse field Ising Hamiltonian

$$\hat{H}_{\mathrm{TI}} = -J\sum_r \hat{\sigma}^z_r\hat{\sigma}^z_{r+1} - h_x\sum_r \hat{\sigma}^x_r, \tag{4.38}$$

where $\hat{\sigma}^{x,z}$ are Pauli matrices. Then local $\hat{\mathcal{B}}$ operators have the following form

$$\begin{aligned}
\hat{\mathcal{B}}^{[1]}_{\mathrm{TI}} &= \begin{pmatrix} -h_x\hat{\sigma}^x & -J\hat{\sigma}^z & \hat{\mathcal{I}} \end{pmatrix}, \\
\hat{\mathcal{B}}^{[1<\alpha<M]}_{\mathrm{TI}} &= \begin{pmatrix} \hat{\mathcal{I}} & 0 & 0 \\ \hat{\sigma}^z & 0 & 0 \\ -h_x\hat{\sigma}^x & -J\hat{\sigma}^z & \hat{\mathcal{I}} \end{pmatrix}, \quad \hat{\mathcal{B}}^{[M]}_{\mathrm{TI}} = \begin{pmatrix} \hat{\mathcal{I}} \\ \hat{\sigma}^z \\ -h_x\hat{\sigma}^x \end{pmatrix},;
\end{aligned} \tag{4.39}$$

as was mentioned before the first and last operators should be modified in order to satisfy open boundary conditions. Then in order to reproduce the transverse Ising Hamiltonian one needs to plug the $\hat{\mathcal{B}}$ operators into (4.36).

If one wants to implement PBC with (4.38) then one extra bond dimension should be used to facilitate the term $-J\hat{\sigma}^z_1\hat{\sigma}^z_M$, describing the interaction of the first and last spins. Then local $\hat{\mathcal{B}}$ operators have the following form

$$\begin{aligned}
\hat{\mathcal{B}}^{[1]}_{\mathrm{TI}} &= \begin{pmatrix} -h_x\hat{\sigma}^x & -J\hat{\sigma}^z & \hat{\mathcal{I}} & -J\hat{\sigma}^z \end{pmatrix}, \\
\hat{\mathcal{B}}^{[1<\alpha<M]}_{\mathrm{TI}} &= \begin{pmatrix} \hat{\mathcal{I}} & 0 & 0 & 0 \\ \hat{\sigma}^z & 0 & 0 & 0 \\ -h_x\hat{\sigma}^x & -J\hat{\sigma}^z & \hat{\mathcal{I}} & 0 \\ 0 & 0 & 0 & \hat{\mathcal{I}} \end{pmatrix}, \quad \hat{\mathcal{B}}^{[M]}_{\mathrm{TI}} = \begin{pmatrix} \hat{\mathcal{I}} \\ \hat{\sigma}^z \\ -h_x\hat{\sigma}^x \\ \hat{\sigma}^z \end{pmatrix}.
\end{aligned} \tag{4.40}$$

In the next example one can consider the case of the Bose-Hubbard model

$$\hat{H}_{\mathrm{BH}} = -J\sum_r (\hat{b}_r\hat{b}^\dagger_{r+1} + \hat{b}^\dagger_r\hat{b}_{r+1}) + \frac{U}{2}\sum_r \hat{n}_r(\hat{n}_r - 1), \tag{4.41}$$

where $\hat{b}_r$ is the annihilation operator on the site r, and $\hat{n}_r = \hat{b}^\dagger_r\hat{b}_r$ is the occupation number operator. Here the hopping between sites is defined via two terms of the Hamiltonian, hence the local tensors will take the form

$$\begin{aligned}
\hat{\mathcal{B}}^{[1]}_{\mathrm{BH}} &= \begin{pmatrix} \frac{U}{2}\hat{n}(\hat{n}-1) & -J\hat{b} & -J\hat{b}^\dagger & 1 \end{pmatrix}, \\
\hat{\mathcal{B}}^{[1<\alpha<M]}_{\mathrm{BH}} &= \begin{pmatrix} 1 & 0 & 0 & 0 \\ \hat{b}^\dagger & 0 & 0 & 0 \\ \hat{b} & 0 & 0 & 0 \\ \frac{U}{2}\hat{n}(\hat{n}-1) & -J\hat{b} & -J\hat{b}^\dagger & 1 \end{pmatrix}, \quad \hat{\mathcal{B}}^{[M]}_{\mathrm{BH}} = \begin{pmatrix} 1 \\ \hat{b}^\dagger \\ \hat{b} \\ \frac{U}{2}\hat{n}(\hat{n}-1) \end{pmatrix}.
\end{aligned} \tag{4.42}$$

The implementation of PBC would require two more extra interaction terms $-J\hat{b}_1\hat{b}^\dagger_M$ and $-J\hat{b}^\dagger_1\hat{b}_M$ which can be implemented via two extra dimensions, in analogy to (4.40).

We can also implement the same idea in the case when hoppings are not only between neighboring spins, for instance the next-next-nearest neighbor Hamiltonian

$$\hat{H}_{\mathrm{NNNTI}} = -J_1 \sum_r \hat{\sigma}_r^z \hat{\sigma}_{r+1}^z - J_2 \sum_r \hat{\sigma}_r^z \hat{\sigma}_{r+2}^z - J_3 \sum_r \hat{\sigma}_r^z \hat{\sigma}_{r+3}^z - h_x \sum_r \hat{\sigma}_r^x, \quad (4.43)$$

has the following local $\hat{\mathcal{B}}$ operators

$$\begin{aligned}
\hat{\mathcal{B}}^{[1]}_{\mathrm{NNNTI}} &= \begin{pmatrix} -h_x\hat{\sigma}^x & -J_1\hat{\sigma}^z & -J_2\hat{\sigma}^z & -J_3\hat{\sigma}^z & \hat{\mathcal{I}} \end{pmatrix}, \\
\hat{\mathcal{B}}^{[1<\alpha<M]}_{\mathrm{NNNTI}} &= \begin{pmatrix} \hat{\mathcal{I}} & 0 & 0 & 0 & 0 \\ \hat{\sigma}^z & 0 & 0 & 0 & 0 \\ 0 & \hat{\mathcal{I}} & 0 & 0 & 0 \\ 0 & 0 & \hat{\mathcal{I}} & 0 & 0 \\ -h_x\hat{\sigma}^x & -J_1\hat{\sigma}^z & -J_2\hat{\sigma}^z & -J_3\hat{\sigma}^z & \hat{\mathcal{I}} \end{pmatrix}, \quad \hat{\mathcal{B}}^{[M]}_{\mathrm{NNNTI}} = \begin{pmatrix} \hat{\mathcal{I}} \\ \hat{\sigma}^z \\ 0 \\ 0 \\ -h_x\hat{\sigma}^x \end{pmatrix}.
\end{aligned} \quad (4.44)$$

Now we can consider a more exotic transverse field Ising model with exponentially decaying correlations

$$\hat{H}_{\mathrm{expTI}} = -J \sum_{r>l} \exp[-\lambda(r-l-1)] \hat{\sigma}_r^z \hat{\sigma}_l^z - h_x \sum_r \hat{\sigma}_r^x, \quad (4.45)$$

which will have the following local $\hat{\mathcal{B}}$ operators

$$\begin{aligned}
\hat{\mathcal{B}}^{[1]}_{\mathrm{expTI}} &= \begin{pmatrix} -h_x\hat{\sigma}^x & -J\hat{\sigma}^z & \hat{\mathcal{I}} \end{pmatrix}, \\
\hat{\mathcal{B}}^{[1<\alpha<M]}_{\mathrm{expTI}} &= \begin{pmatrix} \hat{\mathcal{I}} & 0 & 0 \\ \hat{\sigma}^z & \mathrm{e}^{-\lambda}\hat{\mathcal{I}} & 0 \\ -h_x\hat{\sigma}^x & -J\hat{\sigma}^z & \hat{\mathcal{I}} \end{pmatrix}, \quad \hat{\mathcal{B}}^{[M]}_{\mathrm{expTI}} = \begin{pmatrix} \hat{\mathcal{I}} \\ \hat{\sigma}^z \\ -h_x\hat{\sigma}^x - h_z\hat{\sigma}^z \end{pmatrix}.
\end{aligned} \quad (4.46)$$

A generic monotonically decaying function $f(r)$ can be expanded as a series of decaying exponents. For this one needs to minimize the following functional

$$F(\{a_k\},\{b_k\}) = \sum_k \sum_r \left| f(r) - a_k b_k^{r-1} \right|^2,$$

over the set of $\{a_k\}$ and $\{b_k\}$ for a fixed number of elements and maximal range of interaction (which can alway be bounded by the system size). Then a Hamiltonian with generic decaying interactions,

$$\hat{H}_{\mathrm{decayTI}} = -J \sum_{r>l} f(r-l) \hat{\sigma}_r^z \hat{\sigma}_l^z - h_x \sum_r \hat{\sigma}_r^x, \quad (4.47)$$

can be effectively represented in MPO form. For instance, an algebraically decaying function $f(x) = x^{-2}$ can be expanded as a sum of 9 exponential decays where the error over 100 sites, defined as the functional F above, is below 10^{-6},

which is good enough for many practical calculations.

4.2.2. Examples of Projectors

Sometimes it is useful to construct non-local operators to implement some symmetries in the system. Each symmetry usually implies a conservation law and can be implemented explicitly. This might require a lot of work and restructuring the code completely, or sometimes it is just easier to project out states that do not satisfy those symmetries.

For instance one might want to have an operator conserving the total number of particles in the Bose-Hubbard Hamiltonian (4.41). Let us first introduce a local projector $\hat{p}_n \equiv |n\rangle\langle n|$ that selects only the component of the state with n particles on the site. Then local tensors $\hat{\mathcal{B}}_N$ for the non-local operator

$$\hat{P}_N = \sum_{\sum_\alpha n_\alpha = N} \left[\prod_{\alpha=1}^{M} \hat{p}_{n_\alpha}^{[\alpha]} \right] \tag{4.48}$$

takes the form

$$\begin{aligned} \hat{\mathcal{B}}_N^{[1]} &= \begin{pmatrix} \hat{p}_0 & \hat{p}_1 & \hat{p}_2 & \dots & \hat{p}_N \end{pmatrix}, \\ \hat{\mathcal{B}}_N^{[1<\alpha<M]} &= \begin{pmatrix} \hat{p}_0 & \hat{p}_1 & \hat{p}_2 & \dots & \hat{p}_N \\ 0 & \hat{p}_0 & \hat{p}_1 & \dots & \hat{p}_{N-1} \\ 0 & 0 & \hat{p}_0 & \dots & \hat{p}_{N-2} \\ \vdots & \vdots & \vdots & \ddots & \vdots \\ 0 & 0 & 0 & \dots & \hat{p}_0 \end{pmatrix}, \quad \hat{\mathcal{B}}_N^{[M]} = \begin{pmatrix} \hat{p}_N \\ \hat{p}_{N-1} \\ \hat{p}_{N-2} \\ \vdots \\ \hat{p}_0 \end{pmatrix}. \end{aligned} \tag{4.49}$$

As one can see the bond dimension of local tensors is equal to $N+1$, but the tensors are sparse and have just a few non-zero elements. This makes it possible to do the ground state calculations via DMRG or time evolution preserving the total number of particles, see Sec. 4.3 for more details.

Another practical example is implementation of constraints via MPO projectors. Say one wants to forbid states that have a pair of spin-ups at a distance l in a spin chain described by (4.38). Then one needs to implement the following projector

$$\hat{P}(l) = \prod_r \hat{P}_r(l) = \prod_r (1 - \hat{\sigma}_r^\uparrow \hat{\sigma}_{r+l}^\uparrow), \tag{4.50}$$

which projects out forbidden configurations between all pairs at distance l. Then local tensors of $\hat{P}_r(l)$ would read

$$\begin{aligned} \hat{\mathcal{B}}^{[1\le\alpha<r]} &= 1, & \hat{\mathcal{B}}^{[\alpha=r]} &= \begin{pmatrix} \hat{\sigma}^\uparrow & \hat{\sigma}^\downarrow & \hat{\sigma}^\downarrow \end{pmatrix}, \\ \hat{\mathcal{B}}^{[r<\alpha<r+l]} &= \begin{pmatrix} 1 & 0 & 0 \\ 0 & 1 & 0 \\ 0 & 0 & 1 \end{pmatrix}, & \hat{\mathcal{B}}^{[\alpha=r+l]} &= \begin{pmatrix} \hat{\sigma}^\downarrow \\ \hat{\sigma}^\uparrow \\ \hat{\sigma}^\downarrow \end{pmatrix}, \qquad \hat{\mathcal{B}}^{[r+l<\alpha]} = 1. \end{aligned} \tag{4.51}$$

One can immediately extend this to more complicated configurations of spins or other operators.

4.3. Methods

In this section we now discuss the algorithms used to compute time evolution of ground states using MPSs and MPOs.

4.3.1. Time Evolving Block Decimation (TEBD)

In this section we will discuss one of the first methods developed for evolution of state vectors in MPS form [87]. The main idea of the method was already highlighted in Sec. 3.1.2 where one decomposes the Hamiltonian in two site operators and applies them successively (3.20). Exactly the same idea with two-site updates can be implemented on an MPS (Fig. 4.8).

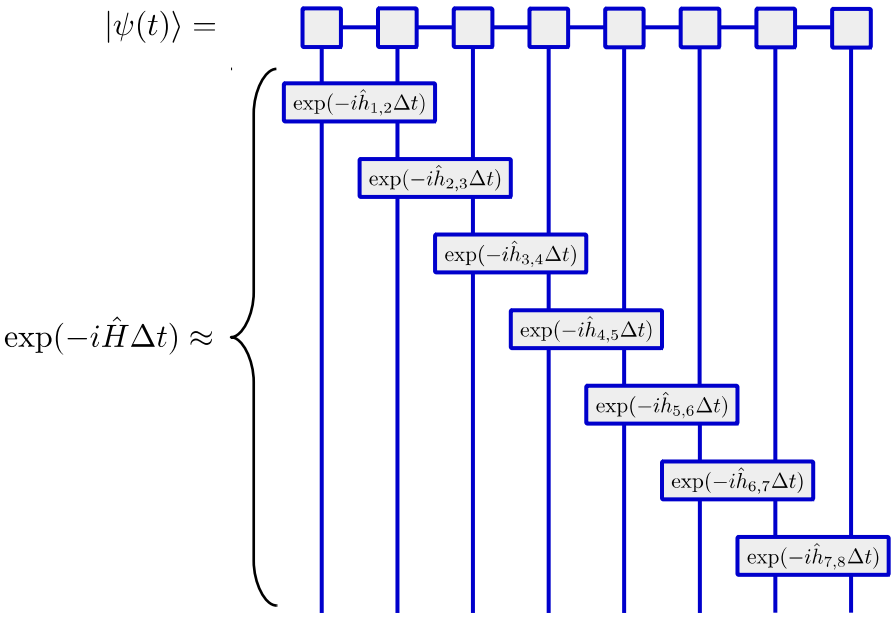

Figure 4.8.: Diagrammatic representation of a single time-evolution step of an MPS from time t to $t + \Delta t$ via Trotter decomposed evolution operator.

In order to avoid exponential growth of bond dimensions of MPS, one needs to perform truncation and keep only the largest Schmidt coefficients. Let us take a close look at a single step of the TEBD algorithm (Fig. 4.9). Initially two neighboring tensors $A^{[l]}$ and $A^{[l+1]}$ on the sites l and $l+1$ are contracted with the unitary tensor. The resulting rank-4 tensor $T^{[l,l+1]}$ is then reshaped to a matrix

$\bar{T}$ of dimensions $dD_L^{[l]} \times dD_R^{[l+1]}$, i.e. the left bond index is combined with the local index of the left tensor, and the right bond index is combined with the local index of the right tensor. Then one performs a singular value decomposition

$$\bar{T} = U \cdot S \cdot V^{\dagger}, \tag{4.52}$$

which was already explained in Sec. 4.1.1. The matrix of the most interest is S, which is a diagonal matrix of Schmidt coefficients $\{\lambda_k\}$ in descending order. In order to stop MPS bond dimensions from uncontrollable growth, one needs to perform truncation of the Schmidt coefficients. Here one introduces the maximum bond dimension $D_{\max}$ for instance and keeps only the first $D_{\max}$ largest Schmidt coefficients. The resulting error of truncation is then

$$\epsilon_{\text{trunc}} = \sum_{k=D_{\max}+1} (\lambda_k)^2,$$

where the summation goes up to the last Schmidt coefficient. Then the corresponding dimensions of U and $V^{\dagger}$ are also truncated in order to match the dimension of S after truncation. The matrix S can now be absorbed into either U or $V^{\dagger}$. The resulting matrices are reshaped back to local tensors for the site l and $l+1$ (Fig. 4.9). That is a short overview of the TEBD method, which of course can be modified in order to increase the precision. For instance, one can use a higher order of Suzuki-Trotter decomposition. It is common to use a fourth order [119] expansion, where one can achieve numerical error scaling as Δt^5.

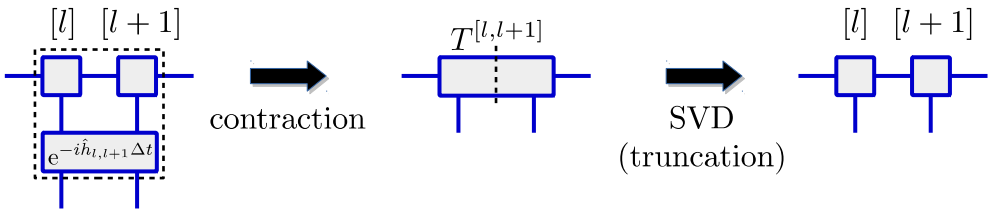

Figure 4.9.: Diagrammatic representation of a single step of the TEBD algorithm. Initially two neighboring tensors on the sites l and $l+1$ are contracted with the unitary tensor. The resulting rank-4 tensor $T^{[l,l+1]}$ is then reshaped to a matrix $\bar{T}$ of dimensions $dD_L^{[l]} \times dD_R^{[l+1]}$, i.e. the left bond index is combined with the local index of the left tensor, and the right bond index is combined with the local index of the right tensor. Then one performs a Singular Value Decomposition. In order to stop the MPS bond dimensions from uncontrollable growth one needs to perform truncation of the Schmidt coefficients. Then depending on the desired orthonormal form of MPS one absorbs the Schmidt coefficients either into the local tensor of the site l or $l+1$.

4.3.2. Variational State Search

In order to find the ground state in MPS form we are first going to take a look at the variational ansatz [81, 120], the idea of which is to minimize the energy of the system

$$E = \min_{|\psi\rangle} \frac{\langle\psi|H|\psi\rangle}{\langle\psi|\psi\rangle}, \tag{4.53}$$

by varying the state vector $|\psi\rangle$. The complexity of the problem scales exponentially with the length of the system, as the Hilbert space dimensionality scales exponentially. However, we would rather try to find the global minimum by doing local optimizations, i.e. variational search. Let us pick an initial guess state vector $|\psi\rangle$ in MPS form. We then fix all parameters in this MPS except for one tensor $A^{[\alpha]}$.

Then one needs to find the extremum of

$$\frac{\partial}{\partial A^{r_\alpha}}[\langle\psi|H|\psi\rangle - E\langle\psi|\psi\rangle] = 0, \tag{4.54}$$

which is diagrammatically presented in Fig. 4.10. This tensor network after all possible internal contractions can be rewritten as

$$v^\dagger H_{\text{eff}} v - E v^\dagger N v = 0, \tag{4.55}$$

where v is the reshaped tensor A^{r_α} of the state $|\psi\rangle$. This expression is equivalent to the generalized eigenproblem

$$H_{\text{eff}} v - E N v = 0, \tag{4.56}$$

where v is a vector of reshaped parameters of $A^{[\alpha]}$, H_{eff} is a matrix form of reshaped tensor (in dash black in Fig. 4.10), and N is a matrix formed from the reshaped tensor (in dash red in Fig. 4.10). The size of the vector v to be found is dD^2 which makes this problem scale linearly with M (number of sites), as the same algorithm should be run on each site subsequently. If one ensures that the site α is the center of orthogonality then the normalization of the state is ensured automatically and (4.56) becomes just an eigenproblem

$$H_{\text{eff}} v - E v = 0. \tag{4.57}$$

After one site is optimized (local minimum is found) then we can repeat with the next one. The global minimum can be reached after a few complete sweeps. Hence one finds the ground state $|\psi_0\rangle$ with energy E_0.

Note that the presented scheme can be easily extended to an n-site algorithm, where n sites are optimized simultaneously, so the length of the vector v becomes equal to $d^n D^2$. This makes the computation more costly, but one does not need

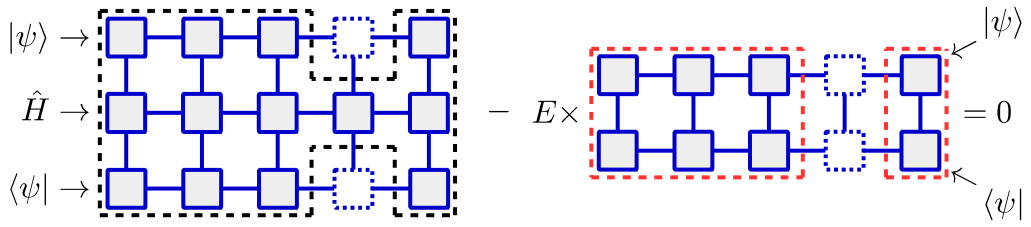

Figure 4.10.: Graphical representation of variational ground state search using a single-site update algorithm (4.54). Local tensors of the state $|\psi\rangle$ and Hamiltonian $\hat{H}$ drawn with solid lines are fixed and dashed blocks $A^{[\alpha]}$ are reshaped to a vector v and are being optimized variationally. The dashed black line denotes the H_{eff} tensor, and the red line denotes the N tensor.

to solve the eigenproblem completely. Since we are interested in only the lowest state we can use a method based on powers of the Hamiltonian, such as Lanczos (see Chap. 3). By simultaneously optimizing several sites' tensors one increases the dimension of the local Hilbert space used for the search, i.e. it improves the convergence to the global minimum.

Another advantage of the multi-site algorithm is that the bond dimension of MPS can be adjusted dynamically, with forced truncation error. By doing this one can do the initial quick search with an MPS of a low bond dimension and then a more precise and long search with increased bond dimensions.

One can also use the method described above for finding excited states. The idea behind this is simple: we still look for local minima, but on top of that we make sure that the state is orthogonal to the ground state. In the literature there are several implementations of this algorithm; below we will describe the simplest. The trick is to replace the effective Hamiltonian H_{eff} from (4.57) with

$$(1 - |\psi_0\rangle\langle\psi_0|)H_{\text{eff}}(1 - |\psi_0\rangle\langle\psi_0|),$$

then the search of the minimum is going to be in a space orthogonal to the ground state $|\psi_0\rangle$. The procedure continues in the same fashion for higher excited states, i.e. one needs to project out all the previous eigenstates and search for the local minimum at each optimization steps.

4.3.3. Time Dependent Variational Principle (TDVP)

It was found [92, 121] that with a few modifications the variational principle method described above can be used for time evolution. This method is called Time-Dependent Variational Principle (TDVP) and unlike time evolution methods based on the Suzuki-Trotter decomposition of the Hamiltonian this method

is based on splitting the projector onto the matrix product state tangent space as it appears in the Dirac-Frenkel time-dependent variational principle.

In order to evolve an arbitrary state $|\psi(t)\rangle$ which belongs to a sub-manifold $\mathcal{H}_1$ of the whole Hilbert space $\mathcal{H}$ (i.e. $\mathcal{H}_1 \subset \mathcal{H}$), at infinitesimal time δt one obtains from the Schrödinger equation

$$|\psi(t+\delta t)\rangle = |\psi(t)\rangle - i\delta t\hat{H}|\psi(t)\rangle, \tag{4.58}$$

where $\hat{H}|\psi(t)\rangle$, in general, does not belong to $\mathcal{H}_1$ any more. The point of the TDVP method is to project $\hat{H}|\psi(t)\rangle$ onto $\mathcal{H}_1$, so that the evolution never leaves the manifold $\mathcal{H}_1$. This means that one needs to find a tangential vector $|\phi\rangle$ that minimizes the functional

$$F[|\phi\rangle] = \left\|(\mathcal{I} - i\delta t\hat{H})|\psi(t)\rangle - |\phi\rangle\right\|^2, \tag{4.59}$$

which will produce the state $|\phi\rangle$ as the closest approximation of $(\mathcal{I} - i\delta t\hat{H})|\psi(t)\rangle$ in the subspace $\mathcal{H}_1$. Whereas formal descriptions of the integration schemes are presented with great details in the above papers, we should note the most successful one [121]. Here the idea is to define an MPO space projector $\hat{P}_{\mathcal{H}_1}$ which will focus on only the subspace $\mathcal{H}_1$, then the Lie-Trotter splitting scheme is used which decomposes $\hat{P}_{\mathcal{H}_1}$ and allows us to perform time evolution of only local block keeping the state in $\mathcal{H}_1$. In other words, the algorithm is based on a Trotter decomposition of the tangent space projector $\hat{P}_{\mathcal{H}_1}$ rather than the Hamiltonian $\hat{H}$, as it was presented in Sec. 4.3.1. In the end it results in local updates of tensors A^{r_α} reshaped to the vector form v (as in Sec. 4.3.2)

$$(\mathcal{I} - i\delta t H_{\text{eff}})v(t) = v(t+\delta t), \tag{4.60}$$

where the effective matrix H_{eff} is defined in Fig. 4.10.

The evolution of the state is then performed on the site dependent basis, with one or several sites being updated at the same time. Due to the decomposition of the projector, the corresponding differential equation for local tensors can be integrated exactly. For instance, one can use a Lanczos integration scheme in order to keep computational cost at $\mathcal{O}(D^3)$, where D is the bond-dimension of the local tensor. It is also possible to use higher order integrations by applying schemes with symmetric integrators. One can go a step forward and instead of a simple first order approximation use $\exp(-i\delta t H_{\text{eff}})$, then the local updates will take the form

$$\exp(-i\delta t H_{\text{eff}})v(t) = v(t+\delta t), \tag{4.61}$$

and can be evaluated using the Krylov subspace algorithm (see Sec. 3.1.1).

Another great advantage of this algorithm is that it can deal with arbitrary long-range Hamiltonians (as in Sec. 4.2.1), unlike the TEBD method that will requires

the application of swap gates to realize long-range interactions.

4.4. Conclusions

In this chapter we presented an overview of advanced numerical techniques used for dealing with large many-body systems. The inevitable exponential growth of the dimensionality of the full Hilbert space with the linear increase of the system size is dealt with via considering only the relevant subspace with low entangled states. This approach was first developed as DMRG and later incorporated the ideas of MPS and MPO representations of states and operators, such that it made numerically feasible to solve quantum many-body problems [80, 81].

Moreover the methods presented in Chap. 3 for the full Hilbert space can be reformulated in the language of MPS. For instance, one finds that the Krylov method of time evolution (Sec. 3.1.1) can be nicely combined with TDVP (Sec. 4.3.3) in order to perform efficient evolution of local tensors. Imaginary time evolution (Sec. 3.1.4) can be used as an alternative method for the ground state search. Also the whole formalism of quantum trajectories (Sec. 3.2.1) can be translated to MPS representation of states.

In the following chapters there is a wide range of results obtained via the methods described in this chapter. For instance in Chap. 6 and Chap. 7 we study quench dynamics of spin models with long-range interactions. In Chap. 5 we simulate constrained spin models and obtain lowest eigenvalues, calculate quench dynamics, and study thermal states. The effective representation of long-range Hamiltonians and constraining projectors in the MPO form allowed us to obtain results on chains of a few hundred spins.

Part III.

Resonance Tunneling in Tilted Optical Lattices

5. Effective Spin Models for Resonant Tunneling Dynamics of Bosons in a Tilted Optical Superlattice

In this chapter we investigate resonant dynamics of bosons in 1D optical lattices, in the presence of a tilted potential. Bosons in a deep optical potential usually have weak tunneling rates, which are not substantially changed by a gradient potential. As a result, they are usually localized at individual sites unless the field is finely tuned to allow resonant tunneling of atoms to nearby sites. The resonance occurs when the potential energy change of a particle that tunnels to a nearby site is compensated by the interaction energy of this particle with a particle initially on the site to which it tunnels. Here we investigate two cases: when atoms can resonantly tunnel to the neighboring site, and when atoms tunnel to the next-neighbor site. We derive effective spin models for each of the cases and analyze the dynamics of atoms from the perspective of effective spins.

5.1. Introduction

Strongly correlated quantum systems had already generated significant interest in physics by the middle of the previous century and form an important part of modern condensed matter physics. The essential feature that defines these systems is that their behavior cannot be described effectively in terms of non-interacting entities, hence collective strong effects play the major role. Some prototypical examples include conventional and high-T_c superconductors [122], magnetic materials, and quantum Hall systems [123].

One of the central objectives of modern condensed matter physics is the understanding of materials with exotic forms of magnetism [122]. Such materials provide a rich phase diagram consisting of magnetically disordered and ordered states. The simplest example of this is transitions between paramagnetic phases and ordered ferromagnets and antiferromagnets. The competition between different types of ordering can cause frustration in spin models, which leads to spin glasses [124] and spin liquids [125]. The interplay of the system geometry and magnetism can lead to topologically ordered states [126]. Study of these models

in the vicinity of phase transitions is a problem of high complexity that presents challenges for most analytical and numerical calculations.

One recent approach to studying such complex systems is to simulate their behavior in quantum emulators with a high degree of controllability [1, 2]. Initial simulation of magnetic systems with trapped ions [71], Rydberg atoms [127], and polar molecules [128] have shown a lot of promise in this direction. In these methods the magnetic spin degrees of freedom were mapped onto the internal degrees of freedom of atoms and molecules.

In this chapter we study an alternative method of mapping between magnetic spin states and the motional degrees of freedom of individual bosonic atoms loaded in a tilted optical lattice. Without the tilt the system is prepared in the unit-filled Mott insulator phase, where the on-site interaction between particles, U, is significantly larger than the tunneling rate J. This leads to suppression of tunneling processes and exponential localization of particles on each site. In the case of a general linear tilt of the lattice, which creates an energy difference E between neighboring sites, bosons stay localized. However if the tilt is tuned to the vicinity of a resonance $E = U/n$ with an integer n, long-range resonantly enhanced tunnelings of $n-$th order are observed [54]. Allowed to time evolve, the system demonstates many-body dynamics [55, 56] far away from the regime of a simple quantum walk of a single particle [57, 58].

In previous theoretical work [59], a mapping scheme was suggested between spatial degrees of freedom of bosons and effective spins in the case of nearest neighbor resonant tunneling ($n = 1$). This maps to an antiferromagnetic Ising chain with a skew field and projective interactions, which constrain the configuration space of the effective spins. In later works non-equilibrium dynamical properties [129] and high order corrections [130] were investigated within this $n = 1$ model.

In this work, we investigate the case of the second neighbor resonant tunneling ($n = 2$). In order to map the dynamics to an effective spin chain, a superlattice geometry was chosen, which further restricts the motional degrees of freedom of particles. We then investigate the corresponding phases of the model as well as its behavior near the phase transition.

In the following sections we first derive effective spin models (Sec. 5.2) and consider their extreme limits by means of perturbation theory (Sec. 5.3), studying the phases of each model. In Sec. 5.4 we focus on the phase transition points and investigate them from the perspective of symmetries and finite size scaling. After that we approach the phase transition point for finite temperatures (Sec. 5.5), which provides a different perspective. Before concluding we consider quench dynamics in the $E = U/2$ regime calculated with the effective spin model (Sec. 5.6) as a comparison with the experimental dynamics without the superlattice geometry. The reader can either follow the sections consecutively, or read only subsections on the model $E = U$ first and then the rest.

5.2. The Models

In this study we consider ultracold bosonic atoms trapped in an optical lattice. As was shown in Sec. 2.3, in the case of sufficiently low temperatures, low density of atoms, and deep optical potentials, the dynamics of atoms obeys the Bose-Hubbard model (2.57), where tunneling only between neighboring sites is allowed, and particles interact if they are located on the same site. Here we will consider a more specialized form of the Hamiltonian

$$H = -J \sum_{\langle r,l \rangle} b_r^\dagger b_l + \frac{U}{2} \sum_r n_r \left(n_r - 1\right) - \sum_r E_r n_r, \tag{5.1}$$

where J is the hopping matrix element, $\langle \cdot, \cdot \rangle$ implies summation only over neighboring sites, U is the on-site interaction between bosons, and the external potential

$$E_r = E \cdot r + (-1)^r \frac{\mu}{2}, \tag{5.2}$$

which has two contributions. The first is the external linear field E that creates a constant gradient potential, which can be generated by either a gravitational force (if the optical lattice sites are oriented vertically) or an external field (electric or magnetic), which changes in space. The second contribution to E_r is the energy offset μ between even and odd sites, established by a superlattice. We will take $\mu = 0$ for the $E = U$ case and $\mu > 0$ for $E = U/2$.

This basic model describes the motion of atoms on the lattice in the presence of the superlattice and tilted potential. One also should note that the model preserves the total number of particles. Let us call the number of sites M and the number of particles N. From now on we will be considering the case of unit filling,

$$N = M, \tag{5.3}$$

i.e., there are as many particles as sites.

We focus on the regime deep in the MI phase $J \ll U$. In the presence of the linear tilt $E \neq 0$ the energy of the Hamiltonian (5.1) for the infinite lattice is not bounded from below, so there is no ground state. It means that the really stationary state is the one in which all particles have left the system falling towards sites with lower and lower energies. On typical experimental timescales we can consider those states that are near resonant to the initial state.

The experiment we have in mind thus would start with a MI state with the same number of particles on each site and $E = 0$, then we would suddenly switch on a space dependent field quenching to the Hamiltonian to (5.1) with $E \neq 0$ (μ is kept at zero at the moment). This experiment has already been realized in a number of labs [54–56], and for generic values of the tilt E (due to the strong interactions

U) the MI phase has been observed to be basically stable during the duration of the experiments. In other words, despite the tilt, the bosons are "trapped" for long times at their initial positions. This phenomenon was expected, since as first discussed in [131], even without interactions a linear tilt produces a localization of the energy eigenstates on single sites. For specific values of the tilt E, namely for $E = U/n$, where n is integer the uniform MI state becomes resonantly coupled to a subset of other states, which was observed experimentally [54–56].

In Sec. 5.2.1 and Sec. 5.2.2 we consider two special cases, $E = U$ and $E = U/2$ respectively, and derive their effective spin models. We will see that the model in the second case takes the form of two subsystems described by the model of the first case, plus some coupling terms between these two subsystems.

5.2.1. $E = U$ Regime

The first case we consider is when a unit filled MI state is suddenly tilted such that the potential energy steps between sites are approximately equal to the on-site interaction, i.e. $E \approx U$, and the super-lattice off-set μ is set to zero, so Eq. (5.1) reads

$$H = -J \sum_{\langle r,l \rangle} b_r^\dagger b_l + \frac{U}{2} \sum_r n_r \left(n_r - 1\right) - E \sum_r r \cdot n_r, \tag{5.4}$$

This Hamiltonian was extensively studied in [59, 60] in the case of one and two dimensions. We will elaborate on this here for comparison with the $E = U/2$ case, which will be considered later.

From the initial MI state (Fig. 5.1(a)) particles can hop to the nearest site (down the tilted lattice) lowering the potential energy by E. Since the simultaneous gain of the interaction energy U exactly compensates this energy change the two states are degenerate and are connected by the tunneling, as shown in Fig. 5.1(b).

It also should be noted that once a boson has tunneled resonantly to the neighboring site, its neighbors cannot tunnel resonantly any more. In Fig. 5.1(b) it can be seen that if a particle from the second site tunnels to the third site the system decreases its energy by $E = U$. In the regime $J \ll U$ this transition is suppressed in perturbation theory by a factor $\propto J/U$, and hence the occupation of such a state is suppressed as $\propto (J/U)^2$. Exactly the same energy argument can be considered for other single-tunneling processes between the states, for which the energy difference is proportional to U.

A small detuning from the resonance condition, i.e. $|U - E| \ll U$, does not qualitatively alter the situation and thus bosons can resonantly tunnel only between two sites — the initial one and its neighbor. The system dynamics is then confined to the subspace of states resonantly connected by tunneling of the indistinguishable bosons to the initial tilted MI with unit filling. Here we exploit

this fact and establish the following mapping with a spin-1/2 chain: we associate a boson in its initial position on the r^{th} site with a spin down $|\downarrow\rangle_r$, and a boson that leaves the r^{th} site via resonant tunneling with a spin up $|\uparrow\rangle_r$. Note, that following this scheme, $|\downarrow\rangle_r$ can be associated with a site with one or two bosons on the r^{th} site of the lattice, but due to the constraint forbidding tunneling from neighboring sites this mapping is actually isomorphic and confusion is always avoided by checking the occupation of the neighboring sites (see Fig. 5.1(a,b)).

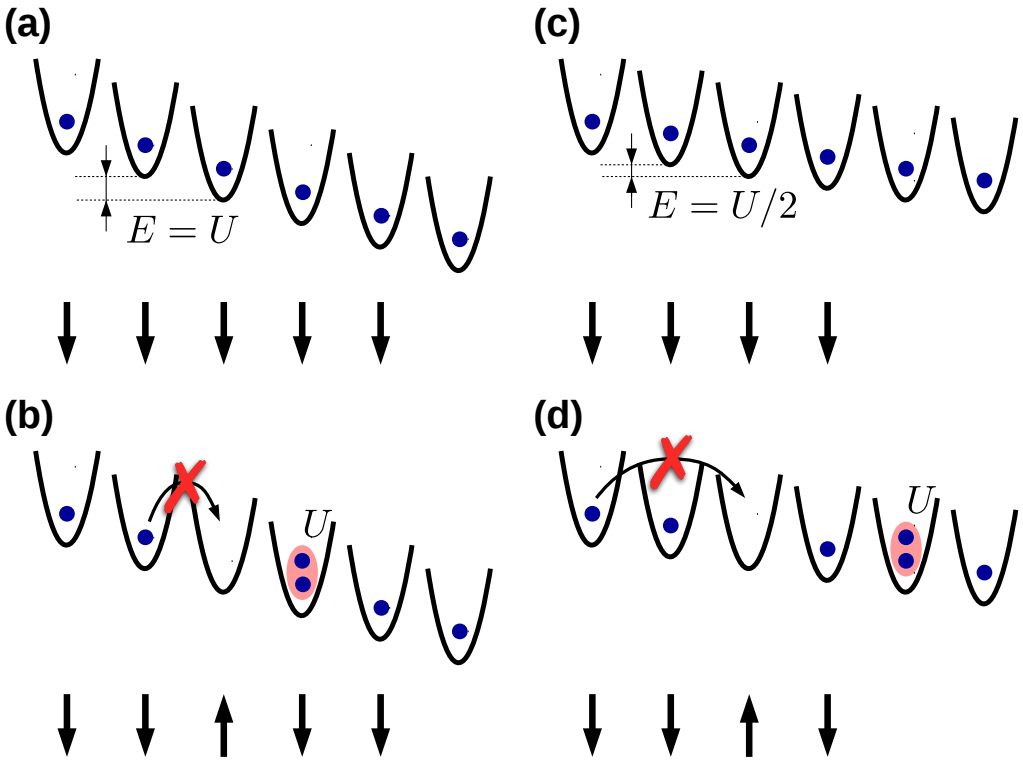

Figure 5.1.: Schematic representation of the initially unit filled MI states in the regime $E = U$ (a) and $E = U/2$ (c) and example states coupled to them (b,d, respectively). In the regime $E = U$ (a,b) all bosons except the last one (if the lattice is finite) can resonantly tunnel to the neighboring site, allowing a mapping to a spin-1/2 model (explained in the main text). Bosons staying at the initial site are mapped to spin-downs; if a boson resonantly tunnels one site down the slope it is mapped to a spin-up. Bosons on neighboring sites cannot both hop down the slope resonantly, which forbids two neighboring spin-ups. In the regime $E = U/2$ (c,d) the situation is similar for sites of the same parity. The bosons staying at the initial sites are mapped to spin-downs, and if a boson tunnels two sites down the slope it is mapped to a spin-up. Bosons on next-neighboring sites cannot hop down the slope resonantly, which forbids two neighboring spin-ups each even/odd sublattice. The corresponding spin representations of the boson configurations are draws underneath each lattice configuration.

Then in the regime of a small detuning

$$|U - E|, J \ll E, U, \tag{5.5}$$

the behavior of bosons at relevant time scales can be mapped to the effective spin model

$$H_U = \sum_r [-\sqrt{2}\sigma_r^x + \lambda\sigma_r^\uparrow + W\sigma_r^\uparrow\sigma_{r+1}^\uparrow], \tag{5.6}$$

where

$$\lambda = \frac{U - E}{J} \tag{5.7}$$

denotes the deviation from resonance, $\sigma^\uparrow = (\sigma^z + 1)/2$ is a projector on spin-up, and $W \to +\infty$ is the constraint term that forbids two neighboring spin-ups. The energy unit is J. By rewriting (5.6) using only the Pauli matrices we see that

$$\tilde{H}_U = \sum_r [\sigma_r^z\sigma_{r+1}^z - \frac{4\sqrt{2}}{W}\sigma_r^x + 2\left(\frac{\lambda}{W} + 1\right)\sigma_r^z] + \text{const.}, \tag{5.8}$$

so that it is equivalent to the antiferromagnetic Ising model in a skew field (AFISF).

Note that the prefactor $-\sqrt{2}$ in front of the spin flipping term in (5.6) is due to the Bose enhancement factor. If we start not from a unit filled MI, but from a MI with $\bar{n}$ bosons per site, then the prefactor would be $-\sqrt{\bar{n}(\bar{n}+1)}$, which would be the only difference from the model considered here (5.6).

5.2.2. $E = U/2$ Regime

Analogously to the regime $E = U$, we now build the effective spin model that describes the behavior of the unit filled MI state, but tilted such that $E = U/2$. For now we will put μ to zero, but in the end we will explain that in order to obtain an effective spin model μ should be non-zero. We will show that in the presence of a superlattice the dynamics of bosons will be confined to sites of the same parity, i.e. bosons from initial odd sites will always move only to odd sites, and the same for bosons on even sites. Hence the resulting effective model in this regime will resemble two spin chains $E = U$ that are coupled.

In Fig. 5.1(c) one can see that if a boson moves two sites down the slope, the new state will be degenerate with the initial MI. Once the tilt is set exactly at $E = U/2$ the initial MI state becomes degenerate with a set of other states, i.e. the contribution of on-site interactions and potential energy of bosons in those states is equal and of the opposite sign. The tunneling part of the Hamiltonian (5.1) will play the role of a perturbation that couples the states of this energy

manifold. The reader can see that in order to go from one state to another in the energy manifold at least two tunneling processes should happen, which means that the construction of the effective Hamiltonian [132] will be done via couplings with other energy manifolds of the Hamiltonian (5.1) separated by energies of the order U.

5.2.2.1. Allowed Transitions

Only transitions where both bosons start or end up on the same site have non-trivial matrix elements. All the non-trivial resonant transitions in the energy manifold of interest can be categorized in three groups.

1. The first type of transitions couple different states via tunneling of a boson over two sites down the slope of the tilted potential. In this case the amplitude of the transition will depend on the occupations of the initial and final sites as well as the intermediate site. For instance, the initial MI site is coupled with

$$\prod_r |1\rangle_r \leftrightarrow |0\rangle_l |2\rangle_{l+2} \prod_{r\neq l,l+2} |1\rangle_r \,, \tag{5.9}$$

   where a single boson tunnels twice ending up on a next-neighboring site. This process can go via two channels: when the boson on site l tunnels to $l+1$ and then from $l+1$ to $l+2$, or the boson from $l+1$ first tunnels to $l+2$ and then the boson from l tunnels to $l+1$. The resulting matrix element of this transition equals $3\sqrt{2}J^2/U$. For each process of this type, there is the opposite, where a particle from a doubly occupied site tunnels back to the empty site. Analogous to the regime $E = U$ one can notice that it is impossible to achieve two doubly occupied sites on next-next-neighboring sites via this kind of transition (Fig. 5.1(d)), as such states are not in the same energy manifold with the original MI state, i.e. their occupation scales only as $\propto (J/U)^4$ in perturbation theory.

2. The second type of resonant tunneling process is one in which a single boson hops to a neighboring site and then hops back to the original site. In this case the configuration of bosons does not change, but each state obtains an energy shift depending on the occupation the sites. For instance, the initial MI state obtains obtains the energy shift of $-16J^2/3U$ per boson because each particle can tunnel one site left (right) and then tunnel right (left) to the initial site. These channels do not cancel each other because the intermediate state's energy offset is different in each channel.

3. The third type of process occurs only for certain configurations of bosons on the lattice. For these processes two bosons from the same site tunnel in the opposite directions, for instance

$$|..., 0, 1, 2, 0, 1, 2, ...\rangle \quad \leftrightarrow \quad |..., 0, 2, 0, 1, 1, 2, ...\rangle \,, \tag{5.10}$$

will be a resonant transition, as the energy of the initial and final states are identical.

The reason why we introduce the superlattice geometry $\mu > 0$ is to restrict the third type of transitions in order to be able to describe the dynamics of bosons via an effective spin-1/2 model. For this reason we introduce the offset energy μ between even and odd sites of the lattice. In order to suppress the transition amplitudes the superlattice offset should satisfy $\mu \gg J$. As the result, the energy difference between states connected by the third type of transitions becomes of the order μ, which means that the occupation of states achieved only via the third type of processes will scale as $\propto (J/\mu)^4$. For simplicity, we also assume from now on that $\mu \ll U$, which will make the derivation of the effective spin model much clearer. In principle, the flexible ratio μ/U provides one extra tunable parameter in the experiment; we will discuss the contribution from it at the end.

The reader might also think that as the states are coupled via two tunneling processes, then two bosons in different parts of the lattice can tunnel to their neighboring sites (in the opposite directions) and hence the effective Hamiltonian will have non-local terms, e.g.

$$|0\overset{\frown}{1}20\overset{\frown}{1}21\rangle \leftrightarrow |0210112\rangle\,. \tag{5.11}$$

However, this process arises from two channels, depending whether it is the boson from the site l or l' that tunnels first. Hence, these channels will have different intermediate states; more precisely the energy difference of these states and the energy of the MI state will have the same amplitude, but different sign. Hence, the amplitudes of this channels added together cancel each other. As the result, all processes of this kind have a zero amplitude.

5.2.2.2. Mapping to Spins

Now we are ready to introduce the mapping between bosons and spins. With only the first and second types of transition left, the dynamics of each boson is confined between the initial site of the MI state and the resonantly connected site. That is why it is enough to consider mapping to spins-1/2, analogously to the regime $E = U$. For each particle located on its initial r^{th} site of the MI state we assign a spin down $|\downarrow\rangle_r$. Then if a boson from the site r tunnels to the resonantly connected site two sites down the slope the corresponding spin becomes $|\uparrow\rangle_r$. Note that in the case of open boundary conditions the bosons on the last two sites can resonantly tunnel only via the second type of process, but not the first one. That is why their corresponding spins always point down and can be eliminated from the spin model.

With this mapping scheme, the first type of process provides the tunneling part

of the effective spin Hamiltonian

$$H_{U/2}^{\text{tun}} = \sqrt{2}\frac{J^2}{U/2}\sum_r(\sigma_r^x + 2\sigma_{r-1}^z\sigma_r^x + 2\sigma_r^x\sigma_{r+1}^z), \tag{5.12}$$

where one can notice the new characteristic energy $J^2/(U/2)$ instead of just J as it was in the regime $E = U$. Another interesting thing is that besides the first term corresponding to spin flipping, one can see additional terms that modify the amplitude of this process depending on the orientation of neighboring spins. This is directly connected to the fact that tunneling of particles depends on the occupation of the intermediate site. The constraint part of the Hamiltonian in the spin language then will forbid two next-neighboring spin-ups, i.e. the constraint is implemented only between sites of the same parity.

By considering all possible configurations one obtains the contribution of the second type of process, namely the interaction part of the effective spin Hamiltonian reads

$$H_{U/2}^{\text{int}} = -\frac{4}{15}\frac{J^2}{U/2}\sum_r\left(5 + 7\sigma_r^z + 6\sigma_r^z\sigma_{r+1}^z + 6\sigma_r^z\sigma_{r+3}^z\right), \tag{5.13}$$

where again one can see that spins at distance three become coupled, as a particle that has tunneled two sites down the lattice can experience an energy shift that depends on the presence of the neighboring atoms, including one three sites along from the initial site.

5.2.2.3. Final Effective Model

Adding together (5.12) and (5.13), and rearranging terms in a way resembling the regime $E = U$ we obtain the effective Hamiltonian

$$\begin{aligned} H_{U/2} \;=\; & \sum_r[-\sqrt{2}\sigma_r^x + \lambda\sigma_r^\uparrow + W\sigma_r^\uparrow\sigma_{r+2}^\uparrow \\ & -2\sqrt{2}(\sigma_r^x\sigma_{r+1}^z + \sigma_r^z\sigma_{r+1}^x) \\ & -\frac{8}{5}(\sigma_r^z\sigma_{r+1}^z + \sigma_r^z\sigma_{r+3}^z) \\ & +\frac{4}{15}(2 - 14\sigma_r^\uparrow)] \end{aligned} \tag{5.14}$$

where $\lambda \equiv \frac{U/2-E}{J^2/(U/2)}$ denotes the detuning from the resonance in the regime

$$\begin{cases} |U/2 - E|\,, J \ll U \\ J \ll \mu \ll U \end{cases}, \tag{5.15}$$

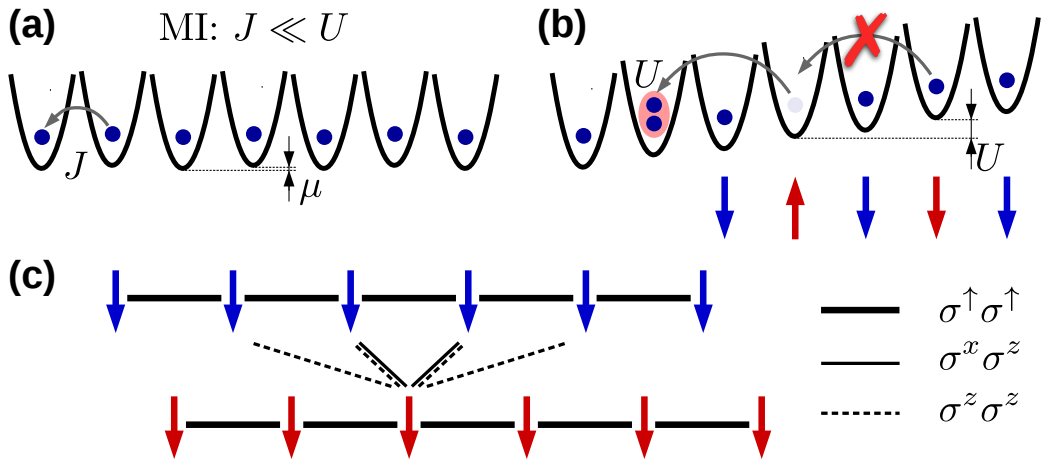

Figure 5.2.: (a) Schematic representation of the unit filled Mott insulator (MI) phase ($J \ll U$) of bosons on the superlattice geometry with detuning μ between even and odd sites. (b) After a sudden quench of the lattice to the regime $E = U/2$ the MI state is resonantly coupled with manifold states via tunneling of bosons over two sites and forming a double occupancy. Furthermore transitions of other bosons to and from the empty or doubly occupied site are not resonant any more. The superlattice suppresses all transitions that would be resonant if not for the superlattice. Each boson staying on the initial site is mapped to $|\downarrow\rangle$; each boson that tunneled to its next neighboring site is mapped to $|\uparrow\rangle$. The bosons on the last two sites down the slope are not able to resonantly tunnel and do not have spins mapped with them. Spins are colored to emphasize their parity only. (c) The resulting effective spin model of spins can be represented as two chains of odd (blue) and even (red) spins coupled with each other via $XZ-$ and $ZZ-$types of interactions (shown only for one spin).

and the weight $W \to +\infty$ implements the constraint. To avoid any confusion, the energy unit is $J^2/(U/2)$. One can notice that terms of the first row alone are identical to (5.6) for even and odd spins, which would happen if tunneling of bosons did not depend on the occupation of neighboring sites (Fig. 5.2). The source of XZ-terms in the second line is tunneling of bosons to next-next-neighboring sites, the amplitude of which depends on the occupation of the intermediate site. The ZZ-terms in the third line are energy shifts due to virtual tunneling with the configuration unchanged. The terms of the last row shift the entire energy spectrum along the energy and detuning λ axes. We can think about the resulting spin chain (5.14) as a combination of two chains in the regime $E = U$ (5.6) coupled together via XZ- and ZZ-interactions.

5.2.3. Benchmarking of the Effective Models

The model (5.1) can also be written as a time-dependent Hamiltonian,

$$H = -\sum \left(J\mathrm{e}^{-iE_r t} b_r^\dagger b_{r+1} + \mathrm{h.c.} \right) + \frac{U}{2} \sum_r n_r \left(n_r - 1 \right), \tag{5.16}$$

which produces exactly the same dynamics. The main advantage of this form of the Hamiltonian is that it directly implements periodic boundary conditions (PBC). The corresponding effective spin models then also have PBC. This fact makes it possible to perform testing of the effective spin models without dealing with boundaries. In Fig. 5.3 we present such a comparison for $M = 8$ bosons and corresponding effective spin models (for 8 spins since PBC) for both values of tilts.

In the case $E = U$ the agreement is excellent. In the case of $E = U/2$ we show the results without and with a small superlattice energy offset μ. One can see that data curves agree only in the last case. In all cases the condition $J \ll U$ is held, in the case of the superlattice we have $J \ll \mu \ll U$. However, due to finite values of μ, small discrepancies can still be observed.

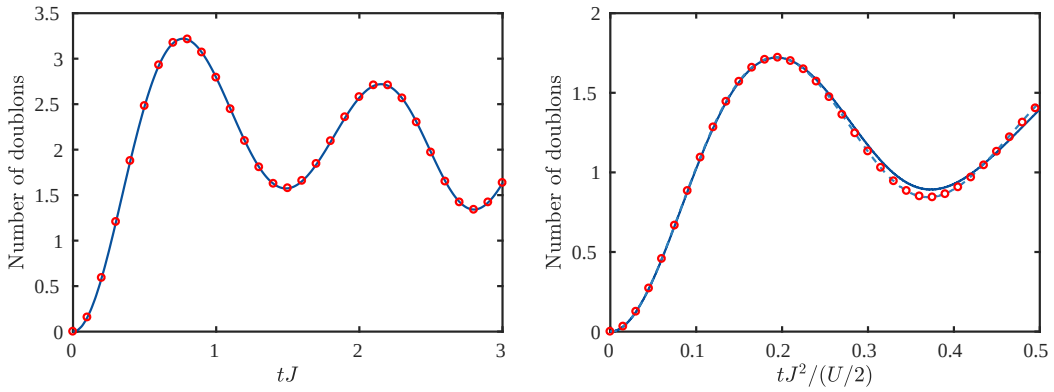

(a) (d)

Figure 5.3.: Comparison of the boson dynamics on tilted lattices captured via the Bose-Hubbard model and the effective spin models in the case of periodic boundary conditions on a lattice of 8 sites. (a) $E = U$ regime: solid line — simulation of (5.16) with $U = 100J$ and $\mu = 0$. (b) $E = U/2$ regime: solid line — simulation of (5.16) with $U = 1000J$ and $\mu = 0$, and dashed line — with $U = 1000J$ and $\mu = 30J$, i.e. it satisfies Eq. (5.15). The red dots in (a,b) are results of the effective models (5.6) and (5.14), respectively, for $\lambda = 0$. The results are obtained via numerical exact diagonalization of corresponding Hamiltonians.

5.3. Effective Models in Limiting Cases

Essential points of the spin models (5.6) and (5.14) will become clear if we first take a look at the extreme cases $\lambda \to \pm\infty$. Here we always assume that the constant term is always larger, i.e. $W \gg |\lambda|$. In these limits one can rewrite Hamiltonians as the system of equations

$$\begin{cases} H = H_0 + H_1 \\ H_{\text{con}} = 0 \end{cases}, \tag{5.17}$$

where

$$H_0 = \lambda \sum_r \sigma_r^{\uparrow}$$

is always the unperturbed Hamiltonian, H_1 is the perturbation, and H_{con} is the constraint forbidding pairs of spin-ups at distance one or two for models (5.6) and (5.14), respectively. We then proceed with the standard perturbation Hamiltonian theory [132], but taking into account the constraint.

The main conclusion of this section is that XZ and ZZ interaction terms of (5.14) couple elementary excitations of subchains of the opposite parity. These coupled excitations play the major role near the quantum critical point as their energy becomes lower than energy of single elementary excitations.

In Sec. 5.4 we will continue the investigation of the model, but near the quantum critical point, then we will see that the predictions of the effective model are compatible with the system's critical behavior.

5.3.1. $E = U$ Regime

We first consider the case of $E = U$, as it will play the role of a building block for the regime $E = U/2$. In the regimes of large longitudinal field $|\lambda| \to +\infty$ spins are aligned along the field. However, due to the constraint, $W \to +\infty$, their configurations are quite different. The perturbative part of the Hamiltonian takes form

$$H_1 = -\sqrt{2} \sum_r \sigma_r^x. \tag{5.18}$$

5.3.1.1. Paramagnetic Phase

In the case of $\lambda \to +\infty$ the model (5.6) is in the paramagnetic (PM) state, where its ground state has all spins aligned along the longitudinal field $\prod_r |\downarrow\rangle_r$, i.e. in the boson language the energy is minimized if all particles stay on their initial sites.

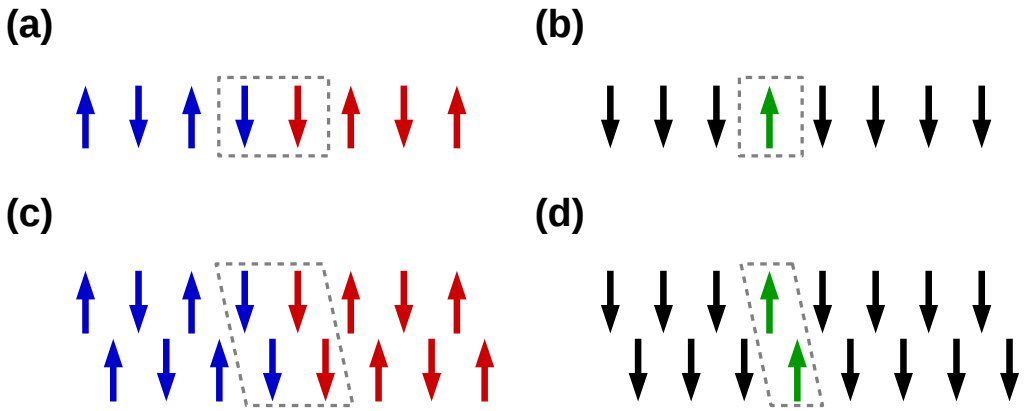

Figure 5.4.: Illustrations of elementary (a,b) vs coupled (c,d) excitations in the extreme cases $\lambda \to -\infty$ (a,c) and $\lambda \to +\infty$ (b,d). The elementary excitations are present in both regimes $E = U$ and $E = U/2$. The coupled excitations are possible only in the regime $E = U/2$, where elementary excitations pair up via the interaction terms between subchains.

The lowest elementary excitations are single spin-up states (Fig. 5.4(b))

$$|l\rangle = |\uparrow\rangle_l \prod_{r\neq l} |\downarrow\rangle_r \,. \tag{5.19}$$

The degeneracy is lifted only in the second order of the perturbation theory in $1/\lambda$, via spin flipping terms that give rise to nearest-neighbor hopping of the spin excitations. The higher excited states at large λ consist of two elementary excitations

$$|l, l'\rangle = |\uparrow\rangle_l |\uparrow\rangle_{l'} \prod_{r\neq l,l'} |\downarrow\rangle_r \,. \tag{5.20}$$

By writing the effective Hamiltonian [132] one can derive the second order correction to the ground state energy

$$E^+_{U,0}(\lambda) = -\frac{2M}{\lambda} + \mathcal{O}\left(\frac{1}{\lambda^2}\right), \tag{5.21}$$

where the energy shift occurs due to interactions with the lowest elementary excitations band. Following the same procedure, one can determine the energy shift of elementary excitations due to interactions with the ground state and with the energy manifold of two excitations

$$E^+_{U,1}(\lambda, k) = \lambda + \frac{2}{\lambda}[4 - M + 2\cos(ka)] + \mathcal{O}\left(\frac{1}{\lambda^2}\right), \tag{5.22}$$

where k is the single excitation momentum

$$|k\rangle = \frac{1}{\sqrt{M}} \sum_l e^{ikla} |l\rangle \,, \tag{5.23}$$

and a is the spatial separation between spins. Higher excited states consist of multiple bands of elementary excitations with interaction corrections.

5.3.1.2. Antiferromagnetic Phase

In the case of a large negative field λ, system favors to maximize the total number of spin-ups, however in order to obey the constraint, the spins should be Néel ordered, i.e., in the state $\prod_r \left(|\downarrow\rangle_{2r-1} |\uparrow\rangle_{2r}\right)$.

Note that for finite-size systems the degeneracy of the ground state depends on the type of boundary conditions as well as on the parity of the number of spins. For instance, the ground state is twofold degenerate in the case of an even number of spins and periodic boundary conditions, and non-degenerate in the case of odd spins and open boundary conditions (it is Néel ordered with spin-ups at the edges). For the sake of simplicity, we define the number of spin-ups in the ground state as $M^{\uparrow}_{\rm gr}$, which in the thermodynamic limit will make the boundary effects and parity irrelevant and approach the value of $M/2$, where M is the total number of spins. Then the ground state energy reads

$$E^{-}_{U,0}(\lambda) = -|\lambda| M^{\uparrow}_{\rm gr} - \frac{2M^{\uparrow}_{\rm gr}}{|\lambda|} + \mathcal{O}\left(\frac{1}{|\lambda|^2}\right). \tag{5.24}$$

The lowest excited states have one fewer spin-up and hence the Néel ordered phase should be broken somewhere. It can be described in the language of domains, where each domain is the Néel ordered phase. There are two types of domain, one with spin-ups on odd sites and the other with spin-ups on even sites. Then domain walls are places where two different domains meet each other (Fig. 5.4(a)). Due to the constraints the domain walls can only be formed of two consecutive spin-downs $|w\rangle \equiv |\downarrow\rangle_w |\downarrow\rangle_{w+1}$ and not consecutive spin-ups. It is important to note that the state with $M^{\uparrow}_{\rm gr} - 1$ spin-ups can have two domain walls, one of which might coincide with the open boundary. The important part is that in thermodynamic limit the boundaries will move independently, i.e. without interaction. For simplicity, we can consider a single domain wall on the infinite chain first, then obtain the correction to the whole energy manifold assuming that domain walls do not meet on the infinite chain. Then the lowest band of domain walls has the following dispersion relation

$$E^{-}_{U,1}(\lambda, k) = -|\lambda|(M^{\uparrow}_{\rm gr} - 1) - 2\frac{M^{\uparrow}_{\rm gr} - 1 + 4\cos(2ka)}{|\lambda|} + \mathcal{O}\left(\frac{1}{|\lambda|^2}\right), \tag{5.25}$$

where k is the momentum of a single domain wall. Interactions between domain

walls and possible open boundaries are of the order of $\mathcal{O}(1/M|\lambda|)$. Note, that unlike spin-ups in the paramagnetic phase domain walls can only move by two sites, which correctly reflects periodicity of the AFM phase.

Then the energy gaps between the ground state and lowest excitations in both limits of λ as $M \to \infty$ take the form

$$\begin{cases} \Delta E_U^+(\lambda) = \lambda + \frac{8+4\cos(ka)}{\lambda} + \mathcal{O}\left(\frac{1}{\lambda^2}\right), & \lambda \to +\infty \\ \Delta E_U^-(\lambda) = |\lambda| + \frac{2-8\cos(2ka)}{|\lambda|} + \mathcal{O}\left(\frac{1}{\lambda^2}\right), & \lambda \to -\infty \end{cases}, \tag{5.26}$$

If one considers only the zeroth order correction ($\sim |\lambda|$), the intersections of lowest excitations (at $\lambda = 0$) will show an approximate position of the QCP. The next non-zero order corrections ($\sim 1/|\lambda|$) correctly predicts that the true QCP is shifted towards negative values of λ, which is compatible with previous numerical simulations [59] (also see Fig. 5.5).

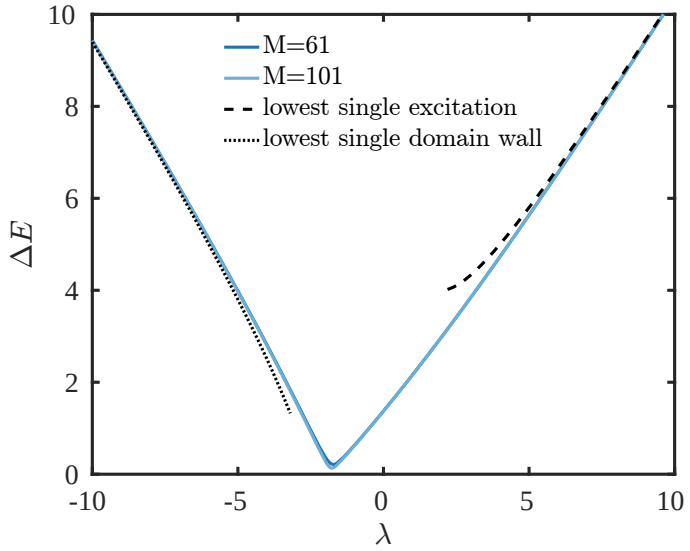

Figure 5.5.: Overview of the energy gap (in units of J) of the $E = U$ model Eq. (5.6) in the case of OBC and an odd number of spins M, so that the ground state is always non-degenerate. Finite size effects can be seen only in the vicinity of the transition. The results of the effective theory are presented for the lowest excitations of (5.26). One can see that the agreement becomes better as $|\lambda| \to \infty$. Also, one can see that the effective theory predicts that the quantum critical point (QCP) is shifted away from $\lambda = 0$ towards negative values.

5.3.2. $E = U/2$ Regime

The derivation the effective model is very similar to the regime $E = U$, just using a different perturbative part of the Hamiltonian

$$H_1 = \sum_r \left[-\sqrt{2}(\sigma_r^x + 2\sigma_r^x\sigma_{r+1}^z + 2\sigma_r^z\sigma_{r+1}^x) - \frac{8}{5}(\sigma_r^z\sigma_{r+1}^z + \sigma_r^z\sigma_{r+3}^z) \right]. \quad (5.27)$$

However we will see that the $ZZ-$interaction terms create first order corrections to the energy levels, which did not exist in the regime $E = U$. The role of $XZ-$interactions is to alter the second order corrections in a sophisticated way and this part will be only briefly discussed. Importantly, a qualitative difference occurs in this model — coupling of elementary excitations on different subchains lowers their mutual energy. This will lead to formation of excitation pairs — new lowest energy excitations, which is the first indicator that the critical behavior of the model may be different from the regime $E = U$.

5.3.2.1. Paramagnetic Phase

For $\lambda \to +\infty$ the ground state of the system is the non-degenerate paramagnetic state $\prod_r |\downarrow\rangle_r$ where spins are aligned with the strong external field λ. The corrections to the ground state energy take the form

$$E^+_{U/2,0}(\lambda) = -\frac{16M}{5} - \frac{18M}{\lambda} + \mathcal{O}\left(\frac{1}{\lambda^2}\right), \quad (5.28)$$

where, in comparison with (5.21), there is a first order correction due to the ZZ interaction terms between subchains, and the second order correction is altered by XZ interactions.

The lowest elementary excitations are states with a single spin-up (as in $E = U$ regime)

$$|l\rangle = |\uparrow\rangle_l \prod_{r\neq l} |\downarrow\rangle_r . \quad (5.29)$$

The energy corrections to the first excited states are

$$E^+_{U/2,1}(\lambda) = \lambda - \frac{16}{5}(M-4) + \mathcal{O}\left(\frac{1}{\lambda}\right), \quad (5.30)$$

where the first correction is due to the ZZ interactions between subchain. The degeneracy of levels is lifted by second-order corrections proportional to $1/\lambda$, but comparing to (5.22) the correction here has a complicated form due to XZ interactions. We omit it here as the main point can be understood from the first order corrections (see below).

The higher excited states at large λ consist of two elementary excitations

$$|l, l'\rangle = |\uparrow\rangle_l |\uparrow\rangle_{l'} \prod_{r \neq l,l'} |\downarrow\rangle_r \,. \tag{5.31}$$

Generally, one should expect that their energies are equal to twice the energy of the elementary excitations, however these excitations can couple with each other via ZZ interactions and lower their mutual energy. Then the energy of the coupled excitations will have the following form

$$E^+_{U/2,2}(\lambda) = 2\lambda - \frac{16}{5}(M-6) + \mathcal{O}\left(\frac{1}{\lambda}\right), \tag{5.32}$$

from where one can immediately see that the binding energy is equal to $32/5$ in units of the Hamiltonian $H_{U/2}$. As the result the energy of elementary and coupled excitations above the ground state reads

$$\begin{cases} \varepsilon^+_{\mathrm{e}}(\lambda) = \lambda + \frac{64}{5} + \mathcal{O}\left(\frac{1}{\lambda}\right) \\ \varepsilon^+_{\mathrm{c}}(\lambda) = 2\lambda + \frac{96}{5} + \mathcal{O}\left(\frac{1}{\lambda}\right) \end{cases}, \tag{5.33}$$

in units of $H_{U/2}$.

5.3.2.2. Antiferromagnetic Phase

In the case of $\lambda \to -\infty$ the ground state maximizes the total number of spin-ups in the system, but due to the constraint condition spins on the even or odd sublattices are Néel ordered, i.e. it is the same as for two spin chains $E = U$. It is important to notice that the degeneracy of the ground state depends on the number of the spins and type of the boundary conditions, as in the $E = U$ case. For instance, in the case of an even number of spins in each subchain and periodic boundary conditions the ground state is fourfold degenerate; in the case of an odd number of spins in both subchains and open boundary conditions the ground state is non-degenerate.

The corrections to the energy in this regime take the form

$$E^-_{U/2,0}(\lambda) = -|\lambda| M^{\uparrow}_{\mathrm{gr}} - \frac{2M^{\uparrow}_{\mathrm{gr}}}{|\lambda|} + \mathcal{O}\left(\frac{1}{|\lambda|^2}\right), \tag{5.34}$$

where $M^{\uparrow}_{\mathrm{gr}}$ denotes the total number of spin-ups in the ground state, which is the same as for two chains in the regime $E = U$. We note that the corrections due to XZ and ZZ interactions cancel out in this case.

The lowest excited states have one extra spin-down compared to the ground state. In the language of domains, this means that spins on the even or odd sublattices remain Néel ordered, and spins on the other sublattice have a pair of domain walls, analogous to elementary excitations in the regime $E = U$. Then the first

correction to the energy takes the form

$$E^{-}_{U/2,1}(\lambda, q) = -|\lambda| \left(M^{\uparrow}_{\mathrm{gr}} - 1 \right) + \frac{16}{5} f(q) + \mathcal{O}\left(\frac{1}{|\lambda|} \right), \tag{5.35}$$

where $f(q)$ is the discrete function that takes one of three values $\{-1, 0, 1\}$ depending on the relative position of the domain walls. This correction is defined by $ZZ-$interactions and the contribution of the $XZ-$interactions appears in the next correction, which has an unnecessary complicated form.

The higher energy band has two extra spin-down compared with the ground state, i.e. the energy gap between these state and the ground state scales $\propto 2|\lambda|$. The expression for energy up to the first correction reads

$$E^{-}_{U/2,2}(\lambda, q) = -|\lambda| \left(M^{\uparrow}_{\mathrm{gr}} - 2 \right) + \frac{16}{5} h(q) + \mathcal{O}\left(\frac{1}{|\lambda|} \right), \tag{5.36}$$

where $h(q)$ is a discrete function that takes only integer values in the interval from -4 to +4, inclusive, depending on the relative position of the domain walls on spin chains of both parities. The important point is that there are excitations for which the energy is lower than the energy of two excitations from the first excited band, i.e. excitations pair up together and lower their mutual energy by $32/5$ in units of $H_{U/2}$ via ZZ interactions. The contribution of the XZ interaction appears in second order corrections, which breaks degeneracy of excitations, but again the key physics can be drawn only from the first order corrections, which is why higher corrections are omitted.

The energy of the lowest elementary and coupled excitations above the ground state reads

$$\begin{cases} \varepsilon^{-}_{\mathrm{e}}(\lambda) = |\lambda| - \frac{16}{5} + \mathcal{O}\left(\frac{1}{|\lambda|} \right) \\ \varepsilon^{-}_{\mathrm{c}}(\lambda) = 2|\lambda| - \frac{64}{5} + \mathcal{O}\left(\frac{1}{|\lambda|} \right) \end{cases}, \tag{5.37}$$

in units of $H_{U/2}$.

5.3.2.3. Comparison with the Full Model

From scalings (5.33) and (5.37) we see that the ZZ interaction term produces the leading contribution to the modification of the spectrum of elementary and coupled excitations (Fig. 5.4) compared to the regime $E = U$. One can see that at low values of the field λ, near the phase transition, coupled excitations have lower energy than elementary excitations, up to first order corrections. This substitution of the lowest excitations in principle means that the critical behavior of the system for $E = U/2$ can belong to a universality class different from the regime $E = U$. In Fig. 5.6 one can see the case of the full model (5.14) labeled as $XZ = 1$ and the case where XZ interactions are omitted in the Hamiltonian.

This last case is well approximated by the effective theory results (5.37) and (5.33), which shows that near the critical point one should expect that coupled interactions have lower energy that single excitations (see the sharp change of the energy gap scaling).

The reason why the full model (labeled as $XZ = 1$) is different from the effective theory near the phase transition point is the significant contribution of the second order corrections (simply matrix elements of H_1 become an order of magnitude larger). The role of XZ interactions is to enhance the amplitude of the dispersion relation of the order $1/|\lambda|$, and becomes important near the phase transition as well as ZZ interactions.

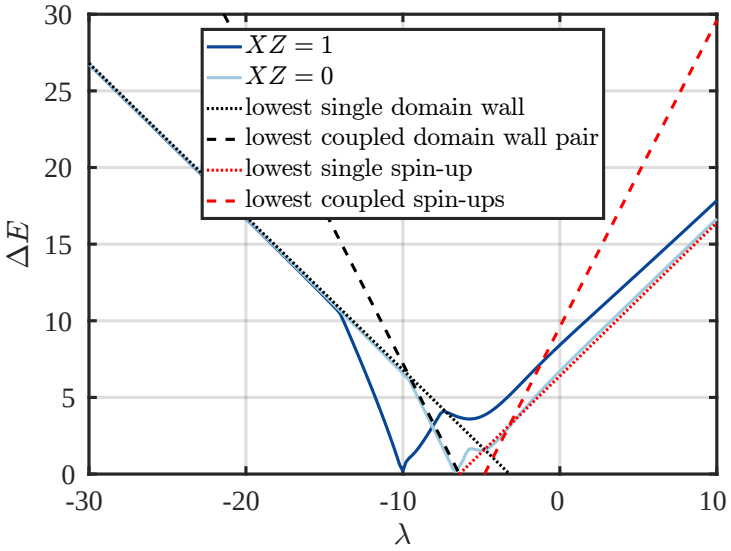

Figure 5.6.: Overview of the energy gap (in units $J^2/(U/2)$) in the case of $M = 26$ and OBC together with results of the effective theory. For this number of spins the ground state is always non-degenerate. The curve denoted $XZ = 1$ represents the full model (5.14); the case $XZ = 0$ denotes the result for (5.14), but without XZ interactions. The effective theory results (up to the first order corrections) are taken from (5.37) for domain walls and from (5.33) for spin-ups. See the main text for more details.

5.4. Phase Transition Analysis

In the following section we present the results of the phase transition investigation in the models (5.6) and (5.14). We start by performing a standard finite size scaling analysis and then support the results we obtain through the analysis of the symmetries of the models. We start from the regime $E = U$ that we use to benchmark our numerics and revisit the model in terms of an equivalence with the antiferromagnetic Ising chain in a skew field (AFISF). The AFISF is known

to undergo a second order phase transition of the Ising universality class. This is fully confirmed by our numerical finite-size scaling analysis, which was done via MPS techniques (Chap. 4). The $E = U/2$ model also undergoes a phase transition from an ordered to a disordered state. Here the numerical results are non conclusive and compatible with a few different scenarios.

We identify the corresponding full symmetry of the $E = U/2$ system in the ordered AFM state as the non-Abelian dihedral group $\mathcal{D}_4$. Though the finite size scaling shows different scaling laws with respect to the Ising universality class, we have not managed yet to identify with certainty which universality class this transition belongs to. However, we have listed possible scenarios that in our opinion are the most probable. Critical exponents are compatible with a weakly first-order transition (with an undetectable order parameter jump) or a second order transition of Potts critical class. In the last case one more option is possible, such that the scaling laws have logarithmic corrections as discussed in Ref. [133].

5.4.1. $E = U$ Regime

In this section we would like to summarize the main aspects of the model (5.6) along with its symmetry content. This goes beyond previous analysis in Ref. [59]. The described model (5.6) is identical to the AF Ising chain in a skew field (AFISF), i.e. both longitudinal and transverse fields are present. By leaving the constant part of the Hamiltonian one can rewrite (5.6) (skew field) in the case of extreme interactions ($W \to \infty$), after regrouping the Hamiltonian, up to constants, reads

$$\tilde{H}_U = \sum_r \left[\sigma_r^z \sigma_{r+1}^z - h_x \sigma_r^x + h_z \sigma_r^z\right], \tag{5.38}$$

where $h_x = \frac{4\sqrt{2}}{W} \to 0$ is the amplitude of the transverse field along the x axis and $h_z = 2\left(\frac{\lambda}{W} + 1\right) \to 2$ — longitudinal field along the z axis.

A previous numerical study [134] of this model investigates the phase diagram in great details. The phase diagram is mapped by studying the behavior of the order parameter

$$\mathcal{M}_U = \frac{1}{M} \sum_{r=1}^{M} (-1)^r \langle \sigma_r^z \rangle \tag{5.39}$$

representing a staggered magnetization. In Fig. 5.7 we summarize the phase diagram obtained numerically in [134]. It has two phases, a Néel ordered antiferromagnetic phase, where $\mathcal{M}_U \neq 0$, and the paramagnetic phase with spins aligned with the skew field where $\mathcal{M}_U = 0$. When the transverse field is exactly zero, the model becomes classical and the phase transition between the two phases is of first order. For any other value of the transverse field the two phases are

separated by a line of second order phase transitions, all in the Ising universality class.

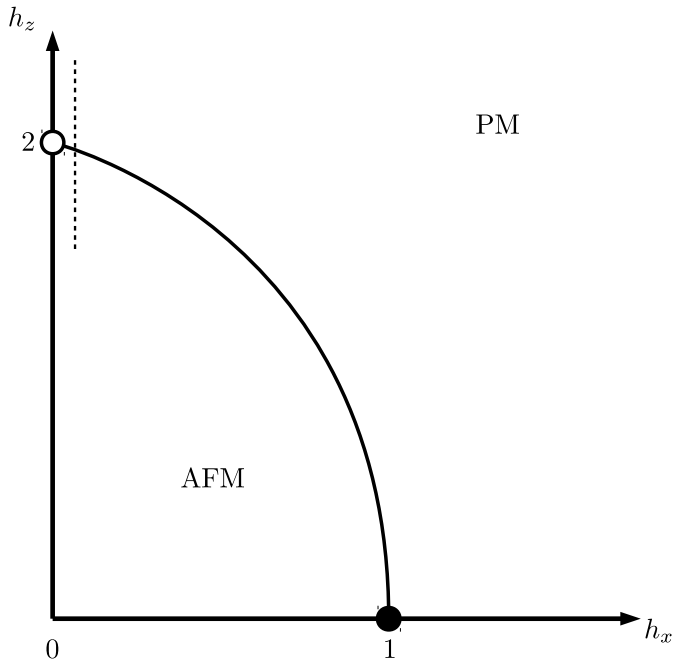

Figure 5.7.: Phase diagram of the model (5.38). For small values of fields spins are in the ordered antiferromagnetic state (AFM), whereas for large fields spins are aligned with the skew field $\vec{h} = (h_x, h_z)$, paramagnetic state (PM). The point $(0, 2)$ is the classical phase transition point (first order). The point $(1, 0)$ is the quantum phase transition point (second order), which corresponds to breaking of the $\mathcal{Z}_2$ symmetry generated by operator G_{TI} (5.42). The line connecting these two points is a second order transition line with the Ising universality class, however the Hamiltonian (5.38) does not commute with (5.42) if $h_z \neq 0$. Our conjecture is that this transition is related to the spontaneous $\mathcal{Z}_2$ symmetry breaking associated with parity (see the main text). Thus it is possible to explain the transition of (5.6): The fine dashed line shows the path $(h_x, h_z) = (\frac{4\sqrt{2}}{W}, -2(\frac{\lambda}{W} + 1))$ that the $E = U$ model undergoes as the longitudinal field λ changes. In the regime when the interaction strength $W \to \infty$ the value of the transverse field h_x becomes infinitesimal but just enough to avoid the first order transition point $(h_x, h_z) = (0, 2)$.

We perform a simple test on the well established nature of the quantum critical point by extracting numerically the dynamical critical exponent z and the correlation length exponent ν. Their values are compatible with $\nu = 1$ and $z = 1$, as expected. This agrees very well with previously published results [59] and shows

that the energy gap obeys

$$\Delta E = M^{-z} f[M^{1/\nu}(\lambda - \lambda_{\text{crit}})], \tag{5.40}$$

with the critical point at $\lambda_{\text{crit}} \approx -1.85$, which is quite close to the asymptotic prediction ((70) in [134]) $\lambda_{\text{crit}}^{\text{asym}} = -\frac{4\sqrt{2}}{3} \approx -1.886$. The phase transition indeed belongs to the Ising universality class. In Fig. 5.8 we present our results on finite-size scaling of even more sensitive observables: the structure factor S_π corresponding to periodicity two and the susceptibility

$$\chi_U = -\partial \mathcal{M}_U / \partial \lambda, \tag{5.41}$$

for the staggered magnetization $\mathcal{M}_U$. We see that not only does the scaling of the structure factor produce the correct Ising exponent $\eta = 1/4$, but also the scaling of the susceptibility agrees with the fluctuation-dissipation theorem which implies that $\chi_U \propto M \cdot \Delta E \cdot S_\pi \propto M^{3/4}$.

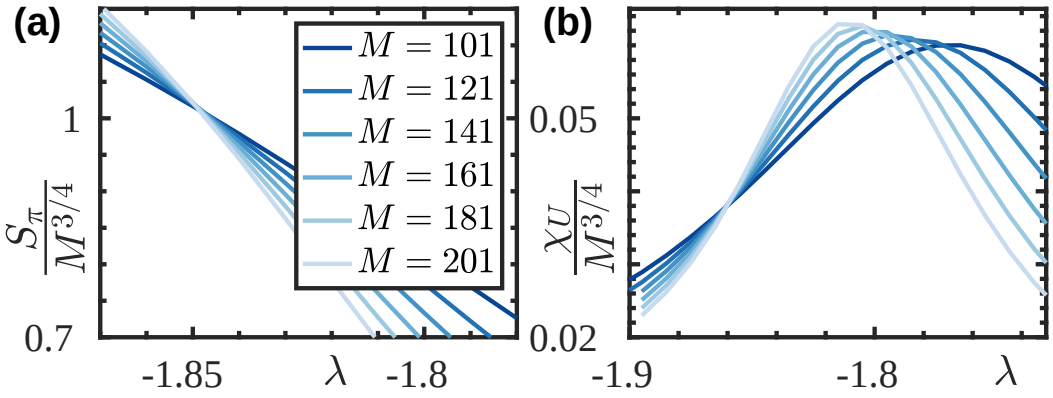

Figure 5.8.: Scaling plots near QCP in the regime $E = U$ for chains of M spins with OBC. (a) Collapse of scaling plots of the structure factor $S_\pi = \frac{1}{M}\langle(\sum_r (-1)^r \sigma_r^z)^2\rangle$ that according to the standard scaling argument should scale as $M^{2-z-\eta} = M^{3/4}$ for the Ising exponent $\eta = 1/4$. (b) Collapse of the susceptibility χ_U with the same exponent 3/4. This result agrees well with the fluctuation-dissipation theorem saying that $\chi_U \propto M \cdot \Delta E \cdot S_\pi$. Calculations or eigenstates were performed using variational eigenstate search techniques (Sec. 4.3.2) and converged with MPS bond dimension $D = 128$.

Despite this numerical evidence it is interesting to understand the nature of the transition from first principles. Considering again the Hamiltonian (5.38) in the case where the longitudinal field h_z vanishes, the model becomes the standard transverse Ising model with a second order phase transition between the paramagnetic and anti-ferromagnetic phases. In this specific case it is easy to identify the symmetry operator that commutes with the Hamiltonian,

$$G_{\text{TI}} = \prod_r \sigma_r^x. \tag{5.42}$$

At the phase transition, the ground state of the system spontaneously breaks the symmetry. As a consequence the ground state is two-fold degenerate and the symmetry operator (5.42) maps one ground state into another flipping the value of the order parameter (5.39). On the other side of the transition, in the symmetric phase, the ground state is unique and is an eigenstate of the symmetry operator with eigenvalue one.

If $h_z \neq 0$ the operator (5.42) does not commute with the Hamiltonian anymore, $[G_{\mathrm{TI}}, H_U] \neq 0$. This is why the observation of a line of second order phase transitions in the same Ising universality class could look surprising. However, by direct investigation, one can see that there is another possible symmetry operator, let us call it G, such that $[G, H_U] \neq 0$. The symmetry of the system is associated with periodicity two, hence $G^2 = \mathcal{I}$. One can define G as a shift operator

$$G[\sigma_r] = \sigma_{r+1}, \tag{5.43}$$

where in the case of the infinite system the translation is applied on all spins. Another way to define G is as an operator that inverts the entire spin chain around the middle of a bond between two neighboring spins (in the limit of the infinite chain it does not matter which bond, just the parity matters):

$$\begin{cases} G[\sigma_r] = \sigma_{M-r}, & \mod (M,2) = 0 \\ G[\sigma_r] = \sigma_{M-r+1}, & \mod (M,2) = 1 \end{cases}. \tag{5.44}$$

Thus G is a $\mathcal{Z}_2$ symmetry operator, it commutes with H_U and squares to the identity, i.e. has only eigenvalues ± 1. The net effect of G is that even and odd spins are exchanged. As expected, the G operator also exchanges the two Néel ordered ground states in the antiferromagnetic phase, and thus is the operator that is spontaneously broken at the line of second order phase transitions.

Summarizing, both the case with zero parallel field and non-zero transverse field and the case with non-zero parallel field and transverse field are described by $\mathcal{Z}_2$ invariant theories, however the symmetry operators are different. In the case without the longitudinal field, the symmetry operator is the standard spin-flip G_{TI} or a more generic G; in the case of a non-trivial longitudinal field it is only G. Independently of the specific form of the symmetry operator the two transitions are second order phase transitions in the Ising universality class.

Despite the infinite interaction term of (5.6) and the equivalent term in (5.38), it exhibits an order transition due to the non-vanishing value of the transverse field, which ensures that quantum fluctuations near the phase transition smooth out the behavior of the order parameter (5.39).

5.4.2. $E = U/2$ Regime

The analysis of the phase transition of (5.14) is a significantly harder task. In Sec. 5.3.2 we considered the limiting cases of the longitudinal fields and listed the corresponding ground states. As a reminder: the paramagnetic phase, $\lambda \to +\infty$, has a single ground state $\prod_r |\downarrow\rangle_r$, whereas the ordered antiferromagnetic phase, $\lambda \to -\infty$, has a fourfold-degenerate ground state in the limit $M \to \infty$, and reads

$$\begin{cases} |(\uparrow\uparrow\downarrow\downarrow)\rangle \\ |(\downarrow\uparrow\uparrow\downarrow)\rangle \\ |(\downarrow\downarrow\uparrow\uparrow)\rangle \\ |(\uparrow\downarrow\downarrow\uparrow)\rangle \end{cases}, \tag{5.45}$$

where brackets represent periodic repetition, so the states have periodicity four.

As one tunes the value of the field, λ, the system undergoes the phase transition associated with breaking of the symmetry. In Sec. 5.4.2.1 we discuss the possible scenarios of symmetry breaking. In Sec. 5.4.2.2 we show the results of the finite size scaling, and list possible scenarios which do not contradict the symmetries and scaling plots.

5.4.2.1. Symmetries

Here we present our considerations regarding the symmetry of (5.14). We split them into 3 parts with separate conclusions:

1. We identify the corresponding full symmetry of the system in the ordered AFM state, $\lambda \to -\infty$, as $\mathcal{D}_4$ ($\mathcal{D}_8$, in some literature), non-Abelian Dihedral group. The group $\mathcal{D}_4$ has 8 distinguishable elements, which can be reached from one to another via just two generators. In the case of the spin chain (5.14) it could be a translation by one site T and any of four possible reflections R (Fig. 5.9). This means that all four ground states of the AFM phase can be visited from one another using these two transformations. The Hamiltonian also commutes with T and R. On the other hand the ground state from the paramagnetic phase is invariant under application of T and R. The symmetry $\mathcal{D}_4$ is quite complex, and we do not know at the moment how to test this scenario, i.e. what finite scaling laws and exponents one should expect.
2. However, the group $\mathcal{D}_4$ has an Abelian subgroup $\mathcal{Z}_4$, four elements of which are generated by the single-site translation operator T. There is a possibility that the phase transition of (5.14) is associated with only this $\mathcal{Z}_4$ symmetry breaking. In this case we know a number of transitions that have the same symmetry breaking, especially the 4-state Potts and clock models. According to [133] the 4-state Potts model has a feature of a marginal field,

which leads to universal multiplicative logarithmic corrections to the scaling laws.

3. The third way of thinking about the symmetries of the system (5.14) is to treat the spin chain $E = U/2$ as two subchains $E = U$, let us call them A and B. Without XZ and ZZ interactions the system has a $\mathcal{Z}_2^A \otimes \mathcal{Z}_2^B$ symmetry with symmetry operators G^A and G^B; acting on the corresponding subchains (G is defined in Sec. 5.4.1), i.e. the transition belongs to the Ising universality class. Neither XZ nor ZZ terms are preserved under the symmetry transformations G^A and G^B, this implies that both XZ and ZZ interactions of the Hamiltonian $H_{U/2}$ explicitly break the $\mathcal{Z}_2 \otimes \mathcal{Z}_2$ symmetry, which exists for two non-interacting chains $E = U$. If this is the case, it must be a first-order phase transition, since in the Ising universality class there is no second-order phase transition in systems without $\mathcal{Z}_2$ symmetry.

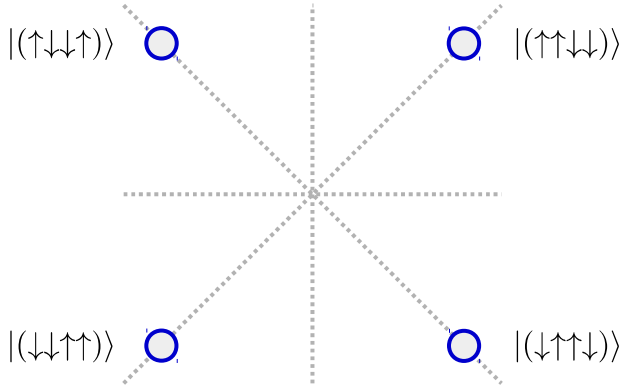

Figure 5.9.: The four ground states of (5.14) in the AFM regime ($\lambda \to -\infty$) are placed in corners of a square to emphasize the symmetries of the system, which is isomorphic to the symmetries of the square, $\mathcal{D}_4$. First, one can translate the spin chain by 1, 2, and 3 sites (limit on the infinite chain), which is equivalent to the rotation of the square by $\pi/2$, π, and $3\pi/2$ with respect to its center. The translation by 4 sites is equivalent to identity as well as the rotation of the square by 2π. Secondly, one can perform two different spin-centered and bond-centered reflections of the entire chain, which are equivalent to the reflection of the square with respect to the horizontal, vertical, and diagonal axes.

5.4.2.2. Finite Size Scaling

In Fig. Fig. 5.10(a) the energy gap scaling is presented, which shows the complicated nature of the lowest excitations. Apart from the interval $-11 \lesssim \lambda \lesssim -4$ the energy gap is $\propto |\lambda|$ for large values of the field. This regime qualitatively matches the scaling of the energy gap in the regime $E = U$, where the QCP is

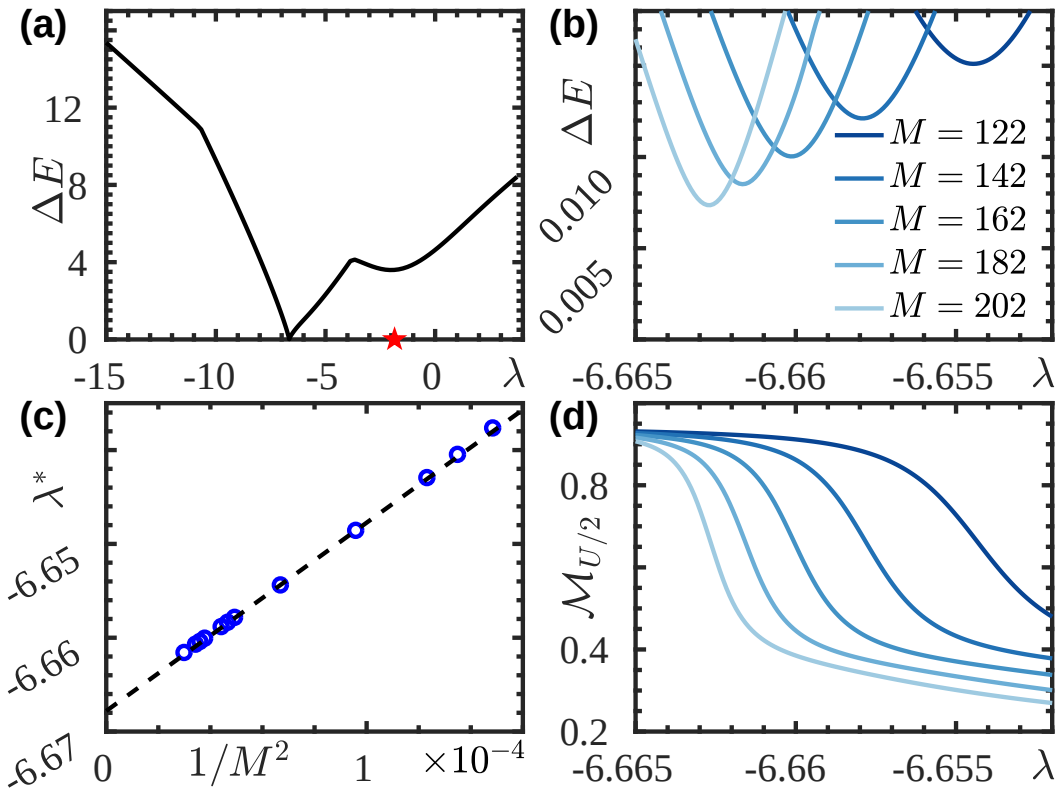

Figure 5.10.: (a) Energy gap ΔE as a function of the field λ of Eq. 5.14 for open boundary conditions and $M = 142$ spins, i.e. the system always has a non-degenerate ground state. This energy gap scaling example shows that the nature of the lowest excitations changes drastically in the interval $-11 \lesssim \lambda \lesssim -4$, outside of which the gap behavior is described by elementary excitations identical to those of the regime $E = U$. Inside the interval, bound excitation pairs have lower energy, which is also confirmed by the fact that the gap scaling rapidly changes from $\sim \lambda$ to $\sim 2\lambda$ (see Fig. 5.6). The red star marks the position of the QCP in the regime $E = U$ [59]. (b) Close-up of the QCP in the regime $E = U/2$ for different system sizes M. The positions of the gap minima, λ^*_M, are shown in (c) to scale with the system size with the correlation length critical exponent $\nu = 1/2$ towards the QCP at $\lambda_{\text{crit}} \approx -6.67$. (d) The order parameter $\mathcal{M}_{U/2}$ for the same system sizes as in (b). Even though the order parameter appear to have smooth behavior it does become remarkably steep at the critical point. Calculations were performed using eMPS method [120], numerical convergence was achieved for bond dimensions $D = 384$. The forbidden spin configurations were excluded from the calculations via MPO projectors.

located at $\lambda = -1.85$ and can still be observed in Fig. 5.10(a) (marked with a red star).

The scaling of the gap in the interval $-11 \lesssim \lambda \lesssim -4$ becomes $\propto 2|\lambda - \lambda_{\text{crit}}|$,

bringing further evidence that bounded pairs of elementary excitations have lower energy than single elementary excitations (see Fig. 5.6). The bounded pairs are formed when two elementary excitations of different subchains lower their mutual energy due to XZ- and ZZ-interactions (Fig. 5.4).

Below we first provide the finite size scaling according to the scenario of a weakly first order transition, and then present some of the scalings as a second order phase transition of the Potts universality class.

We resolve the position of the quantum critical point by extrapolating the gap minima λ_M^* (Fig. Fig. 5.10(b)) to the critical point $\lambda_{\text{crit}} \approx -6.67$. The scaling for large system sizes (Fig. Fig. 5.10(c)) suggests the correlation length exponent $\nu = 1/2$, which is distinctly different from the Ising case in the regime $E = U$. Note that if approximations of the critical point in the thermodynamic limit is done with Potts critical exponent $\nu = 2/3$ it produces a similar position of the critical point.

The insight about the form of these new excitations comes from analyzing the region where the actual closure of the energy gap happens, where the gap scales approximately two times faster with the field λ. This points again to existence of a bound state of two $E = U$ elementary excitations, one in each subchain, bounded together via interaction terms, as we have already discussed in Sec. 5.3.

We also find that the scaling of the energy gap at the critical point λ_{crit} is compatible with the law $\Delta E - \Delta E_0 = M^{-z} f[M^{1/\nu}(\lambda - \lambda_{\text{crit}})]$, with $\lambda_{\text{crit}} \approx -6.67$, $\nu = 1/2$, $z = 2$, and $\Delta E_0 \approx 0.01$. In other words there seems to be a finite gap in the thermodynamic limit ΔE_0 even if small and the dispersion relation on the top of the gap is quadratic. This result seems to suggest that the model with $E = U/2$ has a weakly first order phase transition or simply a crossover.

We then move to other physical quantities, such as the scaling of the order parameter, and its susceptibility. In the regime $E = U/2$ the order parameter is given by

$$\mathcal{M}_{U/2} = \frac{1}{M} \sum_r (-1)^r \langle \sigma_{2r}^z + \sigma_{2r-1}^z \rangle, \tag{5.46}$$

which now has a period four. Even though the order parameter $\mathcal{M}_{U/2}$ appears to have smooth behavior (Fig. 5.10(d)), it does become remarkably steep at the critical point, which does not rule out the possibility of the weakly first order scenario. The smallness of the energy gap makes it extremely difficult to rule out the possibility of the second order transition with unusual critical exponents.

In Fig. 5.11 we present our results on finite-size scaling of the structure factor $S_{\pi/2}$ corresponding to periodicity four and susceptibility $\chi_{U/2}$ of the staggered magnetization $\mathcal{M}_{U/2}$. From the results we appreciate that the scaling unveils trivial exponents expected in a first order transition $S_{\pi/2} \propto M$ and $\chi_{U/2} \propto M^2$. Moreover, by applying the fluctuation-dissipation theorem we check that $\chi_{U/2} \propto M \cdot \Delta E \cdot S_{\pi/2}$.

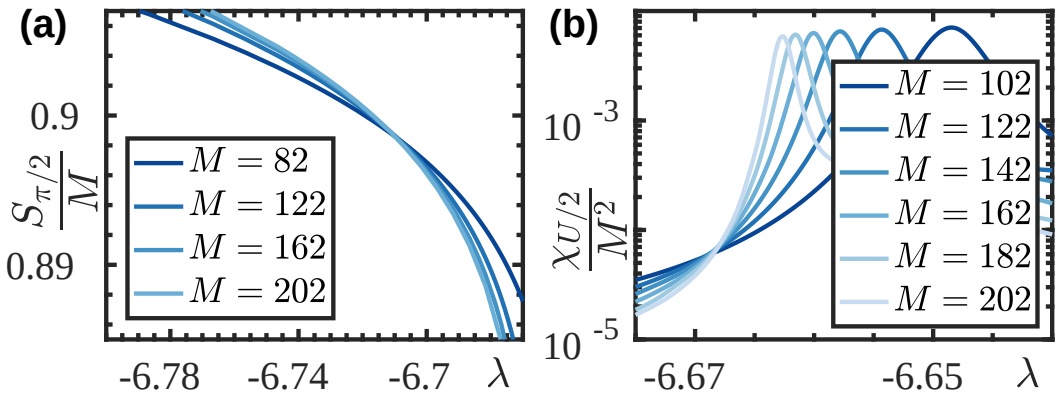

Figure 5.11.: Scaling plots near the QCP in the regime $E = U/2$ for chains of M spins with OBC. (a) Collapse of scaling plots of the structure factor $S_{\pi/2} = \frac{1}{M}\langle(\sum_{r=1}^{M/2}(-1)^r(\sigma^z_{2r}+\sigma^z_{2r-1}))^2\rangle$. (b) Collapse of the susceptibility $\chi_{U/2} = -\partial\mathcal{M}_{U/2}/\partial\lambda$ of the staggered magnetization $\mathcal{M}_{U/2}$. According to the standard scaling argument in the case of the first order transition $S_{\pi/2} \propto M$ and $\chi_{U/2} \propto M^2$, which matches extremely well with numerics. This result agrees well with the fluctuation-dissipation theorem saying that $\chi_{U/2} \propto M \cdot \Delta E \cdot S_{\pi/2}$, where $\Delta E \propto \Delta E_0 + \text{const} \cdot M^{-2}$. Calculations of eigenstates were performed with using DMRG techniques and converged with MPS bond dimension $D = 256$.

The scaling plots presented above are compatible with the scenario of a weakly first-order phase transition. However, if one starts making a more detailed analysis and compare the scaling that are compatible with the Potts model, then the order of the transition becomes unclear.

It is well established in the literature [133, 135] that a $k-$state Potts model has a first order transition for $k > 4$, and a second order transition if $k \leq 4$. The marginal case $k = 4$ however has logarithmic corrections to the scaling laws. In Fig. 5.12 we present all three scenarios side by side. Even though one can argue that the scaling with the Potts model exponents is better, we shall leave this question open until it is cross checked via other methods or other scaling plots. After all it is not clear that if it is the Potts universality class, which corresponds the $\mathcal{Z}_4$ symmetry breaking, why the entire symmetry class $\mathcal{D}_4$ does not matter here. Also the case of the chiral clock model should be included in the consideration as well.

To summarize, the above numerical results are not conclusive (the gap is very small and the finite-size scaling very challenging) but we can identify possible regimes:

- A weakly first order phase transition with a small energy gap and an unde-

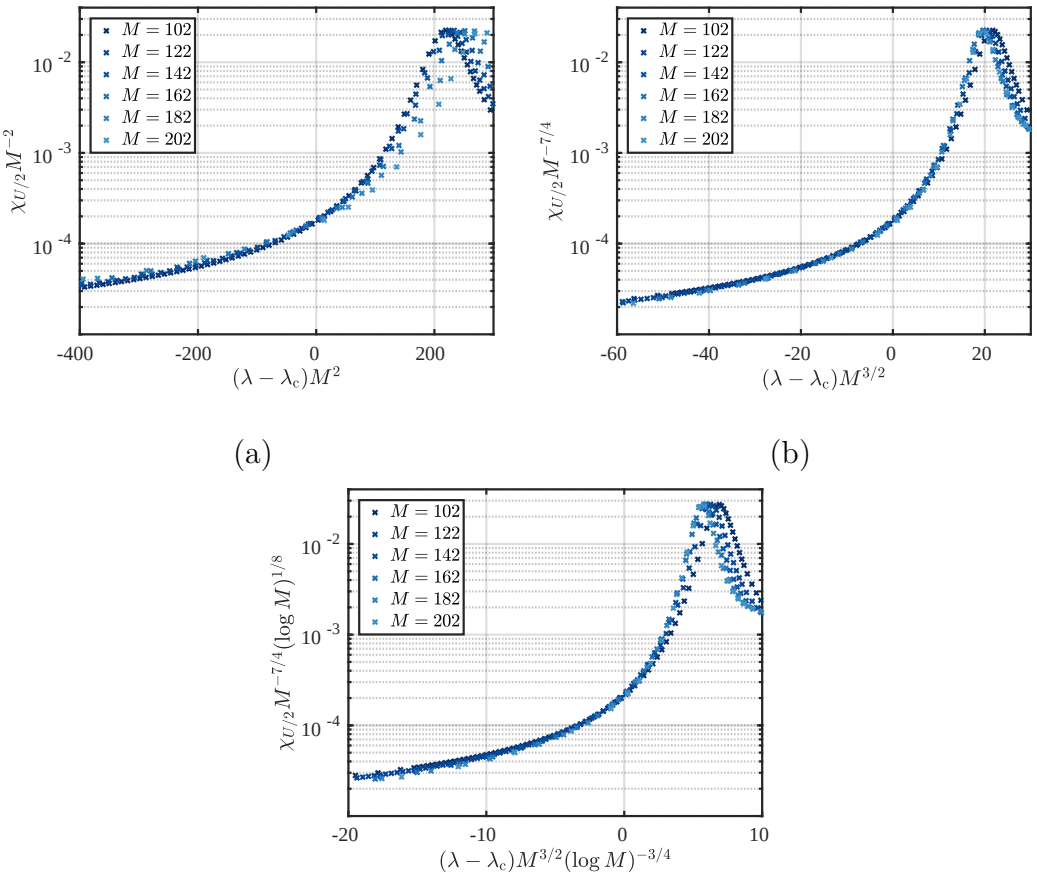

Figure 5.12.: Comparison of the scaling plots for $\chi_{U/2}$ near QCP ($\lambda_c = -6.6695$) in the regime $E = U/2$ for chains of M spins with OBC. (a) Critical exponents are compatible with a weakly first-order transition. (b) Critical exponents are compatible with the second order transition of Potts critical class. (c) The same as (b) but with logarithmic corrections according to [133].

tectable jump of the order parameter:

$$\begin{cases} \nu = 1/2 \\ \chi_{U/2} \propto M^2 \\ \Delta E \propto \Delta E_0 + \text{const} \cdot M^{-2} \end{cases} \tag{5.47}$$

- A second order phase transition of Potts universality class:

$$\begin{cases} \nu = 2/3 \\ \chi_{U/2} \propto M^{7/4} \\ \Delta E \propto M^{-1} \end{cases} \tag{5.48}$$

- A second order phase transition of Potts universality class and logarithmic corrections to scaling laws according to [133, 135].

5.5. Finite Temperature Calculations

In the following section we present results of our investigation of the phase transition at finite temperatures. We study the specific heat capacity

$$C(T,\lambda) = \frac{1}{T^2}\langle \Delta H^2(\lambda)\rangle_T, \tag{5.49}$$

which is a measure of heat transfer from the ground to higher states. Here $\langle \Delta H^2(\lambda)\rangle_T$ means the expectation value of the energy fluctuation evaluated for the thermal state with temperature T. We find that specific heat reflects the nature of the transition in both regimes $E = U$ and $E = U/2$. The complicated energy gap structure of the latter case is correctly reflected in plots of specific heat, where one can observe contributions from both phase transitions: the suppressed phase transition of the elementary excitation and the true phase transition of the coupled excitations.

Quantum systems with phase transitions of second order have a characteristic energy scale of fluctuations above the ground state that vanishes at the critical point. Due to finite size effects the actual size of the gap stays finite and inversely proportional to the system size. Near the critical point the system is especially sensitive to thermal fluctuations, a good measure of which is the specific heat capacity.

The simplest example of heat transfer is in a two level system and known as the Schottky anomaly — the heat capacity has a pronounced peak at a temperature when the higher energy level becomes available for thermal fluctuations. Further increase of the system temperature leads to equalizing of the occupation probabilities and decay of heat transfer. Then the temperature T_{peak} at which the heat capacity has the maximum value plays the role of the energy gap probe.

The situation is more complicated in multilevel systems; however, the leading contribution to the specific heat is still from the energy gap between the ground and first excited states. Hence, the position of T_{peak} as a function of the Hamiltonian parameter λ will reflect the energy gap size accordingly. In the case of second order phase transitions the curvature of the peak temperature line as a function of detuning from the critical point has the following leading term

$$T_{\mathrm{peak}} \propto |\lambda - \lambda_{\mathrm{crit}}|^{\alpha}, \tag{5.50}$$

where the critical exponent α depends on the universality class of the phase transition. In the case of first order phase transitions the energy gap does not

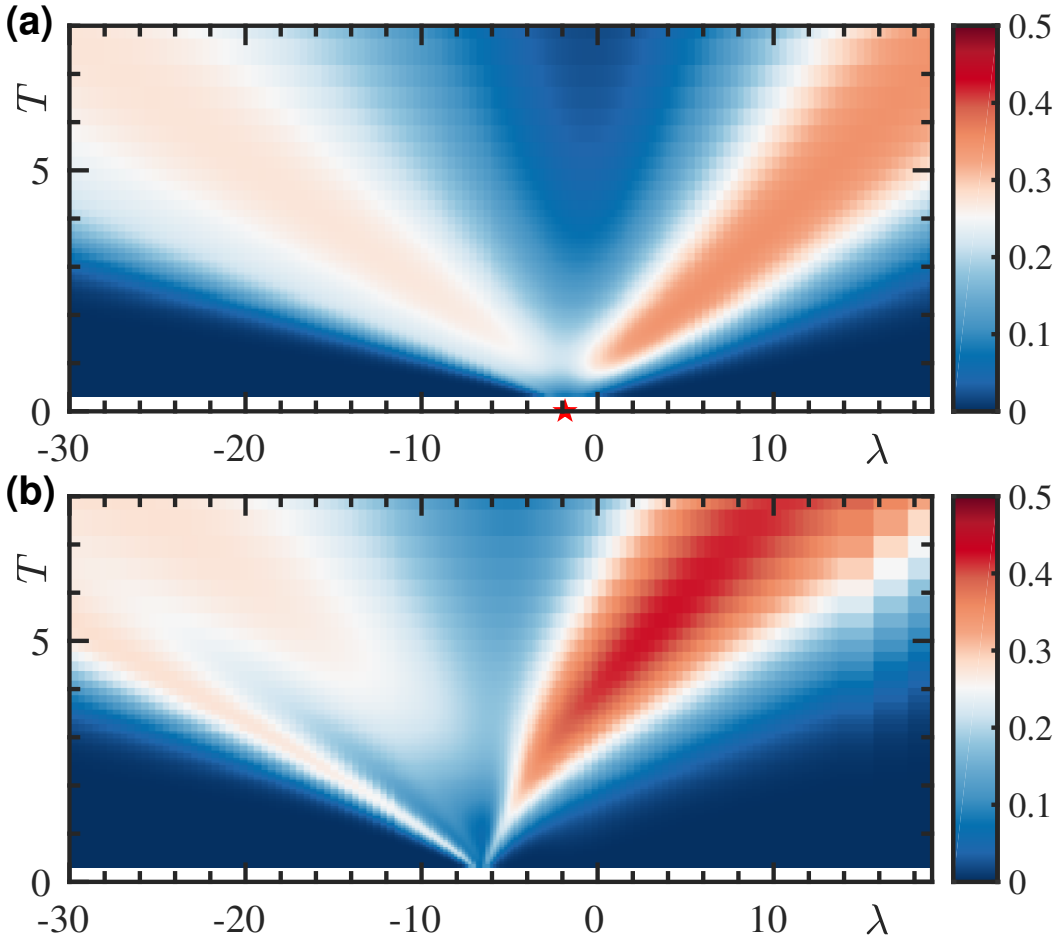

Figure 5.13.: Specific heat capacity per spin $c(T, \lambda) = C(T, \lambda)/M$ near the quantum critical points in the regimes (a) $E = U$ for $M = 101$ spins (b) $E = U/2$ for $M = 102$ spins, both with open boundary conditions. (a) The convergence of the specific heat peaks matches with the position of QCP at $T = 0$ (red star). (b) The complicated structure of the specific heat reflects the energy gap diagram in Fig. 5.10(a), where one can see the suppressed transition of elementary excitations and the transition of coupled excitations — the true quantum phase transition. There are two branches of specific heat peak diverging from *each* phase transition point. Presumably, two right branches merge together and cannot be distinguished, that is why one can observe only three branches. Two of those branches converge to the critical point of $E = U/2$ model. The third and fourth branches correspond to the transition of elementary excitations and vanish at finite temperatures as the corresponding transition is suppressed and the energy gap minimum stays finite. The results are obtained via TDVP evolution (see Sec. 4.3.3) of the infinite temperature density matrix with bond dimension $D = 128$.

close at the critical point in general, hence the above expression can not be always used.

In the regime $E = U$ (Fig. 5.13(a)) one observes that thermal fluctuations wash out the critical point position (denoted by the red star) in both directions almost evenly. The asymmetry about the critical point is expected as the phases on the two sides of the critical point have different symmetries. The important thing is the scaling of the peak temperature T_{peak} with the detuning from the resonance $\lambda - \lambda_{\text{crit}}$. The position of the specific heat peak is very close to the dependence expected for systems from the Ising universality class, i.e. the critical exponent is $\alpha = 1$.

In the regime $E = U/2$ the nature of the transition seems to be more complicated (Fig. 5.13(b)). The specific heat dependence changed on both sides of the transition, i.e., it is not as symmetric as in the case $E = U$. On the right hand side it now has a different curvature of the peak temperature $T_{\text{peak}}(\lambda)$. On the left hand side two peak temperatures can be distinguished.

This dependence of the specific heat can be explained with help of the energy gap diagram in Fig. 5.10(a), where one can see the suppressed transition of elementary excitations and the true transition of coupled excitations.

Each phase transition point has two branches of specific heat peaks diverging from it as the temperatures increases. We think that Fig. 5.13(b) has four branches in total, but one can observe only three of them because the two right branches merge together and cannot be distinguished. Two of those branches converge to the critical point of $E = U/2$ model. The third branch and the fourth one, which is hidden, correspond to the transition of elementary excitations and vanish at finite temperatures as the corresponding transition is suppressed and the energy gap minimum stays finite.

5.6. Quench Dynamics

In this section we simulate the dynamics of the system after a parameter quench. The initially prepared Mott insulator state in the superlattice geometry is allowed to evolve in time. The dynamics is captured via the effective Hamiltonian (5.14). The results of the quench dynamics in the spin system (Fig. 5.14) show a very good agreement with the experimental results in the regime $E = U/2$ [56] even though the geometry of the experiment does not have the superlattice. One can see that the spin model correctly reflects the experimentally detected resonance (Fig. 5.14(a)) near $\lambda = 0$. The peculiar part is that we can indeed see that the oscillations of magnetization are significantly suppressed at resonance (compare with Fig. 2 in [56]).

Moreover, the characteristic times of saturation, as well as the maximal density of doubly occupied sites (Fig. 5.14(b)) also show similar results to the experiment. It is important to note that the effective spin model was derived for the super lattice geometry, which was necessary to suppress certain transitions and hence

confine each bosons only between two resonant sites; the difference in dynamics can be seen in Fig. 5.3.

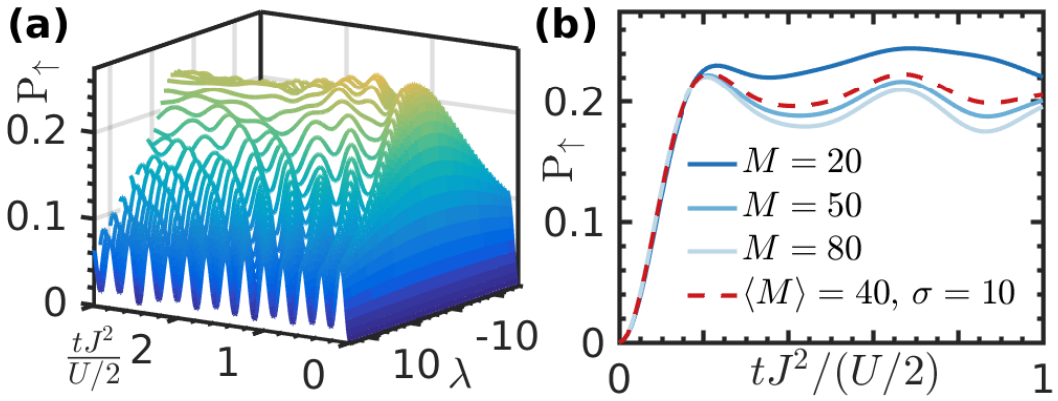

Figure 5.14.: Time-dependence of the averaged number of spin-ups $\mathrm{P}_\uparrow = \sum_r \langle \sigma_r^\uparrow \rangle / M$ after instantaneous quenches from the unit filled MI state in the regime $E = U/2$. The mapping between spins and bosons means that $P_\uparrow = N_\mathrm{d}$ — the average number of double occupancies. (a) A collection of quenches with different detuning λ for $M = 50$ spins. One can observe the emergence of the resonance near QCP as well as the suppression of fast oscillations. (b) Results of the time evolution at $\lambda = 0$ for a collection of different spin chains (solid lines) and for an ensemble of spin chains of the mean length $\langle M \rangle = 40$ and normal dispersion $\sigma_M = 10$ (dash line). Calculations were performed using TDVP method (see Sec. 4.3.3) with MPS of bond dimension $D = 96$.

We also consider the effects of spontaneous emission in order to make a quantitative comparison with the experiments, for instance [56]. We consider quenches (Fig. 5.15) from the unit filling state (in the spin representation: all spins down) to the tilt $\lambda = 0$, in the presence of the dissipation. Thus, the dynamics of the system is described by the master equation in Lindblad form (3.31). The jump operators represent the spontaneous emission and are equal to the local occupation operators, i.e. $L_r = n_r$, which in the spin representation equals

$$L_r = 1 + \sigma_{r-2}^\uparrow - \sigma_r^\uparrow, \tag{5.51}$$

i.e. one needs to take into account not only the number of particles tunneled from the site, but also the number of particles tunneled to the site. The jump operators at the boundaries of the chain are different as particles cannot tunnel outside of the lattice. The rate of quantum jumps γ corresponds to the spontaneous emission rate. In Fig. 5.15 we present the results of the simulation with the superlattice along with the measurement results from [56] without the superlattice. One can see qualitative agreement between times of saturation in the experiment and in the calculation as well as the average number of doublons. The presence of spontaneous emission also leads to the damping of oscillations. The good agreement that we achieve suggests an insignificant role for the ne-

glected transitions in the dynamic of the experiment without the superlattice. However, a more detailed comparison should be made once the experiment with the superlattice is realized.

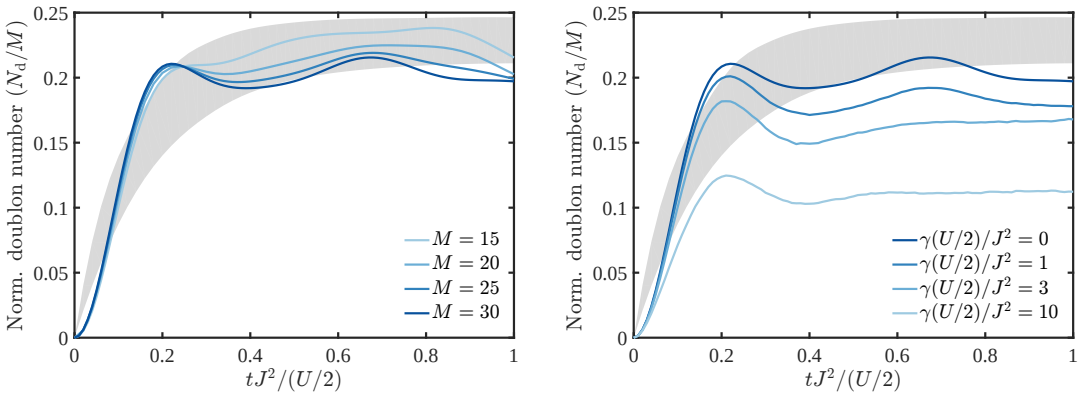

(a) (b)

Figure 5.15.: Number of doublons $N_d = P_\uparrow$ per site of the optical lattice of the length M, simulated via the effective spin model in the case of the superlattice. The results are presented (a) for a range of system sizes M and no dissipation $\gamma = 0$, (b) for $M = 30$ and a range of emission rates γ. The gray area corresponds to experimental measurements of N_d [56] without the superlattice.

5.7. Comments on Numerical Techniques

Our analysis of the critical behavior of the spin models heavily relies on the numerical calculations, as there are no exact analytical solutions. In order to obtain the system behavior in its pure form, i.e. without finite size or boundary effects one needs to perform calculations for comparatively large system sizes. In that case all methods using exact diagonalization (Chap. 3) become inpractical as they can be used only for a few tens of spins, which is often not enough.

Numerical calculations in this chapter were performed using a number of DMRG techniques (Chap. 4), which allowed us to go far beyond the ED by focusing only on the relevant parts of the Hilbert space. We made an extensive use of tensor networks (MPS/MPO) for dealing with spin chains up to ~200 spins.

5.7.1. Realization of Constraints via Projectors

The implementation of the constraint terms in (5.6) and (5.14) via putting W to a large positive number did not prove to be stable enough for DMRG calculations of

eigenstates. For this reason we implemented the constraints via MPO projectors of the following form

$$P_{U/n} = \prod_r (\mathcal{I} - \sigma_r^{\uparrow}\sigma_{r+n}^{\uparrow}), \tag{5.52}$$

which explicitly forbids states with spin-ups at distance n equal 1 or 2, for models in the regime $E = U$ and $E = U/2$, respectively. Then, instead of Hamiltonians $H_{U/n}$ we use

$$\tilde{H}_{U/n} = P_{U/n} H_{U/n} P_{U/n}, \tag{5.53}$$

where the weight terms (the ones with W) in the models were omitted. Furthermore, one can reduce the bond dimension of $\tilde{H}_{U/n}$ in MPO form by performing a procedure developed for compression of MPS (Sec. 2.2 in [136]) via variational minimization of the distance between states. For instance, in the case of open boundary conditions the original bond dimensions of $P_{U/2}$ and $H_{U/2}$ are 9 and 6, respectively, if they are constructed in a sparse way. The resulting bond dimension of $\tilde{H}_{U/n}$ is $9 \times 6 \times 9 = 486$, but it can be compressed down to just 8 with double machine precision.

Using this approach one obtains an MPO representation of restricted models (5.6) and (5.14), which can be used for all sorts of calculations in the restricted Hilbert space, both in statics and dynamics.

5.7.2. T-MPS Calculations

The approach we use involves the evolution of an initial infinite temperature density matrix to finite temperatures by means of the TDVP method [121]. In the Hilbert space without any restrictions the infinite-T density matrix is proportional to the identity, $\rho_0 \propto I$. However, in the presence of restrictions one must take into account only allowed states, so $\rho_0 \propto P_{U/n}\mathcal{I}P_{U/n} = P_{U/n}$, where $P_{U/n}$ is defined in (5.52).

The next step is to evolve the density matrix to finite temperatures, which can be done according to the following formula $\rho(\beta) \propto \mathrm{e}^{-\beta\tilde{H}/2}\rho_0\mathrm{e}^{-\beta\tilde{H}/2}$, here $\beta = 1/T$ and $\tilde{H}$ is the Hamiltonian (5.53) in the subspace of allowed states. In order to preserve positive semidefiniteness of the density matrix we used the purification technique [90, 93]. In this case only one side of the density matrix is evolved $\bar{\rho}(\beta) \equiv \mathrm{e}^{-\beta\tilde{H}/2}\rho_0$, and since $\rho_0^2 = \rho_0$ expectation values can be calculated as

$$\langle \hat{O} \rangle_\beta = \mathrm{tr}[\hat{O}\bar{\rho}(\beta)\bar{\rho}^\dagger(\beta)],$$

where $\hat{O}$ is an arbitrary operator in MPO form.

5.8. Conclusions

In this work we derived and investigated effective spin models for the unit filled Bose-Hubbard model with a tilt enabling resonant transitions between neighboring and next-neighboring sites. For the former a superlattice is required to constrain the motion of atoms and map the dynamics onto effective spins.

The first model (5.6) is derived for tilt values near $E = U$, i.e. bosons resonantly tunnel to neighboring sites. This model is equivalent to the antiferromagnetic Ising chain in skew field (AFISF) with infinite, projective-like interactions. In this regime tuning of the tilt near the resonance coincides with the tuning near a quantum critical point from the Ising universality class. It corresponds to $\mathcal{Z}_2$ symmetry breaking in the spin chain associated with the parity in the system. We believe this is the first time that this fact has been pointed out in this form for the AFISF model.

The second model (5.14) is derived for tilt values near $E = U/2$ and a superlattice geometry, i.e., bosons can resonantly tunnel only to next-neighboring sites. This spin chain is equivalent to a pair of spin chains in regime $E = U$ coupled together via XZ and ZZ interactions. Analogously to the first model, a quantum critical point is also located near the resonance of the tilt, but the nature of the phase transition is different.

We identify the corresponding full symmetry of the system in the ordered AFM state as the non-Abelian dihedral group $\mathcal{D}_4$. Although the finite size scaling shows different scaling laws with respect to the Ising universality class, we have not managed yet to identify with certainty which universality class this transition belongs to. However we have listed three possibilities that in our opinion are the most probable. Critical exponents are compatible with a weakly first-order transition (with an undetectable order parameter jump) or a second order transition of the Potts critical class. In the latter case one more option is possible, such that the scaling laws have logarithmic corrections according to [133].

Besides the symmetry analyses the difference between models can be pointed out from the effective models for extreme values of detuning λ. Without interaction terms the $E = U/2$ model will be equivalent to two independent $E = U$ chains with an independent spectrum of elementary excitations in each chain. However, the ZZ interactions couple these excitations lowering their mutual energy, the XZ interactions then modify the tunneling amplitudes of such coupled excitations. As a result of both ZZ and XZ terms the role of elementary excitations is suppressed by coupled excitations which have a different phase transition point. The original phase transition is observable on the spectrum of elementary excitations (Fig. 5.10(a)).

The results here can be easily extended to the case of not only unit filling, but any uniform integer filling. Then the main difference in spin models will be due to the Bose enhancement factor of tunneling and number of two body on-site

interactions. Also the superlattice offset μ is a free parameter of the model and hence can be exploited. In the generic case of $\mu \lesssim U$ matrix elements for even and odd spins of $E = U/2$ model will be different and depend on μ. Then (5.14) will be obtained in the limit $\mu/U \to 0$. The study of $\mu-$dependence has potential interest as it can allow us to continuously modify the phase transition.

Part IV.

Trapped Ions With Long-Range Interactions

6. Global Quench Dynamics with Long-Range Interactions

In this chapter[1] we will focus on investigating the global quench dynamics for two 1D systems. The exceptional feature of both these systems is that the interactions have a power-law dependence of $1/d^{\alpha}$, with distance d and decay exponent α which can be varied in a wide range. The first model is a long-range transverse field Ising model, which has been realized in chains of trapped ions (see Sec. 2.4), and does not have known analytical solutions in the general case. The second model is a lattice model for spinless fermions with long-range tunneling. The Hamiltonian of this model is diagonalizable.

The idea behind looking at both systems together is to gain more understanding of the spread of correlations and growth of entanglement in the spin system via comparison with analytical solutions of the fermionic system. The spatial entanglement plays an important role for numeral methods based on DMRG methods (see Chap. 4), which we use for the spin system.

We find that for large enough α the correlations in both systems can spread in a light cone and the spatial entanglement grows linearly as a function of time. In the case of long-range interactions (small α) there is no light cone effect and instead correlations spread immediately in both systems.

Moreover, for certain configurations of quench parameters it is also possible to achieve a sublinear growth of entanglement, instead of the usual linear regime. This is a very intriguing result, as it allows us to perform DMRG calculations of quench dynamics for longer times, because of the slower growth of tensor sizes in the MPS representation of quantum states (see Chap. 4 for an introduction to this representation).

[1] This work is taken in part from the publication *Entanglement growth and correlation spreading with variable-range interactions in spin and fermionic tunneling models*, A. S. Buyskikh, M. Fagotti, J. Schachenmayer, F. Essler, and A. J. Daley, Phys. Rev. A **93**, 053620 (2016). The author of this thesis performed all of the analytical and numerical calculations for the spin model, analytical derivations for the fermionic model, wrote most of the article, and produced all of the plots.

6.1. Introduction and Overview

Recently, a large number of quantum spin models with interactions that decay algebraically in distance were realized experimentally. Among the most significant are experiments with trapped ions [2, 66–68, 73, 137], ultracold polar molecules [138, 139], and Rydberg atoms [140–142]. In particular, experiments with ions in Paul and Penning traps, trapping ions in 1D or 2D respectively, give us a possibility to design spin models with variable range interactions by tuning interactions between internal spin states via phonon modes in the ion crystal [105, 143]. A high level of parameter control in these experiments allows us to realize time-dependent dynamics in largely closed quantum systems [68, 103, 104, 144–146].

This opens the question of whether long-range interactions in quantum systems have an important effect on properties of the system and quench dynamics in particular. For instance, it is well known that in systems with local interactions (meaning the range of the interaction is independent of the system size) or interactions exponentially decaying with distance, the spreading of correlations is limited by the Lieb-Robinson bound [74]. It raises the same question of the fundamental bound of interactions in the presence of algebraically decaying interactions. Even though progress has been achieved, allowing gradual improvement of the bound [147–154], it is particularly informative to identify exactly solvable models that reproduce and explain the qualitative behavior of the physical systems being studied. There are a few models with long-range interactions for which the transitions in behavior are well understood, for instance longitudinal Ising models [155] and tunneling bosons [156, 157].

In this chapter we present our work on the comparative study of correlation spreading and entanglement growth after global parameter quenches in the long-range transverse field Ising model for spins and the long-range fermion hopping model. The model for spins [105, 143] was recently realized in a series of experiments [66, 73, 103, 104], and does not have a general analytical solution. The model for fermions is the generalized Kitaev chain [158] with long-range tunneling which is exactly solvable. For the spin model we are able to compute the dynamics numerically in some cases by using Matrix Product State and Operator (MPS and MPO) techniques [80, 91, 136, 159, 160] (see Chap. 4). In addition to that we also make use of the Holstein-Primakoff approximation to gain further insight into dynamics of spins, which at short times gives particularly good agreement with the exact evolution.

Previous studies of the long-range transverse field Ising model [104, 145] showed that we can classify the behavior of correlation spreading into different regimes as a function of the decay exponent α of power-law interactions, which decay as $1/d^\alpha$, where d is the distance between interacting spins. The dynamics can be divided into three distinct regimes: short-range interactions where $\alpha > 2$, mid-range interactions where $1 < \alpha < 2$, and long-range interactions where

$\alpha < 1$. Light-cone-like behavior can be identified quite strongly in the short-range regime, becomes somehow vague in the mid-range regime, and completely disappears when interactions become long-range.

Regarding the entanglement growth after the quench, the dynamics in general show linear growth as a function of time, which resembles the result for systems with local interactions. However, the sublinear growth of the entanglement in time can be obtained for long-range interactions for particular classes of initial states. We characterize this change in entanglement growth based on the contribution of quasiparticles near $k = 0$, where the group velocity and dispersion relation diverge for long-range interactions. These excitations do not provide a lot of entanglement, as they are responsible only for the collective evolution of all parts of the system (either spins or fermions). At short times, we similarly see a suppression of correlation growth at long distances with long-range interactions. It should also be noted that similar comparative works on entanglement growth and correlation-spreading have been published recently [161,162] and further suggest our conclusions.

In Sec. 6.2 we first discuss the long-range transverse field Ising and fermionic hopping models, giving details of the methods we use to solve these. In Sec. 6.3, we discuss the spread of correlations for each of the models after a global quantum quench and discuss for each model the different regimes of short, middle, and long-range interactions. In Sec. 6.4 we discuss the growth of entanglement in both models and then conclude in Sec. 6.5.

6.2. Models with Long-Range Interactions

We start by defining the models of interest. The first one is the long-range transverse field Ising model, and the second is an exactly solvable long-range hopping model for spinless fermions (Fig. 6.1).

6.2.1. Long-Range Transverse Field Ising (LRTI) Model

Let us first introduce the long-range transverse field Ising model of M spins-$1/2$ confined in a linear trap ($\hbar \equiv 1$). The Hamiltonian reads

$$H_{\mathrm{LRTI}} = \sum_{l>j}^{M} J_{lj} \sigma_l^x \sigma_j^x + B \sum_{l=1}^{M} \sigma_l^z, \tag{6.1}$$

where

$$J_{lj} = \frac{J}{|l-j|^{\alpha}}, \tag{6.2}$$

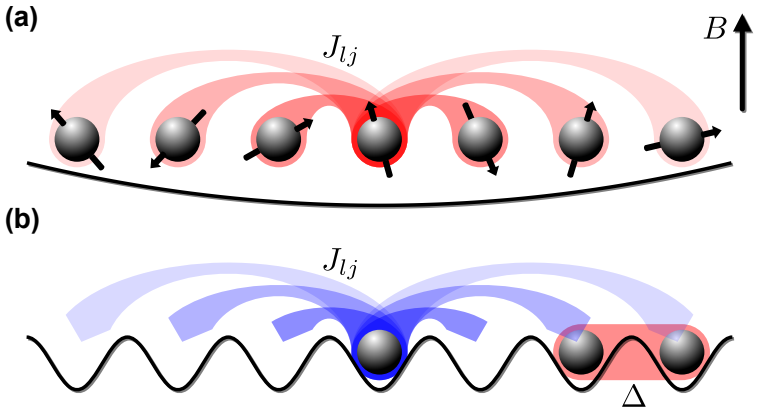

Figure 6.1.: Illustration of (a) the long-range transverse field Ising (LRTI) and (b) long-range fermionic hopping (LRFH) models. LRTI has been experimentally realized with ions in linear traps. Individual spins are encoded on a couple of hyperfine levels of each ion, then phonon modes mediate their long-range interactions J_{lj}, and an effective field B can be applied in the transverse direction. LRFH is a theoretical model for fermions tunnelling between distant sites in a 1D lattice with amplitudes J_{lj}; pairing on neighboring sites is induced with strength Δ.

is the spin-spin interaction matrix, B is the transverse field, and $\sigma_l^{x,z}$ denote local Pauli matrices operating on each spin. This Hamiltonian has been experimentally realized with 1D chains of trapped ions [105] as discussed Sec. 2.4.1. The dynamics of the spin system is mapped to the dynamics of long-lived internal states (denoted $|\uparrow\rangle_l$ and $|\downarrow\rangle_l$ for spin l) of ions. The long-range interactions are generated by coupling spin degrees of freedom through the collective motional degrees of freedom in the crystal. The exponent of the algebraic decay α of interactions then can be tuned in a wide range between 0 and 3. By shifting the internal levels of individual ions an effective magnetic field B_l can be realized, and here we focus on a transverse uniform field.

We will be primarily investigating global quench dynamics, where all spins are initially prepared in a single state, for instance $|\downarrow\rangle_l$, and then the Hamiltonian (6.1) is turned on so the system is allowed to evolve in time. This corresponds to a global quench from $B = \infty$, with the ground state $|\psi(t = 0)\rangle = \otimes_l |\downarrow\rangle_l$, to some finite value of the field.

The model (6.1) does not have a known analytical solution in the presence of long-range interactions, but we approach the problem numerically. For instance, one can tackle this problem using exact diagonalization methods for chain lengths up to almost $M \sim 30$ spins using numerical methods described in Chap. 3. However, if one wants to look at the behavior of larger systems (up to several hundred spins), one has to use techniques on the reduced Hilbert space (see Chap. 4). For these calculations, the convergence in the MPS bond dimension D and time step Δt was tested to ensure accuracy of the calculations. The main limitation of this

method is the growth of entanglement after the quench, which leads to an increase of the computational cost. We can also qualitatively describe the short-time dynamics using a mean field approach — the Holstein-Primakoff approximation (see Sec. 6.3.4).

6.2.2. Long-Range Fermionic Hopping (LRFH) Model

The second model is a 1D lattice with loaded spinless fermions that have long-range hopping

$$H_{\mathrm{LRFH}} = \sum_{l\neq j=1}^{M} \bar{J}_{lj} c_l^\dagger c_j + \Delta \sum_l \left(c_l^\dagger c_{l+1}^\dagger + \mathrm{h.c.} \right), \tag{6.3}$$

where c_l is a fermionic annihilation operator on site l, and

$$\bar{J}_{lj} = \frac{J}{\left| \frac{M}{\pi} \sin\left[\frac{\pi(l-j)}{M} \right] \right|^\alpha} \tag{6.4}$$

is the hopping matrix with long-range couplings analogous to those in the spin model (6.2), but for the case of periodic boundary conditions. Periodicity is chosen to simplify the analytical results, but for numerical calculations we will follow the case of the spin model, and choose open boundary conditions with $\bar{J}_{lj} = J_{lj}$. Here, for each variable derived for the open boundary conditions, there will be an analog for the periodic boundary conditions marked with the bar over the top. We checked that the behavior in each case agrees well in the limit of large system sizes where boundary effects become insignificant. The interactions between fermions are characterized by Δ, which allows the creation or annihilation of pairs of fermions on neighboring sites. The model (6.3) is a generalized Kitaev chain model [158] with long-range hopping, and its properties have been extensively studied as well [162].

Analogously to the spin model, we will consider quantum quenches, typically starting from the ground state for large values of Δ, and quenching to smaller values of Δ. The Hamiltonian (6.3) can be diagonalized via Bogoliubov transformations, analogously to the recent results in [162]. In the case of periodic boundary conditions, the Hamiltonian in momentum space reads

$$H_{\mathrm{LRFH}} = \sum_{k=0}^{M/2-1} \begin{pmatrix} c_k^\dagger & c_{M-1-k} \end{pmatrix} \begin{pmatrix} \bar{\mathcal{J}}(k) & 2i\Delta \sin\left(\frac{2\pi k}{M}\right) \\ -2i\Delta \sin\left(\frac{2\pi k}{M}\right) & -\bar{\mathcal{J}}(k) \end{pmatrix} \begin{pmatrix} c_k \\ c_{M-1-k}^\dagger \end{pmatrix}, \tag{6.5}$$

where

$$c_k = \frac{1}{\sqrt{M}} \sum_{r=1}^{M} \mathrm{e}^{-i\frac{2\pi k r}{M}} c_r, \tag{6.6}$$

is a fermionic annihilation operator for momentum k, and

$$\bar{\mathcal{J}}(k) = 2\sum_{d=1}^{M-1} \bar{J}_{l,l+d}\cos\left(2\pi kd/M\right), \tag{6.7}$$

is the spectral decomposition of the hopping matrix.

Note that in the case of open boundary conditions one can obtain an analytical expression as well, but only via special functions. The analogous spectral decomposition (for $M \to \infty$) then will read

$$\mathcal{J}(k) = J\sum_{\substack{d=-\infty \\ d\neq 0}}^{\infty} \frac{e^{-idk}}{|d|^{\alpha}} = J\Big[\mathrm{Li}_{\alpha}(e^{ik}) + \mathrm{Li}_{\alpha}(e^{-ik})\Big] = 2J\mathrm{Re}[\mathrm{Li}_{\alpha}(e^{ik})] \tag{6.8}$$

where $\mathrm{Li}_n(z)$ is the polylogarithm of order n and argument z.

The Bogoliubov transformation for fermions reads

$$\begin{pmatrix} \alpha_k \\ \alpha^{\dagger}_{M-1-k} \\ \alpha^{\dagger}_k \\ \alpha_{M-1-k} \end{pmatrix} = \begin{pmatrix} u & v & 0 & 0 \\ -v^* & u^* & 0 & 0 \\ 0 & 0 & u^* & v^* \\ 0 & 0 & -v & u \end{pmatrix} \begin{pmatrix} c_k \\ c^{\dagger}_{M-1-k} \\ c^{\dagger}_k \\ c_{M-1-k} \end{pmatrix},$$

where $u = \cos(\theta_k/2)$, $v = i\sin(\theta_k/2)$ in order to obey the constraint

$$|u|^2 + |v|^2 = 1. \tag{6.9}$$

The Hamiltonian then can be diagonalized by choosing the Bogoliubov angle θ_k to satisfy

$$\mathrm{e}^{i\theta_k} = \frac{\bar{\mathcal{J}}(k) + 2i\Delta\sin\left(\frac{2\pi k}{M}\right)}{\sqrt{\bar{\mathcal{J}}^2(k) + 4\Delta^2\sin^2\left(\frac{2\pi k}{M}\right)}}, \tag{6.10}$$

which leads to the dispersion relation of the Bogoliubov particles as

$$E(k) = \pm\sqrt{\bar{\mathcal{J}}^2(k) + 4\Delta^2\sin^2\left(2\pi k/M\right)} \equiv \pm\epsilon(k). \tag{6.11}$$

Then we can derive the same expressions, but for the pre-quench Hamiltonian, which has another value Δ_0 instead of Δ. The pre-quench Bogoliubov particles and angle will be denoted as α^0_k and θ^0_k respectively. Then the dependence on time for the original fermionic operators takes the form

$$\begin{pmatrix} c_k(t) \\ c^{\dagger}_{M-1-k}(t) \end{pmatrix} = \begin{pmatrix} \cos(\theta_k/2) & -i\sin(\theta_k/2) \\ -i\sin(\theta_k/2) & \cos(\theta_k/2) \end{pmatrix} \begin{pmatrix} \mathrm{e}^{-i\epsilon(k)t} & 0 \\ 0 & \mathrm{e}^{i\epsilon(k)t} \end{pmatrix} \begin{pmatrix} \alpha_k \\ \alpha^{\dagger}_{M-1-k} \end{pmatrix}. \tag{6.12}$$

By starting from the vacuum state of the pre-quench Hamiltonian ($\alpha_k^0|\phi_0\rangle = 0$), one can obtain the dependence of the correlation matrix on time

$$\langle c_l^\dagger(t)c_j(t)\rangle = \sum_{k=0}^{M-1} \frac{\mathrm{e}^{-i\frac{2\pi k(l-j)}{M}}}{2M} \left[1 - \cos\theta_k \cos\delta\theta_k + \sin\theta_k \sin\delta\theta_k \cos\left(2\epsilon(k)t\right)\right], \tag{6.13}$$

where the difference of the Bogoliubov angles before and after the quench reads

$$\delta\theta_k = \theta_k - \theta_k^0. \tag{6.14}$$

Let us now look at the spreading of correlations and the growth of entanglement in both the LRTI and LRFH models.

6.3. Spreading of Correlations in Time

In this section we discuss the spread of correlations after a global quench. For this we look at the absolute value of the characteristic two-site correlation functions averaged over the system. One should be careful when choosing the correlation function for investigation, as some of them have trivial dependence on time. For the LRTI system, we choose

$$\tilde{C}_d(t) = \left\langle \left| \left\langle \sigma_l^+(t)\sigma_{l+d}^-(t) \right\rangle \right| \right\rangle_l \tag{6.15}$$

and for the LRFH model,

$$C_d(t) = \left\langle \left| \left\langle c_l^\dagger(t)c_{l+d}(t) \right\rangle \right| \right\rangle_l . \tag{6.16}$$

Here, $\langle \ldots \rangle_l$ indicates the average in space over sites l. Note that in the case of periodic boundary conditions one averages over all M pairs, whereas in the case of open boundary conditions averaging is done over $M - d$ pairs.

It is known [74] that in quantum systems with finite-range interactions (or interactions exponentially decaying with distance) the information spreads with a finite group velocity, which is limited by the Lieb-Robinson bound (see Fig. 6.2). For instance, such light-cone dynamics was observed even in experiments with the quantum gas microscope [163] and bosonic species of atoms. Note that the spread of the information outside of the light cone is exponentially suppressed, i.e. at any fixed time the correlations decay exponentially with distance if one measures them outside of the light cone. The dynamics of correlations inside of the light cone is determined by the Hamiltonian parameters as well as the quench.

In this work we are working with Hamiltonians that do not have local interactions, instead they decay only algebraically with distance. We are going to present here

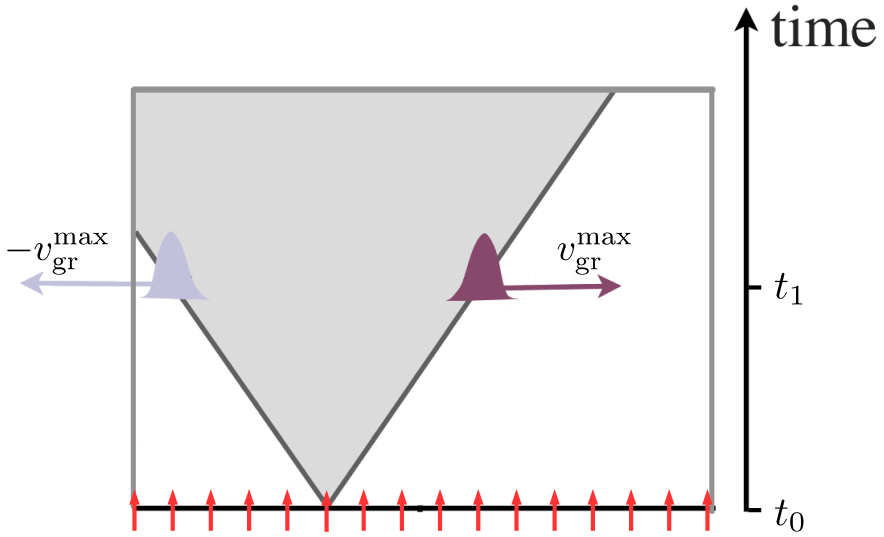

Figure 6.2.: An illustrative example explaining the meaning of the Lieb-Robinson bound [74]. The initial system of uncorrelated spins at time t_0 is allowed to evolve under a Hamiltonian H to a time t_1. If H has only local or exponentially decaying in distance interactions between spins, then there exists a maximum group velocity of excitations, v_{max}. Then any two-point correlation function calculated at time t_1 will be suppressed by a factor of $\mathrm{e}^{-\mu[d-2v_{\mathrm{gr}}^{\mathrm{max}}(t_1-t_0)]}$ if the separation between spins $d > 2v_{\mathrm{gr}}^{\mathrm{max}}(t_1-t_0)$. The exponent of decay $\mu > 0$ depends on the system parameters, in general. The spread of excitations from any given point will be bounded by a light cone with a well defined speed.

our investigation of the light cone properties as the function of the interaction range.

6.3.1. Comparison of the LRTI and LRFH Models

We found that in general one can distinguish three relatively different regimes of the correlation spread after a quantum quench in each model. In Fig. 6.3, we show some examples of the LRTI (left column of subfigures) and LRFH models (right column of subfigures). The first regime of short-range interactions occurs when $\alpha > 2$ (Fig. 6.3(a,d)), the second regime of mid-range interactions happens for $1 < \alpha < 2$ (Fig. 6.3(b,e)), and the third one — long-range interactions — when $\alpha < 1$ (Fig. 6.3(c,f)). The crucial difference between these regimes is the shape of the light cone, and the sharpness of its border.

- In the regime of short-range interactions, $\alpha > 2$, one can see effects resembling a linear light cone. By this we mean that the border of the light cone is almost independent of the level of the threshold (see Fig. 6.3(a,d) for detail). One can see a strongly defined edge and correlations outside of the

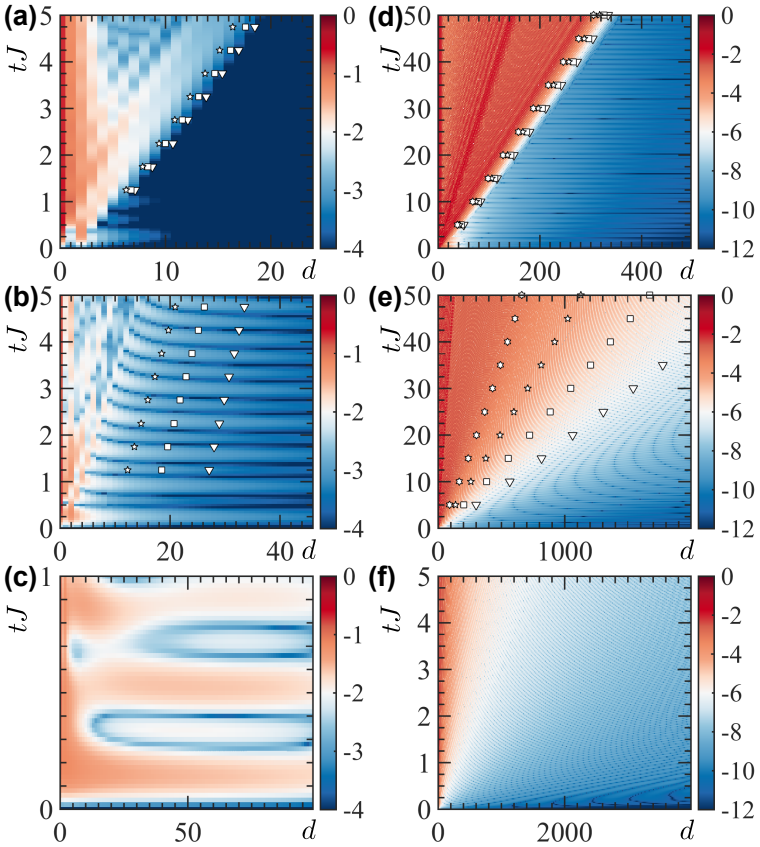

Figure 6.3.: Correlation spreading after global quenches in long-range spin and fermionic models, respectively. (a-c) $\log_{10}|\tilde{C}_d(t)|$ for the LRTI model after the global quench $B/J = \infty \to 1$ is applied. These results are obtained using TDVP approach with MPOs for chains of $M = 100$ spins (converged with MPS bond dimension $D = 256$). (d-f) $\log_{10}|C_d(t)|$ for the LRFH model after the global quench $\Delta/J = 10 \to 1$ is applied. These results are obtained using exact numerical computations for $M = 10^4$ sites. (a,d) $\alpha = 3$, short-range interactions with a strongly suppressed leakage of correlations outside of the light cone $d/t > v_{\mathrm{gr}}^{\mathrm{max}}$ are observed for both models. Markers indicate contour lines at levels $\log_{10}|\tilde{C}_d(t)| = [-4, -3\frac{1}{2}, -3]$ for the LRTI model and $\log_{10}|C_d(t)| = [-6, -5, -4, -3]$ for the LRFH model. (b,e) $\alpha = 3/2$, intermediate-range interactions: the light cone is not sharply defined, but a light-cone effect is observed. Markers indicate averaged contour lines at levels $\log_{10}|\tilde{C}_d(t)| = [-3\frac{1}{4}, -3, -2\frac{3}{4}]$ for the LRTI model and $\log_{10}|C_d(t)| = [-6, -5, -4, -3]$ for LRFH. (c,f) $\alpha = 1/2$, no light cone, instant spread of correlations through the entire system. The suppression of correlations at large distances in (f) is discussed in Sec. 6.3.3.

light cone decay algebraically with distance (as opposed to the exponential decay for local interactions).

- In the mid-range regime, $1 < \alpha < 2$, the edge of the light cone is not so

clear any more, i.e. depending on the threshold values the border is defined differently, as can be seen in Fig. 6.3(b,e). This difference of the quench dynamics between the two models will be discussed later. In the case of the fermionic model we find that the maximum group velocity diverges when $\alpha < 2$, which will be discussed in Sec. 6.3.3 below. This regime is intermediate, with features of both the long- and short-range regimes.

- In the long-range regime, $\alpha < 1$, the light cone effects disappear. The correlations grow over the entire system right after the quench and no light cone can be properly defined. Note the different scales on the time axis in Fig. 6.3(c,f). Again, one can note differences between spin and fermion models: in the case of Fig. 6.3(f) correlations still seem to be suppressed with distance, contrary to Fig. 6.3(c). We will discuss this suppression in more detail in Sec. 6.3.3 below.

The difference between the regimes can be seen more clearly if we take a look at the dependence of the correlation functions at fixed times. In Fig. 6.4, we plot the correlation function $\log_{10}|C_d(t)|$ as a function of separation distance for several fixed times tJ. In the case of short-range interactions, $\alpha > 2$, one can clearly see that the connection region between the fast decaying correlation wave and slowly decaying tail occurs over very short distances. It is opposite to the case of the mid-range regime, $1 < \alpha < 2$, which leads to a very clearly defined light cone. We also note that for both these regimes ($\alpha > 1$) the correlations decay algebraically outside the light cone, as opposed to the exponential decay that would be expected for initially uncorrelated states in models with finite-range or exponentially decaying interactions [74].

We should note that similar studies of the LRTI model show qualitatively similar behavior of the system [144]. Also studies of local quenches in this model identify the same regimes of the dynamics. For instance in [145] it was studied how a single spin perturbation propagates in the spin chain.

The behavior of the LRTI model cannot be analyzed as easily as the LRFH model. In order to better delineate these boundaries, one would need to carry out these calculations for longer times and larger system sizes. Nonetheless, we find in our investigation that for given system size there are quite abrupt changes in the behavior of the LRTI model at $\alpha = 1$ and $\alpha = 2$ for system sizes of the order of $M \sim 100$ spins. This agrees well with findings in other papers, e.g. [156]. At this point we turn to the LRFH model, for which we will discuss analytical results and find an explanation for the behavior for $\alpha > 1$ and $\alpha < 1$ respectively in the next two sections. An analogy with spins will be drawn then.

6.3.2. Dynamics with Short-Range Interactions $\alpha > 2$

In this section we will discuss the regime $\alpha > 2$, in which the boundary of the light cone is defined clearly (Fig. 6.4). We will use analytical solutions for the LRFH

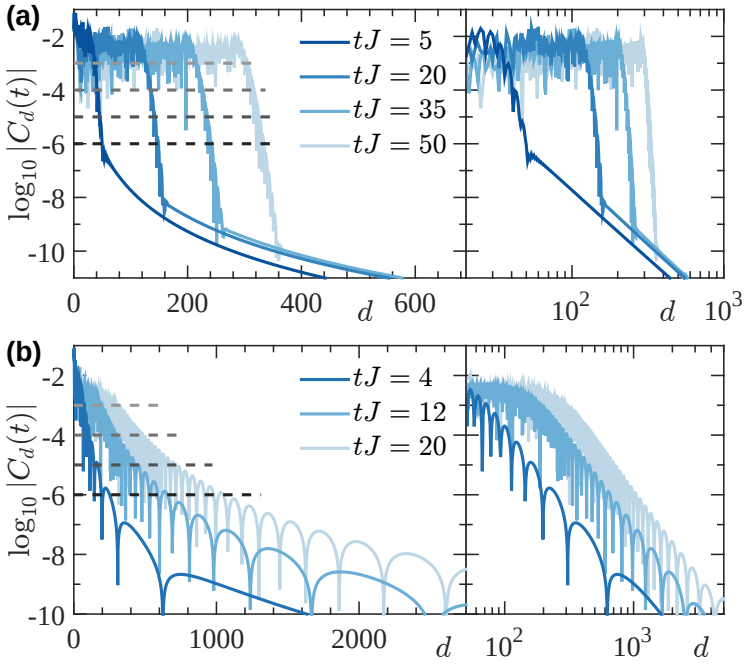

Figure 6.4.: Correlation functions at fixed time for the LRFH model show clear distinction between the regimes. We plot the two-site correlation function $\log_{10}|C_d(t)|$ after global quenches $\Delta/J = 10 \to 1$ in the LRFH model with $M = 10^4$ sites at different times tJ: (a) short-range interactions, $\alpha = 3$; (b) mid-range interactions, $\alpha = 3/2$. Dashed lines indicate different threshold levels $\delta = [-6, -5, -4, -3]$ that the correlation function reaches, see the markers in Fig. 6.3(d,e). Analogous markers for the LRTI model are in Fig. 6.3(a,b). In each case here, on the right hand side, we reproduce the same plots on a double logarithmic scale, showing algebraic decay of correlations outside the light cone as $d \to \infty$ in both cases.

model to explain this via analysis of the density of states in velocity and group velocity. In particular we will see that in order to have such sharp light cone effects one needs to excite a large portion of excitations with the maximum group velocity; in that case the wavefront will propagate without significant dispersion. In Fig. 6.4 we present snapshots of the dynamics at different times tJ, so the reader can see the difference between the sharp and smooth light cone boundary.

In order to approach this problem analytically, we analyze the analytical expression for the dispersion relation $\epsilon(k)$ for the LRFH model; in particular, we want to see the general difference between the regime $\alpha > 2$ and $\alpha < 2$. In Fig. 6.5 one can see a general behavior of the dispersion relation $\epsilon(k)$ as well as the group velocity $v_{\mathrm{gr}}(k)$. We see that for $\alpha > 2$ the dispersion, as well as the group velocity, are always bounded, i.e.

$$v_{\mathrm{gr}}^{\max} = \max_k \epsilon'(k) < \infty. \tag{6.17}$$

From the time-dependent part of the Green's function (6.13) in the thermodynamic limit we obtain

$$F(d,t) = \frac{1}{2}\int_{-\pi}^{\pi} \frac{\mathrm{d}k}{2\pi} \mathrm{e}^{-ikd} \sin\theta_k \sin\delta\theta_k \cos\left(2\epsilon(k)t\right). \tag{6.18}$$

The next step is to consider the "space-time scaling limit" [164] of $d, t \to \infty$, with $u = d/t$ fixed, i.e., one chooses the direction on the space-time reference frame and studies the behavior of the function at the infinite distance from the center of the axis. The idea behind this scaling is to look at the behavior of the function at long distances without perturbations caused by the finite size of the source, in analogy to studying scattering by analyzing the scattering properties only at long distances.

The resulting integral is, in general, exponentially small, unless u is such that there is at least one saddle point. Saddle points exist only if

$$2\epsilon'\left(k_j^*\right) + u = 0, \tag{6.19}$$

has a solution, which is possible if u is smaller than twice the maximum group velocity. In this case one uses the stationary phase approximation near each saddle point. After this Eq. (6.18) can take two possible forms

$$F(d,t) \approx \begin{cases} \mathcal{O}(1/d^{\alpha+2}), & u > v_{\mathrm{gr}}^{\max}, \\ \sum_j A_j \cos(B_j), & u < v_{\mathrm{gr}}^{\max}, \end{cases} \tag{6.20}$$

where $A_j = \left(16\pi\epsilon''\left(k_j^*\right)t\right)^{-1/2} \sin\theta_{k_j^*} \sin\delta\theta_{k_j^*}$, $B_j = \pi/4 + t\left(k_j^* u + 2\epsilon\left(k_j^*\right)\right)$, and k_j^* are the solutions of the saddle point equation (6.19).

In the case of low speed, $u < v_{\mathrm{gr}}^{\max}$, we are inside of the light cone. There are saddle points that give the major contribution to the integral (6.18). Whereas the analysis of the correlations is a study on its own, we skip it here as we are interested in the formation of the light cone. The interesting thing though is that the correlations inside of the light cone decay slowly in time, $\mathcal{O}(t^{-1/2})$, which corresponds to Fick's law of diffusion from classical physics. We find that both approximations agree well with full numerical solutions up to finite size corrections.

On the other hand outside of the light cone, $u > v_{\mathrm{gr}}^{\max}$, the usual argument for the exponential decay of the integral due to the lack of stationary points does not work here as the integrand is non-analytic at $k = 0$. In this case, using 2π-periodicity of the integrand, its non-analytic part was extracted. The contribution of this part decays only algebraically distance d and prevails over the exponentially small contribution of the remaining analytical part. Thus, we obtain the power law exponent of the correlation decay outside of the light cone (see (6.20)). This result is also as expected, as we are working with a system with only algebraically decaying interactions.

Now, let us discuss why the light cone effect is strong only when $\alpha > 2$. To understand this we consider both the dispersion relation and the density of states in velocity as a function of the wave vector (Fig. 6.5),

$$D\left(k\right) = \frac{M}{\pi}\left|\frac{\mathrm{d}v_{\mathrm{gr}}(k)}{\mathrm{d}k}\right|^{-1} = \frac{M}{\pi}\left|\frac{\mathrm{d}^2\epsilon(k)}{\mathrm{d}k^2}\right|^{-1}. \tag{6.21}$$

In the case of $\alpha > 2$, the density of states in velocity diverges exactly at the value of $v_{\mathrm{gr}} = v_{\mathrm{gr}}^{\mathrm{max}}$, which means that a great number of excitations (for finite systems) with the maximum group velocity can be created in the system. This, of course, depends on the type of quench, i.e. quench parameters. If the quench creates a significant number of excitations propagating with the maximum group velocity, then a strong light cone effect will be observed, meaning the light cone boundaries will not experience significant dispersion over time. And as one can see in Fig. 6.5(b) the maximum group velocity is finite in this regime, $v_{\mathrm{gr}}^{\mathrm{max}} < \infty$, i.e. the light cone nature is preserved.

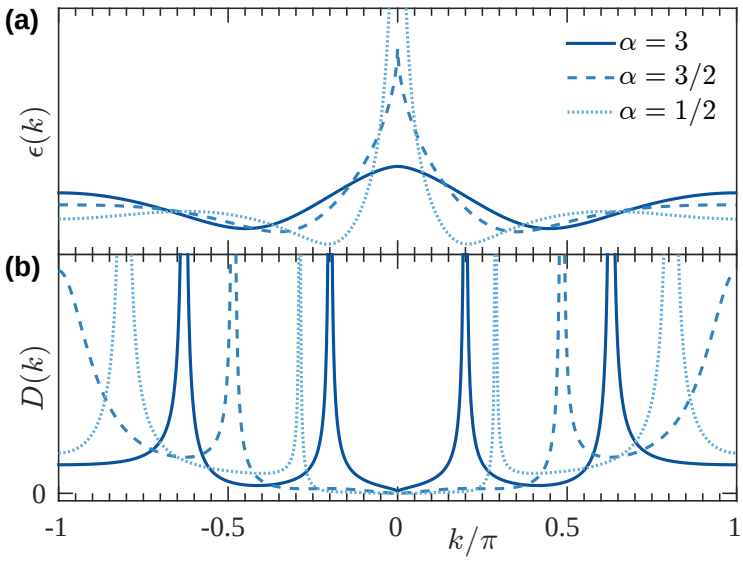

Figure 6.5.: Characteristic examples of (a) the dispersion relation $\epsilon(k)$ and (b) density of states in velocity $D(k)$ for the LRFH model for $\Delta = J$ in various interaction ranges: (i) $\alpha > 2$, (ii) $1 < \alpha < 2$, and (iii) $\alpha < 1$. In the case of short-range interactions ($\alpha > 2$) one can see the smooth behavior of $\epsilon(k)$ leading to a finite maximum group velocity $v_{\mathrm{gr}}^{\mathrm{max}} = \epsilon'(k^*)$. The corresponding density of states in velocity $D(k^*)$ diverges, which justifies the strong light cone effect. In the case $\alpha < 2$, $v_{\mathrm{gr}} \propto k^{\alpha-2}$ for $k \to 0$, but the density of states in velocity is suppressed, $D(k) \propto k^{3-\alpha}$. As a result there is no domination of infinite velocity excitations and the light cone broadens. In the case $\alpha < 1$, the quasiexcitation spectrum become unbounded as well.

6.3.3. Dynamics with Intermediate and Long-Range Interactions ($\alpha < 2$) in the LRFH Model

In this section we will discuss the effect of the infinite maximum group velocity that becomes possible for $\alpha < 2$. First, in the regime $1 < \alpha < 2$ a kink appears at $k = 0$ in the dispersion relation, so

$$\epsilon(k) \propto \epsilon_0 + ck^{\alpha-1}. \tag{6.22}$$

In this regime the dispersion is still bounded, but the velocity already diverges. If we increase the range of the interactions even more, i.e. in the case of $\alpha < 1$ even the dispersion relation diverges for small momenta k

$$\epsilon(k) \propto k^{\alpha-1}, \;\; k \to 0. \tag{6.23}$$

In other words, for $\alpha < 2$ there is no longer a finite maximum group velocity and for $\alpha < 1$ the spectrum of quasi-excitations becomes unbounded. Note that the same results can be obtained for both periodic (6.7) and open (6.8) boundary conditions. As a result the light cone boundary becomes washed out for these regimes.

However, the density of states in velocity around $k = 0$ is suppressed,

$$D(k) \propto k^{3-\alpha}, \;\; \text{for } \alpha < 2. \tag{6.24}$$

Together with the scaling of the group velocity we obtain that the correlations can build up instantly through the entire system but they grow very slowly,

$$v_{\mathrm{gr}}(k)\, D(k) \propto k, \;\; \text{for } k \to 0.$$

Exactly for this reason, the correlation spread for fermions in Fig. 6.3(f) does not seem as immediate as in the case of spins in Fig. 6.3(c), which will be discussed in Sec. 6.3.4.

The equation (6.19) still holds for the case of $\alpha > 2$, but now there is always at least one saddle point, because the group velocity is unbounded, $v_{\mathrm{gr}}^{\max} = \infty$. Therefore we have only the second part of the solution of (6.20).

Now, as the light cone takes up the entire space-time reference frame we will consider the leading contribution to the dynamics inside of the light cone. The leading contribution comes from the saddle point at the smallest velocity u as it has the slowest decay exponent. We focus on the case $d \gg ut$, in this case the saddle point k^* occurs close to zero. The result of the saddle point approximation in this case is

$$F(d,t) \propto \frac{t^{3/2}}{d^2} \begin{cases} (t/d)^{\frac{3-\alpha}{4-2\alpha}}, & \alpha < 1 \\ (t/d)^{\frac{3\alpha-1}{4-2\alpha}}, & 1 < \alpha < 2 \end{cases}. \tag{6.25}$$

Hence, although the entire space-time is occupied by the light cone, long-range correlations grow slowly (algebraically) in time. This suppression of correlations in the case of the fermionic model can be understood via the density of states in velocity and the group velocity. For spins, without an exact analytical solution, this analysis is impossible. However in the next section we will talk about an approximate solution for short times that allows us to gain similar insights into the spin problem as we have for fermions.

6.3.4. Holstein-Primakoff Approximation for the LRTI Model

In this section we consider an analytical treatment of the LRTI model at short times in the Holstein-Primakoff approximation. This approximation relies on the initial ordering of the spins; in particular here we will consider the case of all spins aligned along the z-axis (the initial state we chose previously). As another example one can also choose the case where spins are Néel ordered, i.e. odd spins point in the positive $z-$direction and even spins point in the opposite direction. In that case one would map all even spins onto effective spins pointing in the positive $z-$direction and continue as we will do below, and performing the opposite transformation once the final expression is obtained.

Regardless of the initial state, the approximation is correct as long as this order remains at least to some degree. We will quantify it below. We note that this is expected to be a better approximation for non-zero values of the transverse field B, as this supports retention of the ordering.

We take the initial state as $|\psi_0\rangle = \otimes_l |\downarrow\rangle_l$, and writing $\hbar \equiv 1$, we can rewrite (6.1) using the exact transformation [165]

$$\begin{cases} S_l^z = \tilde{a}_l^\dagger \tilde{a}_l - S \\ S_l^- \equiv S_l^x - iS_l^y = \sqrt{2S - \tilde{a}_l^\dagger \tilde{a}_l} \cdot \tilde{a}_l \\ S_l^+ \equiv S_l^x + iS_l^y = \tilde{a}_l^\dagger \cdot \sqrt{2S - \tilde{a}_l^\dagger \tilde{a}_l} \end{cases}, \tag{6.26}$$

where $S^{x,y,z} = \sigma^{x,y,z}/2$ are spin operators for spin-$1/2$ (i.e. $S = 1/2$) and $\tilde{a}_l$ is the bosonic annihilation operator on the site l. Starting from the initially fully polarized state we consider dynamics only on timescales when the initial order is still preserved, i.e.

$$\frac{\left\langle \tilde{a}_l^\dagger \tilde{a}_l \right\rangle}{2S} \ll 1, \tag{6.27}$$

then we can obtain the approximate expressions

$$\begin{cases} S_l^z = \tilde{a}_l^\dagger \tilde{a}_l - S \\ S_l^- \approx \sqrt{2S} \cdot \tilde{a}_l \\ S_l^+ \approx \sqrt{2S} \cdot \tilde{a}_l^\dagger \end{cases}. \tag{6.28}$$

The LRTI model can be rewritten in this approximation as

$$H_{\mathrm{HP}} = S\sum_{l\neq j} J_{lj}\left(\tilde{a}_l\tilde{a}_j + \tilde{a}_l^\dagger\tilde{a}_j + \mathrm{h.c.}\right) + 2B\sum_l \tilde{a}_l^\dagger\tilde{a}_l + \mathrm{const.}, \tag{6.29}$$

where the constant has no role in the dynamics. Then one can take operators in the momentum space representation

$$a_k = \frac{1}{\sqrt{M}}\sum_{l=1}^{M} \mathrm{e}^{-i\frac{2\pi kl}{M}}\tilde{a}_l, \tag{6.30}$$

and obtain the momentum space version of the Hamiltonian as

$$\begin{aligned} H_{\mathrm{HP}} = 2\sum_{k=0}^{M/2-1} \Big[& S\mathcal{J}(k)\left(a_{M-1-k}a_k + a_k^\dagger a_{M-1-k}^\dagger\right) \\ & + (S\mathcal{J}(k)+B)\left(a_k^\dagger a_k + a_{M-1-k}a_{M-1-k}^\dagger\right)\Big], \end{aligned} \tag{6.31}$$

where $\mathcal{J}(k)$ is defined in (6.8). It can be diagonalized via the Bogoliubov transformations for the bosonic field

$$\begin{pmatrix} \gamma_k \\ \gamma_{M-1-k}^\dagger \end{pmatrix} = \begin{pmatrix} u & v \\ v^* & u^* \end{pmatrix}\begin{pmatrix} a_k \\ a_{M-1-k}^\dagger \end{pmatrix}, \tag{6.32}$$

where $u = \cosh(\phi_k/2)$, $v = \sinh(\phi_k/2)$ in order to obey the constraint

$$|u|^2 - |v|^2 = 1, \tag{6.33}$$

with the Bogoliubov angle ϕ_k. Note that the Bogoliubov transformations for fermions (6.9) and bosons (6.33) have different signs, in order to satisfy anticommutation and commutation relations respectively. Eq. (6.31) can be diagonalized if

$$\mathrm{e}^{2\phi_k} = 1 + \frac{2S\mathcal{J}(k)}{B}. \tag{6.34}$$

From this expression one can obtain the dispersion relation as

$$\epsilon(k) = 2B\sqrt{1 + \frac{2S\mathcal{J}(k)}{B}}. \tag{6.35}$$

Note that in order for $\epsilon(k)$ to be real, the expression under the root can not be negative. Then, using (6.8), we obtain the following constraint

$$\left|\frac{B}{J}\right| \geq -2\,\mathrm{sign}\left(\frac{B}{J}\right)\,\mathrm{Li}_\alpha\left(-\mathrm{sign}\left(\frac{B}{J}\right)\right), \tag{6.36}$$

which sets the limits for B values such that the Holstein-Primakoff transformation

is stable for all modes k.

In the same fashion as was done for the Bogoliubov transformation for spins, here we can repeat the derivation for the pre-quench parameters of the Hamiltonian. Hence we will denote the angle and annihilation operator as ϕ_k^0 and a_k^0, respectively.

Now it is interesting to take a look at the behavior of the dispersion relation. Using the limiting behavior of the polylogarithm, we then obtain the divergence of the dispersion relation for $\alpha < 1$,

$$\epsilon(k) \propto k^{\frac{\alpha-1}{2}}, \, (\alpha < 1, \, k \to 0) \, . \tag{6.37}$$

We see that the dispersion relation and density of states in velocity have similar features as for the LRFH model in Fig. 6.5, in particular the dispersion relation diverges at $k = 0$ for $\alpha < 1$.

The difference between the regimes of the long-range ($\alpha < 1$) interaction from the other regimes can be observed via looking at the jump of the Bogoliubov angle

$$\delta\phi_k = \phi_k - \phi_k^0, \tag{6.38}$$

where ϕ_k^0 is the pre-quench Bogoliubov angle for the Hamiltonian with the field $B_0 = \infty$.

In the case $\alpha < 1$, the modes near $k = 0$ will dominate the spread of correlations, and we will observe a transition of behavior with respect to $\alpha > 1$, where the dispersion relation is regular for $k = 0$. This explains the transition in behavior at $\alpha = 1$.

For further comparison we will consider the correlation matrix for the bosonic particles

$$\hat{C}_d(t) = \left\langle \left| \left\langle a_l^\dagger(t) a_{l+d}(t) \right\rangle \right| \right\rangle_l , \tag{6.39}$$

after a global quench of the transverse field and compare it with the analogous correlation function for spins.

It is always interesting to see how well approximate solutions describe the exact dynamics, which can be accurately evaluated via DMRG methods as the error is well controlled. For instance in Fig. 6.6 we can see the comparison of correlation functions for the LRTI model calculated with MPS/MPO methods described in Chap. 4 and via the Holstein-Primakoff transformation after the system is quenched from the fully polarized state. The initial order of the state is preserved only at times of a fraction of tJ for moderate fields B, which does not allow us to use this approximation for quantitative analysis for longer times. By increasing the absolute value of the field one can extend the lifetime of the order, and the Holstein-Primakoff transformation will be valid for longer times. At the same time, the exchange term becomes stronger for longer range interactions

and the initial spin order lasts for shorter times. It should be noted, although the quantitative agreement lasts for short times, key qualitative aspects of the dynamics are typically captured over longer timescales.

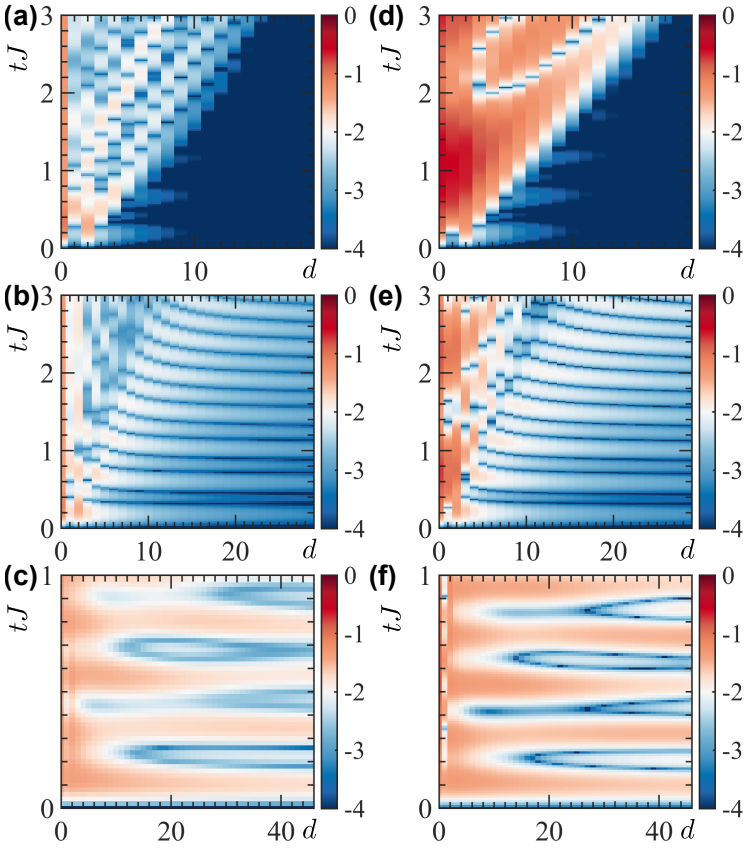

Figure 6.6.: Correlation spreading in the LRTI model after the global quench $B/J = \infty \to 2$ is applied in the system of $M = 100$ spins. (a-c) $\log_{10}|\tilde{C}_d(t)|$ calculated numerically via MPS/MPO methods (as in Fig. 6.3(a-c)), and (d-f) $\log_{10}|\hat{C}_d(t)|$ calculated analytically via the Holstein-Primakoff approximation. (a,d) $\alpha = 3$, short-range interactions case. (b,e) $\alpha = 3/2$, intermediate-range interactions. (c,f) $\alpha = 1/2$, long-range interactions.

6.4. Entanglement Growth

In this section we quantify the time-dependence of another system observable that heavily relies on the interaction part between different subsystems of the system. We present here our investigations of the spatial entanglement, and in particular how fast it grows after global quenches. We are doing to use the bipartite von Neumann entanglement entropy S_{vN} as a measure of the spatial entanglement (see Sec. 4.1.2.1 for definitions).

It is known [166, 167] that in the case of local interactions or interactions that exponentially decay with distance, the bipartite entanglement entropy grows linearly in time after a quench. This is related to a finite speed of excitations propagating in the system, which leads to a linear rate of quantum information exchange between partitions and linear growth of entanglement. In this section we would like to extend our consideration to the case when interactions decay only algebraically in distance. Another question concerns the rate of growth of the entanglement in time, whether it stays linear or not.

In the sections below we first consider the entanglement growth for the LRTI model. Due to the lack of theoretical treatment we do it only numerically using MPS/MPO techniques. We then analyze the entanglement growth in the LRFH model, which is done analytically.

We find that for $\alpha > 1$ the behavior mostly follows the same form as for short range interactions, i.e. linear growth of entanglement in time. However, in the case of long-range interactions with $\alpha < 1$ exceptions are possible if the symmetry of the initial state and Hamiltonian confine the post-quench dynamics to a subspace of the Hilbert space. For instance, if one starts with a state with N out of M spins pointing along the axis of the field and after the quench the field is turned to large values, then the dynamics will be almost purely confined in the subspace of all states with N spins along the field, i.e. the total magnetization in this direction will be preserved. In the same fashion the growth of entanglement can be suppressed in the case of long-range interactions when all spins are aligned with the magnetic field.

6.4.1. Entanglement Growth in the LRTI Model

In order to describe the general behavior of the entanglement in the spin model, let us first take a look at some particular examples that will help us to build the whole picture. In Fig. 6.7, we present examples of the entanglement entropy growth in the LRTI model, beginning from a selection of different initial states.

In Fig. 6.7(a) we see clearly the change in characteristic behavior as we go from the nearest-neighbor interaction limit ($\alpha \to \infty$) to long-range interactions, beginning in a fully polarized state with all spins down. As one reduces α the linear growth of entanglement first slows down, but stays linear, due to the change of the group velocity of excitations (compare $\alpha = 2$ with $\alpha \to \infty$). A qualitative difference in scaling happens for $\alpha < 1$ as the growth is notably sublinear. Note that due to the finite size of the system ($M = 20$ spins) we observe the saturation of entanglement for the linear regimes. In Sec. 6.4.1.1 we will discuss the limiting cases.

In Fig. 6.7(b), we focus on the interesting case of the long-range interaction ($\alpha < 1$) and compare different initial states. This growth is approximately linear on a logarithmic scale, but depends strongly on the structure of the initial state, with

much slower growth at intermediate times for the initially fully polarized state, compared with other spin configurations or with short-range interactions. The intuitive explanation for this restriction of entanglement growth at intermediate times is that the structure of the initial state, when combined with the symmetry of the Hamiltonian, prevents the system from accessing large sections of the Hilbert space at short to intermediate times, as it becomes somewhat stuck in its initial symmetry sector. The ultimate limit of this occurs when $\alpha \to 0$, where the Hamiltonian is fully symmetric. In that case, if we begin with a completely polarized spin state, the system will be at all times restricted to completely symmetric spin states, substantially limiting the maximum entanglement entropy that can be reached [144].

In Fig. 6.7(c,d) we look at simple perturbations of the initial fully polarized state. We locate perturbations at different distances from the middle of the chain. We see that both the linear behavior for $\alpha > 1$ and the sublinear behavior for $\alpha < 1$ are quite robust to small changes in the initial state like this at short times. However the difference between the two cases is the time of the response. In the case of short-range interactions the perturbation require some finite time to reach the middle of the chain (Fig. 6.7(c)). Once this time passes the dynamics is identical again. On the other hand, in the case of long-range interactions, $\alpha < 1$, the response is always immediate (Fig. 6.7(d)).

6.4.1.1. Behavior in Limiting Cases

In this section we will discuss entanglement growth in the extreme cases of the neighboring interactions ($\alpha \to \infty$) and all-to-all interaction ($\alpha = 0$). These analytically approachable cases will help us to develop the intuition for more general cases.

In the case of the nearest-neighbor interactions ($\alpha \to \infty$) the transverse field Ising model can be studied analytically and the dynamics after global quantum quenches has been considered in numerous works, see e.g. [164, 168–178]. In this limit the Ising chain can be mapped onto a model of free fermions, which has the twofold degenerate dispersion relation

$$\epsilon(k) = 2\sqrt{(J-B)^2 + 4JB\sin^2\left(\frac{k\lambda}{2}\right)}, \tag{6.40}$$

for $k \neq 0$, where λ is the distance between spins. The fastest quasiparticles in this model move at the Lieb-Robinson velocity

$$\begin{cases} v_{\mathrm{LR}} = v_{\mathrm{gr}}^{\max} = 2\lambda J, & B \geq J \\ v_{\mathrm{LR}} = v_{\mathrm{gr}}^{\max} = 2\lambda B, & B < J \end{cases}. \tag{6.41}$$

By performing a global quench of the system parameters we excite counter-

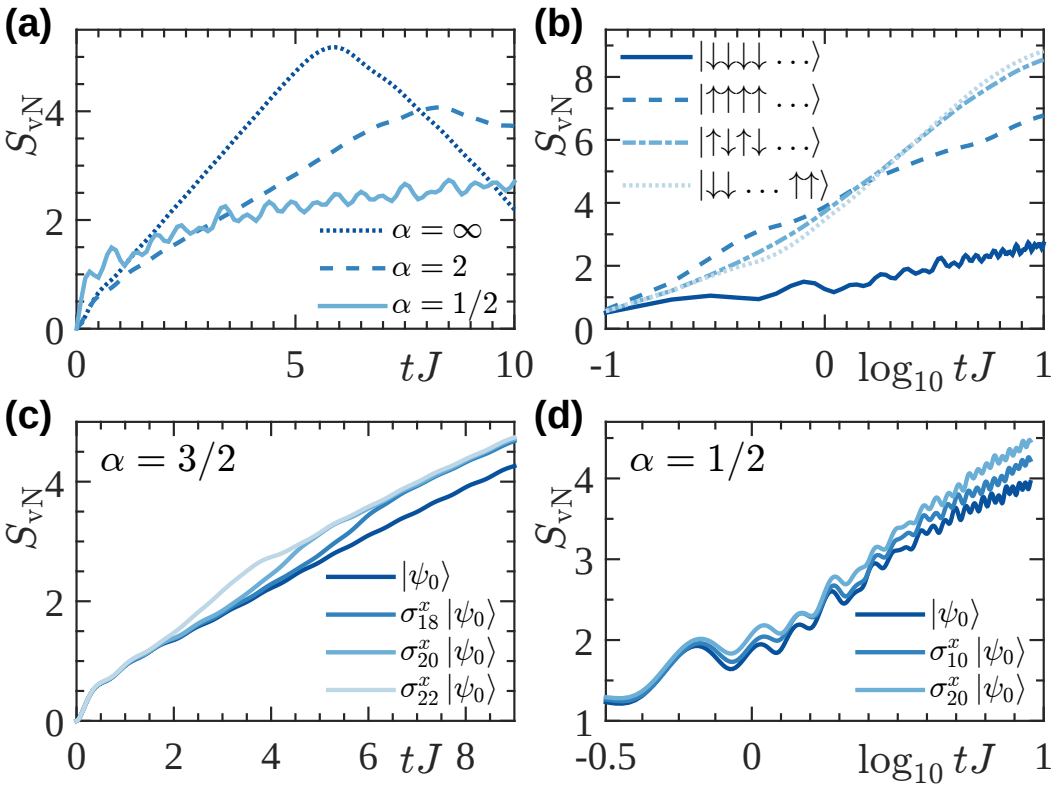

Figure 6.7.: Examples of bipartite entanglement growth after the global quench in LRTI model with open boundary conditions. (a) Half-chain entanglement entropy as a function of time for $M = 20$ spins beginning in the fully polarized state $|\psi_0\rangle = |\downarrow\downarrow\downarrow\ldots\rangle$ along the axis of the magnetic field $B = J$ (from exact diagonalization). (b) The same as (a), but for $\alpha = 1/2$, and starting from a selection of initial states (2 fully polarized states in the opposite directions, Néel ordered state, and a product state with spins down in the left half of the chain and up in the right half). (c) Linear and (d) sublinear growth of entanglement entropy (shown on a logarithmic scale) for the LRTI model and selection of initial states, now for $M = 50$ spins, computed with MPS methods (converged with MPS bond dimension $D = 256$).

propagating entangled pairs of quasiparticles at certain points of the system. The spatial entanglement between two parts of the system grows as one quasiparticle of a pair crosses the border. Since the pairs are spreading with a finite maximum speed the spatial entanglement entropy is limited by the Lieb-Robinson bound, which leads to a linear growth of the entanglement entropy

$$S_{\mathrm{vN}} \leq C_1 v_{\mathrm{LR}} t + C_2, \tag{6.42}$$

where C_1 and C_2 are constants, as is discussed in more detail in Sec. 6.4.2.1.

In the opposite case of all-to-all interactions with $\alpha = 0$, the model can also be analytically solved via mapping to the Lipkin-Meshkov-Glick model, for which

entanglement properties have been studied [179, 180]. By starting from a fully polarized initial state with spins aligned with the external field B, the dynamics is fully restricted to the subspace of Dicke states with finite well defined maximum spatial entanglement [181]. Hence, the entanglement entropy will always be restricted

$$S_{\mathrm{vN}} \leq \log_2\left(\frac{M}{2}+1\right), \tag{6.43}$$

where M is the number of original spins, intuitively explaining the slow and bounded growth of entanglement in the case of long-range interactions.

6.4.2. Entanglement Growth in the LRFH Model

In this section we discuss analytical results for the growth of the entanglement in the LRFH model.

The derivation and the use of the method, based the Toeplitz matrix representation of entanglement entropy, was first presented in [167, 173]. Here we use the generally derived integral forms and evaluate them numerically with our quench parameters.

We will see here the same behavior as we saw for the LRTI model: linear growth for all α for generic initial states, but sublinear behavior for long-range interactions for some initial states. We can understand this analytically from the behavior of and contribution to the entanglement growth from the quasiparticles with $k \to 0$.

6.4.2.1. Quench from $\Delta = 4J$ to $\Delta = J/5$

Here we consider the dependence of the entanglement entropy on the bipartite splitting as well. We divide the system of M sites in a block of size μ and then everything else. The analytical approach gives especially good agreement with the bulk limit, i.e. when

$$\begin{cases} \mu/M \to 0 \\ \mu,\, M \to \infty \end{cases}, \tag{6.44}$$

the analytical expressions for the entanglement entropy become exact.

In Fig. 6.8 we show numerical results for the growth of the entanglement entropy in a quench within the LRFH model from $\Delta = 4J$ to $\Delta = J/5$. The subplot Fig. 6.8(a) shows the half-chain entanglement entropy $\mu = M/2$ which is closer to what we expect for spin systems, and in Fig. 6.8(b), we consider uneven splitting $\mu \ll M$, where we can approach the bulk prediction. In each case, we see a fairly

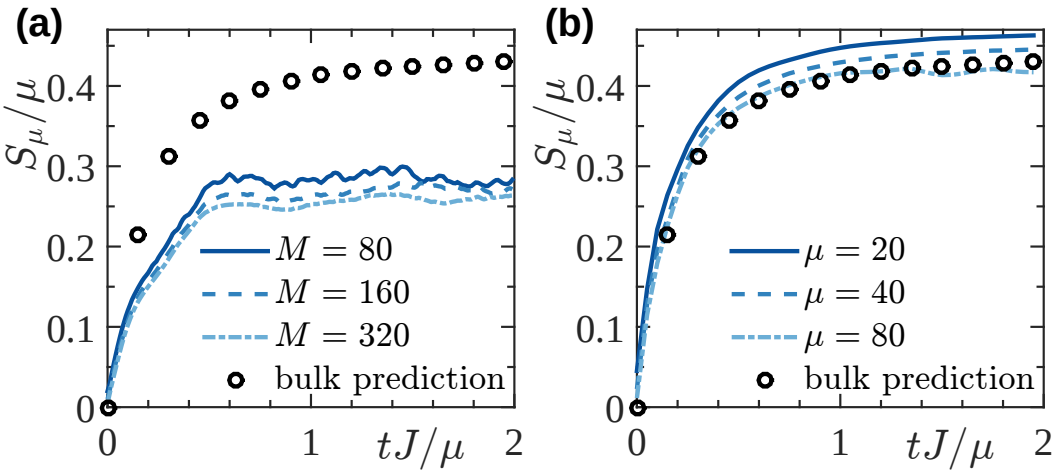

Figure 6.8.: The entanglement entropy in the LRFH model with $\alpha = 0.8$, computed using exact numerical techniques for various system sizes M and subsystem sizes μ after the global quench of $\Delta/J = 4 \to 1/5$. (a) Entanglement dynamics for the equal partition case with $\mu = M/2$. The circular markers show the limit described by (6.45) for large subsystems in the bulk (i.e., $\mu, M \to \infty$ and $\mu \ll M$). (b) Entanglement dynamics for a selection of system and subsystem sizes, which is shown to converge to the prediction (6.45) with increasing μ for $\mu \ll M = 640$. The circular markers again indicate (6.45) for large subsystems in the bulk.

typical generic form for the entanglement growth, in which it saturates at a value and time that are proportional to the size of the subsystem, μ.

Let us now take a look at the exact analytical forms of the entanglement entropy per unit length that one can obtain in the thermodynamic limit, i.e. ignoring boundary effects. In the case where the pre-quench Hamiltonian is reflection symmetric and can be diagonalized by the Bogoliubov transformation the time dependence of the entanglement entropy can be obtained [167, 172] as

$$\frac{S_\mu}{\mu} \sim \int_0^\pi \frac{\mathrm{d}k}{\pi} \min\left(1, 2\,|\varepsilon'(k)|\,\frac{t}{\mu}\right) G\left(\cos \delta\theta_k\right), \tag{6.45}$$

where

$$G(x) = -\frac{1+x}{2}\log\frac{1+x}{2} - \frac{1-x}{2}\log\frac{1-x}{2}, \tag{6.46}$$

plays the role of the density of excitations that contribute to the growth of the entanglement between partitions A and B. The angle $\delta\theta_k$, defined in (6.14), is the difference of the Bogoliubov angles before and after the quench. In Fig. 6.8(a) one can see this dependence for equal partition splitting and for the case of uneven splitting Fig. 6.8(b), which resembles the bulk prediction.

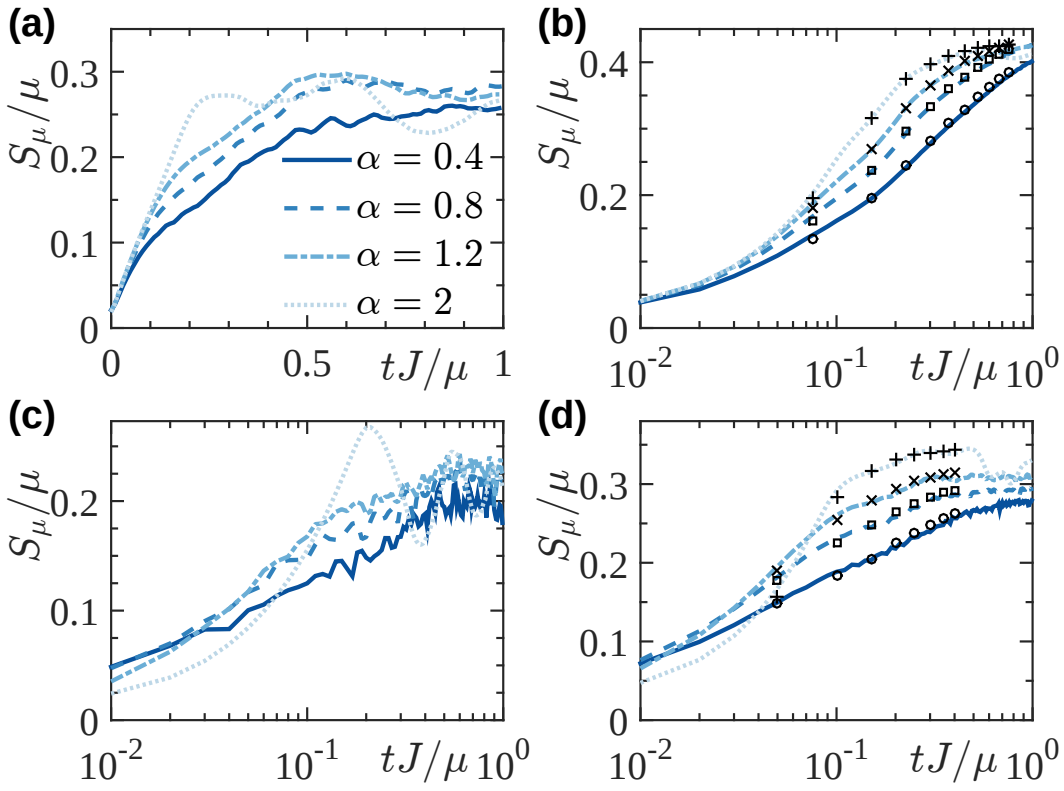

Figure 6.9.: The entanglement entropy in the LRFH model after global quenches computed using exact numerical techniques for a selection of interaction range exponents α. (a,b) Beginning from the ground state for $\Delta = 4J$ to $\Delta = J/5$, and (c,d) beginning from the ground state of a critical Ising model (as detailed in the text) to $\Delta = J/5$ as well. Different partition μ is chosen to emphasize the bulk prediction: (a,c) The half-chain entanglement entropy $\mu = M/2 = 40$, and (b,d) the subsystem entanglement entropy for $\mu = M/8 = 40$. Markers denote the bulk prediction from (6.45). (a) One can see a time window of clean linearity for all α, but it gets shorter as $\alpha \to 0$. At short times the leading behavior seems to be linear, but the subleading terms (in tJ/μ) are also affected by the divergence of the dispersion relation. (b) The agreement with the bulk prediction is very good, but at sufficiently large tJ/μ the discrepancy due to the finiteness of M is clearly visible. (c) There are evident differences with respect to (a) due to the fact that quasiparticles with momentum close to zero turn out to give a finite contribution to the entropy. While for $\alpha \geq 2$ the entropy seems to grow linearly, for small α the leading contribution at short time growth logarithmically in time. (d) The agreement with prediction (6.45) is very good.

It is clear that (6.45) can be simply bounded by the velocity term

$$\int_0^\pi \frac{\mathrm{d}k}{\pi} \min\left(1, 2\left|\varepsilon'(k)\right| \frac{t}{\mu}\right) G\left(\cos\delta\theta_k\right) \leq 2\frac{t}{\mu}\int_0^\pi \frac{\mathrm{d}k}{\pi}|\varepsilon'(k)|G\left(\cos\delta\theta_k\right). \quad (6.47)$$

This might seem a very simple step, but one can draw interesting conclusions out of it. Let us look at the long-range case, $\alpha < 1$, first. The velocity (6.17) diverges as $k^{\alpha-2}$ when $k \to 0$ and the short time behavior of the entropy could be strongly influenced by the modes close to zero momentum if these are affected by the quench, i.e. if the initial and final parameters of the Hamiltonian are chosen such that one creates excitations near $k = 0$.

If now one looks at the quenches we presented in Fig. 6.8, it can be calculated from (6.14) that the change in the Bogoliubov angle $\delta\theta_k \to 0$ as $k \to 0$. In other words the quench does not generate new quasiparticles at $k = 0$, and existing quasiparticles just pick up a phase, which does not affect the entanglement between partitions A and B. Consequently, these play no role in the change of entanglement. Mathematically it means that the density of excitations G approaches 0 faster than the group velocity $\varepsilon'(k)$ diverges as $k \to 0$ and the integrand in the right hand side of (6.47) tends to zero. In Fig. 6.9(a,b) a weak dependence on α for the qualitative behavior of the entanglement entropy is shown clearly for this quench. In Fig. 6.9(a) this is shown for $\mu = M/2$, which is the usual case that we deal with. In Fig. 6.9(b), this is shown for the subsystem in the bulk, $\mu \ll M$.

6.4.2.2. Quench from Critical Ising to $\Delta = J/5$

In this section, instead of just quenching the interaction strength Δ we quench the interaction range as well. The idea is to excite quasiparticles near $k = 0$ that on one hand have infinite range, but on the other hand do not give any contribution to the entanglement growth. As we saw above the divergence of the group velocity clearly depends on the range of the interactions α, we would like to see how the contribution of those excitations with $k \to 0$ will affect the growth of the entanglement as we vary α.

Analogously to what we saw in the previous section for the LRTI model, we need to consider ground states with a different structure than the $\Delta = 4J$ ground state, as in that case the density of excitations G was converging to 0 faster than the divergence of the group velocity. Specifically, we look for situations where the integrand $|\varepsilon'(k)|\, G\left(\cos\delta\theta_k\right)$ in (6.45) diverges as $k \to 0$. It turns out that if we choose the ground state of the critical transverse field Ising (CTI) chain, the Hamiltonian of which in fermionic operators reads

$$H_{\mathrm{CTI}} = \sum_l c_l^\dagger (c_{l+1}^\dagger + c_{l+1} - c_l) + \mathrm{h.c.}, \quad (6.48)$$

then then the corresponding Bogoliubov angle will be $\cos\theta_k^0 \sim |k|/2$ and hence

$G(\cos\delta\theta_k) = \log 2$. The quasiparticles with momentum close to zero then dominate the dynamics at short times.

In Fig. 6.9(c,d) we show the entropy per unit length for the time evolution under the long-range Hamiltonian (6.3) with $\Delta = J/5$, but now starting from the ground state of (6.48). Again we show the equal partition splitting in Fig. 6.9(c) and the bulk regime in Fig. 6.9(d). These calculations start from the ground state of the CTI Hamiltonian (with open boundary conditions).

Whereas the short-range regime is not affected much, as the group velocity is always finite, the most interesting changes occur for the long-range regime, $\alpha < 1$. In that case the dominant contribution to S_μ is not linear any more. If we take the leading order term of Eq. (6.45) at short times, we find that this behavior is polynomial, and see that

$$S_\mu \propto t^{1/(2-\alpha)}, \tag{6.49}$$

at short times.

As one shortens the range of the interactions and $\alpha \to 1$, the timescales over which the power law (6.49) holds become shorter. Also note that the growth of entanglement in case $\alpha < 1$ is faster at very short times, but slower at intermediate times than the linear behavior of short-range interactions, $\alpha > 1$.

This counterintuitive result can actually be well explained. In this section we put a focus on quenching the system in such a way that quasiparticles with zero momenta are excited as much as possible. These excitations, propagating immediately over the entire system, just slightly entangle it. This is analogous to the case of all-to-all interactions (see Sec. 6.4.1.1), where the bipartite entanglement of the system is bounded and reached almost immediately. Other excitations with momenta away from zero just give corrections at later times as it takes finite time for them to cross the border between partitions. Hence, we see in Fig. 6.9(c,d) that the entanglement at short times is larger in the case of long-range interactions, $\alpha < 1$, than in the case of the short-range interactions, $\alpha > 1$.

The scaling in the case of the long-range interactions, $\alpha < 1$, seems to be sublinear, with the leading sublinear term (6.49) extracted analytically.

6.5. Summary and Outlook

In this chapter we presented our work on correlation spreading and entanglement growth after global parameter quenches in the long-range transverse field Ising model and a long-range fermion hopping model.

For both models in was found that in the case of short-range interaction the dynamics closely resembles the case of local (or exponentially decaying with distance) interactions, such as light cone effects of the correlation spreading and

linear in time growth of entanglement. The main difference is in the form of higher order corrections, which decay algebraically now, and not exponentially.

Also for both models we find a clear delineation of long range behavior for $\alpha < 1$, and an intermediate regime where the entanglement still shows linear growth on short time-scales, but correlation spreading does not have a well defined light cone any more.

We find that for particular classes of initial states, the sublinear time scaling of the bipartite entanglement growth can be obtained for long-range interactions. We can characterize this change in entanglement growth based on the contribution of quasiparticles near $k = 0$, where the group velocity and dispersion relation diverge for long-range interactions. These excitations do not provide a lot of entanglement, as they are performing only collective evolution of all parts of the system (either spins or fermions). At short times, we similarly see a suppression of correlation growth at long distances with long-range interactions.

In the future it would be interesting to extend this study in two major directions. First, the obvious one is to study the correlation spreading and entanglement growth in higher dimensions. In this case, the numerical methods presented here are not the most optimal tool, as the amount of spatial entanglement generated after global quench scales linearly with the system size (here we talk about the entanglement entropy), hence it requires exponentially large tensors to store the state.

Secondly, it would be interesting to take advantage of the entanglement suppression and use this trick for extending the simulation time with DMRG techniques, which heavily rely on it (see Chap. 4). For this, one needs to perform more systematic study of symmetries in the system, as the suppression of the entanglement growth relies on confinement of the system dynamics in a certain symmetry sector of the Hilbert space.

The results for the long-range transverse field Ising model correspond directly to dynamics of ongoing experiments with trapped ions highlighted in Sec. 2.4. The collaboration with an experimental group in Innsbruck on development of a new method of quantum state characterization for trapped ions is presented in Chap. 7.

7. Certified MPS Tomography of Quantum States

In this chapter[1] we continue the work started in Chap. 6 on a long-range spin model experimentally realized on trapped ions in one and two dimensions (Sec. 2.4.1). Rather than purely theoretical investigation, this chapter will focus on the application of the model to experiment, in which the first demonstration of a new method of quantum state estimation, certified Matrix Product State (MPS) tomography [182], is given.

7.1. Introduction

Currently, quantum state tomography (QST) is the state of the art method for determination of states of small quantum systems [75]. This method relies on the measurement of the system state in all bases, hence it can be efficiently used only in the case of relatively small systems. The linear growth of the system size will require an exponential increase of the number of measurements, making it highly inefficient for larger systems. That is why the development of new efficient techniques is particularly interesting now, as developing experiments are well beyond the reach of QST. For instance modern experiments already operate with up to tens of thousands of neutral atoms in optical lattices (Sec. 2.3) and with a few hundreds of ions confined in the Penning trap (Sec. 2.4).

Here we present a collaborative work on realization of a recently proposed technique [76], which is theoretically proven to allow the states of a broad class of quantum systems to be accurately estimated with an effort that increases only polynomially with the number of constituents in the system. The method is called Matrix Product State (MPS) tomography and can be applied to a wide range of quantum states, in particular those that are well approximated by matrix product states (see Chap. 4).

[1] This work is taken in part from the publication *Efficient tomography of a quantum many-body system*, B. Lanyon, C. Maier, M. Holzäpfel, T. Baumgratz, C. Hempel, P. Jurcevic, I. Dhand, A. Buyskikh, A. Daley, M. Cramer, M. Plenio, and R. Blatt, arXiv:1612.08000 (accepted for publication in Nature Physics). The author of this thesis performed calculations to compare with experimental time evolution and to analyze the scaling of the measurement scheme, and wrote the code used for calculation of reduced density matrices.

The idea behind MPS tomography is essentially the same as the idea of the MPS representation of quantum states when one wants to treat the problem numerically. The full QST method is a universal method that works for any type of state as long as the system size is small enough. MPS tomography is aimed at states with low entanglement, which can be efficiently represented in the MPS form [183, 184], i.e., represented with a small bond dimension.

In this work we focus on the case of the quench dynamics of spin chains from initially unentangled pure states, which can be written in the MPS form with the bond dimension just one, i.e., they are product states. The quench triggers the spread of correlations in the system and a build up of entanglement (see Chap. 6). In the case of only local interactions the spread of correlations in the system follows the light cone dependence [74, 163, 185], hence only the spins which were reached by the light cone become entangled with each other. The distance on which correlations decay exponentially for further spins is called the *correlation length* L.

In this work we take this idea that only local spins are entangled after a short-time evolution following a global quench and reconstruct the state of the system by measuring only reduced density matrices (*reductions*) of all blocks of k consecutive spins. Besides this a certification of the method is provided that produces a lower bound on the fidelity between the real lab state ρ_{lab} and the MPS state estimate $|\psi_{\text{c}}^{k}\rangle$.

In the following sections we will first present the model that is experimentally realized in the group of Christian Roos and Rainer Blatt in Innsbruck. The model has a linear chain of spins with interactions decaying algebraically in distance with variable exponents. This allows us to test the capabilities of MPS tomography beyond local interactions. We then summarize the main methods of state estimation and present the result with experimentally obtained data. Before concluding we estimate the resource cost of MPS tomography showing its efficiency, i.e. polynomial growth of the required number of measurements with the system size.

7.2. Notation

This chapter presents results measured in experiments, calculated for the idealized time evolution numerically, and obtained from certified MPS tomography. In order to avoid confusion we find it useful to present here the list of the most important notation for this chapter, so the reader can always refer to the definitions:

- M — number of sites in the spin chain
- L — correlation length
- $|\phi\rangle$ — ideal state of the system, calculated numerically

- ρ_{lab} — density matrix of the experimental state, which in general can be mixed
- k — size of the block of consecutive spins in the spin chain, the reduced density matrix (reduction) of which is measured via QST
- $|\psi_{\text{c}}^k\rangle$ — certified MPS state, obtained via the MPS tomography method with reductions of size k.
- H_{par} — gapped parent Hamiltonian, constructed as an intermediate tool to find the best $|\psi_{\text{c}}^k\rangle$, which is its non-degenerate ground state. The energy gap of H_{par} is $\Delta E = E_1 - E_0$
- $F \equiv \langle\psi_{\text{c}}^k|\rho_{\text{lab}}|\psi_{\text{c}}^k\rangle$ — actual fidelity of MPS tomography
- F_{c}^k — certified fidelity lower bound for $|\psi_{\text{c}}^k\rangle$, i.e. $F \geq F_{\text{c}}^k$

7.3. Methods

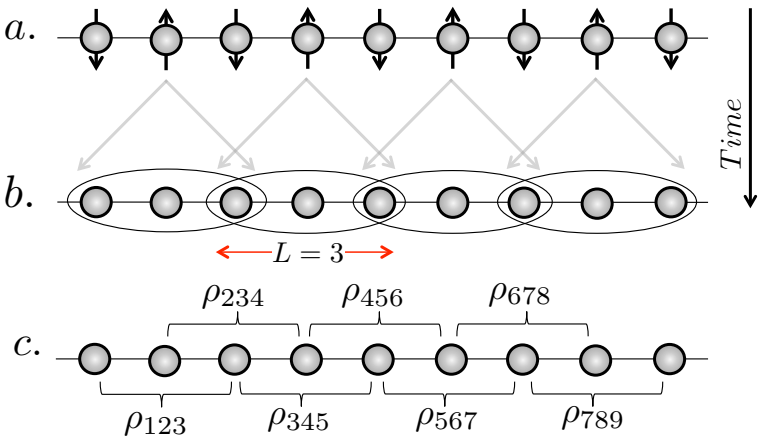

Figure 7.1.: Graphical representation of the experimental sequence used for the Matrix Product State (MPS) tomography. (a) Initially the chain of M spins is prepared in the Néel ordered pure state, which is not an eigenstate of the system Hamiltonian. Then the Hamiltonian is suddenly quenched on and the correlations spread out [103, 104, 163] as shown by arrows (only a few shown). (b) After some time quantum correlations have reached neighboring spins as indicated by ellipses (not all shown). (c) MPS tomography requires only measurements to reconstruct all $k-$spin reduced density matrices — local reductions (all necessary reductions for $k = 3$ are shown). The experimental effort therefore increases only polynomially in spin number M. This figure was reproduced from [182].

In this section we present the model Hamiltonian and explain the sequence of the experiment aimed at using certified MPS tomography. We work with a system

of $^{40}Ca^{+}$ ions trapped in a linear Paul trap, which was already explained in Sec. 2.4.1. Two long-lived internal states can be singled out in each ion and we can map them to two states of a single qubit. Then via interaction of these internal states with the external fields, as well as with the phonon modes of the ion crystal, the dynamics of the system can be made to obey the long-range transverse field Ising Hamiltonian

$$H_{\mathrm{LRTI}} = \sum_{r<l}^{M} J_{rl}\sigma_r^x\sigma_l^x + \sum_{r}^{M}(B+\delta B_r)\sigma_r^z, \tag{7.1}$$

where J_{rl} is the spin-spin coupling matrix, B is the external uniform field, δB_r is the non-uniform component of the field, and σ_r^x and σ_r^z are the Pauli x and z matrices for spin r. The strength of spin-spin interactions reduces with distance approximately as

$$J_{rl} \approx \frac{J}{|r-l|^{\alpha}}, \tag{7.2}$$

where J is the averaged value of the interactions between neighboring spins. In Chap. 6 we studied the global quench dynamics of this Hamiltonian in the idealized situation without the non-uniform field δB_r, and where interactions decayed exactly according to the power law. As this chapter is a logical continuation of the previous one but with a bias towards practical applications, we find it useful to give more technical details on the system.

The parameters for the two experimental set-ups realized here can be found in Tab. 7.1. In the case of the large external field $B \gg |J_{rl}|, \delta B$ (which is the case here), Eq. (7.1) is equivalent to the long-range XY analogue

$$H_{\mathrm{LRXY}} = \sum_{r<l}^{M} J_{rl}(\sigma_r^+\sigma_l^- + \sigma_r^-\sigma_l^+) + B\sum_{r}^{M}\sigma_r^z, \tag{7.3}$$

where the site-dependent perturbation δB_r is also omitted. For this situation the total magnetization along the $z-$axis is preserved, i.e. if the initial state has N out of M spin-ups, then the Hamiltonian will preserve this number during the evolution.

The experiment (sketched in Fig. 7.1) was performed for two sets of spin chains. First, it was done with 8 spins, which is still accessible via full QST. Secondly, it was repeated with 14 spins, beyond reasonable length measurements and reconstruction with QST. In both cases the system was initially prepared in the pure Néel ordered state

$$|\phi(0)\rangle = |\uparrow,\downarrow,\uparrow,\downarrow ...\rangle, \tag{7.4}$$

and then it will be allowed to evolve until a certain time where the MPS tomography measurements will be performed. The system at that point will be in some, in

	8 ions	14 ions
$\max_{r,l}(J_{rl})$	$2\pi \cdot 25$ Hz	$2\pi \cdot 15$ Hz
α	1.58	1.27
B	$2\pi \cdot 3$ kHz	$2\pi \cdot 5$ kHz
$\max_r(\delta B_r)$	$2\pi \cdot 1$ Hz	$2\pi \cdot 1$ Hz

Table 7.1.: Approximate experimental parameters of the Hamiltonian (7.1). Whereas all parameters are mentioned approximately, δB_r is only defined up to an order of magnitude, it was estimated in the experiment as the fluctuation of the magnetic field.

general mixed, state ρ_{lab}. The measurements will be used to reconstruct reduced density matrices (reductions) of $k = 1$, 2, or 3 neighboring spins. For each of these cases the certified MPS state $|\psi_c^k\rangle$ will be obtained, with a lower bound on fidelity F_c^k. We will see that the increase of the reduction size k used in tomography significantly improves the state reconstruction and its fidelity bound. Then we provide the values of fidelity, which can be estimated via the Direct Fidelity Estimation (DFE) method [186, 187].

The interaction decay exponent α in both cases belongs to the interval between 1 and 2. As we saw in our investigation in Chap. 6 this is the transition regime between long- and short-range interactions. Whereas light cone effects are still observed in the spread of correlations, the border of the light cone is somehow poorly defined and the correlation tails outside of the light cone spread at distances comparable to the system size [104, 145, 188]. The growth of entanglement in this regime is still linear. Hence, strictly speaking we are going to use (7.1) in the regime of non-local interactions.

Below we will first explain how full QST works and why this method becomes unfeasible for large system sizes (Sec. 7.3.1). Then we will describe the main principles of the MPS tomography, along with the certification scheme (Sec. 7.3.2). After that, the results for the two experimental setups will be presented showing the reconstruction of the laboratory state via MPS tomography (Sec. 7.4). Before the conclusion we will present extra results on the numerical simulation of MPS tomography for a various chain lengths to demonstrate efficient (polynomial) scaling of the number of measurements required for the constant estimation error in MPS tomography (Sec. 7.5).

7.3.1. Full Quantum State Tomography (QST)

In this section we will give an overview of full quantum state tomography (QST) and its limitations. For this let us consider a composite quantum system where each element is a two-level quantum system, e.g., a qubit or spin-$1/2$. In order to reconstruct the density matrix of a single spin one needs to perform measurements

in 3 bases: σ^x, σ^y, and σ^z. In each basis one has only two distinct outcomes, i.e. either +1 or -1 for each spin in the chosen basis, however the state is in a superposition of both of them. After a sufficient number of samples in each basis one obtains the probability for each projection of the qubit. The next step is to use a Maximum Likelihood Estimation (MLE) scheme to obtain the density matrix which is maximally close to the real one. The method guarantees that the state is properly normalized, its density matrix is positive semi-definite, and produces the best agreement with the data.

In the case of 2 spins, the number of bases in which the state must be measured rises to $3^2 = 9$:

$$\begin{array}{lll} [\sigma^x \otimes \sigma^x] & [\sigma^x \otimes \sigma^y] & [\sigma^x \otimes \sigma^z] \\ [\sigma^y \otimes \sigma^x] & [\sigma^y \otimes \sigma^y] & [\sigma^y \otimes \sigma^z] \\ [\sigma^z \otimes \sigma^x] & [\sigma^z \otimes \sigma^y] & [\sigma^z \otimes \sigma^z] \end{array} ,$$

where the first element shows the measurement operator on the first spin and the second element shows the measurement operator for the second spin. Each measurement now has $2^2 = 4$ outcomes.

In the general case of M spins, the measurement should be made in 3^M bases. For a fixed basis one can obtain 2^M distinguishable outcomes. This means that one needs to have sufficiently many samples in each basis to reduce statistical fluctuations.

The greatest advantage of QST is that the estimation error depends only on the sample size and experimental noise and the method does not rely on certain characteristics of the state. This means QST will work both on a product state, when the system is prepared in a fully polarized state and on a highly entangled state after quench dynamics (see our investigation of the entanglement growth in Chap. 6).

The down side of QST is the exponential growth of the number of bases in which measurements have to be taken. For instance the largest application of full QST was for 8 qubits, and required measurements in $3^8 = 6561$ different bases, which took over ten hours [189]. The reconstruction of the state from these measurements is also a complex computational problem.

7.3.2. Certified MPS Tomography

In this section, we give an overview of certified MPS tomography, which is based on previous results from [76, 190] and is explained in detail in the supplementary material of [182].

For a given state of the system ρ_{lab}, the experimental group measures reduced density matrices (reductions) of k consecutive spins. This step is done via the full QST method described above. In total it is performed for all $(M - k + 1)$

reductions, where M is the total number of spins. Each of the reductions requires measurements in 3^k bases with 2^k distinct measurement outcomes. It should also be mentioned that non-overlapping reductions can be measured in parallel, i.e. for instance 3-spin reductions ρ_{123} and ρ_{456} do not have common spins and hence can be measured simultaneously. In [182] another step forward is taken and the measurement of *all* reductions is made simultaneously, which brings the total number of the measurement bases down to 3^k instead of $3^k(M-k+1)$.

At this point the experimental work is done and the post-processing starts, which consists of two main parts:

- A search for the MPS estimate $|\psi_{\mathrm{c}}^k\rangle$ of the lab state ρ_{lab}. This forms uncertified MPS tomography.
- Finding a lower bound on the fidelity F_{c}^k, such that the actual fidelity $F > F_{\mathrm{c}}^k$. This is the certification to MPS tomography.

The search for the MPS estimate is based on the combination of two methods: modified Singular Value Thresholding (SVT) [76] and iterative MLE [190]. The SVT method produces a first guess of the estimate state $|\psi_{\mathrm{est}}\rangle$, which is passed to MLE, which iteratively tunes the state and improves the match with data. Both algorithms scale polynomially with the number of spins M. One could also consider the possibility of using more advanced versions of MLE, where besides local expectation values one provides all two-point correlations matrices as input, but this was not done here.

At this point we have a state estimate $|\psi_{\mathrm{est}}\rangle$, but the convergence of the above methods is not proven. In what follows in this section we define the general procedure to obtain a lower bound for the state fidelity.

In order to define the bound we now look for a pure state $|\psi_{\mathrm{GS}}\rangle$, which is the ground state of some gapped parent Hamiltonian H_{par}, i.e. the two lowest eigenvalues of H_{par}, $E_0 < E_1$, have a gap. The optimal parent Hamiltonian should satisfy 2 conditions: $|\psi_{\mathrm{GS}}\rangle$ is close to $|\psi_{\mathrm{est}}\rangle$ and the energy gap of H_{par} should be as large as possible.

The optimal H_{par} is called the parent Hamiltonian and its ground state becomes the certified estimate state $|\psi_{\mathrm{c}}^k\rangle$. The fact of the parent Hamiltonian's existence allows [76] us to define the lower bound on the fidelity as

$$F \equiv \langle\psi_{\mathrm{c}}^k|\rho_{\mathrm{lab}}|\psi_{\mathrm{c}}^k\rangle \geq \frac{E-E_0}{E_1-E_0} \equiv F_{\mathrm{c}}^k, \tag{7.5}$$

where

$$E = \mathrm{tr}(\rho_{\mathrm{lab}} H_{\mathrm{par}}), \tag{7.6}$$

is the energy of the lab state assuming the parent Hamiltonian interactions, and is useful for calculating F, but otherwise has no physical meaning. Now one uses the knowledge about $k-$site reductions to determine the energy E. In order

to ensure statistical independence, the measured data is first separated into two parts: one of them is required to obtain the optimal parent Hamiltonian H_{par} and its ground state $|\psi_{\text{c}}^k\rangle$, and the second part is used for the estimation of E and its uncertainty, which will produce F_{c}^k and its uncertainty. The splitting of the data is done to avoid overestimating the fidelity bound by choosing a parent Hamiltonian tuned to the particular set of statistical fluctuations in a single set of measurable data.

In the supplementary materials of [182] it was proven that indeed in the case of a Hamiltonian with local interactions the algorithm of MPS tomography requires polynomial growth of resources in the size M, inverse polynomial with the tolerated infidelity of characterization, and exponential in the evolution time t. The last scaling is an expected result taking into account the light cone effects of the information propagation in systems with finite interactions [74] and reflect the exponential cost of full QST. The number of locally entangled spins after a global quench grows linearly in time, so one needs to increase the size of measured reductions linearly in time as well.

7.4. Experimental Results

In this section we apply the method of MPS tomography on the system of spin chains realized on linearly trapped ions of $^{40}Ca^{+}$. The general scheme of the experimental sequence was highlighted in Sec. 7.3 and Fig. 7.1, the initially prepared product state will be allowed to propagate for a short period of time obeying interactions described by the Hamiltonian (7.1). Then local reductions of k consecutive spins are measured. We will show that by increasing k from 1 to 3 one can significantly increase the fidelity of the state obtained via the MPS tomography. This will also be seen from the calculation of the certified bound.

The increase of the correlation length L in the system after the quench can also be calculated. In Sec. 4.1.2 we already presented several possible measures of entanglement for pure states. Here we are interested in the entanglement between partitions of the system, e.g. the entanglement between two particular spins. The state of the two spins of interest of the multi-spin system is not pure in general. In Sec. 7.4.1 we introduce an appropriate measure — the logarithmic negativity. In the later sections we present the results of the MPS tomography with 8 and 14 spins.

7.4.1. Logarithmic Negativity

For a generic system that consists of two partitions A and B described by the density matrix ρ_{AB} (in general mixed) the bipartite logarithmic negativity [114,

191] can be defined as

$$LN_2(\rho_{AB}) = \log_2 \left\| \rho_{AB}^{T_A} \right\|_1 , \tag{7.7}$$

where $\rho_{AB}^{T_A}$ defines partial transposition of the partition A and $\|...\|_1$ denotes the trace norm. In the case where A and B are not entangled the logarithmic negativity is equal to zero.

We also introduce the tripartite logarithmic negativity as the geometric mean of three bipartite logarithmic negativities. For a system of three parts A, B, and C, described by the state ρ_{ABC}, it reads

$$LN_3(\rho_{ABC}) = \sqrt[3]{LN_2(\rho_{A(BC)}) \cdot LN_2(\rho_{B(AC)}) \cdot LN_2(\rho_{C(AB)})}, \tag{7.8}$$

where

$$LN_2(\rho_{A(BC)}) = \log_2 \left\| \rho_{ABC}^{T_A} \right\|_1 , \tag{7.9}$$

i.e. the B and C parts are combined in one.

If A and B are two spin-$1/2$, as in our case, then

$$LN_2(\rho_{AB}) = \log_2(2|\sum_n \mu_n| + 1), \tag{7.10}$$

where μ_n are negative eigenvalues of $\rho_{AB}^{T_A}$.

7.4.2. Results of MPS Tomography

In this section we use certified MPS tomography on the experimental data for states of 8 and 14 ions.

7.4.2.1. 8 Ions

In Fig. 7.2 we present the compilation of results on the quench dynamics of the chain of $M = 8$ spins. The experiment starts with Néel ordered spins (7.4), which are allowed to evolve to approximately 10 ms with interactions modeled by (7.1). In Fig. 7.2(a) one can see the evolution of the magnetization. The two light cones drawn in the figure are guides for the eye showing an estimate of group velocity. This is first calculated assuming nearest neighbor interactions and rescaled accordingly for the long-range interaction (see [182] for more details). Fig. 7.2(b) shows an example of the two spin reduction (absolute values), the reconstruction is done using data later used to MPS tomography. As one can see from Fig. 7.2(c,d), a few milliseconds of evolution time is enough to significantly entangle all neighboring spins and Fig. 7.2(c,d) shows the bipartite LN_2 and tripartite LN_3 logarithmic negativities respectively.

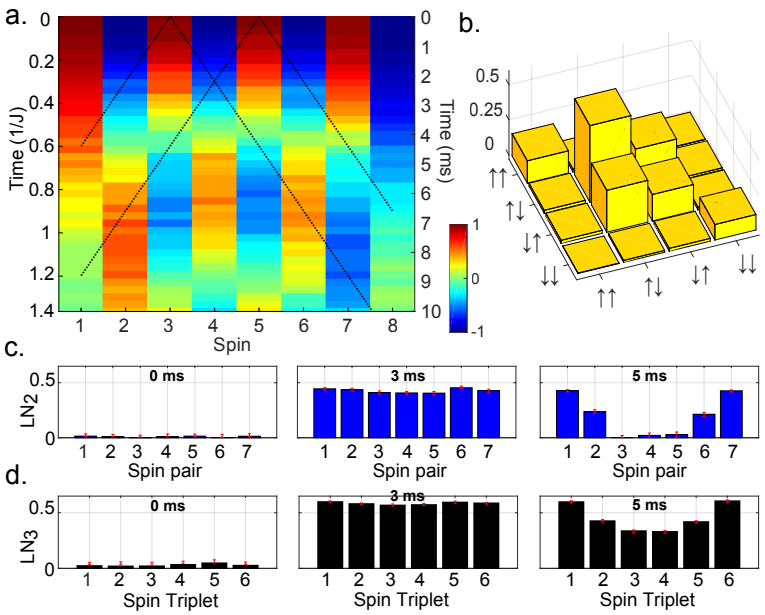

Figure 7.2.: Results of quench dynamics with the chain of 8 spins. (a) Single spin magnetization $\langle \sigma_i^z(t) \rangle$ after quench dynamics. Two light cones are shown, exemplifying an estimate for the group velocity at which correlations spread. (b) Absolute values of the elements of the local density matrix $\hat{\rho}_{34}$ at time $t = 3$ ms, reconstructed via the full QST and standard MLE [192]. The estimation fidelity against the theoretical model of $F = 0.99 \pm 0.01$. The state is entangled, with a bipartite logarithmic negativity of $LN_2 = 0.41 \pm 0.01$. (c-d) Bipartite LN_2 and tripartite LN_3 logarithmic negativities for all neighboring spin pairs at times $t = 0$, 3, and 5 ms. This figure was reproduced from [182].

Now it is important to see how well the state $|\psi_c^k\rangle$ estimated via MPS tomography can capture correlations between spins at long distances, noting that we used reductions of the size $k = 3$ to obtain the state estimate. In Fig. 7.3 we show three types of correlation matrices obtained in three different ways for the system of 8 ions at time 3 ms. Fig. 7.3(a) is obtained if one evolves the ideal initial state (7.4) as

$$|\phi(t)\rangle = \mathrm{e}^{-itH_{\mathrm{LRTI}}}|\phi(0)\rangle, \tag{7.11}$$

i.e. ignoring all imperfections in the system. The case in Fig. 7.3(b) with direct measurements shows the level of imperfections of measurements in the experiment with the chosen sampling. The case in Fig. 7.3(c) is the most interesting as it is obtained from the MPS tomography state $|\psi_c^3\rangle$. This case shows that MPS tomography captures strong spin-spin correlations successfully in this system. One can also see that correlations between spins at distances larger than $k = 3$ are captured as well. By this we mean that the majority of the correlation matrix elements' signs are captured, as well as their distribution pattern.

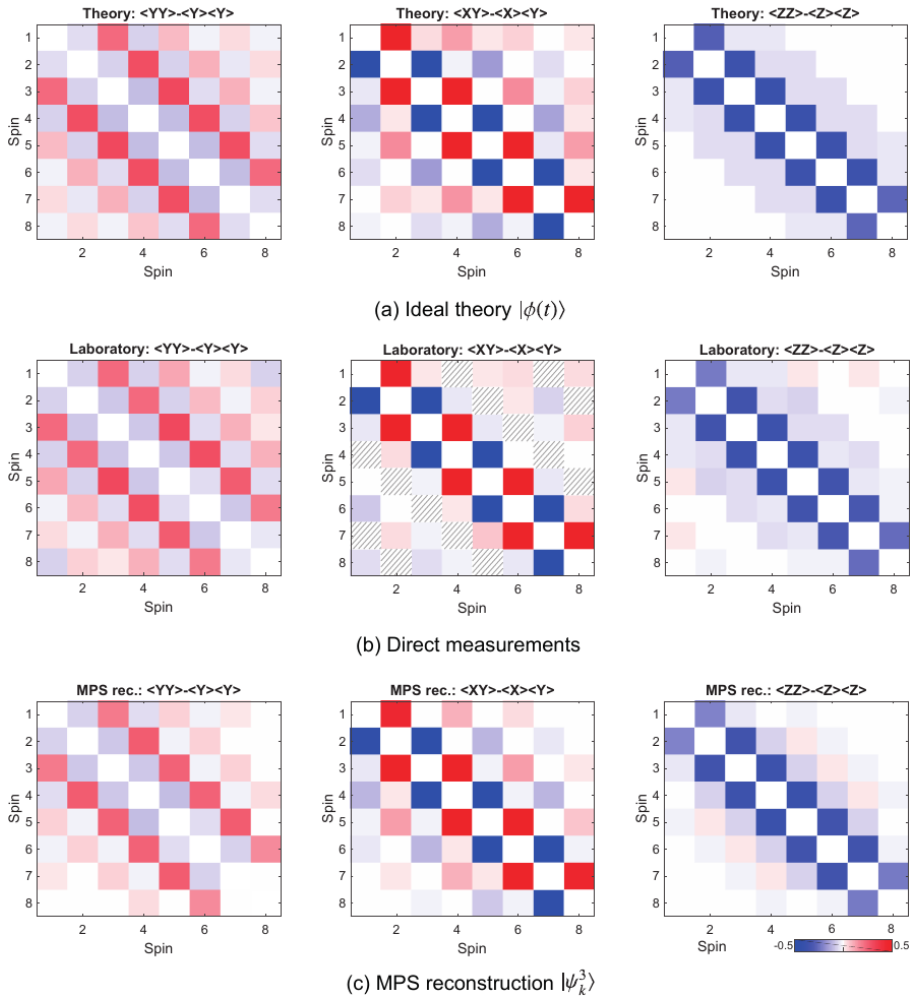

Figure 7.3.: Spin-spin correlation matrices at time $t = 3$ ms obtained from (a) the idealized case $|\phi(t)\rangle$ calculated numerically, (b) the direct experimental measurements, and (c) the reconstructed MPS state $|\psi_c^3\rangle$ (with $F_c^3 > 0.84 \pm 0.05$). The legend above each figure identifies the type of the correlations matrix, X, Y, or Z denote the base of the measurement/calculation so $\langle ZZ\rangle - \langle Z\rangle\langle Z\rangle$ means the correlation matrix $C_{ij}^{zz} = \langle\sigma_i^z(t)\sigma_j^z(t)\rangle - \langle\sigma_i^z(t)\rangle\langle\sigma_j^z(t)\rangle$. The hatched squares denote correlations that were not measured. This figure was reproduced from [182].

In Fig. 7.4 we present the certified bounds F_c^k for data obtained in the experiment and two theoretical models:

- The simulation done with the ideal time evolution (7.11) and exact calculation of reductions as $\rho_A = \mathrm{tr}_B(|\phi(t)\rangle\langle\phi(t)|)$ for each block of 3 spins.
- The ideal time evolution (7.11) with 1000 simulated measurements per observables (as in the lab), which also accounts for the expected statistical errors of measurements.

One can see that the second case approaches the experimental results quite closely. There are two main sources of discrepancy. First, non-ideal measurements in the experiment are made due to the finite number of samples. Secondly, the certification of the MPS tomography relies on the fact that the initial state is pure, which is not necessarily true in the experiment. The mixture happens at the stage of the state preparation. For instance, the preparation of the initial state can be estimated via single site MPS tomography, which produces $|\psi_c^1\rangle$. The overlap with the Néel ordered initial state is $|\langle\phi(0)|\psi_c^1\rangle|^2 = 0.98$ and the certified fidelity bound $F_c^1 = 0.98 \pm 0.01$. This shows that the system is initially well described by the state (7.4).

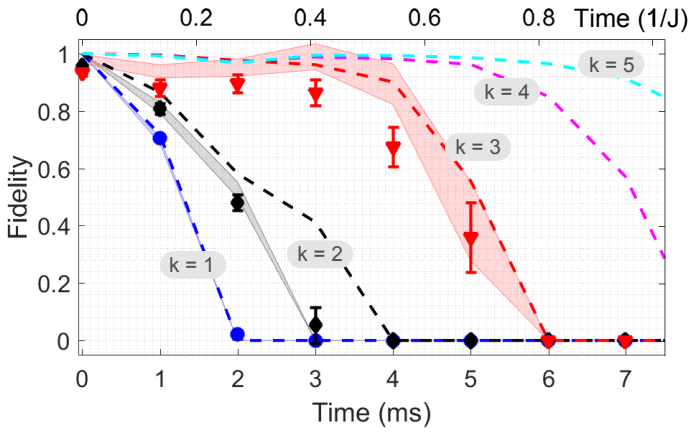

Figure 7.4.: Certified lower bounds on the fidelity F_c^k between $|\psi_c^k\rangle$ (the MPS tomography reconstructed state with $k-$spin reductions) and the quantum simulator state ρ_{lab}, i.e. obtained experimentally. **Shapes** shows the MPS tomography results based on experimental measurements for $k = 1$, 2, and 3. **Dashed lines** are obtained if one uses the MPS tomography on idealized simulator dynamics $|\phi(t)\rangle$ (i.e. calculated numerically) for $k = 1$ to 5. **Shaded area**: the MPS tomography is done on the ideal $|\phi(t)\rangle$, but calculations of each observable is simulated with 1000 samples (as in the lab) for $k = 1$, 2, and 3. This figure was reproduced from [182].

As expected, the fidelity lower bound for $k = 1$ quickly degrades in Fig. 7.4 due to entangling of neighboring spins, which makes it impossible to estimate the state with a product state. As one increases the size of reductions k, the certified fidelity lower bound starts degrading at later and later times.

Note that experimentally this case of 8 spins is still possible for estimation via the full QST, however it requires measurements in all 3^8 bases, which was done in [189] and took over ten hours (this number depends on the number of samples per each base as well). Here the largest reductions of $k = 3$ spins each required measurements in 3^3 bases and 1000 samples for each basis. This reduced the experimental measurement time to approximately 10 minutes [182].

7.4.2.2. 14 Ions

The case of 14 ions is already far beyond capabilities of the full QST, which would require measurements in 3^{14} bases and hence the method of obtaining the results presented in this section is unique. A certified MPS estimate is obtained with measurement of local reductions of all block of $k = 3$ neighboring spins.

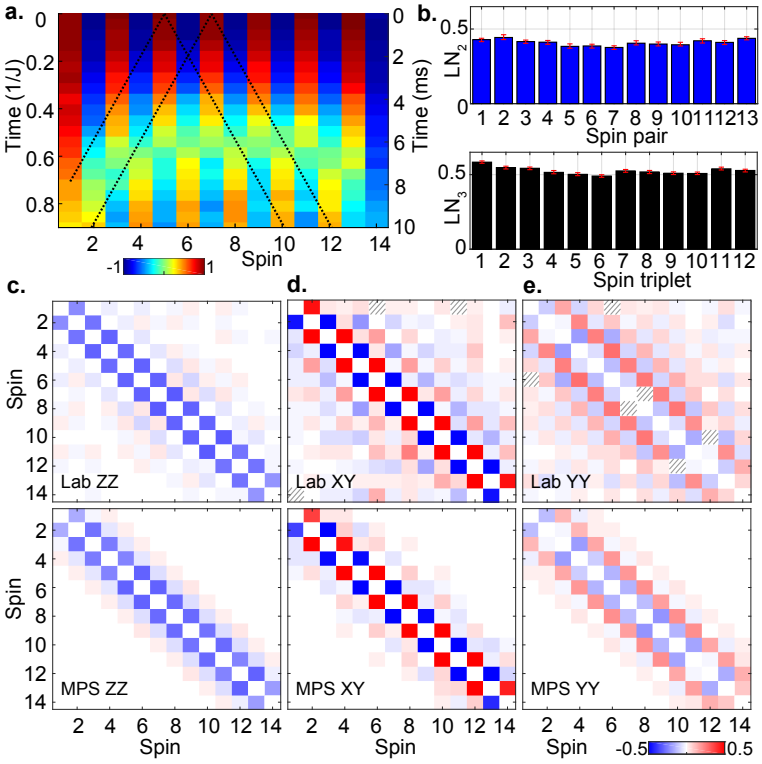

Figure 7.5.: Results of the quench dynamics with the chain of 14 spins. (a). Measurements of the single spin magnetization $\langle \sigma_i^z(t) \rangle$ with two estimated light-like cones as guides of eye. (b). Bipartite LN_2 and tripartite LN_3 logarithmic negativities for all neighboring spins at time $t = 4$ ms. The reductions are reconstructed via the full QST. (c-e) Comparison of the correlation matrix C_{ij}^{zz}, C_{ij}^{xy}, and C_{ij}^{yy} at $t = 3$ ms measured on ρ_{lab} and derived from $|\psi_c^3\rangle$. The 14-spin MPS estimate $|\psi_c^3\rangle$ is seen to capture many of the correlations between spins up to 4 spins apart. The development of weak correlations over greater distances in the laboratory state is due to the long-range interactions (7.2). This figure was reproduced from [182].

In Fig. 7.5 one can see the result of the quench dynamics with 14 spins initially prepared in the Néel ordered pure state (7.4). The decay of the spin-spin interactions in the Hamiltonian (7.1) can be best approximated by the power law (7.2) with the decay exponent $\alpha \approx 1.27$. Comparing to the case of 8 ions we have longer-range interactions here, hence the spread of the correlations should be more distinguished from the linear case, e.g., algebraically decaying correlations

outside of the light cone span over larger distances (see Fig. 6.3(b)).

The values of the bipartite LN_2 and tripartite LN_3 logarithmic negativities measured for local reductions at $t = 4$ ms clearly show the build up of entanglement after the quench. By looking at Fig. 7.5(c-e) one can see how well various correlations matrices are captured. We first notice that the signs and the general pattern in near order of correlations obtained via $|\psi_c^3\rangle$ matches quite closely with those obtained in the lab. This also shows evidence of the limitations of MPS tomography. Since the system Hamiltonian is non-local it leads to long-range interactions building up between distant spins right after the quench (see Sec. 6.3 where we investigated it in great detail). These correlations are not captured via measuring reductions of only neighboring spins.

The certified minimum fidelity of the MPS estimated state $|\psi_c^3\rangle$ is $F_c^3 = 0.39 \pm 0.08$ at $t = 4$ ms. It is possible to ask for the exact fidelity. In order to obtain it one needs to calculate the overlap between the lab state ρ_{lab}, which in general can be mixed, and the output of the MPS tomography $|\psi_c^3\rangle$, which reads

$$F(|\psi_c^3\rangle, \rho_{\text{lab}}) = \langle\psi_c^3|\rho_{\text{lab}}|\psi_c^3\rangle. \tag{7.12}$$

This requires exponentially many measurements (in the number of spins M) and stumbles over the same experimental problem. That is why this problem was resolved via the Direct Fidelity Estimation (DFE) method [186,187]. In short the DFE method estimates the overlap sampling only the most feasible contributions, for details on the realizations please read the supplementary material of [182]. The actual overlap from the DFE method gives the fidelity equal $F = 0.74 \pm 0.05$, which is larger than the certified lower bound F_c^3.

It is clear from our results that certified MPS tomography provides a good estimate of the 14-ion state and that the provided fidelity lower bound F_c^3 is correct as well. However it can be seen from the actual numbers that the bound F_c^3 is quite far from the actual value of the fidelity F. One of the main sources of this discrepancy is the error of the initial state preparation in the lab, including the mixture of the state, i.e. the state is not fully pure ($|\langle\phi(0)|\psi_c^1\rangle|^2 = 0.89 \pm 0.01$).

7.5. Resource Cost

In this section we will answer the question that naturally comes to mind to everyone who hears about a new method of state estimation: What is the actually resource cost? MPS tomography for a system of M spins requires measurement of $M - k + 1$ reduced density matrices, each of them requires measurement in the 3^k bases. Measurements in each basis have 2^k distinguishable outcomes (see Sec. 7.3.1). If N_{meas} measurements are taken for each basis, then the total number of the measurements per state is

$$N_{\text{meas}}^{\text{total}} = N_{\text{meas}}(M - k + 1)3^k. \tag{7.13}$$

By performing parallel measurements it is possible to reduce it down to

$$N_{\text{meas}}^{\text{total}} = N_{\text{meas}} 3^k, \tag{7.14}$$

where the measurement is done not for $k-$spin block, but rather for the entire chain of M spins.

Then MPS tomography is efficient only if the total number of measurements required for a constant error scales polynomially with M. In other words we want to know how N_{meas} should grow with M in order to contain the error at the same level.

We quantify the error as the trace distance

$$D = \sqrt{1 - |\langle\phi|\psi_{\text{est}}\rangle|^2}, \tag{7.15}$$

where $|\psi_{\text{est}}\rangle$ is the MPS estimated state and $|\phi\rangle$ is the ideal state that we want to estimate.

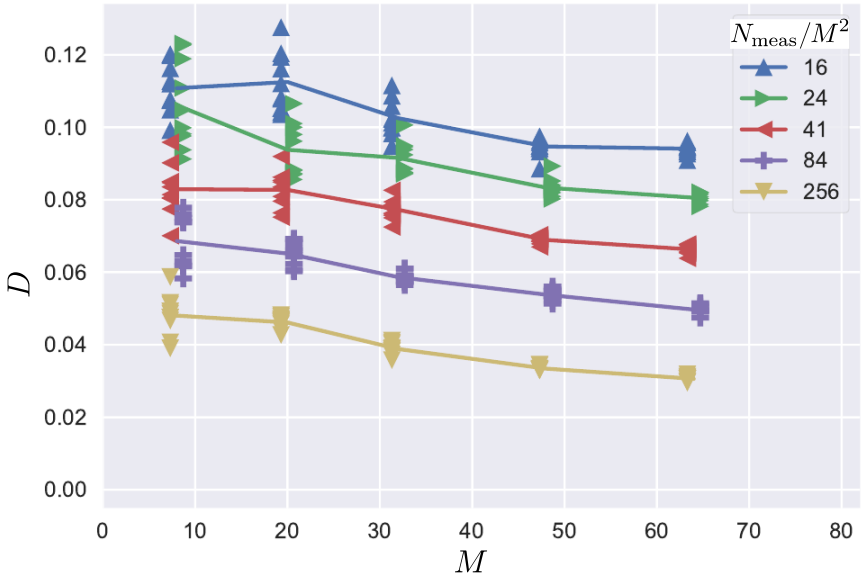

Figure 7.6.: Error estimation for MPS tomography. The dependence of the trace distance D (between the MPS estimated state with $k = 3$ and the ideal state) vs the system size M. As long as the number of measurements N_{meas} changes proportional to M^2 the error, D, can be bounded by a constant. This figure was reproduced from [182].

In order to estimate the error, we performed numerical calculations and generated

the series of ideal states $|\phi\rangle$ for $M = \{8, 20, 32, 48, 64\}$ spins at time $t = 3$ ms. The Hamiltonian was chosen to be in the nearest-neighbor form, i.e. $\alpha \to \infty$ with parameters taken from the 8-spin case (see Sec. 7.3). The states were obtained numerically via the TDVP method with MPS [121] (see Sec. 4.3.3 for details).

We then simulated N_{meas} measurements in each 3^k bases for all $M - k + 1$ blocks. By this we mean that for each local spin block there are 3^k different Pauli observables with 2^k distinguishable outcomes each (see Sec. 7.3.1). For each outcome the exact probability is computed (since we know the exact state). The simulation of measurements means that we draw N_{meas} outcomes out of this pool of 2^k outputs with appropriate probabilities. In the limit $N_{\text{meas}} \to \infty$ we find the exact probabilities, and the expectation values are reconstructed. However the finite number of samples leads to fluctuations of the expectation values.

Each reconstruction was also repeated 10 times in order to account for fluctuations in the reconstruction error due to the finite number of measurements. In Fig. 7.6 one can see the results for $k = 3$, in the case when $N_{\text{meas}} \propto M^2$ the trace distance D can be contained at a constant level. This means that the total number of measurements $N_{\text{meas}}^{\text{total}}$ grows polynomially with the system size M as well. This makes MPS tomography efficient compared to the full QST, which requires an exponential growth of measurements.

7.6. Conclusions

We have presented here a successful application of a new technique for the quantum state estimation — certified MPS tomography. It allows us to reliably estimate the state of a broad class of many-body quantum systems. In comparison to QST, certified MPS tomography aims at efficient estimation of only weakly entangled states. We show that by performing only a polynomial number of measurements one can obtain a certified state estimate in a form of an MPS with a low bond dimension. This method is particularly useful for large system sizes, whereas QST is not applicable due to its exponential cost in the number of system constituents.

We find that MPS tomography is well-suited for characterization of the states generated at short times of the quench dynamics as the majority of correlations are short-ranged and can be captured via measurement of local reduced density matrices. Nonetheless, there is always a potential to extend the idea of MPS tomography to systems with non-local interactions or state at later times of evolution by using measurement of reductions beyond neighboring spins.

Results presented here are for one dimensional systems for which the accuracy of the reconstructed pure state is certified by the fidelity lower bound. It is possible to generalize the method to higher spatial dimensions and to mixed-states via Matrix Product Operators [190, 193]. However, there is no certification method for mixed states [194] at the moment.

8. Conclusions and Outlook

The work presented in this thesis illustrates the range of possibilities offered by cold neutral atoms in optical lattices and trapped ions in terms of quantum simulation. It was shown that resonant long-range tunneling dynamics of atoms in a tilted periodic potential can be effectively modeled by a spin chain with long-range interactions, which causes unusual magnetic ordering in the ground state. Trapped ions, due to their high degree of experimental control and tunable range of interactions, have extensive applications from fundamental questions of entanglement to efficient quantum computation of problems that are intractable by classical computers. Of course, these topics do not cover all the perspectives opened by these two systems, but they provide examples of the capabilities that exist. Below we list a further more detailed outlook for each of the systems.

As was shown in Chap. 5, systems of ultracold atoms loaded into optical lattices can play a role of quantum simulators of complex strongly-correlated systems, for instance, systems with exotic magnetically ordered phases. Beyond the characterization of the phase transition in the case of the next-next neighboring resonant tunneling ($E = U/2$), which will be finalized in [195, 196], this project can take several possible directions in the future. First, it would be very interesting to see experimental implementation of the tilted superlattice geometry that is modeled by effective spins in Sec. 5.2.2. This work is already possible in existing experiments and would provide an opportunity to realize a model with exotic magnetism in the laboratory. Secondly, the project can progress in the direction of higher dimensionality and different geometries, as was considered for the $E = U$ case in Ref. [60]. Then questions of frustration and coexisting phases in different directions can be studied. This would also extend the range of exotic magnetic systems simulated via optical lattices. Last, the model in Sec. 5.2.2, can be studied away from the context of optical lattices. A gradual decrease of interactions between even and odd spins decouples the subchains; the nature of this transition can be studied by means of finite-size scaling, and current DMRG methods.

In the future it would be interesting to extend the study of long-range spin chains (Chap. 6) in three major directions. First, it would be interesting to take advantage of the slow logarithmic growth of entanglement and use this for extending the time evolution with DMRG techniques. For this, a more systematic study of symmetries has to be performed, which in general also depends on the initial state of the dynamics. Secondly, an analogous study can be performed with two dimensional spin systems, e.g. $^9Be^+$ ions stored in a Penning trap [68, 107]. The

potential of finding regimes where the quench dynamics produces slowly growing or small entanglement makes it suitable for efficient simulations with DMRG methods. Last, there is growing interest in hybride quantum systems, in particular with ion chains [197]. This idea is aimed to solving the problem of scalability of ion chains by connecting small, well controlled, systems via quantum channels of flying qubits. One can think about the entire system as about coupled ion chains, which makes the problem quasi two dimensional. Numerical simulations with existing DMRG methods might lead us to future possibilities and limitations of such quantum computing architectures.

In Chap. 7 we applied a new quantum state estimation technique (the certified MPS tomography) on ion chains modeled by the long-range Ising model. We find that MPS tomography is well-suited for estimation of the states generated at short times by quench dynamics, as the majority of correlations are short-ranged and can be captured via measurement of only local reduced density operators. Nonetheless, there is always a potential to extend the idea of MPS tomography to systems with non-local interactions or states generated at later times of the evolution. This could be done via the use of extended maximum likelihood estimation (MLE) techniques with measurements of reductions beyond neighboring spins [76]. It is also possible to implement an uncertified version of MPS tomography for two dimensional spin systems, as well as to include the possibility for mixed states due to imperfections of the state initialization or coupling with the environment. This version would be called MPO tomography [190, 193].

The work presented in this thesis heavily relies on the efficiency of DMRG methods combined with matrix product representations of states and operators for 1D systems. The development of other tensor network techniques, such us PEPS [80] and MERA [113], might help us in the future to achieve equal success for higher dimensional quantum systems. In either case more effort should be invented in these methods and incorporated, for example, with any of the above projects.

Bibliography

[1] I. Bloch, J. Dalibard, and S. Nascimbéne, "Quantum simulations with ultracold quantum gases," *Nature Physics*, vol. 8, no. 4, pp. 267–276, 2012.

[2] R. Blatt and C. F. Roos, "Quantum simulations with trapped ions," *Nature Physics*, vol. 8, no. 4, pp. 277–284, 2012.

[3] A. J. Leggett, "What DO we know about high Tc?," *Nature Physics*, vol. 2, no. 3, pp. 134–136, 2006.

[4] P. W. Shor, "Polynomial-time algorithms for prime factorization and discrete logarithms on a quantum computer," *SIAM Review*, vol. 41, no. 2, pp. 303–332, 1999.

[5] F. Dalfovo, S. Giorgini, L. P. Pitaevskii, and S. Stringari, "Theory of Bose-Einstein condensation in trapped gases," *Rev. Mod. Phys.*, vol. 71, pp. 463–512, 1999.

[6] A. J. Leggett, "Bose-Einstein condensation in the alkali gases: Some fundamental concepts," *Rev. Mod. Phys.*, vol. 73, pp. 307–356, 2001.

[7] L. P. Pitaevskii and S. Stringari, *Bose-Einstein Condensation*. Oxford University Press, 2003.

[8] C. J. Pethick and H. Smith, *Bose-Einstein Condensation in Dilute Gases*. Cambridge University Press, 2008.

[9] M. H. Anderson, J. R. Ensher, M. R. Matthews, C. E. Wieman, and E. A. Cornell, "Observation of Bose-Einstein condensation in a dilute atomic vapor," *Science*, vol. 269, no. 5221, pp. 198–201, 1995.

[10] C. C. Bradley, C. A. Sackett, J. J. Tollett, and R. G. Hulet, "Evidence of Bose-Einstein condensation in an atomic gas with attractive interactions," *Phys. Rev. Lett.*, vol. 75, pp. 1687–1690, 1995.

[11] K. B. Davis, M. O. Mewes, M. R. Andrews, N. J. van Druten, D. S. Durfee, D. M. Kurn, and W. Ketterle, "Bose-Einstein condensation in a gas of sodium atoms," *Phys. Rev. Lett.*, vol. 75, pp. 3969–3973, 1995.

[12] H. J. Metcalf and P. van der Straten, *Laser Cooling and Trapping*. Springer New York, 2012.

[13] W. Ketterle and N. V. Druten, "Evaporative cooling of trapped atoms," *Advances In Atomic, Molecular, and Optical Physics*, vol. 37, pp. 181 – 236, 1996.

[14] A. E. Leanhardt, T. A. Pasquini, M. Saba, A. Shirotzek, Y. Shin, D. Kielpinski, D. E. Pritchard, and W. Ketterle, "http://www.guinnessworldrecords.com/world-records/lowest-manmade-temperature/," 2003.

[15] E. A. Donley, N. R. Claussen, S. T. Thompson, and C. E. Wieman, "Atom-molecule coherence in a Bose-Einstein condensate," *Nature*, vol. 417, no. 6888, pp. 529–533, 2002.

[16] T. Loftus, C. A. Regal, C. Ticknor, J. L. Bohn, and D. S. Jin, "Resonant control of elastic collisions in an optically trapped Fermi gas of atoms," *Phys. Rev. Lett.*, vol. 88, p. 173201, 2002.

[17] M. Theis, G. Thalhammer, K. Winkler, M. Hellwig, G. Ruff, R. Grimm, and J. H. Denschlag, "Tuning the scattering length with an optically induced Feshbach resonance," *Phys. Rev. Lett.*, vol. 93, p. 123001, 2004.

[18] C. Chin, R. Grimm, P. Julienne, and E. Tiesinga, "Feshbach resonances in ultracold gases," *Rev. Mod. Phys.*, vol. 82, pp. 1225–1286, 2010.

[19] S. Inouye, M. R. Andrews, J. Stenger, H.-J. Miesner, D. M. Stamper-Kurn, and W. Ketterle, "Observation of Feshbach resonances in a Bose-Einstein condensate," *Nature*, vol. 392, no. 6672, pp. 151–154, 1998.

[20] E. Timmermans, P. Tommasini, M. Hussein, and A. Kerman, "Feshbach resonances in atomic Bose-Einstein condensates," *Physics Reports*, vol. 315, no. 1, pp. 199 – 230, 1999.

[21] M. Greiner, C. A. Regal, and D. S. Jin, "Emergence of a molecular Bose-Einstein condensate from a Fermi gas," *Nature*, vol. 426, no. 6966, pp. 537–540, 2003.

[22] M. W. Zwierlein, C. A. Stan, C. H. Schunck, S. M. F. Raupach, S. Gupta, Z. Hadzibabic, and W. Ketterle, "Observation of Bose-Einstein condensation of molecules," *Phys. Rev. Lett.*, vol. 91, p. 250401, 2003.

[23] B. DeMarco and D. S. Jin, "Onset of Fermi degeneracy in a trapped atomic gas," *Science*, vol. 285, no. 5434, pp. 1703–1706, 1999.

[24] B. DeMarco, S. B. Papp, and D. S. Jin, "Pauli blocking of collisions in a quantum degenerate atomic Fermi gas," *Phys. Rev. Lett.*, vol. 86, pp. 5409–5412, 2001.

[25] A. G. Truscott, K. E. Strecker, W. I. McAlexander, G. B. Partridge, and R. G. Hulet, "Observation of Fermi pressure in a gas of trapped atoms," *Science*, vol. 291, no. 5513, pp. 2570–2572, 2001.

[26] F. Schreck, G. Ferrari, K. L. Corwin, J. Cubizolles, L. Khaykovich, M.-O. Mewes, and C. Salomon, "Sympathetic cooling of bosonic and fermionic lithium gases towards quantum degeneracy," *Phys. Rev. A*, vol. 64, p. 011402, 2001.

[27] G. Roati, F. Riboli, G. Modugno, and M. Inguscio, "Fermi-Bose quantum degenerate ^{40}K−^{87}Rb mixture with attractive interaction," *Phys. Rev. Lett.*, vol. 89, p. 150403, 2002.

[28] K. E. Strecker, G. B. Partridge, and R. G. Hulet, "Conversion of an atomic Fermi gas to a long-lived molecular Bose gas," *Phys. Rev. Lett.*, vol. 91, p. 080406, 2003.

[29] S. Jochim, M. Bartenstein, A. Altmeyer, G. Hendl, S. Riedl, C. Chin, J. Hecker Denschlag, and R. Grimm, "Bose-Einstein condensation of molecules," *Science*, vol. 302, no. 5653, pp. 2101–2103, 2003.

[30] T. Bourdel, L. Khaykovich, J. Cubizolles, J. Zhang, F. Chevy, M. Teichmann, L. Tarruell, S. J. J. M. F. Kokkelmans, and C. Salomon, "Experimental study of the BEC-BCS crossover region in Lithium 6," *Phys. Rev. Lett.*, vol. 93, p. 050401, 2004.

[31] D. Jaksch, C. Bruder, J. I. Cirac, C. W. Gardiner, and P. Zoller, "Cold bosonic atoms in optical lattices," *Phys. Rev. Lett.*, vol. 81, pp. 3108–3111, 1998.

[32] M. Greiner, O. Mandel, T. Esslinger, T. W. Hänsch, and I. Bloch, "Quantum phase transition from a superfluid to a Mott insulator in a gas of ultracold atoms," *Nature*, vol. 415, no. 6867, pp. 39–44, 2002.

[33] M. Greiner, O. Mandel, T. W. Hansch, and I. Bloch, "Collapse and revival of the matter wave field of a Bose-Einstein condensate," *Nature*, vol. 419, no. 6902, pp. 51–54, 2002.

[34] R. Jordens, N. Strohmaier, K. Gunter, H. Moritz, and T. Esslinger, "A Mott insulator of fermionic atoms in an optical lattice," *Nature*, vol. 455, no. 7210, pp. 204–207, 2008.

[35] K. Günter, T. Stöferle, H. Moritz, M. Köhl, and T. Esslinger, "Bose-Fermi mixtures in a three-dimensional optical lattice," *Phys. Rev. Lett.*, vol. 96, p. 180402, 2006.

[36] J. G. Danzl, M. J. Mark, E. Haller, M. Gustavsson, R. Hart, J. Aldegunde, J. M. Hutson, and H.-C. Nagerl, "An ultracold high-density sample of rovibronic ground-state molecules in an optical lattice," *Nature Physics*, vol. 6, no. 4, pp. 265–270, 2010.

[37] A. Chotia, B. Neyenhuis, S. A. Moses, B. Yan, J. P. Covey, M. Foss-Feig, A. M. Rey, D. S. Jin, and J. Ye, "Long-lived dipolar molecules and Feshbach molecules in a 3d optical lattice," *Phys. Rev. Lett.*, vol. 108, p. 080405, 2012.

[38] D. Jaksch and P. Zoller, "The cold atom Hubbard toolbox," *Annals of Physics*, vol. 315, no. 1, pp. 52 – 79, 2005. Special Issue.

[39] L. Santos, M. A. Baranov, J. I. Cirac, H.-U. Everts, H. Fehrmann, and M. Lewenstein, "Atomic quantum gases in Kagomé lattices," *Phys. Rev. Lett.*, vol. 93, p. 030601, 2004.

[40] S. Safaei, C. Miniatura, and B. Grémaud, "Triangular and honeycomb lattices of cold atoms in optical cavities," *Phys. Rev. A*, vol. 92, p. 043810, 2015.

[41] L. Guidoni, C. Triché, P. Verkerk, and G. Grynberg, "Quasiperiodic optical lattices," *Phys. Rev. Lett.*, vol. 79, pp. 3363–3366, 1997.

[42] S. Peil, J. V. Porto, B. L. Tolra, J. M. Obrecht, B. E. King, M. Subbotin, S. L. Rolston, and W. D. Phillips, "Patterned loading of a Bose-Einstein condensate into an optical lattice," *Phys. Rev. A*, vol. 67, p. 051603, 2003.

[43] O. Mandel, M. Greiner, A. Widera, T. Rom, T. W. Hänsch, and I. Bloch, "Coherent transport of neutral atoms in spin-dependent optical lattice potentials," *Phys. Rev. Lett.*, vol. 91, p. 010407, 2003.

[44] S. Folling, F. Gerbier, A. Widera, O. Mandel, T. Gericke, and I. Bloch, "Spatial quantum noise interferometry in expanding ultracold atom clouds," *Nature*, vol. 434, no. 7032, pp. 481–484, 2005.

[45] W. S. Bakr, J. I. Gillen, A. Peng, S. Folling, and M. Greiner, "A quantum gas microscope for detecting single atoms in a Hubbard-regime optical lattice," *Nature*, vol. 462, no. 7269, pp. 74–77, 2009.

[46] J. F. Sherson, C. Weitenberg, M. Endres, M. Cheneau, I. Bloch, and S. Kuhr, "Single-atom-resolved fluorescence imaging of an atomic Mott insulator," *Nature*, vol. 467, no. 7311, pp. 68–72, 2010.

[47] E. Haller, J. Hudson, A. Kelly, D. A. Cotta, B. Peaudecerf, G. D. Bruce, and S. Kuhr, "Single-atom imaging of fermions in a quantum-gas microscope," *Nature Physics*, vol. 11, no. 9, pp. 738–742, 2015.

[48] L. W. Cheuk, M. A. Nichols, M. Okan, T. Gersdorf, V. V. Ramasesh, W. S. Bakr, T. Lompe, and M. W. Zwierlein, "Quantum-gas microscope for fermionic atoms," *Phys. Rev. Lett.*, vol. 114, p. 193001, 2015.

[49] M. F. Parsons, F. Huber, A. Mazurenko, C. S. Chiu, W. Setiawan, K. Wooley-Brown, S. Blatt, and M. Greiner, "Site-resolved imaging of fermionic ^{6}Li in an optical lattice," *Phys. Rev. Lett.*, vol. 114, p. 213002, 2015.

[50] D. Clément, N. Fabbri, L. Fallani, C. Fort, and M. Inguscio, "Exploring correlated 1d Bose gases from the superfluid to the Mott-insulator state by inelastic light scattering," *Phys. Rev. Lett.*, vol. 102, p. 155301, 2009.

[51] N. Gemelke, X. Zhang, C.-L. Hung, and C. Chin, "In situ observation of incompressible Mott-insulating domains in ultracold atomic gases," *Nature*, vol. 460, no. 7258, pp. 995–998, 2009.

[52] S. Will, T. Best, U. Schneider, L. Hackermuller, D.-S. Luhmann, and I. Bloch, "Time-resolved observation of coherent multi-body interactions in quantum phase revivals," *Nature*, vol. 465, no. 7295, pp. 197–201, 2010.

[53] C. Weitenberg, M. Endres, J. F. Sherson, M. Cheneau, P. Schausz, T. Fukuhara, I. Bloch, and S. Kuhr, "Single-spin addressing in an atomic Mott insulator," *Nature*, vol. 471, no. 7338, pp. 319–324, 2011.

[54] J. Simon, W. S. Bakr, R. Ma, M. E. Tai, P. M. Preiss, and M. Greiner, "Quantum simulation of antiferromagnetic spin chains in an optical lattice," *Nature*, vol. 472, no. 7343, pp. 307–312, 2011.

[55] F. Meinert, M. J. Mark, E. Kirilov, K. Lauber, P. Weinmann, A. J. Daley, and H.-C. Nägerl, "Quantum quench in an atomic one-dimensional Ising chain," *Phys. Rev. Lett.*, vol. 111, p. 053003, 2013.

[56] F. Meinert, M. J. Mark, E. Kirilov, K. Lauber, P. Weinmann, M. Gröbner, A. J. Daley, and H.-C. Nägerl, "Observation of many-body dynamics in long-range tunneling after a quantum quench," *Science*, vol. 344, no. 6189, pp. 1259–1262, 2014.

[57] Q. Thommen, J. C. Garreau, and V. Zehnlé, "Atomic motion in tilted optical lattices: an analytical approach," *Journal of Optics B: Quantum and Semiclassical Optics*, vol. 6, no. 7, pp. 301–308, 2004.

[58] P. M. Preiss, R. Ma, M. E. Tai, A. Lukin, M. Rispoli, P. Zupancic, Y. Lahini, R. Islam, and M. Greiner, "Strongly correlated quantum walks in optical lattices," *Science*, vol. 347, no. 6227, pp. 1229–1233, 2015.

[59] S. Sachdev, K. Sengupta, and S. M. Girvin, "Mott insulators in strong electric fields," *Phys. Rev. B*, vol. 66, p. 075128, 2002.

[60] S. Pielawa, T. Kitagawa, E. Berg, and S. Sachdev, "Correlated phases of bosons in tilted frustrated lattices," *Phys. Rev. B*, vol. 83, p. 205135, 2011.

[61] P. O. Schmidt, T. Rosenband, C. Langer, W. M. Itano, J. C. Bergquist, and D. J. Wineland, "Spectroscopy using quantum logic," *Science*, vol. 309, no. 5735, pp. 749–752, 2005.

[62] D. Leibfried, D. M. Meekhof, B. E. King, C. Monroe, W. M. Itano, and D. J. Wineland, "Experimental determination of the motional quantum state of a trapped atom," *Phys. Rev. Lett.*, vol. 77, pp. 4281–4285, 1996.

[63] J. I. Cirac and P. Zoller, "Quantum computations with cold trapped ions," *Phys. Rev. Lett.*, vol. 74, pp. 4091–4094, 1995.

[64] B. E. King, C. S. Wood, C. J. Myatt, Q. A. Turchette, D. Leibfried, W. M. Itano, C. Monroe, and D. J. Wineland, "Cooling the collective motion of trapped ions to initialize a quantum register," *Phys. Rev. Lett.*, vol. 81, pp. 1525–1528, 1998.

[65] H. Häffner, C. Roos, and R. Blatt, "Quantum computing with trapped ions," *Physics Reports*, vol. 469, no. 4, pp. 155 – 203, 2008.

[66] K. Kim, S. Korenblit, R. Islam, E. E. Edwards, M.-S. Chang, C. Noh, H. Carmichael, G.-D. Lin, L.-M. Duan, C. C. J. Wang, J. K. Freericks,

and C. Monroe, "Quantum simulation of the transverse Ising model with trapped ions," *New Journal of Physics*, vol. 13, no. 10, p. 105003, 2011.

[67] B. P. Lanyon, C. Hempel, D. Nigg, M. Müller, R. Gerritsma, F. Zähringer, P. Schindler, J. T. Barreiro, M. Rambach, G. Kirchmair, M. Hennrich, P. Zoller, R. Blatt, and C. F. Roos, "Universal digital quantum simulation with trapped ions," *Science*, vol. 334, no. 6052, pp. 57–61, 2011.

[68] J. W. Britton, B. C. Sawyer, A. C. Keith, C.-C. J. Wang, J. K. Freericks, H. Uys, M. J. Biercuk, and J. J. Bollinger, "Engineered two-dimensional Ising interactions in a trapped-ion quantum simulator with hundreds of spins," *Nature*, vol. 484, pp. 489–492, 2012.

[69] S. Olmschenk, K. C. Younge, D. L. Moehring, D. N. Matsukevich, P. Maunz, and C. Monroe, "Manipulation and detection of a trapped yb^+ hyperfine qubit," *Phys. Rev. A*, vol. 76, p. 052314, 2007.

[70] K. Kim, M.-S. Chang, R. Islam, S. Korenblit, L.-M. Duan, and C. Monroe, "Entanglement and tunable spin-spin couplings between trapped ions using multiple transverse modes," *Phys. Rev. Lett.*, vol. 103, p. 120502, 2009.

[71] K. Kim, M.-S. Chang, S. Korenblit, R. Islam, E. E. Edwards, J. K. Freericks, G.-D. Lin, L.-M. Duan, and C. Monroe, "Quantum simulation of frustrated Ising spins with trapped ions," *Nature*, vol. 465, no. 7298, pp. 590–593, 2010.

[72] E. E. Edwards, S. Korenblit, K. Kim, R. Islam, M.-S. Chang, J. K. Freericks, G.-D. Lin, L.-M. Duan, and C. Monroe, "Quantum simulation and phase diagram of the transverse-field Ising model with three atomic spins," *Phys. Rev. B*, vol. 82, p. 060412, 2010.

[73] R. Islam, E. E. Edwards, K. Kim, S. Korenblit, C. Noh, H. Carmichael, G.-D. Lin, L.-M. Duan, C.-C. Joseph Wang, J. K. Freericks, and C. Monroe, "Onset of a quantum phase transition with a trapped ion quantum simulator," *Nature Communications*, vol. 2, p. 377, 2011.

[74] E. H. Lieb and D. W. Robinson, "The finite group velocity of quantum spin systems," *Commun. Math. Phys.*, vol. 28, no. 3, pp. 251–257, 1972.

[75] K. Vogel and H. Risken, "Determination of quasiprobability distributions in terms of probability distributions for the rotated quadrature phase," *Phys. Rev. A*, vol. 40, pp. 2847–2849, 1989.

[76] M. Cramer, M. B. Plenio, S. T. Flammia, R. Somma, D. Gross, S. D. Bartlett, O. Landon-Cardinal, D. Poulin, and Y.-K. Liu, "Efficient quantum state tomography," *Nature Communications*, vol. 1, p. 149, 2010.

[77] R. M. Noack and S. R. Manmana, "Diagonalization- and numerical renormalization-group-based methods for interacting quantum systems," *AIP Conference Proceedings*, vol. 789, no. 1, pp. 93–163, 2005.

[78] W. H. Press, B. P. Flannery, S. A. Teukolsky, and W. T. Vetterling, *Numerical Recipes in Fortran 77: The Art of Scientific Computing*. Cambridge University Press, 1992.

[79] Y. Saad, *Numerical Methods for Large Eigenvalue Problems*. Cambridge University Press, 2011.

[80] F. Verstraete, V. Murg, and J. I. Cirac, "Matrix product states, projected entangled pair states, and variational renormalization group methods for quantum spin systems," *Advances in Physics*, vol. 57, no. 2, pp. 143–224, 2008.

[81] U. Schollwoeck, "The density-matrix renormalization group in the age of matrix product states," *Annals of Physics*, vol. 326, pp. 96–192, 2011.

[82] S. R. White, "Density matrix formulation for quantum renormalization groups," *Phys. Rev. Lett.*, vol. 69, pp. 2863–2866, 1992.

[83] S. R. White, "Density-matrix algorithms for quantum renormalization groups," *Phys. Rev. B*, vol. 48, pp. 10345–10356, 1993.

[84] S. Östlund and S. Rommer, "Thermodynamic limit of density matrix renormalization," *Phys. Rev. Lett.*, vol. 75, pp. 3537–3540, 1995.

[85] S. Rommer and S. Östlund, "Class of ansatz wave functions for one-dimensional spin systems and their relation to the density matrix renormalization group," *Phys. Rev. B*, vol. 55, pp. 2164–2181, 1997.

[86] F. Verstraete and J. I. Cirac, "Matrix product states represent ground states faithfully," *Phys. Rev. B*, vol. 73, p. 094423, 2006.

[87] G. Vidal, "Efficient classical simulation of slightly entangled quantum computations," *Phys. Rev. Lett.*, vol. 91, p. 147902, 2003.

[88] A. J. Daley, C. Kollath, U. Schollwock, and G. Vidal, "Time-dependent density-matrix renormalization-group using adaptive effective Hilbert spaces," *Journal of Statistical Mechanics: Theory and Experiment*, vol. 2004, no. 04, p. P04005, 2004.

[89] S. R. White and A. E. Feiguin, "Real-time evolution using the density matrix renormalization group," *Phys. Rev. Lett.*, vol. 93, no. 7, p. 076401, 2004.

[90] F. Verstraete, J. J. García-Ripoll, and J. I. Cirac, "Matrix product density operators: Simulation of finite-temperature and dissipative systems," *Phys. Rev. Lett.*, vol. 93, p. 207204, 2004.

[91] I. P. McCulloch, "From density-matrix renormalization group to matrix product states," *Journal of Statistical Mechanics: Theory and Experiment*, vol. 2007, no. 10, p. P10014, 2007.

[92] J. Haegeman, J. I. Cirac, T. J. Osborne, I. Pižorn, H. Verschelde, and F. Verstraete, "Time-dependent variational principle for quantum lattices," *Phys. Rev. Lett.*, vol. 107, p. 070601, 2011.

[93] G. D. las Cuevas, N. Schuch, D. Pérez-García, and J. I. Cirac, "Purifications of multipartite states: limitations and constructive methods," *New Journal of Physics*, vol. 15, no. 12, p. 123021, 2013.

[94] K. Mølmer, Y. Castin, and J. Dalibard, "Monte Carlo wave-function method in quantum optics," *J. Opt. Soc. Am. B*, vol. 10, no. 3, pp. 524–538, 1993.

[95] A. J. Daley, "Quantum trajectories and open many-body quantum systems," *Advances in Physics*, vol. 63, no. 2, pp. 77–149, 2014.

[96] D. Steck, "Alkali D line data, http://steck.us/alkalidata/."

[97] R. Grimm, M. Weidemüller, and Y. B. Ovchinnikov, "Optical dipole traps for neutral atoms," *Advances In Atomic, Molecular, and Optical Physics*, vol. 42, pp. 95 – 170, 2000.

[98] C. Gerry and P. Knight, *Introductory Quantum Optics*. Cambridge University Pr., 2004.

[99] W. Kohn, "Analytic properties of Bloch waves and Wannier functions," *Phys. Rev.*, vol. 115, pp. 809–821, 1959.

[100] T. Giamarchi, *Quantum Physics in One Dimension*. Oxford University Press, 2004.

[101] T. D. Kühner and H. Monien, "Phases of the one-dimensional Bose-Hubbard model," *Phys. Rev. B*, vol. 58, pp. R14741–R14744, 1998.

[102] T. D. Kühner, S. R. White, and H. Monien, "One-dimensional Bose-Hubbard model with nearest-neighbor interaction," *Phys. Rev. B*, vol. 61, pp. 12474–12489, 2000.

[103] P. Richerme, Z.-X. Gong, A. Lee, C. Senko, J. Smith, M. Foss-Feig, S. Michalakis, A. V. Gorshkov, and C. Monroe, "Non-local propagation of correlations in quantum systems with long-range interactions," *Nature*, vol. 511, pp. 198–201, 2014.

[104] P. Jurcevic, B. P. Lanyon, P. Hauke, C. Hempel, P. Zoller, R. Blatt, and C. F. Roos, "Quasiparticle engineering and entanglement propagation in a quantum many-body system," *Nature*, vol. 511, no. 7508, pp. 202–205, 2014.

[105] D. Porras and J. I. Cirac, "Effective quantum spin systems with trapped ions," *Phys. Rev. Lett.*, vol. 92, p. 207901, 2004.

[106] A. Sørensen and K. Mølmer, "Quantum computation with ions in thermal motion," *Phys. Rev. Lett.*, vol. 82, pp. 1971–1974, 1999.

[107] J. G. Bohnet, B. C. Sawyer, J. W. Britton, M. L. Wall, A. M. Rey, M. Foss-Feig, and J. J. Bollinger, "Quantum spin dynamics and entanglement generation with hundreds of trapped ions," *Science*, vol. 352, no. 6291, pp. 1297–1301, 2016.

[108] U. M. Ascher, *Computer Methods for Ordinary Differential Equations and Differential-Algebraic Equations*. Cambridge University Press, 1998.

[109] K. Atkinson, *An Introduction to Numerical Analysis*. John Wiley and Sons (WIE), 1989.

[110] R. B. Sidje, "Expokit: a software package for computing matrix exponentials," *ACM Transactions on Mathematical Software*, vol. 24, no. 1, pp. 130–156, 1998.

[111] T. Kimura, "Explicit description of the zassenhaus formula," *Progress of Theoretical and Experimental Physics*, vol. 2017, no. 4, p. 041A03, 2017.

[112] C. Gardiner and P. Zoller, *Quantum Noise*. Springer, 2004.

[113] G. Vidal, "Class of quantum many-body states that can be efficiently simulated," *Phys. Rev. Lett.*, vol. 101, p. 110501, 2008.

[114] G. Vidal and R. F. Werner, "Computable measure of entanglement," *Phys. Rev. A*, vol. 65, p. 032314, 2002.

[115] M. B. Hastings, "An area law for one-dimensional quantum systems," *Journal of Statistical Mechanics: Theory and Experiment*, vol. 2007, no. 08, p. P08024, 2007.

[116] J. Eisert, M. Cramer, and M. B. Plenio, "Colloquium: Area laws for the entanglement entropy," *Rev. Mod. Phys.*, vol. 82, pp. 277–306, 2010.

[117] C. Holzhey, F. Larsen, and F. Wilczek, "Geometric and renormalized entropy in conformal field theory," *Nuclear Physics B*, vol. 424, no. 3, pp. 443–467, 1994.

[118] P. Calabrese and J. Cardy, "Entanglement entropy and quantum field theory," *Journal of Statistical Mechanics: Theory and Experiment*, vol. 2004, no. 06, p. P06002, 2004.

[119] A. T. Sornborger and E. D. Stewart, "Higher-order methods for simulations on quantum computers," *Phys. Rev. A*, vol. 60, pp. 1956–1965, 1999.

[120] M. L. Wall and L. D. Carr, "Out-of-equilibrium dynamics with matrix product states," *New Journal of Physics*, vol. 14, no. 12, p. 125015, 2012.

[121] J. Haegeman, C. Lubich, I. Oseledets, B. Vandereycken, and F. Verstraete, "Unifying time evolution and optimization with matrix product states," *Phys. Rev. B*, vol. 94, p. 165116, 2016.

[122] E. Dagotto, "Correlated electrons in high-temperature superconductors," *Rev. Mod. Phys.*, vol. 66, pp. 763–840, 1994.

[123] D. Tong, "Lectures on the quantum Hall effect," *arXiv:1606.06687*.

[124] K. Binder and A. P. Young, "Spin glasses: Experimental facts, theoretical concepts, and open questions," *Rev. Mod. Phys.*, vol. 58, pp. 801–976, 1986.

[125] L. Balents, "Spin liquids in frustrated magnets," *Nature*, vol. 464, no. 7286, pp. 199–208, 2010.

[126] A. Kitaev, "Anyons in an exactly solved model and beyond," *Annals of Physics*, vol. 321, no. 1, pp. 2 – 111, 2006.

[127] M. Saffman, T. G. Walker, and K. Mølmer, "Quantum information with Rydberg atoms," *Rev. Mod. Phys.*, vol. 82, pp. 2313–2363, 2010.

[128] K.-K. Ni, S. Ospelkaus, M. H. G. de Miranda, A. Pe'er, B. Neyenhuis, J. J. Zirbel, S. Kotochigova, P. S. Julienne, D. S. Jin, and J. Ye, "A high phase-space-density gas of polar molecules," *Science*, vol. 322, no. 5899, pp. 231–235, 2008.

[129] M. Kolodrubetz, D. Pekker, B. K. Clark, and K. Sengupta, "Nonequilibrium dynamics of bosonic Mott insulators in an electric field," *Phys. Rev. B*, vol. 85, p. 100505, 2012.

[130] M. H. Muñoz Arias, J. Madroñero, and C. A. Parra-Murillo, "Off-resonant many-body quantum carpets in strongly tilted optical lattices," *Phys. Rev. A*, vol. 93, p. 043603, 2016.

[131] J. H. Davies and J. W. Wilkins, "Narrow electronic bands in high electric fields: Static properties," *Phys. Rev. B*, vol. 38, pp. 1667–1680, 1988.

[132] G. L. Bir and G. E. Pikus, *Symmetry and strain-induced effects in semiconductors*. Wiley, 1974.

[133] J. Salas and A. D. Sokal, "Logarithmic corrections and finite-size scaling in the two-dimensional 4-state Potts model," *Journal of Statistical Physics*, vol. 88, no. 3, pp. 567–615, 1997.

[134] A. A. Ovchinnikov, D. V. Dmitriev, V. Y. Krivnov, and V. O. Cheranovskii, "Antiferromagnetic Ising chain in a mixed transverse and longitudinal magnetic field," *Phys. Rev. B*, vol. 68, p. 214406, 2003.

[135] M. Caselle, R. Tateo, and S. Vinti, "Universal amplitude ratios in the 2d four-state Potts model," *Nuclear Physics B*, vol. 562, no. 3, pp. 549 – 566, 1999.

[136] J. J. García-Ripoll, "Time evolution of matrix product states," *New Journal of Physics*, vol. 8, p. 305, 2006.

[137] C. Schneider, D. Porras, and T. Schaetz, "Experimental quantum simulations of many-body physics with trapped ions," *Reports on Progress in Physics*, vol. 75, no. 2, p. 024401, 2012.

[138] B. Yan, S. A. Moses, B. Gadway, J. P. Covey, K. R. A. Hazzard, A. M. Rey, D. S. Jin, and J. Ye, "Observation of dipolar spin-exchange interactions with lattice-confined polar molecules," *Nature*, vol. 501, no. 7468, pp. 521–525, 2013.

[139] A. Micheli, G. K. Brennen, and P. Zoller, "A toolbox for lattice-spin models with polar molecules," *Nature Physics*, vol. 2, no. 5, pp. 341–347, 2006.

[140] P. Schausz, M. Cheneau, M. Endres, T. Fukuhara, S. Hild, A. Omran, T. Pohl, C. Gross, S. Kuhr, and I. Bloch, "Observation of spatially ordered structures in a two-dimensional Rydberg gas," *Nature*, vol. 491, no. 7422, pp. 87–91, 2012.

[141] H. Weimer, M. Muller, I. Lesanovsky, P. Zoller, and H. P. Buchler, "A Rydberg quantum simulator," *Nature Physics*, vol. 6, no. 5, pp. 382–388, 2010.

[142] T. Pohl, E. Demler, and M. D. Lukin, "Dynamical crystallization in the dipole blockade of ultracold atoms," *Phys. Rev. Lett.*, vol. 104, no. 4, p. 043002, 2010.

[143] X.-L. Deng, D. Porras, and J. I. Cirac, "Effective spin quantum phases in systems of trapped ions," *Phys. Rev. A*, vol. 72, no. 6, p. 063407, 2005.

[144] J. Schachenmayer, B. P. Lanyon, C. F. Roos, and A. J. Daley, "Entanglement growth in quench dynamics with variable range interactions," *Phys. Rev. X*, vol. 3, p. 031015, 2013.

[145] P. Hauke and L. Tagliacozzo, "Spread of correlations in long-range interacting quantum systems," *Phys. Rev. Lett.*, vol. 111, p. 207202, 2013.

[146] Z.-X. Gong and L.-M. Duan, "Prethermalization and dynamic phase transition in an isolated trapped ion spin chain," *New Journal of Physics*, vol. 15, no. 11, p. 113051, 2013.

[147] M. B. Hastings and T. Koma, "Spectral gap and exponential decay of correlations," *Commun. Math. Phys.*, vol. 265, no. 3, pp. 781–804, 2006.

[148] J. Eisert, M. van den Worm, S. R. Manmana, and M. Kastner, "Breakdown of quasilocality in long-range quantum lattice models," *Phys. Rev. Lett.*, vol. 111, p. 260401, 2013.

[149] Z.-X. Gong, M. Foss-Feig, S. Michalakis, and A. V. Gorshkov, "Persistence of locality in systems with power-law interactions," *Phys. Rev. Lett.*, vol. 113, p. 030602, 2014.

[150] D.-M. Storch, M. van den Worm, and M. Kastner, "Interplay of soundcone and supersonic propagation in lattice models with power law interactions," *New Journal of Physics*, vol. 17, no. 6, p. 063021, 2015.

[151] M. Foss-Feig, Z.-X. Gong, C. W. Clark, and A. V. Gorshkov, "Nearly linear light cones in long-range interacting quantum systems," *Phys. Rev. Lett.*, vol. 114, p. 157201, 2015.

[152] M. F. Maghrebi, Z.-X. Gong, M. Foss-Feig, and A. V. Gorshkov, "Causality and quantum criticality in long-range lattice models," *Phys. Rev. B*, vol. 93, p. 125128, Mar 2016.

[153] J. Schachenmayer, A. Pikovski, and A. M. Rey, "Dynamics of correlations in two-dimensional quantum spin models with long-range interactions: a

phase-space Monte-Carlo study," *New Journal of Physics*, vol. 17, no. 6, p. 065009, 2015.

[154] M. A. Rajabpour and S. Sotiriadis, "Quantum quench in long-range field theories," *Phys. Rev. B*, vol. 91, p. 045131, Jan 2015.

[155] K. R. A. Hazzard, M. van den Worm, M. Foss-Feig, S. R. Manmana, E. G. Dalla Torre, T. Pfau, M. Kastner, and A. M. Rey, "Quantum correlations and entanglement in far-from-equilibrium spin systems," *Phys. Rev. A*, vol. 90, p. 063622, 2014.

[156] L. Cevolani, G. Carleo, and L. Sanchez-Palencia, "Protected quasilocality in quantum systems with long-range interactions," *Phys. Rev. A*, vol. 92, p. 041603, Oct 2015.

[157] M. Tezuka, A. M. García-García, and M. A. Cazalilla, "Destruction of long-range order by quenching of the hopping range in one dimension," *Phys. Rev. A*, vol. 90, p. 053618, 2014.

[158] A. Y. Kitaev, "Unpaired Majorana fermions in quantum wires," *Physics-Uspekhi*, vol. 44, no. 10S, p. 131, 2001.

[159] B. Pirvu, V. Murg, J. I. Cirac, and F. Verstraete, "Matrix product operator representations," *New Journal of Physics*, vol. 12, no. 2, p. 025012, 2010.

[160] G. M. Crosswhite, A. C. Doherty, and G. Vidal, "Applying matrix product operators to model systems with long-range interactions," *Phys. Rev. B*, vol. 78, no. 3, p. 035116, 2008.

[161] M. Van Regemortel, D. Sels, and M. Wouters, "Information propagation and equilibration in long-range kitaev chains," *Phys. Rev. A*, vol. 93, p. 032311, Mar 2016.

[162] D. Vodola, L. Lepori, E. Ercolessi, and G. Pupillo, "Long-range Ising and Kitaev models: phases, correlations and edge modes," *New Journal of Physics*, vol. 18, no. 1, p. 015001, 2016.

[163] M. Cheneau, P. Barmettler, D. Poletti, M. Endres, P. Schauß, T. Fukuhara, C. Gross, I. Bloch, C. Kollath, and S. Kuhr, "Light-cone-like spreading of correlations in a quantum many-body system," *Nature*, vol. 481, pp. 484–487, 2012.

[164] P. Calabrese, F. H. L. Essler, and M. Fagotti, "Quantum quench in the transverse-field Ising chain," *Phys. Rev. Lett.*, vol. 106, p. 227203, 2011.

[165] T. Holstein and H. Primakoff, "Field dependence of the intrinsic domain magnetization of a ferromagnet," *Phys. Rev.*, vol. 58, pp. 1098–1113, Dec 1940.

[166] P. Calabrese and J. Cardy, "Evolution of entanglement entropy in one-dimensional systems," *Journal of Statistical Mechanics: Theory and Experiment*, vol. 2005, no. 04, p. P04010, 2005.

[167] M. Fagotti and P. Calabrese, "Evolution of entanglement entropy following a quantum quench: Analytic results for the XY chain in a transverse magnetic field," *Phys. Rev. A*, vol. 78, p. 010306, 2008.

[168] F. Iglói and H. Rieger, "Long-range correlations in the nonequilibrium quantum relaxation of a spin chain," *Phys. Rev. Lett.*, vol. 85, pp. 3233–3236, 2000.

[169] D. Rossini, A. Silva, G. Mussardo, and G. E. Santoro, "Effective thermal dynamics following a quantum quench in a spin chain," *Phys. Rev. Lett.*, vol. 102, p. 127204, 2009.

[170] D. Rossini, S. Suzuki, G. Mussardo, G. E. Santoro, and A. Silva, "Long time dynamics following a quench in an integrable quantum spin chain: Local versus nonlocal operators and effective thermal behavior," *Phys. Rev. B*, vol. 82, p. 144302, 2010.

[171] H. Rieger and F. Iglói, "Semiclassical theory for quantum quenches in finite transverse Ising chains," *Phys. Rev. B*, vol. 84, p. 165117, 2011.

[172] P. Calabrese, F. H. L. Essler, and M. Fagotti, "Quantum quench in the transverse field Ising chain: I. time evolution of order parameter correlators," *Journal of Statistical Mechanics: Theory and Experiment*, vol. 2012, no. 07, p. P07016, 2012.

[173] P. Calabrese, F. H. L. Essler, and M. Fagotti, "Quantum quenches in the transverse field Ising chain: II. stationary state properties," *Journal of Statistical Mechanics: Theory and Experiment*, vol. 2012, no. 07, p. P07022, 2012.

[174] D. Schuricht and F. H. L. Essler, "Dynamics in the Ising field theory after a quantum quench," *Journal of Statistical Mechanics: Theory and Experiment*, vol. 2012, no. 04, p. P04017, 2012.

[175] L. Foini, L. F. Cugliandolo, and A. Gambassi, "Dynamic correlations, fluctuation-dissipation relations, and effective temperatures after a quantum quench of the transverse field Ising chain," *Journal of Statistical Mechanics: Theory and Experiment*, vol. 2012, no. 09, p. P09011, 2012.

[176] F. H. L. Essler, S. Evangelisti, and M. Fagotti, "Dynamical correlations after a quantum quench," *Phys. Rev. Lett.*, vol. 109, p. 247206, 2012.

[177] M. Fagotti and F. H. L. Essler, "Reduced density matrix after a quantum quench," *Phys. Rev. B*, vol. 87, p. 245107, 2013.

[178] J.-S. Caux and F. H. L. Essler, "Time evolution of local observables after quenching to an integrable model," *Phys. Rev. Lett.*, vol. 110, p. 257203, 2013.

[179] J. Vidal, G. Palacios, and C. Aslangul, "Entanglement dynamics in the Lipkin-Meshkov-Glick model," *Phys. Rev. A*, vol. 70, p. 062304, 2004.

[180] J. Wilms, J. Vidal, F. Verstraete, and S. Dusuel, "Finite-temperature mutual information in a simple phase transition," *Journal of Statistical Mechanics: Theory and Experiment*, vol. 2012, no. 01, p. P01023, 2012.

[181] J. I. Latorre, R. Orús, E. Rico, and J. Vidal, "Entanglement entropy in the Lipkin-Meshkov-Glick model," *Phys. Rev. A*, vol. 71, p. 064101, 2005.

[182] B. P. Lanyon, C. Maier, M. Holzäpfel, T. Baumgratz, C. Hempel, P. Jurcevic, I. Dhand, A. S. Buyskikh, A. J. Daley, M. Cramer, M. B. Plenio, R. Blatt, and C. F. Roos, "Efficient tomography of a quantum many-body system," *arXiv:1612.08000 (accepted for publication in Nature Physics)*.

[183] F. G. S. L. Brandão and M. Horodecki, "An area law for entanglement from exponential decay of correlations," *Nature Physics*, vol. 9, no. 11, pp. 721–726, 2013.

[184] F. G. S. L. Brandão and M. Horodecki, "Exponential decay of correlations implies area law," *Commun. Math. Phys.*, vol. 333, no. 2, pp. 761–798, 2015.

[185] B. Nachtergaele and R. Sims, "Much ado about something: Why Lieb-Robinson bounds are useful," in *IAMP News Bulletin*, pp. 22–29, 2010.

[186] S. T. Flammia and Y.-K. Liu, "Direct fidelity estimation from few Pauli measurements," *Phys. Rev. Lett.*, vol. 106, no. 23, p. 230501, 2011.

[187] M. P. da Silva, O. Landon-Cardinal, and D. Poulin, "Practical characterization of quantum devices without tomography," *Phys. Rev. Lett.*, vol. 107, no. 21, p. 210404, 2011.

[188] P. Jurcevic, P. Hauke, C. Maier, C. Hempel, B. P. Lanyon, R. Blatt, and C. F. Roos, "Spectroscopy of interacting quasiparticles in trapped ions," *Phys. Rev. Lett.*, vol. 115, p. 100501, 2015.

[189] H. Haffner, W. Hansel, C. F. Roos, J. Benhelm, D. Chek-al kar, M. Chwalla, T. Korber, U. D. Rapol, M. Riebe, P. O. Schmidt, C. Becher, O. Guhne, W. Dur, and R. Blatt, "Scalable multiparticle entanglement of trapped ions," *Nature*, vol. 438, no. 7068, pp. 643–646, 2005.

[190] T. Baumgratz, A. Nüßeler, M. Cramer, and M. B. Plenio, "A scalable maximum likelihood method for quantum state tomography," *New Journal of Physics*, vol. 15, no. 12, p. 125004, 2013.

[191] M. B. Plenio, "Logarithmic negativity: A full entanglement monotone that is not convex," *Phys. Rev. Lett.*, vol. 95, p. 090503, 2005.

[192] M. Ježek, J. Fiurášek, and Z. c. v. Hradil, "Quantum inference of states and processes," *Phys. Rev. A*, vol. 68, p. 012305, 2003.

[193] T. Baumgratz, D. Gross, M. Cramer, and M. B. Plenio, "Scalable reconstruction of density matrices," *Phys. Rev. Lett.*, vol. 111, no. 2, p. 020401, 2013.

[194] I. H. Kim, "On the informational completeness of local observables," *arXiv:1405.0137*, 2014.

[195] A. S. Buyskikh, L. Tagliacozzo, D. Pekker, C. A. Hooley, D. Schuricht, and A. J. Daley, "Spin model for 2-site resonant tunneling dynamics of bosons in a tilted optical superlattice," *In preparation, to be submitted to Phys. Rev. Lett.*, 2017.

[196] A. S. Buyskikh, L. Tagliacozzo, D. Pekker, C. A. Hooley, D. Schuricht, and A. J. Daley, "Spin models for resonant tunneling dynamics of bosons in tilted optical lattices," *In preparation, to be submitted to Phys. Rev. A*, 2017.

[197] C. Monroe and J. Kim, "Scaling the ion trap quantum processor," *Science*, vol. 339, no. 6124, pp. 1164–1169, 2013.